A Study of Raman Spectroscopy as a Clinical Diagnostic Tool for the Detection of Lynch Syndrome/Hereditary Non-Polyposis Colorectal Cancer (HNPCC)

Riana Gaifulina

Department of Cell and Developmental Biology

University College London

Submitted for the degree of Doctor of Philosophy

September 2016

Committee in charge:

Primary Supervisor: Prof. Geraint Thomas

Secondary Supervisor: Dr Manuel Rodriguez-Justo

Industrial Supervisor: Dr Katherine Lau

Dr Catherine Kendall

Signed declaration

I, Riana Gaifulina confirm that the work presented in this thesis is my own.

Where information has been derived from other sources, I confirm that this has been indicated in the thesis.

Abstract

Lynch syndrome also known as hereditary non-polyposis colorectal cancer (HNPCC) is a highly penetrant hereditary form of colorectal cancer that accounts for approximately 3% of all cases. It is caused by mutations in DNA mismatch repair resulting in accelerated adenoma to carcinoma progression. The current clinical guidelines used to identify Lynch Syndrome (LS) are known to be too stringent resulting in overall underdiagnoses. Raman spectroscopy is a powerful analytical tool used to probe the molecular vibrations of a sample to provide a unique chemical fingerprint. The potential of using Raman as a diagnostic tool for discriminating LS from sporadic adenocarcinoma is explored within this thesis.

A number of experimental parameters were initially optimized for use with formalin fixed paraffin embedded colonic tissue (FFPE). This has resulted in the development of a novel cost-effective backing substrate shown to be superior to the conventionally used calcium fluoride (CaF_2). This substrate is a form of silanized super mirror stainless steel that was found to have a much lower Raman background, enhanced Raman signal and complete paraffin removal from FFPE tissues.

Performance of the novel substrate was compared against CaF_2 by acquiring large high resolution Raman maps from FFPE rat and human colonic tissue. All of the major histological features were discerned from steel mounted tissue with the benefit of clear lipid signals without paraffin obstruction. Biochemical signals were comparable to those obtained on CaF_2 with no detectable irregularities.

By using principal component analysis to reduce the dimensionality of the dataset it was then possible to use linear discriminant analysis to build a classification model for the discrimination of normal colonic tissue (n=10) from two pathological groups: LS (n=10) and sporadic adenocarcinoma (n=10). Using leave-one-map-out cross-validation of the model classifier has shown that LS was predicted with a sensitivity of 63% and a specificity of 89% - values that are competitive with classification techniques applied routinely in clinical practice.

Acknowledgements

This work was funded in part by the UCL IMPACT Scheme and Renishaw plc (Spectroscopy Division), and involved collaboration between Gloucestershire Biophotonics Research Units.

First and foremost I would like to extend my sincerest gratitude to my primary supervisor Prof. Geraint Thomas, without whom this would not have been possible. Thank you for all your patience, motivation, and immense support through this very bumpy journey. I am especially indebted to my industrial supervisor Dr Katherine Lau, whose immense knowledge and witty personality has helped shape me into the researcher I hope to become. I would also like to thank my secondary supervisory Dr Manuel Rodriguez-Justo for his help with the clinical aspects of the work, insightful comments and support. In addition, I would also like to extend my gratitude to our collaborators Dr Gavin Lloyd and Dr Catherine Kendall. I am especially thankful to Dr Lloyd for his endless support with Matlab. I could not have imagined a better combination of mentors during my Ph.D. study.

Besides my advisors, I would like to thank the Renishaw team for their help and hospitality upon my visits. In particular, Dr Tim Batten for helping me with my AFM measurements and Dr Stephanie Ohrel for her continuous instrumental support in keeping the Raman system in check. I would also like to show my appreciation to Mr Robert Brown for his continuous motivation and insightful comments during my late night measurements at Renishaw. I am particularly indebted to Dr Ian Bell for helping to run my data through the Renishaw Data Classification Tool.

In addition I would like to show my appreciation to Mr Mark Turmaine for help with SEM imaging and Dr Richard Thorogate for assisting with my contact angle measurements. I would also like to extend my gratitude to Mr Martyn Towner and Dr Alan Philcox for keeping me safe from my crazy idea of using piranha solution. Without your help I would probably be missing a digit or two.

I would like to acknowledge the UCL/UCLH Biobank for Studying Health and Disease for providing access to all the human tissue samples used

within this study. I am especially thankful to Dr Joanne McDonald for helping me push through the last part of my application after much delay.

I would like to express my gratitude to the entire Advanced Diagnostics team at UCLH. In particular, Ms Amanda Simione and Mrs Surekha Gajree for helping me cut my samples in the early stages of my PhD and their helpful hints and tips on cutting my own paraffin blocks. Ms Gabrielle Elshtein for training me to use the microtome, Mr Pep Linares for always making me feel welcome in AD (and lending me his keys) and last but not least Dr Naomi Guppy for helping me with all my histochemical staining. It has been an absolute pleasure learning from you all.

I would like to thank my fellow lab members, in particular Gordon Walsh, Robert Stanley, Myriam Leon and Dr Mae Woods. Without their support and encouragement my Matlab struggles would have been far more depressing. I am especially thankful to Mr Andrew Maher, who I have thoroughly enjoyed working with to produce my first original paper. Thank you for all your patience, helpful discussion and tutoring to help me gain a better understanding of the world of coding.

I would like to thank Dr Sandra Martelli for keeping me sane during office hours through our shared love and admiration of cats, and on a more serious note for her advice and insightful comments on formalin fixation. In addition, I would like to express my utmost gratitude to Prof. Tim Arnett for sharing his lab space with me and always finding the time to shed some much needed wisdom and knowledge.

I would also like to thank Dr James Nelson, who unfortunately is no longer with us but has been a true inspiration during the final stages of my thesis. Your enthusiasm and perseverance to help me get to grips with Matlab has been second to none.

Most of all I would like to thank my mum Rosa and partner Lewis for their patience and love to help me get through my Ph.D. with my sanity relatively intact. I cannot apologize enough for all the moodiness and short fuses in my final year, all I can say is, I have learnt a lot from it.

This thesis is dedicated to my mother, Rosa Gaifulina, who has provided her support and encouragement during the hardest of times.

Contents

List of Figures

List of Tables

List of Abbreviations

AFM	Atomic force microscopy
ANN	Artificial Neural Networks
ANOVA	Analysis of variance
APES	3-aminopropyltriethoxysilane
AUC	Area under the curve
CA	Contact angle
CARS	anti-Stokes Raman Scattering
CCD	Charge coupled device
CD	Crohn's disease
CRC	Colorectal cancer
DA	Discriminant analysis
DAB	3,3′-Diaminobenzidine
EMSC	Extended Multiplicative Scatter Correction
FAP	Familial Adenomatous Polyposis
FFPE	Formalin Fixed Paraffin Embedded
FFT	Fast Fourier Transform
FN	False negatives
FP	False Positives
FTIR	Fourier Transform Infrared Spectroscopy
FWHM	Full width half maximum

HCA	Hierarchical Cluster Analysis
HNPCC	Hereditary Non-Polyposis Colorectal Cancer
IBD	Irritable bowel syndrome
ICC	Interstitial cells of Cajal
IHC	Immunohistochemistry
KMCA	K-Means Cluster Analysis
KNN	K nearest neighbour analysis
kNN	k-Nearest Neighbour Algorithm
LDA	Linear Discriminant Analysis
LOMO	Leave one map out
LS	Lynch Syndrome
MAP	MUTYH-associated polyposis
MCR-ALS	Multivariate curve resolution-alternating least square
MMR	Mismatch repair
MSI	Microsatellite instability
MSI-H	High microsatellite instability
MSI-L	Low microsatellite instability
NA	Numerical aperture
NIR	Near Infrared Raman Spectroscopy
PC	Principal Component
PCA	Principal Component Analysis
PCR	Principal Component Regression

PLS	Partial least-squares
PTFE	Polytetrafluoroethylene sheet
ROC	Receiver operator characteristic
SEM	Scanning electron microscopy
SERDS	Shifted excitation Raman difference spectroscopy
SNR	Signal to Noise ratio
SVD	Singular value decomposition
SVM	Support Vector Machines
TN	True negatives
TNM	Tumour-Nodes-Metastasis classification
TP	True positives
UC	Ulcerative colitis
UVRR	Ultraviolet resonance Raman
WD	Working distance

Chapter One

Introduction

1.1 Colorectal cancer

1.1.1 Epidemiology

Colorectal cancer (CRC) also known as bowel cancer encompasses cancers of the large colon and rectum. It is one of the major malignancies of the western world, ranking third worldwide and fourth in the UK. In 2013, around 41,112 new cases of bowel cancer were registered in the UK, 22,957 (56%) in men and 18,155 (44%) in women. With over 1.3 million new cases occurring worldwide and 690,000 deaths annually, CRC is the fourth most common cause of cancer deaths worldwide. Bowel cancer incidence rates over time have undergone a gradual increase by 14% in Great Britain since the late 1970s, with a slightly larger increase in men over women (1). Figure 1.1 depicts the age-standardised incidence rates for Great Britain between 1979 and 2013.

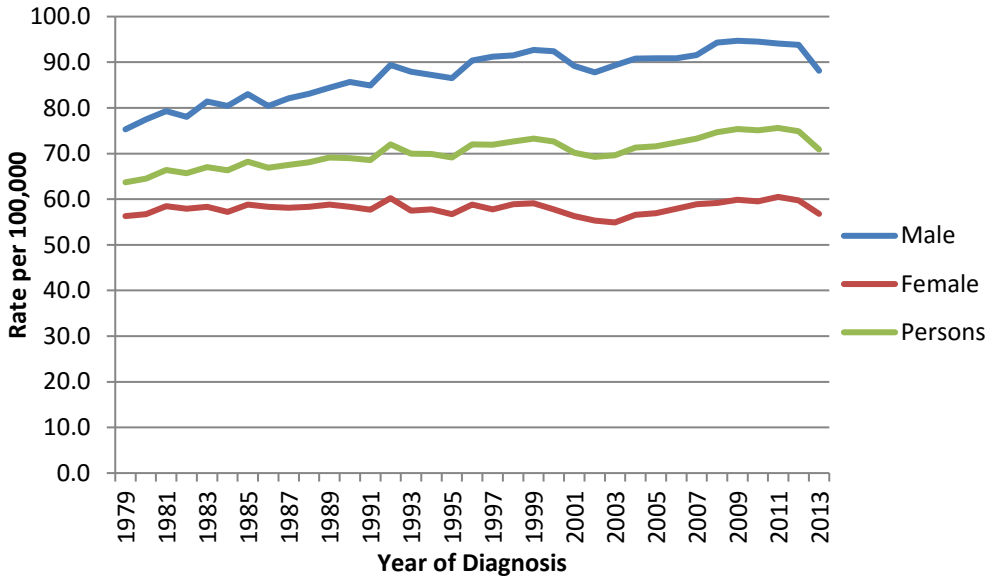

Figure 1.1: European age-standardised incidence rates of colorectal cancer occurrence between 1979 and 2013 in Great Britain (1).

Approximately 60-70% of all cases are of sporadic origin with no previous family history of the disease, 15-30% are familial cancers with a multifactorial inheritance pattern where a combination of genes and environmental factors govern the risk of cancer development. The remaining 5-6% arise from highly penetrant well-defined inherited syndromes, the most common being Lynch Syndrome (LS) that accounts for 1-3% of all CRCs. Other rarer hereditary

conditions include Familial Adenomatous Polyposis (FAP) which accounts for less that 1% of CRCs. Attenuated FAP, juvenile polyposis syndrome, Peutz-Jeghers, Cowden Syndrome and MUTYH-associated polyposis (MAP) are even rarer (2,3). It is therefore quite clear that colorectal cancer within itself is a multi-pathway disease and correct recognition and associated management will dramatically impact the survival of those affected.

1.1.2 Structure and function of a healthy colon

To gain a better understanding of CRC we must first look into the structure of the colon as well as its basic function.

1.1.2.1 Macroscopic features

At approximately 1.5 metres in length the colon is subdivided into six interconnected regions: cecum, ascending colon, transverse colon, descending colon, sigmoid colon and rectum (*fig.1.2*). The colon is essentially a waste processing plant receiving some 600-700 ml of chime each day along with approximately 1-2 litres of water. Around 90% of total water content is absorbed by the ascending portion of the colon, while the descending portion and rectum are responsible for the storage of solid faecal matter. Under stress the colon can be pushed to absorb an impressive 5-6 litres of water. Not only responsible for the absorption of water and electrolytes from the waste it also plays a pivotal role in the salvage and processing of proteins and carbohydrates that escape digestion in the foregut. In addition, around 400 different strains of bacteria (the microbiome) reside in the colon and assist in the fermentation of the starches and proteins (4,5).

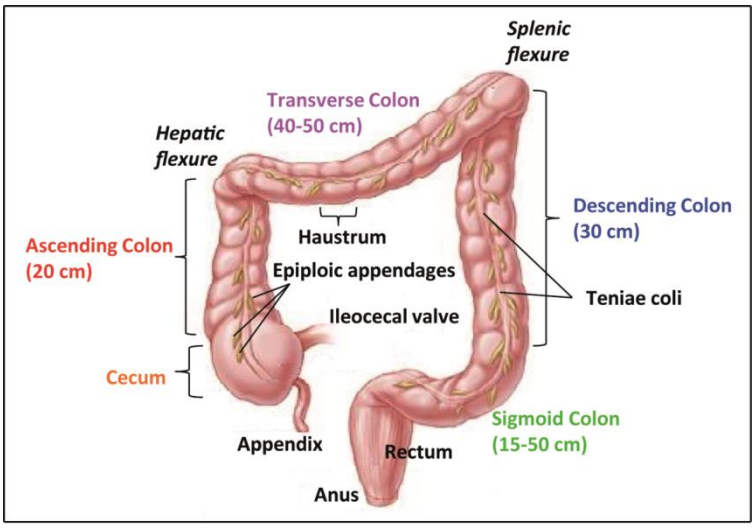

Figure 1.2: Diagrammatic representation of a normal healthy colon (adapted from (6)).

The distribution of cancer throughout the colon also varies. The greatest proportions of cancers occur in the rectum and sigmoid colon, with recorded estimates of ~29% and ~18%, respectively. Other less prevalent sites include the cecum with around ~13% and rectosigmoid junction with 7%. The remaining anatomical sites have a cancer occurrence of 5% and less – ascending colon (5%), transverse colon (4%), hepatic flexure (2%), splenic flexure (2%), descending colon (2%), anus (2%) and appendix (1%) (7).

1.1.2.2 Microscopic features

Taking a cross section through the colon reveals several distinct layers: the mucosa, muscularis mucosa, submucosa, muscularis propria and the serosa (*fig.1.3*). The mucosa is the workhorse of the large intestine and is the most critical structure in the initiation and progression of cancer.

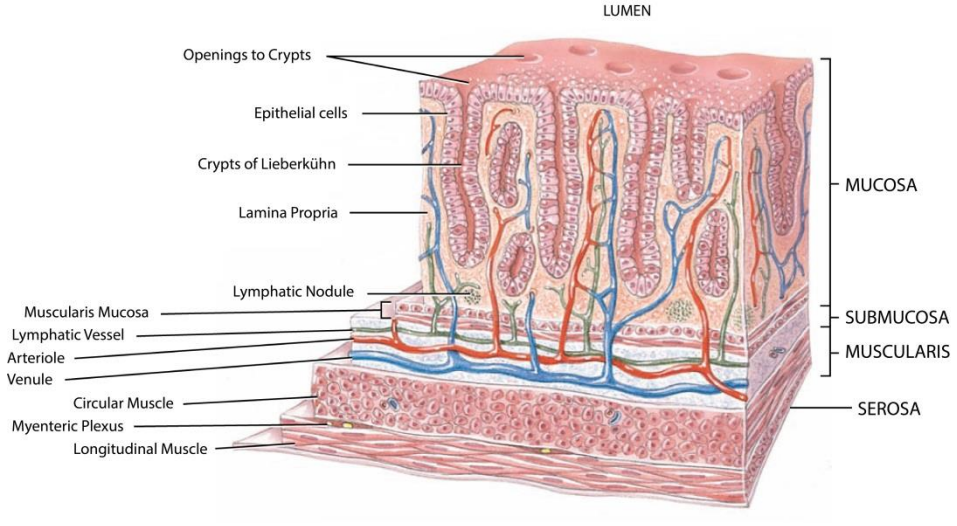

Figure 1.3: Three dimensional representation of the full thickness of the colonic wall (8).

The innermost region of the colon contains the mucosa lined with multiple crypts of Lieberkühn; this region is known to provide the critical barrier between the interior of the host and the microbiome contained within the lumen. At the interface between each crypt lies the lamina propria which contains a wide variety of cells arranged among loosely organized strands of collagen. The cells confined to the lamina propria are responsible for local host defence in the event of a breach by harmful agents delivered through the lumen. The predominant cells types are plasma cells (B-cells) and T-lymphocytes, with the majority of the T-cells being helper/suppressor cells with a small percentage of killer cells. Macrophages are also commonly found here and are responsible for the processing and presentation of antigenic materials. Another common feature of the mucosa are lymphoid follicles known as lymphoglandular complexes, these are thought to play a crucial part in the immune protection of the mucosa (9–11).

The mucosa sits on a thin layer of muscle known as the muscularis mucosa, contractions of this region deforms the mucosa and is thought to contribute to the absorptive, secretory and proliferative processes of the epithelium. Below this is the submucosa with similar constituents to the lamina propria. Here, reside lymphocytes, plasma cells, fibroblasts and lipid cells along with other structures such as arterioles, venules, lymphatics and larger blood vessels. Just below the muscularis mucosa lies

the submucosal plexus of Meissner composed of neurons and glial cells intermingled among the stromal elements (9).

Beneath the submucosa lies the external smooth muscle layer organised into the inner circular muscle and outer longitudinal muscle. Between these two muscle layers lies some more neural tissue commonly known as the myenteric plexus, which is encapsulated in a connective tissue capsule. Contraction of this layer allows the luminal contents to be pushed along the colonic passage. The outermost region of the muscle is composed of a thin layer of connective tissue encased by a serosal lining of mesothelial cells (9).

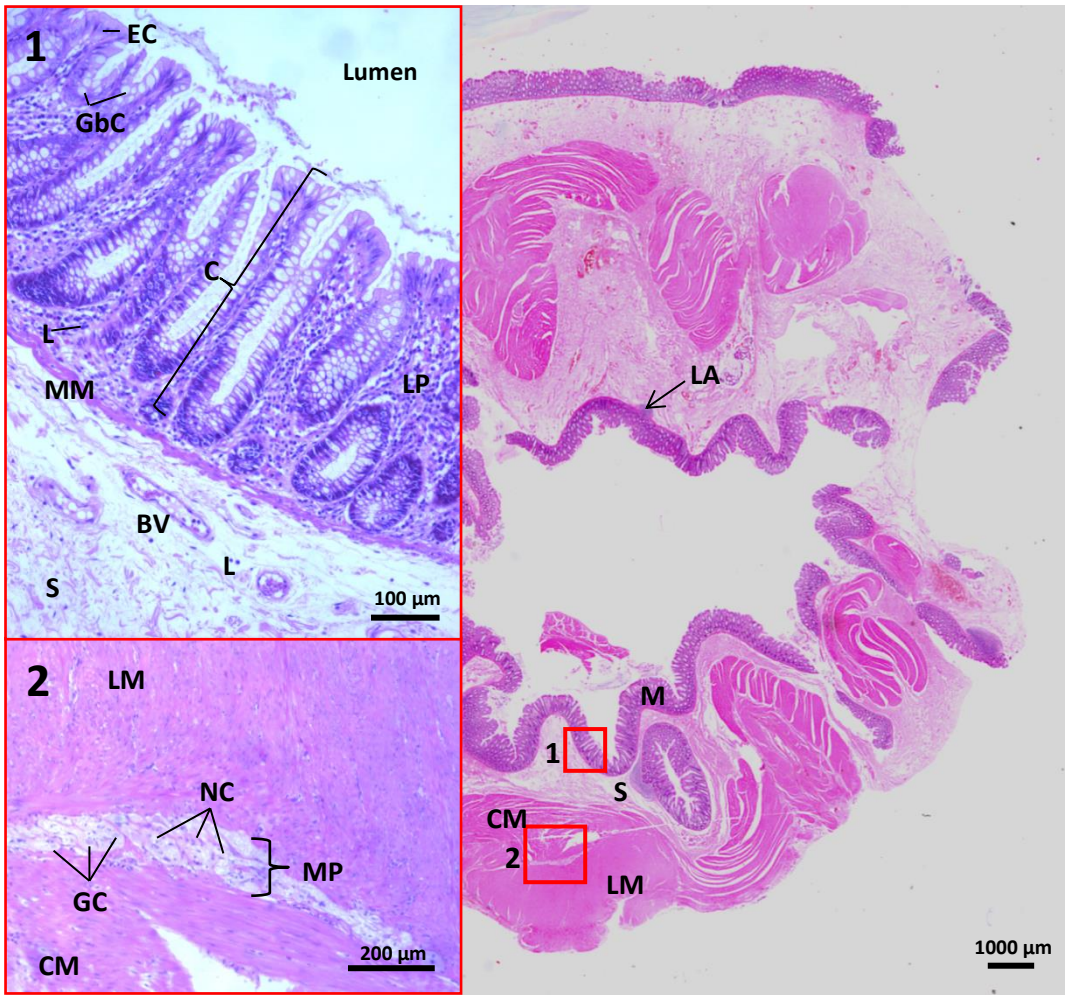

Figure 1.4: Annotated H&E of normal human colonic resection, red boxes indicated magnified regions. *Region 1 is a 10x magnification of the mucosa, region 2 is a 5x magnification of the muscle transition. M: mucosa, S: submucosa, CM: circular muscle, LM: longitudinal muscle, LA: lymphoid aggregate, EC: epithelial cells, GbC: goblet cells, L: lymphocytes, C: crypt, LP: lamina propria, MM: muscularis mucosa, BV: blood vessels, NC: nerve cells, GC: ganglion cells, MP: myenteric plexus.*

The extent of disease is often characterised by the invasion of the cancer through the colon wall. A tumour-nodes-metastasis (TNM) classification of CRC has become a well-established and preferred staging system. Early cancers are classified as Tis and are confined within the mucosa with no extension through the muscularis mucosa. T1 tumours invade the submucosa, whilst T2 invade the muscularis propria, T3 tumours invade through the muscularis propria into the subserosa or into the pericolic or perirectal tissue. The final stage T4, is characterised by the invasion of other organs or structures and/or perforation into the peritoneum. The other parameters that are taken into consideration in this staging system is the involvement of regional lymph nodes and distant metastasis (12,13).

1.1.2.3 Crypt cell populations

The average crypt in the human large bowel is believed to be about 80 cells in height in both the colon and rectum. The mean crypt circumference is approximately 40 cells in the sigmoid colon and 45 in the rectum. This gives a total of about 2040 cells per crypt in the colon and 2190 cells per crypt in the rectum (14). The average crypt height is estimated to be around 360 ± 80 μm following standard histological processing (15).

There are five terminally differentiated cell types within the crypt: the colonocytes (absorptive enterocytes), goblet cells, enteroendocrine cells and tuft cells. Unlike the small intestine there is a general absence of Paneth cells, however a small number can be found confined to the cecum and proximal colon (16). A recent study has demonstrated the presence of Paneth-like goblet cells at the base of the crypt that express unique factors capable of supporting the stem cell niche (17). At the base of the crypt lies the stem cell niche with approximately 19 multi-potent stem cells that undergo self-renewal and repopulate the whole crypt cell population. It is believed that the first mutational hit occurs in these long-lived stem cells that gradually accumulate oncogenic mutations. Once transformation these cancer stem cells then go on to colonize the stem cell niche and give rise to new proliferating cancer cells (18–20).

Refer to table 1.1 for a comprehensive list of the microscopic structures, cell populations and functions across all the layers of the colon.

Table 1.1: Microscopic colon structures, composition and the associated functions

Region	Sub region	Composition	Function	Reference
Mucosa	Crypts of Lieberkühn	Epithelial cells	Serves a protective role between the host and its luminal environment. Responsible for water absorption at the luminal edge.	(21)
		Goblet cells	Synthesize, store and secrete mucous granules by exocytosis.	
		Enteroendocrine cells	Secrete hormones.	
		Tuft cells	Role is poorly understood, but thought to secrete opioids and enzymes necessary for prostaglandin synthesis.	
		Paneth cells	Only present in the cecum and ascending colon.	
		Transit amplifying cells	Precursor cells of all cell populations residing in the crypt.	
		Stem cells	Repopulate all crypt cell populations.	
	Basement membrane	50% type IV collagen,	To separate the cells of the crypts from the underlying connective tissue of the lamina propria.	(22,23)
		Heparin sulphate proteoglycans		
		Laminin		
		Nidogen/entactin		
	Lamina propria	Collagen type I, III, IV and V	Lamina propria supports the delicate mucosal epithelium and provides for immune defence. Inflammatory cells fill between 30% to 50% of the 'free' lamina propria space. Fibroblasts within the lamina propria are responsible for collagen secretion into the surrounding space.	(21), (24), (9,25)
		Elastin		
		T and B lymphocytes, eosinophils, plasma cells, mast cells, macrophages and some neutrophils		
		Fibroblasts		
		Lymphatic channels, capillary beds and peripheral nerves		

Muscularis mucosa	-	Muscle cells Submucosal plexus Is traversed by lymphoglandular complexes, vascular channels and neural twiglets	Responsible for the separation of the mucosa from the deeper submucosa. Contractions of this layer facilitate absorptive, secretory and proliferative functions of the epithelium.	(24), (9)
Submucosa	-	Collagen type I and III Blood vessels and lymphatics Ganglion cells Few lymphocytes, plasma cells, fibroblasts and macrophages Few smooth muscle bundles Little adipose tissue	Connective tissue layer responsible for supporting the mucosa, allowing a degree of flexibility during peristalsis. It also binds the mucosa to the bulk of the muscular wall.	(9,21,24)
Muscularis Propria	Inner circular muscle Outer longitudinal muscle	Smooth muscle cells Collagen fibrils (type I and III) Myenteric plexus (neurons and glial cells surrounded by stroma) Interstitial cells of Cajal (ICCs) Blood vessels and lymphatics	Coordinated contraction of these muscle layers is responsible for rhythmic peristalsis. The contractions of the taeniae coli and circular muscle layers draws the colon into sacculations called haustra.	(24), (26)
Serosa	-	Mesothelial cells Connective tissue	The serosa reduces friction from muscle movement via secretion of serous fluid.	(21)

1.1.2.4 Crypt dynamics

The entire colonic mucosa undergoes complete renewal with a turnover time estimated to be between 4-8 days in humans. All the cells that populate the crypts arise from a small population of stem cells that reside at the base of the crypt. There is a distinct level of organisation along the full length of the crypt with designated zones, which are stringently controlled by various signals from surrounding cells. The cellular proliferative activity varies depending on the location within the crypt and hence gives rise to four distinct regions (*fig.1.5*):

1. Stem cell zone
2. Proliferative zone
3. Transitional zone
4. Mature cell zone

Within the stem cell zone the overall proliferative activity remains relatively low and the duration of the cell cycle is substantially longer compared to the stem cell progenitor counterpart (14,27,28). However, each stem cell can give rise to a progenitor cell type called the transit amplifying cells, known for their highly proliferative nature. These cells reside within the proliferative zone just above the stem cell zone and here the proliferative activity is at its peak. As the cells undergo rapid DNA synthesis they also simultaneously undergo rapid upward migration towards the lumen. As the cells enter the transitional zone DNA synthesis and mitosis ends and the cells begin to differentiate and mature. Proliferative activity almost ceases two-thirds of the distance up the length of the crypt (28). This continuous proliferation of cells at the base of the crypt and migration along the crypt length towards the colonic lumen serves to replace cells sloughed off into the lumen and lost from the body as part of the normal operation of the colon.

Expansion of the proliferative zone has previously been shown to be a good prognostic indicator of the frequency of adenoma formation and an individual's increased susceptibility to the development of CRC (29). Such expansion has also been observed from hereditary forms of CRC, namely FAP (30).

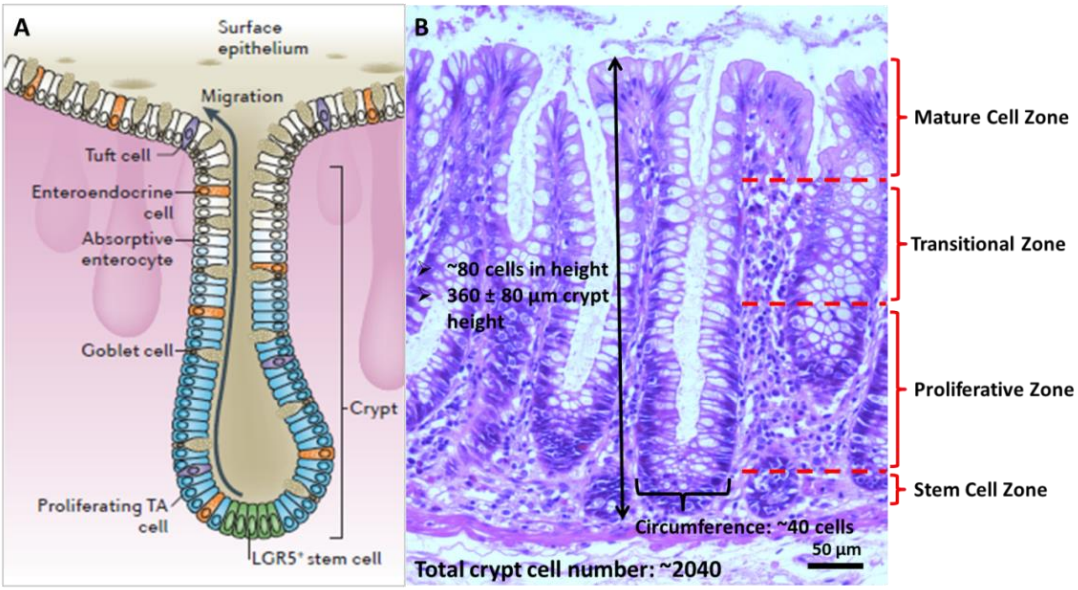

Figure 1.5: *A) Annotated diagrammatic representation of a colonic crypt* ***(19)****. B) H&E stained magnification of a normal human colonic crypt with marked subdivisions of the different zones within the crypt.*

1.2 Colorectal cancer pathways

In colorectal cancer, there are at least three distinct genomic instability pathways:

1. Chromosomal Instability (CIN)
2. Microsatellite Instability (MSI)
3. CpG island methylator phenotype (CIMP)

Chromosomal instability also referred to as the classic adenoma-to-carcinoma pathway is by far the most common cause of colorectal tumours, accounting for approximately 80-85% of all cases. It is characterised by a large heterogeneity in chromosomal copy number (aneuploidy) as well as structure, and a general loss of heterozygosity (LOH). CIN is thought to be correlated with inactivation of at least three tumour suppressor genes: Adenomatous polyposis coli (APC), TP53 and heterozygosity for the long arm of chromosome 18 (e.g. SMAD4). Inactivation of APC results in inappropriately and constitutively activated Wnt signalling known to control cellular activation, this is regarded as the initiating event in CRC. Inactivation of the p53 pathway, which is the second key genetic step in CRC development results in the loss of cell-cycle arrest and cell-death checkpoints

(31,32). LOH is defined as the loss of one of the two copies or alleles of a gene, around 70% of CRCs exhibit a loss of the DCC (Deleted in Colorectal Cancer) gene resulting in abnormal cell survival as well as SMAD4 resulting in tumorigenesis via the transforming growth factor β (TGFβ) pathway (32,33). CIN also constitutes to activation of proto-oncogenes such as KRAS, vital in cell division, cell differentiation, and apoptosis (33). Despite the fact that CIN based tumours are the most frequent, the general understanding of the underlying mechanisms of CIN are rudimentary (34).

Microsatellite instability exhibits frequent mutations in short tandem repeat fragments of DNA sequence, commonly known as micro-satellites. These are often a result of defective DNA mismatch repair proteins that correct errors that have been missed by the proofreading function of DNA polymerase. MSI is the hallmark of Lynch Syndrome LS. Unlike CIN-based tumours, MSI tumours are near-diploid with few karyotypic abnormalities (32). However, around 15-20% of all sporadic CRC cases are related to MSI and are caused by silencing of the MMR gene MLH1 by promoter methylation, this is known as the CpG island methylator phenotype. These tumour subclasses also commonly have BRAFV600E mutations (35). As a result, these tumour subtypes may be mistaken for germline mutations in MMR genes characteristic of LS.

1.3 Lynch Syndrome

1.3.1 Prevalence and penetrance

Lynch Syndrome accounts for approximately 1–3% of total CRC burden and is also one of the most prevalent (36). It is known as an autosomal dominant cancer caused by a deleterious germline mutation in one of the four key DNA mismatch repair (MMR) genes: MSH2, MLH1, MSH6 or PMS2. LS mutation carriers are predisposed to a broad spectrum of cancers, especially those of the colorectum and endometrium. The cumulative incidence of developing any cancer was found to be higher at 72% for MLH1 and MSH2 mutation carriers but lower in MSH6 (52%) and PMS2 (18%) mutation carriers. MLH1 and MSH2 mutation carriers tend to develop cancer from 25 years of age and onwards, whereas MSH6 and PMS2 develop no cancer before 40 years of age (*fig.1.6, left panel*) (37).

Although, MMR deficiency has been described in many malignancies (endometrium, ovaries, stomach, uterus) CRC was the most frequent first cancer to be observed. As before, the cumulative incidence of developing CRC was found to be higher at 46% for MLH1 mutation carriers and 35% in MSH2 mutation carriers with lower incidence for carriers of mutations in MSH6 and PMS2 (*fig.1.6,right panel*) (37). The lifetime risk for an MMR mutation carrier to develop colorectal cancer is 78% while for endometrial cancer it is 48% (38).

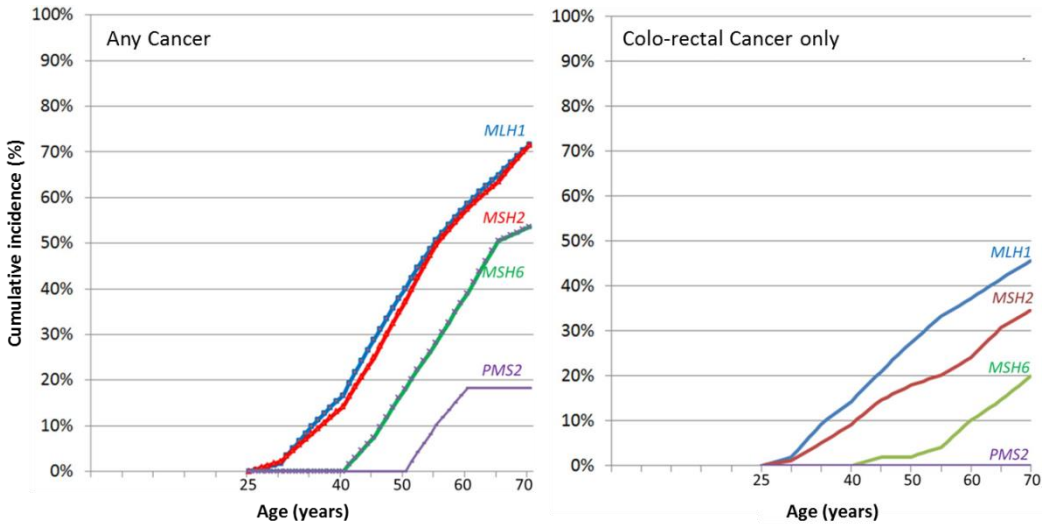

Figure 1.6: The cumulative incidence of developing any cancer (left) and colorectal cancer only (right) by individual MMR mutation (adapted from (37)***).***

1.3.2 Clinical manifestation

Alongside a higher lifetime risk of developing CRC, LS individuals develop cancer at a much earlier age (mean 45 years). The majority of tumours are located in the proximal colon (including caecum, ascending colon, hepatic flexure and transverse colon) with synchronous and metachronous tumours observed in 35% of the patients. In addition to CRCs, there is an excess of extracolonic cancers such as that of the endometrium (second only to colorectal cancer in frequency), ovaries, stomach, small bowel, pancreas, hepatobiliary tract, brain, and upper uroepithelial tract. Tumours originating from LS tend to have an advanced rate of malignant transformation, whereby a small adenoma can develop into CRC in as little as 2-3 years compared to 8-10 years in sporadic CRC (38,39).

1.3.3 Pathological features of LS-associated cancers

Although no individual histologic feature is specific to LS, some features are diagnostically useful. LS cancers are often poorly differentiated, with an excess of mucus (*fig.1.7a*), signet-cell features, medullary growth pattern, a Crohn's like inflammatory reaction and high lymphatic infiltration (*fig.1.7b*) (32). Presenting adenomas tend to be of an advanced stage often showing a characteristic villous component with areas of high-grade-dysplasia (40,41). LS cancers are also found to have a near-diploid DNA content (39,42).

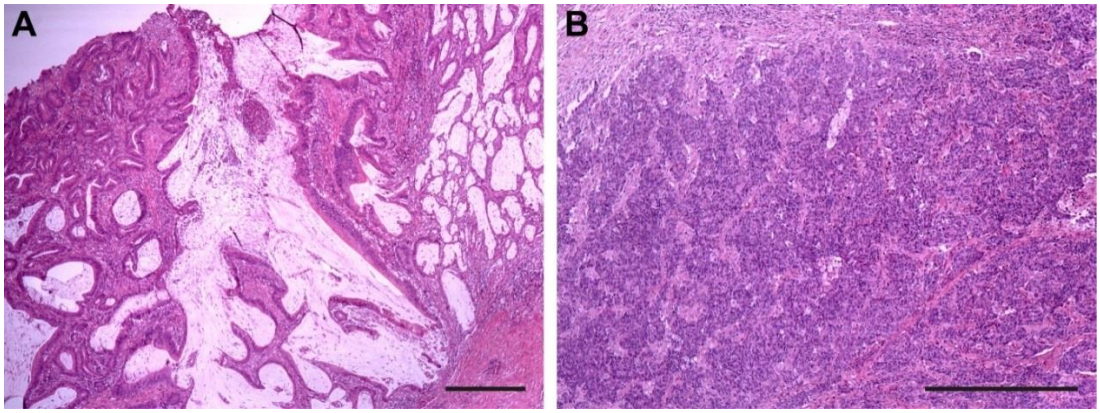

Figure 1.7: Histologic features of LS-associated cancers. A) *Moderately differentiated mucinous cancer with large extracellular mucin pools.* ***B)*** *Tumour infiltrating lymphocytes in poorly differentiated LS cancer. Scale: 500 µm.*

1.3.4 Acquired genetic changes in LS

A key molecular feature of LS tumours is microsatellite instability, recognised by the frequent occurrence of insertion and deletion mutations in short tandem repeats known as microsatellite repeats. Microsatellites are small stretches of repetitive DNA, composed of mononucleotide, dinucleotide and trinucleotide tandem repeats. During DNA replication, strand slippage may occur resulting in DNA polymerase stutter, this is more frequently observed in areas of microsatellites. If the MMR proteins are defective as in LS, these errors are not repaired leaving the genome with microsatellites that are longer or shorter than the parent DNA strand. For a tumour to be categorised as 'microsatellite high' (MSI-H), instability needs to be present in over 30% of the markers. MSI occurs in 90% of all LS tumours, however it is important to bear in mind that it is not

unique to LS as somatic inactivation of MLH1 by aberrant methylation causes MSI in approximately 15% of sporadic cancers (32,34,38). CIN-based sporadic tumours are often defined as ‘microsatellite low’ (MSI-L) as instability is only present in 10-29% of the markers (32).

1.3.5 Standardized clinical guidelines for the diagnosis of LS

The Amsterdam criteria provided the first diagnostic guideline developed for the clinical diagnosis of LS and is solely based on family history and age of onset. Table 1.2 lists the gradual evolution of a number of these clinical guidelines as well as an outline of the parameters considered to fulfil the criteria. Amsterdam I was however found to be too stringent and led to the exclusion of some real LS families. Consequently, the Bethesda criteria were developed to provide a set of clinical criteria to identify individuals that did not fulfil the Amsterdam criteria but would benefit from genetic testing for LS. This Bethesda criteria was found to be too unspecific and were later followed by a more stringent Amsterdam II criteria. This modified criteria included extracolonic cancers as well as some minor modifications to apply to very small families. Another revision was later made to the Bethesda guideline to include an additional step before conducting genetic testing. The guideline states that individuals who do not match the revised Amsterdam criteria should first have microsatellite instability or immunohistochemical analysis conducted as a pre-test to determine those who would benefit from genetic testing (38,42).

A study comparing the performance of each of these guidelines found that the sensitivity and specificity for the Amsterdam I criteria was 61% and 67%, respectively. Amsterdam II criteria had a sensitivity and specificity of 72% and 78%, respectively. The most sensitive criteria was found to be the revised Bethesda guidelines with a sensitivity of 94% and specificity of 25% (43). This is not unexpected as it takes the pathophysiological changes into consideration, something the other guidelines lack.

Table 1.2: Standardised clinical criteria for the diagnosis of LS affected individuals (38)**.**

Amsterdam I	**Amsterdam II**
At least one person was diagnosed before the age of 50 years	At least one person was diagnosed before the age of 50 years
At least 3 relatives with histologically confirmed colorectal cancer	There are at least three relatives with an LS-associated cancer (large bowel, endometrium, small bowel, ureter, or renal pelvis)
One affected person is a first-degree relative of the other two	One affected person is a first-degree relative of the other two
At least two successive generations are affected	At least two successive generations are affected
Familial adenomatous polyposis has been excluded	Familial adenomatous polyposis has been excluded
Tumours have been verified by pathologic examination	Tumours have been verified by pathologic examination
Revised Bethesda	
Colorectal cancer diagnosed in a patient who is less than 50 years of age	
Presence of synchronous, metachronous colorectal or other Lynch-associated tumours, regardless of age	
Colorectal cancer with the MSI-H histology diagnosed in a patient who is less than 60 years of age	
Colorectal cancer diagnosed in one or more first-degree relatives with a Lynch associated tumour, with one of the cancers being diagnosed under age 50 years	
Colorectal cancer diagnosed in two or more first- or second-degree relatives with Lynch associated tumours, regardless of age	

1.3.6 Why search for affected individuals?

In light of the diagnostic techniques outlined above it is clear that there is a lack of unique LS-only specific attributes that confidently exclude the possibility of sporadic tumours as a result of chromosomal instability. Although the revised Bethesda criteria proved to be superior in its performance, the low overall specificity suggests that the rate of false positives will be high resulting in laborious and time-consuming molecular testing with no benefit.

A study by Hampel *et al* found that out of 1066 newly diagnosed CRC patients, 208 had MSI, but only 23 had an LS causing mutation (2.2%). Out of

these probands, 10 were over 50 and only 3 fulfilled the Amsterdam criteria emphasising the need for an alternative approach in the identification of LS individuals (44).

A systematic review of the diagnostic strategies for LS further highlight a large degree of variation in the sensitivity and specificity values obtained for IHC and MSI testing. For IHC, the sensitivity ranged between 73.3% and 100.0%, while the specificity was found to be somewhere between 12.5% and 100.0%. For MSI, testing the sensitivity of the collected studies ranged between 88.8% to 100.0%, whilst the specificity was between 68 to 84%. The existence of MLH1 silencing in approximately 15% of sporadic cases lends itself to false-positive LS results (45). This indicates that the overall performance and accuracy of these two molecular tests cannot be confidently established at this time.

An additional benefit to finding individuals with MMR deficiencies lies in the prognostic and prediction implications. Tumours that exhibit high microsatellite instability such as those prevalent in LS have been demonstrated to have better survival rates compared with tumours that have low microsatellite instability prevalent in CIN tumours (46). While the mechanism for this is not fully understood, it is thought that an enhanced antitumor immune response may be a contributing factor (47). Some studies have also shown that deficient MMR tumours do not benefit from 5-fluorouracil-based adjuvant chemotherapy (48). The MMR status can therefore be used to provide valuable prognostic information and therefore predict the outcome of adjuvant chemotherapy.

In conclusion, Lynch Syndrome is already known to be an underdiagnosed hereditary condition and by increasing our efforts to identify these individuals we are more likely to ensure that they benefit from life-saving intensive-care surveillance.

1.4 Evolution of Raman spectroscopic studies in the colon

1.4.1 Tissue analysis

The first reported application of Raman spectroscopy towards colorectal cancer diagnostics dates back to the early 1990s. In 1993 Raman was initially trialled on several bulk tissue types in an attempt to discriminate malignancies from normal tissue counterparts; formalin-fixed colonic tissue was among the few that were tested using UV light (49). A year later a group in Massachusetts USA began to actively

apply Raman for a wide array of tissues with a focus on colorectal material using ultraviolet resonance Raman (UVRR). Manoharan *et al* initially attempted to discriminate frozen normal colonic tissue from adenocarcinoma using UVRR at 250 nm. They found that nucleic acid associated peaks at 1580, 1480 and 1335 cm^{-1} were more pronounced in adenocarcinoma (50).

A more detailed study later revealed that different aspects of the tissue components are more or less pronounced when interchanging between 240 nm and 250 nm. A wavelength at 240 nm is mainly used to selectively enhance the protein components of the tissue (51), while 250 nm is used to selectively enhance the nucleic acid components (52), namely adenine and guanine due to their larger Raman cross section. It was shown that probing the mucosal surface of the tissue using 240 nm illumination reveals an almost identical protein dominated spectra from both the normal mucosa as well as the adenocarcinoma. Furthermore, the 240 nm-based analysis is particularly insensitive to nucleic acid modes and hence was a poor discriminator between normal mucosa and adenocarcinoma. By applying single point measurements at 250 nm they were able to discriminate normal mucosa from adenocarcinoma using nucleic acid band intensity variations at 1485 cm^{-1} and 1335 cm^{-1}, which were shown to be more intense in cancer. This is in agreement with the notion that adenocarcinoma exhibits an increased cellular nuclear content/size. They were further able to show the spectral difference between the mucosa, muscularis mucosa and the peri-colonic fat of the serosa (53). This highlights that careful selection of the excitation wavelength is critical for the diagnostic capabilities of Raman spectroscopy as a whole. Around roughly the same time the same group went on to carry out yet another preliminary study but this time utilizing near-IR Raman spectroscopy on colon, bladder, breast carcinoma tissues (54).

Having established that UVRR can be used to discriminate normal colonic tissue from adenocarcinoma, the same researchers then attempted to use a least square fitting technique to identify the contribution of 10 different biochemical constituents to the overall tissue spectra. Reference spectra of individual nucleotides, aromatic amino acids and lipids were all tested against the tissue spectra. Although the changes in the individual biochemical parameters did not correlate with normal or diseased states, they did establish that the sum of all the nucleotides and the sum of tyrosine and tryptophan amino acids varied

consistently. The nucleotides were found to increase in diseased states, while amino acids were found to decrease (55).

Only in 2000 did the group attempt to analyse the first colon tissue cryosections to establish the diverse spectral signatures from the different anatomical layers (56). This was not only useful in identifying the variability across the colon as a whole but also allowed them to establish where the majority of the signals originated from – a refinement not possible from bulk tissue analysis. Crypt cells were found to be dominated by nucleic acid signals; this was also true for the connective tissue of the lamina propria likely to be caused by the high lymphocyte numbers. The spectrum of the submucosal extracellular matrix was found to resemble collagen with some nucleic acid signals likely to originate from the few lymphocytes cells residing within the submucosa. This prominent study paved the way towards histopathological applications of Raman spectroscopy in colon tissue diagnostics.

Molckovsky *et al* were one of the first groups to assess the diagnostic potential of near infrared (NIR) Raman spectroscopy in 33 polyp samples (57). Using a custom-built, fibre optic probe in combination with principal component analysis and linear discriminant analysis (PCA-LDA) they were able to generate diagnostic algorithms for classifying adenomatous from hyperplastic polyps. Using a leave-one-out cross validation procedure they were able to achieve a sensitivity of 91% and a specificity of 95% in *ex vivo* studies and a sensitivity of 100% and specificity of 89% for *in vivo* study. A similar study by Widjaja *et al* used support vector machines in combination with PCA to classify normal colon from hyperplastic polyps and adenocarcinoma (58). Using a total of 105 colonic specimens (normal: 41, hyperplastic: 18, adenocarcinoma: 46). The performance was exceptional with a sensitivity of 100% and specificity ranging between 98.1%–99.7%. Since then there have been a number of other studies attempting to use multivariate analysis for colorectal cancer classification (59–62).

Chowdary *et al* evaluated the applicability of novel in-house developed discrimination parameters: Mahalanobis distance, spectral residuals, and a multi-parametric limit test to differentiate normal from cancerous colon tissue (63). NIR Raman spectroscopy was applied to 11 normal and 11 malignant *ex vivo* colon tissues. They found that the mean malignant spectra exhibit stronger bands indicating the presence of multiple additional biomolecules such as protein (stronger amide III and I), lipids (1100, 1300 cm^{-1}), and DNA (1340, 1470 cm^{-1}) compared to those

found in normal tissue. The performance of the multi-parametric limit test was found to be exceptional with a sensitivity and specificity of 99.5%. A similar study with a focus on chemometric techniques compared the performance of a number of already existing multivariate statistical tools in their classification of normal and malignant tissues of the breast, cervix, oral cavity, colon and larynx (64). Each model was compared on their classification efficiency defined as the percentage of times the test is correct. There was very little difference in the performance of each classifier with efficiencies above 94.6%. The performance of the limit test however was found to be variable.

Studies that might be considered to be the most comparable in terms of subtlety in biochemical variation to the study proposed in this thesis are those carried out on irritable bowel syndrome (IBD). A study by Bi *et al* showed that two variants of IBD: Crohn's disease (CD) and ulcerative colitis (UC) can be distinguished using a custom designed Raman fibre-optic probe (65). A more detailed study by Bielecki *et al* used support vector machines and a 10-fold cross validation to show that it was possible to separate between healthy controls, CD and UC with an accuracy of 98.9% (66). Bi's group then went on to show that UC and CD can be distinguished using both *in vivo* and *ex vivo* studies resulting in a sensitivity of 75% for UC and 80% for CD (67). This is very promising as these studies demonstrate that it is possible to discriminate variants of a wider inflammatory condition.

Other studies have gone on to use Raman spectroscopy to create label-free annotations of tissues generating false-coloured images to identify the different histological features. Mavarani *et al* used 532 nm excitation to identify the finer features within colonic crypts, namely erythrocytes and lymphocytes (68). They also went on to identify regions which they suspected to be carry p53 mutations. Others compared Raman imaging of normal tissue to other sophisticated techniques such as Fourier Transform Infrared Spectroscopy (FTIR) and Coherent anti-Stokes Raman Scattering (CARS) (69,70). While Lloyd *et al* proposed a novel way of displaying and interpreting data which can significantly enhance the features of a histological section based on biochemical information (71). This was demonstrated on a snap frozen colon polyp section.

Andrade *et al* attempted to use Raman spectroscopy to identify the spectral variance between individuals where colorectal malignancy was absent (72). Three

distinct groups were observed with each found to contain different colon tissue constituents. These results are not unexpected as Raman spectra where not collected from histologically comparable sites. A more recent study by Sylvest Bergholt *et al* performed *in vivo* analysis to discriminate the various normal colorectal anatomical locations (i.e., ascending, transverse, descending, sigmoid, rectum) (73). Partial least-squares (PLS)-discriminant analysis (DA) was used to identify the different sites. The sensitivities SE and specificities SP were as follows: ascending colon: SE: 1.10%, SP: 91.02%; transverse colon: SE: 14.06%, SP: 78.78%; descending colon: SE: 40.32%, SP: 81.99%; sigmoid: SE: 19.34%, SP: 87.90%; rectum: SE: 71.55%, SP: 77.84%. This demonstrates that the spectral variation between the anatomical sites were very subtle, with the rectum being the most distinct.

A few studies have also gone on to explore the effects of experimental and instrumental parameters. The first group to test formalin-fixed tissue was in Leeds, UK using a 782 nm excitation source. Their preliminary results showed that formalin fixation does not alter the observed Raman peaks and is therefore a suitable method of fixation for Raman spectroscopic studies. They then went to identify spectral differences in tissues with varying blood saturations, highlighting that difference in tissue blood content must not be mistakenly correlated to pathological changes (74).

Spectral artefacts from sample freezing and thawing has been reported using colonic tissue snap-frozen in liquid nitrogen and measured using 251 nm excitation (75). A global reduction in adenylate content (1337, 1485, and 1585 cm^{-1}) was observed as a result of freezing and subsequent thawing to room temperature. Photobleaching was shown to be a result of oxidative as well as thermal damage and consisted of a decrease in the intensity of the purine spectral bands as well as broadening and intensity increases of the aromatic amino acid bands.

Several studies have also explored the influence of laser excitation wavelength and optical mode on the quality of the Raman spectra and manifestations of CRC tissue markers. Li *et al* compared the performance of 785 nm vs 830 nm and single mode vs multimode analysis (76). A lower background was achieved using 830 nm when compared against 785 nm at the same optical mode; however this was at the expense of the signal strength and signal to noise ratios (SNR). A comparison of different optical modes for the same excitation showed that single mode is superior, in that the background is reduced and SNR improved. This study emphasizes the importance of careful selection of instrumental parameters that are best suited for the

tissues in question. Synytsya *et al* analysed the impact of different laser excitation wavelengths (532, 785, 1064 nm) on the discrimination of normal colon from CRC (77). It was found that neither of the wavelengths was superior but combinations of all three offer better possibilities for detection of CRC. This is due to the selective signal enhancement of a number of molecular constituents at each wavelength.

1.4.2 Single cell analysis

In addition to whole tissue analysis NIR Raman spectroscopy has been applied to live single cell analysis for CRC diagnosis (78). Living epithelial cells extracted from 8 patients, 20 normal and 20 cancerous cells were measured using near-infrared laser-trapping Raman spectroscopy. By using PCA and a logistic regression algorithm 124 out of 160 cancerous cells and 130 out of 160 normal cells were correctly identified, corresponding to 77.5% sensitivity and 81.3% specificity. The same group then went on to use artificial neural networks to improve the classification achieved using logistic regression (79). The new sensitivity achieved was 86.3% an 8.8% improvement while the specificity improved by 5% to 86.3%. Sensitivity map analysis was also conducted whereby the contribution of the individual vibrational bands to the classification of cancer versus normal was obtained.

Scalfi-Happ *et al* used confocal Raman spectroscopy to identify lipid bodies from colorectal adenocarcinoma cell line Caco-2 and rat intestine epithelial cell line IEC-6 (80). K-means cluster analysis was used to produce spectral unmixing images providing an insight into the chemical composition of the cells. The number of lipid bodies was found to be significantly greater in colorectal cancer cells as opposed to normal cells. Fraction analysis revealed that an increase of 13.8% (n=21) was observed in malignant cells.

The influence of cell fixation methods on the discrimination of cancerous cells from mononuclear cells were explored by Ranc *et al* (81). Breast (BT 549) and colorectal (HCT 116) cancer cells were compared against lymphocytes following three different cell fixation techniques: 1) paraformaldehyde, 2) methanol and 3) simple drying. Using PCA the best discrimination was obtained from cells that have undergone drying only. The use of methanol and paraformaldehyde (which is essentially very pure formaldehyde) was found to induce a number of spectral

changes particularly in the protein and carbohydrate regions as well as lipid leaching which may be crucial for successful classification of the cell lines.

1.4.3 Raman probes

The work of Shim *et al* was one of the first studies to use an *in vivo* NIR Raman probe during routine clinical GI endoscopy (82). Measurements were taken from normal and malignant sites of the colon. PCA and LDA analysis were introduced but there were no specific results relating to the diagnostic accuracy. They did however find that peristaltic movement of the GI tract prohibits prolonged placement of the probe over a localised site.

Coupling Raman to endoscopic probes has allowed real-time monitoring of anti-cancer drug treatments of colorectal tumours. By using a miniaturized Raman endoscope (mRE) system Taketani *et al* was able to monitor the effects of an anti-cancer drug 5-fluorouracil treatment in live model mice (83). PCA was used to analyse the Raman spectra before and after drug administration with a notable molecular alteration in the tumour post drug treatment.

In vitro studies using a confocal fibre optic Raman probe on snap frozen colonic specimens were conducted by Wood *et al* (84). A total of 356 colon biopsies (81 normal, 79 hyperplastic polyps, 92 adenomatous polyps, 64 adenocarcinoma, 40 ulcerative colitis) from 177 patients were measured from the mucosal surface. Using a PCA-LDA and leave-one-spectrum-out cross-validation procedure resulted in accuracies of 72.1 to 95.9% comparing two pathologies and 74.1% comparing three pathologies (normal, adenoma, adenocarcinoma). Performance was found to diminish when the acquisition time was reduced from 10 seconds to 1 second. The Stone group are the main contributors to the use of Raman probes, although there has not yet been any *in vivo* or clinical trials, the results are very promising (85).

1.4.4 Serum analysis

By using Raman spectroscopy in combination with laser induced fluorescence spectroscopy Li et al managed to identify colon and rectal cancers to an accuracy of 80.7% and 82.5%, respectively (86). This was achieved using serum samples from 82 colon cancer patients and 69 rectal cancer patients. A more sophisticated study performed later by the same group classified the serum from healthy volunteers, colon cancer patients and post-operative cancer patients using PCA and k-nearest

neighbour analysis (KNN) (87). Six Raman peaks (750, 1083, 1165, 1321, 1629 and 1779 cm^{-1}) assigned to nucleic acids, tryptophan and chromophores were found to be significantly different between the two groups. The diagnostic accuracy of the model was found to be 91% with sensitivities of 87% and 91% for pre-operative and post-operative groups, respectively.

1.5 Disease classification

The successful application of Raman spectroscopy in a clinical setting greatly depends on the effective implementation of diagnostic algorithms, also commonly known as supervised machine learning. Machine learning is therefore used as a way to find patterns in the data and build discriminant models from known inputs (training dataset) to make predictions of the response from a new unseen dataset (test set). As a result classification algorithms play a pivotal role in the application of Raman spectroscopy in early diagnosis and understanding disease progression. There are two main classification methods in pattern recognition: 1) Unsupervised and 2) Supervised.

1.5.1 Unsupervised classification algorithms

Unsupervised methods depend on finding hidden structures and patterns within the data without prior knowledge of the data groupings. These techniques are often known as cluster analysis algorithms with some of the most common being principal component analysis (PCA), k-means cluster analysis (KMCA) and hierarchical cluster analysis (HCA).

K-means is one of the simplest partitional algorithms and works by partitioning the data into *k* number of clusters such that the squared error between the empirical mean of the cluster and the data points within the cluster is minimized, in other words the distance is at its minimal. K-means is typically used alongside Euclidian metrics for calculating the distance between data points and cluster centres (88). Like KMCA hierarchical cluster analysis also requires a distance metric to determine the similarity between spectra. Clustering is achieved either through an agglomerative mode where each data point is within its own cluster where similar clusters are successively merged together or a divisive (top-down) mode where all data points begin in a single cluster that is recursively dividing into smaller similar sub clusters. Unlike KMCA that finds all clusters

simultaneously, HCA produces a hierarchy of clusters in the form of a dendrogram tree (89). Principal component analysis relies on the deconstruction of the complex dataset instead of amalgamating spectra of certain similarity. It does so by reducing the dimensionality of the dataset by projecting it onto a lower component subspace. A high number of variables is therefore reduced to a small set of orthogonal and independent principal components in the direction of maximal variation (90).

Unsupervised methods are often used as a precursor step to supervised methods when working on very large datasets. This is especially important as not every single wavenumber or variable in the spectral dataset will have an equal discriminatory weighting. By passing the data through an unsupervised clustering algorithm each unlabelled data point can be assigned with a dominant class label for that particular cluster. This kind of approach produces a type of algorithm known as semi-supervised (90).

1.5.2 Supervised classification algorithms

Supervised classification methods depend on class labels of the data points prior to discrimination. Construction of supervised classification algorithms depends on two stages:

1) Training phase
2) Prediction phase

The training stage involves the initial building stage of the classifier using data from known group classes to find patterns. This then outputs a number of model parameters that can then be used to classify data from unknown classes. This is also called the prediction or validation phase and is carried out using data that was not originally used to train the classifier. Such machine learning algorithms facilitates the construction of disease predictive models using a number of different approaches:

- Linear Discriminant Analysis (LDA)
- Support vector machines (SVM)
- Artificial Neural networks (ANN)
- *k*-Nearest Neighbours (kNN)
- Decision Trees Classification

1.5.2.1 Linear Discriminant Analysis

Linear discriminant analysis first introduced by Fisher is one of the simplest and most classical classification algorithms. LDA works somewhat similarly to PCA in that it outputs latent axes that explain data variance. Unlike PCA where the data is projected to maximize data variance, LDA looks for projections that maximises between-class severability whilst at the same time minimizing within-class variability. LDA weighs and linearly combines information from a set of *p*-dependent variables in a way that forces the *k* groups to be as distinct as possible. The final LDA output is a new dimensional space where each observation belonging to the same class is centred around a cluster and each cluster is clearly segregated from other classes. LDA is often paired with PCA to reduce the dimensionality of the dataset to ensure that each observation within the class cluster possesses fewer of only the highly discriminant variables. This improves the efficacy of the classifier as the most diagnostically significant features are found (91–93).

1.5.2.2 Support Vector Machines

Support vector machines separate the observations of different classes by identifying the decision boundaries or hyperplanes between the classes, such that the gap between the classes in the n-dimensional space is as wide as possible (94). Unlike most linear classifiers that simply attempt to separate the data based on their classes, support vector machines go a step further and attempt to maximize the margin i.e. the distance between the boundaries of observations belonging to separate classes (95–97).

1.5.2.3 Artificial Neural Networks

Artificial neural networks are computation algorithms that have been inspired by the functionality of the human brain, in essence ANNs are digitized models of the brain that simulate the way our brains process information. Like us ANNs learn through experience not from programming and gather their knowledge for detecting patterns and relationships in data.

Like our brain, ANNs are composed of hundreds of single units also known as artificial neurons connected with coefficients (weights) which organise the neural

structure. These coefficients are often referred to as processing elements (PE) and they possess weighted inputs, transfer functions and one output. In essence they are equations that balance the inputs and outputs and represent the memory of the system. ANNs used for supervised learning have an input layer that receive incoming spectral data, an output layer that provided a response, and the hidden layers between them. The hidden layer can be thought of as a group of specialists, each of whom are trained on specific features of the data. The hidden layer, as a whole, then goes on to advise each of the output layer specialists of their observations, which then go on to make their own individual assessments of whether or not the sample in question belongs to a specific class. The number of neurons within the hidden layer affects the number of connections, and hence influences the network performance (98–100).

1.5.2.4 k-Nearest Neighbours (kNN)

The *k*-nearest neighbour algorithm works by neighbourhood classification whereby a *k* number of objects or training points is found closest to the query point. The *k* nearest neighbours are found based on the Euclidian distance metric with the minimum distance from the query point to the training sample points. The prediction of the query point is based on the majority class of the *k*-nearest neighbours found (99,101,102).

1.5.2.5 Decision Trees Classification

Decision trees are hierarchical 'tree-like' constructs that take in an input described by a set of properties and outputs a Boolean yes/no response. Classification therefore takes place through repetitive use of Boolean yes/no questions about specific attributes of the input data. Each question or parent node of the decision tree splits into two daughter nodes, which can either be parent nodes themselves or output nodes giving the final discrete classification (103,104).

1.5.3 Quantitative multivariate analysis

Aside from the qualitative classification algorithms mentioned so far, there exists a number of quantitative chemometric approaches using regression to help to discern the exact quantitative relationship between the spectral change and the property of interest. Some of the most common multivariate regression methods currently used

in spectroscopy are Principal Component Regression (PCR) and Partial Least Squares (PLS) (90).

Like with any manmade computational system, the performance of these diagnostic algorithms whether it be qualitative or quantitative is variable. There have been a number of different spectroscopic studies that compare the performance of different classification algorithms against the same diagnostic problem. A study by Gao *et al* conducted a comparison of *k*-NN, SVM and PLS-DA (Partial Least Squares Discriminant Analysis) supervised classifiers in the discrimination of expired and non-expired paracetamol drugs. They found that the accuracies of the classifiers were 89.37%, 96.80% and 90.12%, respectively (105). Liu *et al* compared the performance of PCA-LDA against PLS-DA in the discrimination of normal and cancerous colorectal tissue. They found that PCA-LDA produced a diagnostic accuracy of 79.2%, whereas PLS-DA yielded a diagnostic accuracy of 84.3%, very marginally higher than that of LDA-based models (106). Whereas Dingari *et al* compared the performance of decision tree classification, k-nearest neighbour and support vector machine analysis only to find that SVM was far superior (107). This suggests that not all classification algorithms may be universally suitable for diagnostic studies employing Raman spectroscopy and that a number of algorithms would need to be tried to elucidate the best performing classifier.

There is also a steady inflow of new and improved classification algorithms such as the Gaussian Process (GP) classifier shown to be an enhancement to the already existing SVM classifier (108).

1.6 Back to Basics: A problem of substrates

Our current practice in diagnostic histopathology thrives on the use of slide backing substrates as cheap means of supporting and viewing tissues under transmission white light microscopy. These glass slides however are unsuitable for Raman analysis as the abundance of impurities means that the Raman background originating from the slides is much stronger than the weak Raman scatter from the mounted tissue samples.

A cost effective substrate for Raman application has been an intense subject of multiple studies (109–112). Some of the materials that have currently undergone

extensive scrutiny include synthetic fused silica (quartz), sapphire, plexiglass, mica (109), MirrIR (110), Raman grade and IR polished CaF_2, magnesium fluoride, aluminium (100 nm and 1500 nm thin films on glass), glass, potassium bromide, sodium chloride, zinc selenide (111), silicon with a native ~2 nm oxide layer, 100 nm SiO_2 on Si, highly oriented pyrolytic graphite, standard objective glass as well as gold substrates (112). Thus far, there have been no backing substrates that provide equivalent performance to CaF_2 at a cheaper price. As a result most resort to using quartz and lose a small fraction of the wavenumber region due to intense substrate peaks. There has however been a recent study by Kamemoto *et al* who reported that front-coated aluminium glass (mirrors) yield a very low Raman background, an up to 4 times enhancement of the Raman scatter as well as improving the visual contrast of the unstained tissue sections (109). A detailed investigation into alternative Raman substrates as well as testing the compatibility and performance of the front coated aluminium slides will be carried out in chapter three.

1.7 Aims and Objectives

This project is a multidisciplinary collaboration between Renishaw plc (Spectroscopy Division), UCLH Department of Histopathology, UCL Department of Pathology, UCL Cancer Institute, Gloucester Biophotonics Research Unit and Prof. Thomas's group. We endeavoured to carry out an investigative study in the use of Raman spectroscopy for the diagnosis of a more subtle variant of CRC, Lynch Syndrome, from its more common sporadic counterpart originating from chromosomal instability. With a strong emphasis on translation this project was carried out using a specially designed Renishaw prototype Raman spectrometer created for pathology applications, and an accompanying Renishaw Data Classification Tool. It is widely acknowledged that one of the main obstacles standing in the way of translation of Raman technology into the clinic is the availability of a simple and robust spectrometer and also an affordable and robust backing substrate on which to present tissue sections. This second issue is also extensively studied here.

Specific aims were:

- To identify the best experimental parameters suitable for obtaining spectra with exceptional signal to noise ratios.
- To find a suitable backing substrate for Raman tissue analysis that is also a cost effective alternative to CaF_2.
- Evaluate the suitability of the new substrate and associated tissue processing steps in Raman based studies carried out on FFPE colonic tissue.
- Using the new instrument and backing substrate and empirical and multivariate statistical techniques to test whether the spectra obtained from two pathological groups (CIN adenocarcinoma, LS MSI-H) can be reliably distinguished from each other as well as normal mucosa.

Chapter Two

Methods and Instrumentation

2.1 Introduction

This chapter begins by outlining the methodologies used in the acquisition and processing of all the tissues used within this thesis. Section 2.3 covers the background and theory of Raman spectroscopy, while section 2.4 provides a breakdown of the instrumentation used to gather the Raman spectra. Section 2.5 and 2.6 covers the data pre-processing techniques used prior to analysis and the analytical methods used to analyse the spectral data. The final section of this chapter provides an overall study roadmap of the whole thesis covering the tissues, techniques and analytical methods employed.

2.2 Pathology

2.2.1 Tissue collection

2.2.1.1 Rat samples

Colonic and liver samples were acquired from a single male Wistar rat obtained from the University College London Biological Services. Euthanasia was conducted using a CO_2 flow chamber. Complete euthanasia was verified using the blink reflex, the colon and liver were then immediately removed and irrigated with ice cold phosphate buffered saline. Multiple colonic resections approximately 5 mm in length were excised along with 5 mm × 5 mm punch biopsies from the liver, these were then fixed in standard 10% neutral buffered formalin for 24 hours at room temperature.

Research was conducted in full compliance with the UK Animals (Scientific Procedures) Act 1986 (A(SP)A).

2.2.1.2 Human samples

Existing pre-2006 FFPE human colonic tissue blocks were obtained from the UCL/UCLH Biobank for Health and Disease under REC: 10/H1306/42.

Post-2006 blocks were later acquired from the same biobank under REC: 15/YH/0311. All human blocks have an undetermined fixation time however standard practice states that all biopsies undergo 4-6 hours of fixation, while resections undergo 24-48 hours of fixation. The pathologies and number of

samples used within each study of this thesis will be outlined within the relevant sections.

2.2.2 Histopathological processing

Following lapse of the fixation time all the rat samples underwent further processing to create standard FFPE sample blocks. Tissues were processed in a Leica TP 1050 automated tissue processor (Leica Biosystems Ltd., UK) and embedded in standard laboratory histological paraffin wax Tissue Tek II (Sakura Finetek Ltd., UK). The tissue processor workflow for the Leica TP1050 can be found in *Appendix 1*.

Human samples were supplied as pre-existing FFPE blocks that only required sectioning and mounting onto a suitable backing substrate.

2.2.2.1 Sectioning

Paraffin blocks were manually sectioned using a Leica RM 2235 microtome (Leica Biosystems Ltd., UK); the resulting paraffin ribbons were then floated onto a 45ºC water bath and finally mounted onto a backing substrate. Tissues were cut at thicknesses ranging from 3 µm through to 16 µm. All sections destined for conventional staining (e.g. H&E, IHC) were cut at 3 µm to ensure that a single cell monolayer was captured for easy histological identification using light microscopy. The specific tissue thicknesses used for each study in this thesis is outlined within the designated chapters.

2.2.2.2 Slide substrates

Backing substrates used within the optimization experiments in chapter three were acquired from a number of different sources. UV grade CaF_2 was bought from Crystran (Crystran Ltd., UK). Other backing substrates included borosilicate glass, synthetic fused silica (quartz photomask grade) and front coated aluminium mirror glass slides (300 nm coating thickness) all obtained from LG Optical (LG Optical Ltd., UK). Conventional microscopy slides made of extra white soda lime glass were kindly provided by Karina Schöngen (Thermo Fisher Scientific Inc., UK). Samples of additional optical glasses thought to have similar optical properties to CaF_2 – N-FK51A (Schott) and S-FPL53 (Ohara) – were kindly provided by Bernd Ullmann (Excelitas Technologies Corp., DE). A MirrIR slide sample was kindly provided by

Craig Virnelson (Kevley Technologies, USA). Super mirror 304L stainless steel slides were kindly supplied by Wes Heawood (Renishaw PLC, UK).

The preliminary rat study outlined in chapter four was carried out using CaF_2. All remaining studies were conducted on 304L super mirror stainless steel slides.

2.2.2.3 Paraffin removal

Following 24 hour incubation at 37°C the unstained tissue sections were immersed in a series of baths to remove paraffin wax prior to Raman mapping. Four successive ten minute baths in xylene (VWR International Ltd., UK) with gentle agitation were used to remove the paraffin, followed by a series of rehydration steps in graded ethanol absolut (VWR International Ltd., UK). Rehydration took place via two sequential immersions in each of 100%, 90%, 70% and 50% graded ethanol baths for five minutes each; followed by a final immersion in distilled water for ten minutes.

2.2.3 Pathology analysis

All human samples were obtained from previously analysed cases. All the H&E stains obtained from the blocks were re-analysed by a registered consultant pathologist (Dr Manuel Rodriguez-Justo) and cross-referenced with the patients' diagnostic information on file.

2.3 Raman Spectroscopy – background and theory

2.3.1 Molecular motion

Molecules are not static in nature but instead undergo periodic motion. A molecule consisting of N atoms has 3N internal degrees of freedom (three coordinates (x_i, y_i, z_i) for each atom *i*. There are three different types of molecular movement:

1) Translation *(movement in space)*
2) Rotational *(spinning about an axes)*
3) Vibrational *(internal deformation)*

Three of these degrees of freedom can be assigned to 'translation' of the whole rigid molecular structure along three independent directions in space. Three more degrees of freedom relate to rotations of the whole rigid molecular structure along three independent axes in space. For linear molecules there are only two degrees of freedom for rotational motion. The remaining type of motion corresponds to internal deformations of the molecule (bonds between atoms are not rigid), whereby the atoms oscillate about their equilibrium position. This motion is known as molecular vibration, and it is this type of motion that Raman spectroscopy is able to detect (113,114).

If N is the number of atoms in a molecule, then the number of vibrational modes of freedom possible is 3N–6 for all molecules except linear ones, where it is 3N–5. The freedom of these motions is constrained not only by the type of chemical bond present between the atoms but also the atoms themselves. For a linear diatomic molecule such as oxygen O_2 (3×2-5) there is only one possible vibrational mode – a simple stretching vibration. A more complex triatomic molecule such as water H_2O has (3×3-6) a total of three modes of vibration: 1) symmetric stretching, 2) asymmetric stretching and 3) bending or deformation modes (scissoring, rocking, wagging and twisting) (*fig.2.1*) (114).

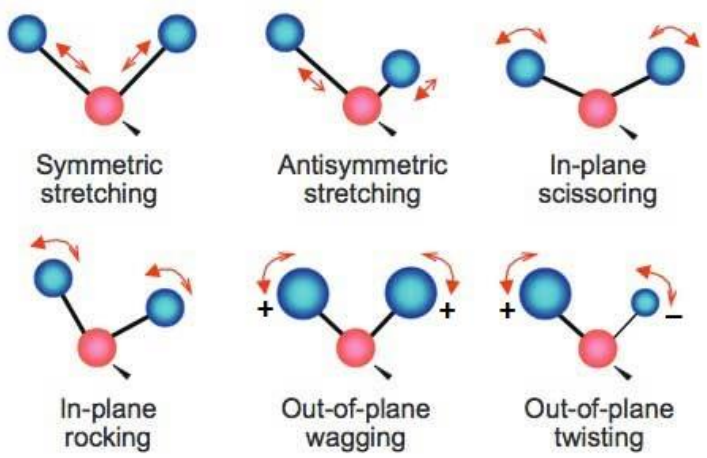

Figure 2.1: Possible molecular vibrational modes. *Stretching modes can be either symmetric or asymmetric, while bending motions can be referred to as scissoring, twisting, wagging and rocking. Adapted from (81).*

2.3.2 Selection rules

For a molecular vibration to be Raman active there must be a change in the polarizability α of the molecular mode. The intensity of the Raman active band depends on the ease with which the electron cloud around a molecule is distorted at a specific molecular vibration (115).

2.3.3 Raman theory

2.3.3.1 Classical wave theory

When considering the classical Raman interpretation it is best to first consider the organization of a simple diatomic molecule. A simple diatomic molecule can be modelled mathematically as two masses connected by a spring, where *m* represents the atomic mass, *x* represents the displacement and *K* the bond strength (*fig.2.2*).

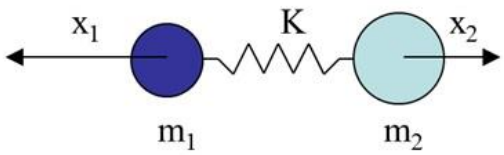

Figure 2.2: Diatomic molecule represented as two masses connected by a vibrating spring (taken from (116)***).***

The displacement or stretching and release of the spring corresponds to a simple stretching vibration. The frequency ν_m of the molecular vibration, mass of the atoms and bond strength for diatomic molecules can be described by Hooke's law:

$$\nu_m = \frac{1}{2\pi c}\sqrt{\frac{K}{\mu}} \tag{2.1}$$

where in this case *c* is the speed of light, *K* is the force constant of the bond between masses M_A and M_B, and μ is the reduced mass of atoms *A* and *B* of masses M_A and M_B:

$$\mu = \frac{M_A M_B}{M_A + M_B} \tag{2.2}$$

Hence, the vibrational frequency of the molecule is proportional to the square root of the bond strength and inversely proportional to the square root of the reduced mass. Where the reduced mass is a simplification of motion of a two mass/body system whereby the motion of one body is considered in a reference frame centred around the other body thought to not be moving. As a result, the lighter the atoms, the higher the vibrational frequency. Each molecule will therefore have its own unique vibrational signature determined not only by the atoms in the molecule but also by the characteristics of the type of bonds present. Through the Raman effect these vibrational frequencies can be measured via the polarizability of a molecule (114).

Exposure of a linear diatomic molecule to a static electric field induces some distortion – the positively charged nuclei is attracted towards the negative pole of the field, while the electrons to the positive pole. This charge separation causes an *induced electric dipole moment* to be established and the molecule is said to be *polarized*. The magnitude of the induced dipole P, is dependent on both the strength of the applied field, $\bar{E}$, and on the ease with which the molecule can be distorted, α, the *polarizability* :

$$P = \alpha\bar{E} \tag{2.3}$$

The electric field of the incident beam of electromagnetic radiation, E, can be expressed by the following equation:

$$\bar{E} = E_0 \cos(2\pi \nu_0 t) \tag{2.4}$$

where E_0 is the amplitude and ν_0 is the frequency of the incident beam , and t is the time. Since the electric field of the incident beam interacts with the polarizable electron cloud of the sample molecule, a temporary change in the dipole moment P is induced. By substituting equation 2.4 into 2.3 yields a time dependent induced dipole moment:

$$P = \alpha\bar{E} = \alpha E_0 \cos(2\pi \nu_0 t) \tag{2.5}$$

The relative distortion of the local electron cloud of a molecule is dependent upon the relative position of the atoms; hence polarizability is also a function of the

momentary position of the atoms. The vibrational energy E_{vib} of a particular mode is given by:

$$E_{vib} = \left(j + \frac{1}{2}\right) h\, \nu_{vib} \tag{2.6}$$

whereby j is the vibrational quantum number (j = 0,1,2…), ν_{vib} is the frequency of the vibrational mode, and h is the Planck's constant.

If a molecule is vibrating with frequency ν_{vib}, the nuclear displacement q can be written as:

$$q = q_0 \cos(2\pi\, \nu_{vib} t) \tag{2.7}$$

where q_0 is the vibrational amplitude. To capture the dependence of polarizability α on nuclear displacement q, the polarizability can be expanded into a Taylor series (describing small displacements within a wave) for small nuclear deviations of up to 10%:

$$\alpha = \alpha_0 + \left(\frac{\partial \alpha}{\partial q}\right)_{q=0} q \tag{2.8}$$

Here α_0 is the polarizability at equilibrium position, and $(\partial\alpha/\partial q)$ is the rate of change of α with respect to the change in nuclear displacement q, evaluated at the equilibrium position $q = 0$. Substituting equation 2.7 into equation 2.8, gives the polarization in relation to nuclear displacement:

$$\alpha = \alpha_0 + \left(\frac{\partial \alpha}{\partial q}\right)_{q=0} q_0 \cos(2\pi\, \nu_{vib} t) \tag{2.9}$$

Finally, inserting the electric field, $\bar{E} = E_0 \cos(2\pi\, \nu_0 t)$, and equations 2.7 and 2.8 into equation 2.3 yields:

$$P = \alpha_0 E_0 \cos(2\pi\, \nu_0 t) + \left(\frac{\partial \alpha}{\partial q}\right)_{q=0} q_0 \cos(2\pi\, \nu_{vib} t)\, E_0 \cos(2\pi\, \nu_0 t) \tag{2.10}$$

Applying a trigonometric identity for the product of two cosines:

$$cosAcosB = \frac{1}{2}\{cos(A+B) + cos(A-B)\}$$

leads to:

$$P = \alpha_0 E_0 \cos(2\pi \nu_0 t) + \frac{1}{2}\left(\frac{\partial\alpha}{\partial q}\right)_0 E_0 q_0 [cos(2\pi(\nu_0 - \nu_{vib})t) + (cos2\pi(\nu_0 + \nu_{vib})t)] \quad (2.11)$$

The above equation depicts two resultant effects from the interaction with incident light. The first scattered frequency corresponds to Rayleigh scattering where there is no change in the incident frequency (ν_0). The second effects corresponds to the Raman scattered component where the frequency of the incident light is shifted by the molecular vibration. A decrease in the frequency of the incident light corresponds to a Stokes shift ($\nu_0 - \nu_{vib}$), while an increase in the incident light frequency corresponds to an anti-Stokes shift ($\nu_0 + \nu_{vib}$) (115,117–119).

2.3.3.2 Quantum theory

Raman scattering can also be understood using the quantum theory of radiation, whereby light of a frequency ν is thought of as a stream of particles called photons having energy $h\nu$, where h is the Planck's constant. When an incident beam is directed towards the sample in question, these photons can be thought of as undergoing collisions with the molecules within the sample. When the collision is perfectly elastic the molecule will relax back to its original energy state and emit a photon of equal energy to the incident photon $h\nu$, this is called *Rayleigh* scattering and is the dominant process (*fig.2.3*). However, around one in every 1×10^6 to 1×10^8 photons will scatter inelastically, whereby energy is exchanged between the photon and the molecule. The molecule can gain or lose energy only in accordance with the quantum law (120):

'its energy change, ΔE in Joules, must be the difference in energy between two of its allowed energy states'

At room temperature, most molecules are present in the lowest vibrational energy level *m*, upon interaction with incident light, energy can be absorbed by the molecule promoting it to a short-lived 'virtual energy state'. This state however is not stable and the molecule quickly relaxes to one of the allowed higher energy excited vibrational states *n*, following an emission of a photon with reduced energy $h\nu - \Delta E$ (*fig.2.3*). Radiation scattered with a frequency lower than that of the incident beam is known as *Stokes* shifted light, and is the dominant process. Alternatively, some molecules may already be present in an excited state *n*, whereby interaction with incident light will cause the molecule to lose energy and relax to a lower vibrational state *m*, here energy will be transferred to the scattered photon $h\nu + \Delta E$. This is known as *anti-Stokes* shifted light (120).

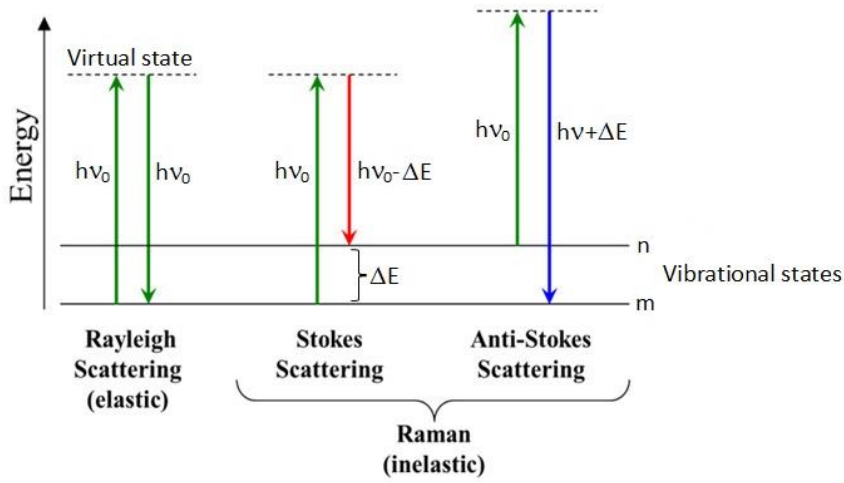

Figure 2.3: A Jablonski energy diagram representing quantum energy transitions for Raman and Rayleigh scattering. *The lowest vibrational state m, represent the ground vibrational state of molecules at room temperature. The excited vibrational state n corresponds to molecules with higher energy at elevated temperatures. Interaction with incident light of frequency ν, promotes the molecule to an unstable transient virtual state from which it can return to the same energy state as before (Rayleigh), a higher energy state (Stokes) or a lower energy state (anti-Stokes) (modified from* (116)*).*

The ratio of the intensities of the Stokes and anti-Stokes scattering is dependent on the number of molecules in the ground and excited vibrational states. This can be determined using the Boltzmann equation:

$$\frac{N_n}{N_m} = \exp\left(-\frac{E_n - E_m}{kT}\right) \qquad (2.12)$$

Where N_n is the number of molecules in the excited vibrational state n, N_m is the number of molecules in the ground vibrational state m, E_n–E_m is the difference in energy between the vibrational energy levels, T is the absolute temperature and k is the Boltzmann constant (1.3807×10^{-23} JK^{-1}). Seeing as most molecules will be found at the ground energy state m at room temperate, Stokes radiation is generally more intense (121).

2.3.4 Raman intensity

The Raman signal intensity is dependent on both the molecular (*outlined in blue*) and experimental (*outlined in red*) parameters used, and can be expressed as:

$$I_{Stokes} \propto N \left(\frac{\partial\alpha}{\partial q}\right)^2_{q=0} (\nu_0 - \nu_{vib})^4 E_0^2, \tag{2.13}$$

where N is the volume density of the scattering molecules and ($\partial\alpha/\partial q$) corresponds to the derivative of the polarizability with respect to nuclear coordinates and frequency of the molecular vibration ν_{vib}. Whereas the experimental parameters constitute the excitation laser intensity E^2 and its frequency ν_0 (122).

The fourth power dependence on the frequency difference $(\nu_0 - \nu_{vib})^4$ indicates that the Raman intensity is inversely proportional to the excitation wavelength. As a result, the shorter the excitation wavelength the greater the Raman intensity (122).

The change in energy of the Raman scattered light is independent of the wavelength of the incident light. Hence, the Raman shift remains unchanged whether the molecule is illuminated with green (532 nm) or red laser light (785 nm) (123).

2.3.5 Convention

Wavelength and frequency are often used interchangeably in spectroscopy. The frequency, ν, is the number of waves in the distance light travels in one second. Wavelength λ and frequency ν are inversely proportional:

$$\nu = \frac{c}{\lambda} \tag{2.14}$$

where c is the velocity of the electromagnetic wave.

A third parameter known as the 'wavenumber' $\bar{\nu}$ expressed in cm^{-1} is defined as the number of waves λ contained in a one centimetre length and can be expressed as:

$$\bar{\nu} = \frac{1}{\lambda} = \frac{\nu}{c} \tag{2.15}$$

Raman scattering is often expressed as a shift in the wavenumber from the wavenumber of the incident photon, rather than the absolute wavenumber. This is the preferred convention as it is easier to convey the shift from incident light and is irrespective of the excitation wavelength used. The Raman shift is therefore expressed as (115,123):

$$\bar{\nu} = \frac{1}{\lambda_{incident}} - \frac{1}{\lambda_{scattered}} \tag{2.16}$$

2.4 Raman instrumentation

Optimization and preliminary studies outlined in chapters three and four were conducted on a commercially available Renishaw inVia Raman spectrometer. The remaining studies were conducted on a bench top Renishaw RA802 series prototype instrument geared specifically for pathological application. It was not possible to conduct the entirety of the studies on a single instrument due to availability issues.

2.4.1 Renishaw inVia spectrometer

A schematic representation of the Renishaw inVia spectrometer is shown in figure 2.4. Two adjustable alignment mirrors are found at the base of the spectrometer box. Mirror A steers the laser into the spectrometer and focuses it onto the beam expander B that increases the beam diameter, this optimizes the entry of the laser light into the back aperture of the objective. The expanded laser light is then steered by the second adjustable alignment mirror C towards the laser-line rejection apparatus D. The laser-line rejection apparatus contains a Rayleigh rejection filter that reflects all the excitation light and hence directs the laser light towards the optical microscope E (Leica DM2500 light microscope), which is used to illuminate the sample and collect the Raman scatter.

Following interaction with the sample, the collected Raman scatter as well as Rayleigh scatter is directed horizontally at the Rayleigh rejection filter, where light of longer or shorter frequencies is transmitted through while Rayleigh scattered light is reflected back into the microscope. Raman shifted light is allowed to pass through to the focusing lens F and directed through the monochromator entrance slit G. The slit is adjustable and is responsible for the rejection of scattered light from out-of-focus regions of the sample, hence eliminating the fluorescence contribution from the tissue and improving spatial resolution. The scattered light is then collimated onto a prism mirror H responsible for directing the light onto the grating I, as well as focusing the dispersed light onto the charge coupled device (CCD) focusing lens J. A CCD detector sensitive in the infrared region was used to measure the dispersed light.

The principal operation of the RA802 bench top prototype system is the same as that of the inVia spectrometer.

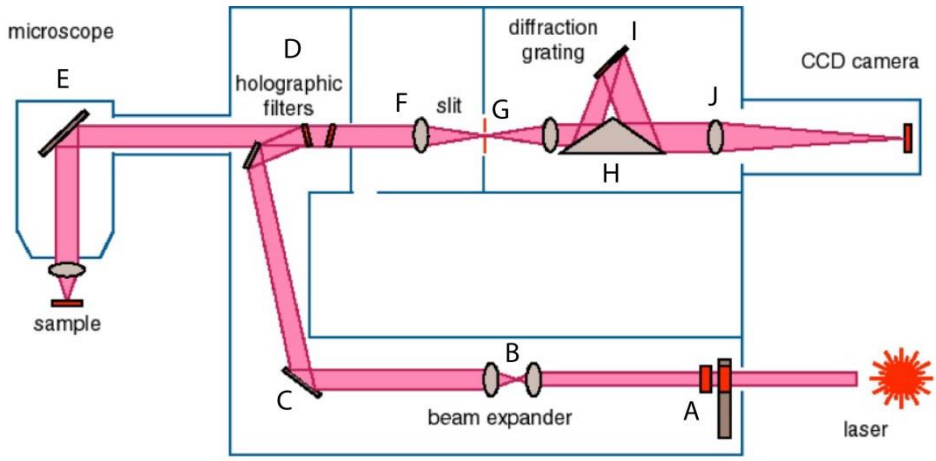

Figure 2.4: Internal schematic diagram of a Renishaw inVia micro-spectrometer. *The beam describes the pathway of the laser from the source to the CCD detector. A: beam steering mirror, B: beam expander, C: beam steering mirror, D: laser-line rejection apparatus, E: microscope, F: focusing lens, G: entrance slit, H: prism mirror, I: grating, J: CCD focusing lens. (Reproduced with kind permission from Renishaw Spectroscopy Division (Renishaw PLC, UK)).*

By coupling Raman spectroscopy with a microscope allows the laser beam with a Gaussian intensity profile to be tightly focused onto the sample via the objective. This facilitates the acquisition of spectra with a high spatial resolution. Although this is also dependent upon the wavelength of choice, a trade-off must be made between

spatial resolution and sample fluorescence. Through the use of a high speed encoded automated stage the Renishaw StreamLine™ mode synchronises sample motion with the movement of the signal on the CCD detector. This facilitates the rapid generation of chemical images of large sample areas at high spatial resolution.

2.4.2 Performance checks

2.4.2.1 Laser power:

Prior to measurements on the inVia, laser power checks were conducted using a handheld Edmund optics power meter (Edmund Optics Ltd., UK). It was not possible to carry out power measurements on the RA802 due to the inability to override the interlock. Laser stability overtime was monitored remotely by Renishaw engineers.

2.4.2.2 Calibrations

inVia

The alignment of the beam path is ascertained by checking that the laser spot is centred on the cross hair in the live video image. The beam path was manually adjusted via the motorized beam steer functionality. This allows the user to move the laser beam steer mirrors A and C. The concentricity of the beam was also checked and adjusted using the same beam steer functionality.

The Raman spectrum x-axis was calibrated to ensure the wavenumber position recorded was correct. This assigns Raman shift wavenumbers to the different pixel numbers on the CCD chip. The known silicon Raman spectral peak at 520 cm^{-1} was used as a calibration reference standard.

To ensure that the maximum amount of light is collected, manual lateral slit alignment was carried out; this ensures that maximum signal can be obtained.

Prototype RA802 Bench top Series

The RA802 series undergoes a fully automated calibration and optimization sequence. Prior to performing any measurements a Performance Qualification (PQ) is initiated to ensure that the system performance is within the specified

limits. This automated routine runs a series of alignments and calibrations outlined below (*Miss Stephanie Ohrel, Renishaw plc, personal communication*):

- Automatic adjustment of stage height to ensure the test samples are in focus.
- Slit lateral offset adjusted to maximise signal (silicon standard).
- Calibration of the spectrum x-axis in absolute wavenumber (using internal neon source) and in Raman shift (silicon standard).
- Main spectral properties (signal, bandwidth, asymmetry) are tested on silicon standard.
- Repeatability and reproducibility of response and wavenumber calibrations are tested using a standard internal sample of polystyrene.

After measurement completion an automated Post Measurement Check (PMC) is run. This uses a silicon calibration standard to ensure that the system performance and calibration remained unchanged throughout the data collection period.

2.5 Data pre-processing

Spectral pre-processing is an essential step prior to data analysis as it enhances the uniformity and differentiation capability of the data groups. A quality control measure to remove any outliers was first employed prior to this step. Outliers were identified as spectra that deviate significantly from the expected spectral shape or mean spectrum of the dataset. This was done manually by visually inspecting all the acquired spectra.

The majority of all of the pre-processing and analytical techniques applied to the remaining data was carried out using a series of scripts written in MATLAB R2013b by Dr Gavin Rhys Lloyd of Gloucester Biophotonics research unit. Saturation removal scripts were kindly provided by Renishaw plc, courtesy of Dr Lee Harper. Scripts for similarity maps, principal component analysis based image analysis and linear fits were written by Mr Andrew Maher. Scripts for reimporting MATLAB pre-processed data back into WiRE 4 were also provided by Mr Maher.

Outline descriptions of the pre-processing and analytical rationales are given below in the appropriate sections.

2.5.1 Saturation effects

Highly fluorescent samples may result in spectral saturation. Saturation occurs when the charge for a given pixel exceeds its charge well capacity on the CCD chip. Saturated spectra were removed using MATLAB R2013b. Saturations were identified as spectra containing five consecutive points with zero intensity values.

2.5.2 Cosmic ray removal

Cosmic rays are high energy radiation particles capable of interacting with the CCD during data collection. Collision with the detector results in spurious sharp spikes that contaminate the spectra (*fig.2.5*). Cosmic rays were removed using a combination of nearest neighbour and peak width methods using WiRE 4 software. This allowed manual cycling and visualization of all spectra prior to selection of a peak for removal.

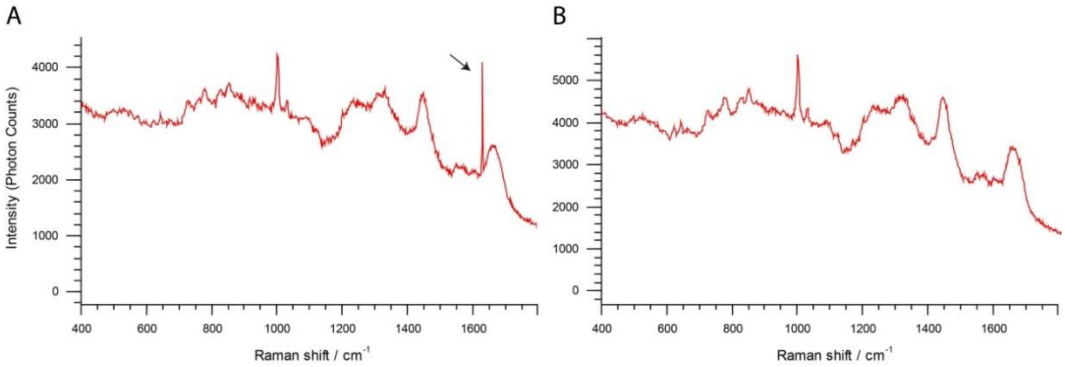

Figure 2.5: Cosmic ray removal. A) *Spectrum contaminated with a cosmic ray (arrow) at approximately 1600 cm^{-1} (t=10s, power=158 mW).* ***B)*** *Spectrum following comic ray removal using Renishaw WiRE 4 software (Renishaw plc,UK).*

2.5.3 Baseline correction

Complications in Raman analysis of histological samples can arise from auto-fluorescence originating from both tissue components and fixation artefacts. The effect on the results is an elevation of the spectrum baseline and unfortunately the magnitude of the shift drifts from one spectrum to the next (119,124). The intensity and variability in the baseline drift makes it challenging to interpret and compare the spectra. A modified polyfit method developed by Lieber and Mahadevan-Jensen was used to subtract the fluorescence baseline from the Raman spectra (*fig.2.6*). This method ensures that the Raman peaks remain intact

following the baseline removal as well as eliminating the subjectivity and variability of user intervention.

An initial least-square polynomial curve is fitted to the entire spectrum. The baseline is then defined such that all data points in the generated polynomial curve that have a higher intensity value than the original value in the input spectrum are reassigned the original spectrum value, the fit for all other data points is retained. In the next iteration a new polynomial is calculated to fit to this new baseline. The procedure is then repeated multiple times until no further improvement in the baseline is obtained. This new baseline is then subtracted from each spectrum (125).

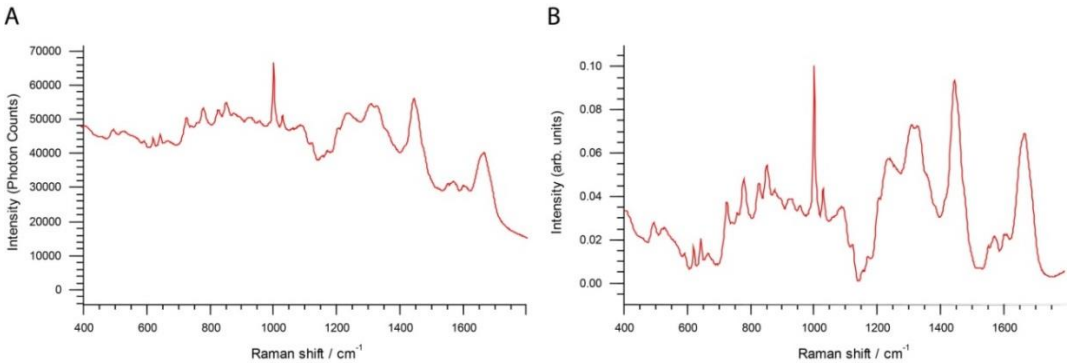

Figure 2.6: Baseline correction. A) *Original spectrum without baseline correction (t=20s, power=158 mW).* ***B)*** *Spectrum following the modified least-square based curve fit baseline correction using a third order polynomial in MATLAB R2013b.*

2.5.4 Normalisation

It is essential that the intensity ranges of spectra are on the same or similar scales before any comparisons are made. This can be achieved through a pre-processing step known as normalisation.

Here the total area under the spectral curve was normalised, whereby the intensity at each frequency in the spectrum is divided by the square root of the sum of the squares of all the intensities, where the sum is over all frequencies (*fig.2.7*) (90,126).

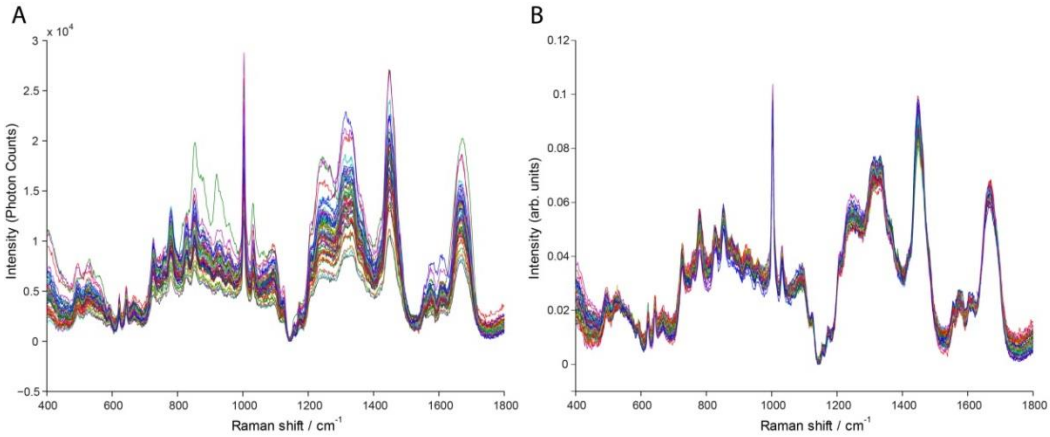

Figure 2.7: Normalisation. A) *Original spectra after undergoing baseline correction (t=20s, power=158 mW).* ***B)*** *Spectra following normalisation to the total area under the spectral curve using MATLAB R2013b.*

2.6 Analytical methods

2.6.1 Signal to axis measurements

Signal to y-axis (area under the spectrum) measurements across the fingerprint region were carried out on the raw spectral dataset to estimate the total fluorescence. This was done within the WiRE 4 software (Renishaw plc). Data values were then exported into Microsoft Excel 2010 and plotted.

2.6.2 Peak intensity measurements

Peak intensities were calculated with the aid of the curve-fitting function in WiRE 4. A peak of interest is first curve fitted, with the fit region constrained around the base of the peak. Limits within one to three wavenumbers were applied to the band centre. The curve-fit parameters were then saved and applied towards a simple univariate peak intensity analysis of the entire spectral dataset. Peak intensity values were then exported into Microsoft Excel 2010 and plotted for comparison.

2.6.3 Spectral similarity maps

To determine the similarity between each pixel of the tissue map and each reference spectrum, cosine similarity was computed, defined as:

$$\theta = \frac{m \cdot s}{|m||s|} = \frac{\sum_i m_i s_i}{\sqrt{(\sum_i m_i^2)(\sum_i s_i^2)}}, \tag{2.17}$$

where s_i denotes the Raman intensity at Raman shift i in the reference spectrum, and m_i denotes the Raman intensity at Raman shift i in the tissue map spectrum (90).

The similarity score is bounded such that $-1 \leq \theta \leq 1$. A value of $\theta = 1$ implies that the two spectra are identical, i.e., that $m = s$; if $\theta = -1$, then the two spectra are opposite, i.e., that $m = -s$. A value of θ near zero indicates no correspondence between m and s. As such, a large positive value of θ suggests that the pixel constitutes, to some degree, the reference spectrum. By plotting the value of θ across the whole map, we can determine which areas of the tissue are most similar to the reference spectrum at hand, and thereby deduce the distribution of that reference biomolecule within the tissue.

A background mask was applied to prevent the reference spectra from being matched against pixels associated with the backing substrate supporting the sample. To choose which pixels to discard, we first formed an average "background" spectrum from a separate Raman map that contained only a CaF_2 slide. We then computed the spectral similarity between all pixels of our Raman map and the average background spectrum. Any pixels with a similarity value greater than some threshold τ were discarded, ensuring only biological tissue was analysed. For this work, we set the threshold to be τ=0.98.

2.6.4 Principal Component Analysis

Principal component analysis (PCA) is an unsupervised multivariate analysis technique that allows an effective reduction in the dimensionality of the spectral dataset. PCA facilitates the identification of combinations of highly correlated variables that best describe the variance in the data. Major trends within the data are displayed using principal component (PC) variables generated using a combination of the original variables. The first PC (PC1) demonstrates the maximum variance in

the data with the second component (PC2) demonstrating the largest residual variance and so forth through third, fourth and higher components (PC3, PC4 etc) (119).

Highly multidimensional spectral data can therefore be presented within a 2D scatter plot by plotting PC1 and PC2 on the axes, whereby each data point represents an individual spectrum. The associated PC loadings reveal the variables that facilitate data separation.

PCA was performed using WiRE 4 software as well as MATLAB R2013b. Prior to the performance of PCA all spectra were pre-processed as outlined in section 2.5 and mean centred.

2.6.4.1 Linear fit of PCA

To explore the molecular basis of the difference underpinning the PCA analysis, a linear combination of reference spectra was fitted to each component. That is, each PC was formulated as:

$$p = w^{(1)}s^{(1)} + w^{(2)}s^{(2)} + \cdots + w^{(n)}s^{(n)}, \tag{2.18}$$

where $w^{(i)}$ is the weight of reference spectrum $s^{(i)}$ in the linear sum.

In this way, one can establish which biomolecules contribute most strongly to each PC. Note that $w^{(i)}$ can be positive or negative—the specific sign does not denote the importance of the biomolecule; rather it is $|w^{(i)}|$ the absolute magnitude of $w^{(i)}$ that does so.

The value of $w^{(i)}$ for each PC was determined by implementing least squares linear regression.

2.6.5 Multivariate curve resolution-alternating least square analysis

Multivariate curve resolution-alternating least square (MCR-ALS) analysis decomposes the spectral data matrix into a linear combination of pure spectra. This technique is thought to provide a considerable improvement on the interpretation of the results (127).

MCR-ALS makes the assumption that each pixel within the data image can be described as a linear combination of a set of pure component spectra, weighted

according to their abundance in each pixel. A 'pure component' can be described as a pure chemical compound or a region of the sample with a consistent spectral signature – whereby the homogenous mixture of compounds cannot be unmixed any further.

MCR decomposes the experimental data matrix D into the product of two smaller matrices C and S^T:

$$D = CS^T + E \tag{2.19}$$

C is the matrix of concentration profiles for each modelled component (relative concentration of the component in each pixel) and S^T being the matrix of the corresponding pure spectral profiles. E is the residual matrix with the data variance unexplained by the product CS^T. Equation 2.19 is then solved iteratively by an ALS algorithm which calculates the concentration C and pure spectra S^T matrices, optimally fitting the experimental data matrix D using the proposed number of N_s conformations. Iteration continue until an optimal solution is obtained (128,129).

The number of spectroscopically distinct conformations N_s was estimated by the number of unique histological features present within the analysed region. This however is commonly done using singular value decomposition (SVD) or PCA. In this case the MCR-ALS analysis was repeated for a number of different possibilities and the results were evaluated in terms of the quality of the resolved profiles and the identification of different histological regions.

MCR-ALS was conducted using WiRE 4 software due to the current limitations encountered when using the MATLAB platform. MATLAB-written scripts within a graphical user interface provided by Felten *et al* was found to be a very user friendly and straightforward means of applying MCR-ALS to a hyperspectral dataset, however this was only feasible for a small dataset of around 10,000-20,000 spectra (129). The datasets analysed within this thesis (chapter five) however ranged from 150,000-300,000 spectra. These Raman based images therefore possess a much higher spatial resolution than those acquired by previous studies (59,68,69).

The termination method used to perform MCR-ALS in WiRE 4 was via a user defined number of components, whereby the MCR-ALS result is limited by a maximum number of components. Constraints applied included non-negativity for the spectral and concentration profiles, as well as closure on the estimated concentrations. This ensures that the sum total of the component intensities

(concentrations) at each map pixel is 100%. Additional pre-processing steps were run prior to MCR-ALS which included offset removal where the minimum value on the y-axis is set to zero, as well as scaling each spectrum such that the sum of all points equals one. An additional option was selected to accelerate the algorithm to run sub-sampling for large datasets.

2.6.6 Linear Discriminant Analysis

One of the limitations of PCA is that it is an unsupervised technique and as a result does not take into consideration different sample groupings. PCA is therefore not ideal for the discrimination and classification of groups. A technique related to PCA known as Linear Discriminant Analysis (LDA) can be used to find linear combinations of variables to define directions in spectral space that maximize the between group variance while minimizing the within group variance (119).

PCA and LDA are often combined into a single PC-LDA model, which results in an improved efficiency of the classification, as the most diagnostically significant features are automatically identified (90). PCA was first applied to the dataset, of which the first few PC are retained for LDA analysis. The PCs are then used to compute linear discriminant (LD) functions that display the maximum resultant variance between the datasets. These LD functions are then combined to produce a diagnostic prediction model. The weights of the discriminant functions of each spectrum are then plotted against each other in a scatter plot (130).

2.6.6.1 Cross validation

The predictive accuracy of the model was tested using a cross-validation procedure whereby each sample measurement was withheld in turn, while the remaining measurements were used as the training set for the classifier. The withheld measurement was then used as a test set to predict the pathological status of any tissue using the classifier. This process is iterated until the pathologies of all the tissue samples measured had undergone prediction.

This process also known as leave-one-map-out cross-validation ensures that the training set and test set never contained the same patients. This method of cross validation whereby each patient was unseen by the model provides the closest representation to a real clinical environment.

2.6.6.2 Assessment of the classification method

To assess the performance of the classification model the following parameters were quantified using values for true positives (TP), true negatives (TN), false positives (FP) and false negatives (FN) (131):

1. **Sensitivity**, the ability of the test to correctly identify the disease in question (true positives), this is defined as:

$$Sensitivity = \frac{TP}{TP+FN} \tag{2.20}$$

2. **Specificity**, the ability of the test to correctly identify those without the disease (true negatives), defined as:

$$Specificity = \frac{TN}{TN+FP} \tag{2.21}$$

Whereby true positive and negative conditions result in correct identification of the presence and absence of the condition, respectively. The same principle applies to false positives and negatives where the presence or absence of disease is incorrectly identified. The diagnostic results of all samples included within the study were confirmed by a resident consultant pathologist Dr Manuel Rodriguez-Justo.

2.7 Experimental roadmap

Chapter three begins with a series of optimization experiments where the best instrumental and experimental parameters were selected for use with FFPE tissues. A substantial part of this chapter included an in-depth investigation into alternative Raman backing substrates and how they compare to the conventionally used CaF_2 substrates.

Chapter four covers a preliminary study involving Raman mapping of FFPE rat colonic tissue mounted on the conventionally used CaF_2 slides. Rat tissue was used due to the precious nature of human samples and the slow overall progress of the ethical approval process to gain access to human material. This chapter was done to facilitate a direct comparison of FFPE tissue on CaF_2 compared to the performance of FFPE tissues mounted on super mirror stainless steel slides presented in chapter

five. Chapter four primarily employs cosine similarity in an attempt to match image pixels to biomolecular reference standards as well as exploratory unsupervised principal component analysis to understand which histological regions can be identified with relative ease. As well as comparing the performance of CaF_2 against super mirror steel chapter five expands on the chemometric approaches used previously by utilising multivariate curve resolution alternating least square analysis.

Following the optimization of a novel Raman backing substrate in chapter three and confirming its suitability for both histological and Raman use in chapters four and five, the final chapter demonstrates its application towards a clinical problem. Chapter six covers the application of Raman spectroscopy in LS cases mounted onto silinized super mirror steel slides and the development of a linear discriminant analysis classification model for LS discrimination from sporadic cancer, as well as model validation. The conclusions drawn from all the combined chapters are presented in chapter seven.

Chapter Three

Optimization of Experimental Parameters

3.1 Introduction and Aims

To date the application of Raman spectroscopy on FFPE colonic tissue sections has not been extensively studied. The main purpose of this section is to try and optimize the best working parameters for Raman studies on FFPE colonic tissue that is rapid and cost effective to facilitate rapid sample turnaround time essential in diagnostic pathology.

To summarise, this chapter aims to:

- Compare and contrast different instrumental and extrinsic working parameters for FFPE colonic tissue sections.
- Identify the most suitable and cost effective backing substrate for Raman analysis.
- Ascertain the most likely cause of variable paraffin contamination of different backing substrates.

3.2 Materials and Methods

To ensure that Raman spectroscopy stands as a viable technique in routine pathological practice all tissues used within the study underwent standard pathological processing as would be done in normal practice. Around 90% of all tissues examined in pathology labs are processed into paraffin blocks and so all the tissues used here have undergone similar treatment.

Optimization was primarily carried out on either human colonic tissue or colonic and/or liver samples obtained from a single Wistar rat. The origin of the tissue, sections thicknesses and substrates will be specified within each specific section of the chapter. Tissue acquisition and preparation has previously been outlined in chapter two.

3.2.1 Raman measurements

Raman spectroscopic measurements were conducted on the Renishaw inVia system (Renishaw plc, Wotton-under-Edge, UK) with interchangeable laser wavelengths, slit widths and objectives. The system is coupled to a standard Leica DM2500 microscope used to focus the laser and collect the Raman scatter. A

thermoelectrically cooled charge coupled device (CCD) camera was used for signal detection.

Before any data is collected several system checks are conducted: laser power, alignment and laser illumination concentricity. The system is then calibrated using a piece of silicon using the well-described peak at 520.5 cm^{-1}.

3.2.2 Data pre-processing and analysis

Raman spectra were pre-processed to reduce spectral variances originating from non-chemical effects. This ensures that any instrumental artefacts are removed and the chemical information within the spectra is enhanced.

All collected spectra were put through a cosmic ray removal tool in WiRE 4 software (Renishaw plc, Wotton-under-Edge, UK). This facilitated manual isolation and removal of sharp cosmic spikes using the width of feature and nearest neighbour methods. Some spectra had further undergone normalisation over the fingerprint region to standardise the spectral intensity range and facilitate direct comparison. The processing steps used for each spectral comparison will be outlined in the specific sections of the chapter.

Signal to noise (SNR) values were estimated by calculating the magnitude of a selected peak using the Renishaw curve fitting tool and dividing this value by the magnitude of the noise directly adjacent to the peak. The 1450 cm^{-1} CH deformation peak was used for all SNR estimates where the 1441 cm^{-1} paraffin band was absent, where the paraffin band was present, the phenylalanine band at 1003 cm^{-1} was used instead.

Signal-to-axis measurements across the fingerprint region were used to determine the area under the spectral curve (AUC). This was done on the raw spectral data set to estimate the total fluorescence. Data values were then exported into Microsoft Excel 2010 and plotted.

3.2.3 Scanning Electron Microscopy

Scanning electron microscopy was carried out on Jeol JSM-7401F Field Emission scanning electron microscope, operating at an accelerating voltage of 3kV. Non-conductive slide substrates (standard microscopy slides, synthetic fused silica and CaF_2) underwent ion vapour deposition to produce an ultrathin coat of carbon to

promote conduction for SEM analysis. Super mirror steel slides were used without any pre-treatment.

3.2.4 Atomic Force Microscopy

Atomic Force Microscopy (AFM) was conducted using a Bruker Innova AFM system (Bruker Corp., USA) to investigate the surface roughness of each slide substrate. Measurements were taken at room temperature in dry air conditions.

The spring constant k of the Si OTESPA cantilevers (Bruker Corp. USA) used for all slide substrates was 12-103 N/m with a resonance frequency f_o of 312-348 kHz.

WSxM 4.0 Beta 8.1 freeware software was used to pre-process the images. A flattening filter was applied to correct for abrupt height changes and a global plane filter to adjust for deviations in the image slope.

3.2.5 Contact angle measurements

Contact angle (CA) measurements were taken using a Drop Shape Analysis System type DSA10-Mk2 (KRÜSS, Optronics GmbH, Hamburg, Germany) equipped with a video camera. A 4 µl droplet of xylene was dropped onto the surface of each slide substrate (CaF_2, synthetic fused silica, standard glass, super mirror steel as well as silanized mirror steel) using a micropipette. A time course of CA measurements was obtained by taking the tangent to the drop on each surface. The CA was too small to facilitate static angle measurements. Four time course CA measurements were taken across each surface.

Prior to measurements all substrates were incubated for 1 hour in piranha solution (3:1 mixture of sulfuric acid (H_2SO_4) and 30% hydrogen peroxide (H_2O_2)) to remove any surface grease and debris. The silanized steel was fully dried prior to measurement. All measurements were conducted at standard room temperature in ambient air.

3.3 Results and Discussion

3.3.1 Fluorescence evaluation

Biological samples are known to exhibit a high degree of fluorescence originating from intrinsic tissue fluorophores. This results in a broad background

signal several orders of magnitude greater than the Raman signal. Fluorescence can be successfully supressed through a number of signal processing techniques as well as instrumental modifications.

Signal pre-processing methodologies include Fast Fourier Transform (FFT) filtering where the generally smooth low frequency fluorescence profile can be discerned and selectively removed from the high frequency Raman signals in the Fourier transformation (FT) domain. This however can lead to under- or over-filtering resulting in artefacts (132). Curve-fitting relies on fitting a fourth to sixth order polynomial to the fluorescence background followed by its subtraction from the original spectrum (125), this however can also lead to spectral artefacts (133). Alternatively, instrumental modifications include time gating and shifted excitation Raman difference spectroscopy (SERDS). Time gating relies on time resolved detection whereby a pico-second or femto-second short pulsed laser is used for excitation coupled with a picosecond Kerr gated optical shutter. Raman scattering occurs almost instantaneously with a laser pulse, fluorescence lifetimes on the other hand are at longer temporal ranges. A short pulsed Raman signal is allowed to pass through the opened Kerr gate via transient anisotropy of the Raman light, the majority of the longer lived fluorescence however is rejected upon the decay of the anisotropy of the Kerr medium (134). Alternatively SERDS is based on the knowledge that fluorescence emission is unaltered with a small change in the excitation wavelength, however Raman shifts are dependent on the excitation photon wavelength. As a result subtraction of two spectra collected at very slightly shifted excitation wavelengths yields a fluorescence free Raman difference spectrum (135). Such instrumental modifications can prove to be costly and may not mitigate the problem completely especially in the case of SERDS and photo-bleaching effects.

Alternatively, by shifting to longer wavelengths the overall effect of fluorescence can be reduced, principally because the photon energy is substantially lower resulting in a reduced likelihood of electronic transitions. The intensity of the Raman scatter is however inversely proportional to the fourth power of the laser wavelength. This means that the longer the wavelength, the weaker the Raman scatter and hence the weaker the overall Raman signal. Hence there is a trade-off between the increased Raman scattering efficiency and total fluorescence.

In this section, the overall tissue fluorescence intensity was evaluated at four different wavelengths 532, 633, 785 and 830 nm. It was not possible to maintain identical spectral acquisition parameters due to the variable optical properties of formalin fixed paraffin embedded (FFPE) colonic tissue at each wavelength. Nonetheless, the overall aim was to obtain the best quality raw spectra with a low Raman background contribution regardless of the acquisition time or laser power. Hence, a multitude of laser powers and exposure times were tested to avoid saturating the CCD camera. It is also important to note that the laser power for each excitation wavelength differed significantly; see *Appendix 2* for approximate laser power measurements with and without a microscope objective lens in the light path.

3.3.1.1 Laser wavelength dependent fluorescence

Selection of the optimum excitation source for work with colon tissue samples was achieved following the collection of 10 point spectra at wavelengths covering the visible and NIR range – five from colon crypt cells and five from the lamina propria. Substantial variation in spectral background drift is observed across all wavelengths, this indicates that some regions of the tissue are more fluorescent than others (*fig.3.1*). Hence, regardless of the wavelength selected the nature of the tissue plays a significant role in the variability of the spectral background. Following normalisation the greatest amount of baseline drift was observed when using a 785 nm excitation source; with the least amount of variation exhibited when using 532 nm (*fig.3.2a*).

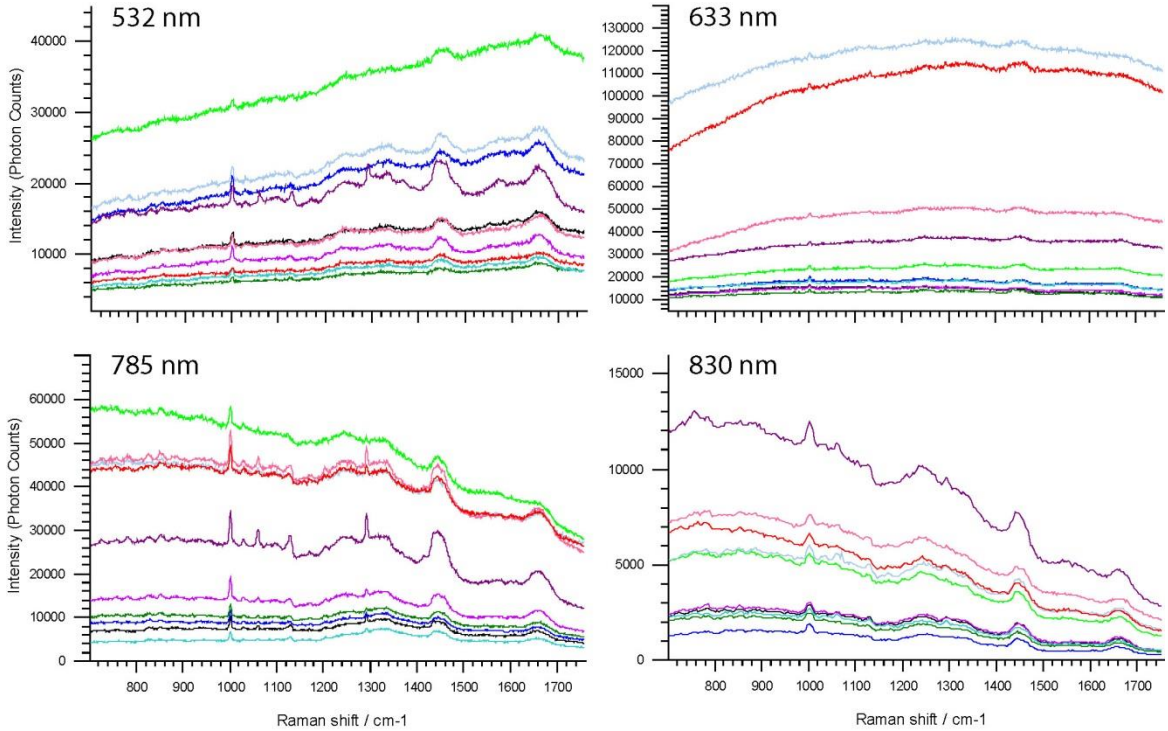

Figure 3.1: Original Raman spectra collected from 10 random regions across human colonic tissue at different wavelengths using different laser powers and acquisition times. *The highest spectral background with fewest visible Raman peaks was observed using 633 nm excitation (top right). Spectra with the most prominent Raman peaks and level spectral background was observed using 785 nm excitation (bottom left).*

Aside from baseline drifts, the slope of the baseline can also have a considerable effect on the quality of spectral pre-processing. Baseline correction of large sloping backgrounds can not only effect the band shapes but also introduce severe band distortions (133). To determine the linearity of the background, the gradient of all the average spectra for each wavelength was calculated. The greatest slope was observed when using 785 nm, with similar slopes present at 532 and 633 nm and minimal slope variation with 830 nm (*fig.3.2b*). Given that on average 830 nm results in minimal alteration of the baseline shape, suggests that utilizing this wavelength reduces the likelihood of introducing band distortions during spectral pre-processing.

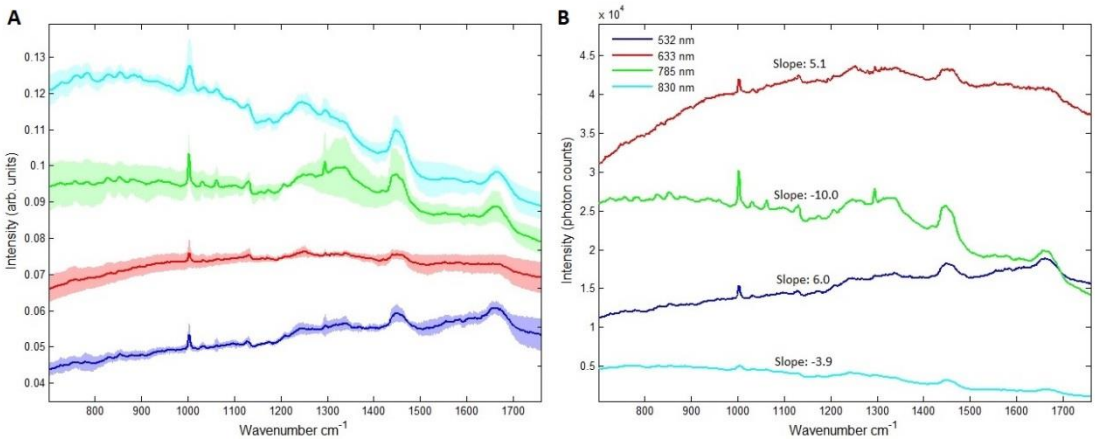

Figure 3.2: Average spectra showing the spectral slopes and baseline variations when using different excitation wavelengths. A) *Average normalised spectra from each wavelength with shaded regions representing ±1 standard deviation; spectra were offset for visual clarity.* ***B)*** *Average spectra portraying the expected shape and gradient of the slope obtained when using different excitation wavelengths.*

Signal-to-axis measurements across the 700–1760 cm^{-1} wavenumber region were calculated for each spectrum to approximate the overall level of tissue fluorescence at a given wavelength. An overall reduction in the intensity of the spectral background is observed from 633 nm through to 830 nm (*fig.3.3a*). This is not unexpected as shifting to longer wavelengths in turn reduces the incident photon energy resulting in a reduced likelihood of electronic transitions, and hence lower fluorescence (133). The shortest wavelength of 532 nm did not contribute to the highest Raman background as was originally anticipated; this was however due to the substantially lower laser power and added photo-bleaching time used to acquire the spectra. It was not possible to utilise 100% laser power (110 mW) at 532 nm due to the saturation of the CCD chip but also due to photo-thermal degradation of the tissue.

Signal to noise ratios (SNR) were calculated for each individual spectrum by dividing the peak intensity of the CH deformation peak at 1450 cm^{-1} by the intensity of the noise directly adjacent to the peak. SNRs were the highest for the two longest wavelengths, with a marginally greater average SNR calculated for 785 nm; however they also exhibited the greatest variation (*fig.3.3b*). This could be due to the presence of previously reported ‘hot’ and ‘cold’ spots in tissue – resulting in large range variations in intensity background as well as SNRs (76).

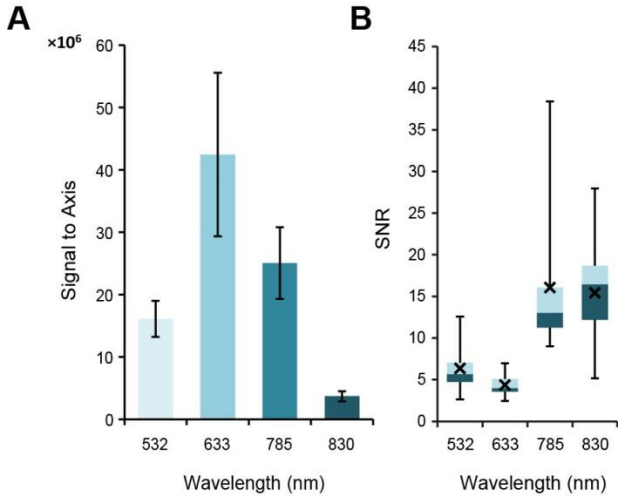

Figure 3.3: Plots evaluating the overall tissue fluorescence and signal to noise exhibited by different excitation sources. A) *Bar plot of the AUC averages (encompassing 700-1760 cm-1 region) used to quantify the degree of fluorescence exhibited for each wavelength with standard errors of the mean. Highest fluorescence was exhibited by 633 nm with lowest observed from 830 nm.* ***B)*** *Box and whisker plots of SNR values for each excitation wavelength. S/N ratio averages are marked by the black crosses across the boxplots. Highest S/N ratios were observed for the two longer wavelengths (785 and 830 nm), however the greatest degree of variation was also observed.*

Selection of the optimal excitation wavelength for measuring colonic tissue must be balanced between the level of fluorescence that masks the weakened Raman signal and the intensity of the Raman scatter. The longer excitation wavelengths (785 and 830 nm) were shown to optimally balance this trade-off producing the highest S/N ratios in FFPE colonic tissues. Nevertheless, the total time taken to acquire a spectrum using 785 nm at equivalent S/N ratios is approximately five times shorter than that of 830 nm, which in turn facilitates faster sample measurement times. A summary of the total acquisition time and SNRs per excitation wavelength can be found in table 3.1.

Table 3.1: Summary of the total acquisition time and SNR values for each excitation wavelength. *Best performing wavelengths are highlighted in red.*

Wavelength (nm)	Acquisition time (sec)	Bleaching Time (sec)	Total time (sec)	SNR average
532	10	15	25	6.1
633	15	15	30	4.3
785	10	0	10	16.2
830	50	0	50	15.6

3.3.1.2 Tissue dependent fluorescence

To evaluate the effects of tissue dependent fluorescence variation, signal to axis analysis of 400-1800 cm^{-1} wavenumber region was performed on a raw dataset of a healthy human colonic mucosa. A heat map displays variable optical properties associated with different histological regions (*fig.3.4*). The highly fluorescent regions shown in figure 3.4 are located within the lamina propria densely populated with lymphocytes. These regions exhibit higher levels of fluorescence ranging from 2,000 photon counts through to 12,000 counts. Regions with low fluorescence correspond with the crypt cells and muscularis mucosa. Previous reports have shown areas of fluorescence above a certain threshold being assigned to p53 active areas in cancerous colonic tissue samples (68). The results here however indicate that caution must be exercised when assigning p53 active areas to regions with elevated auto-fluorescence without any accompanying spectral features.

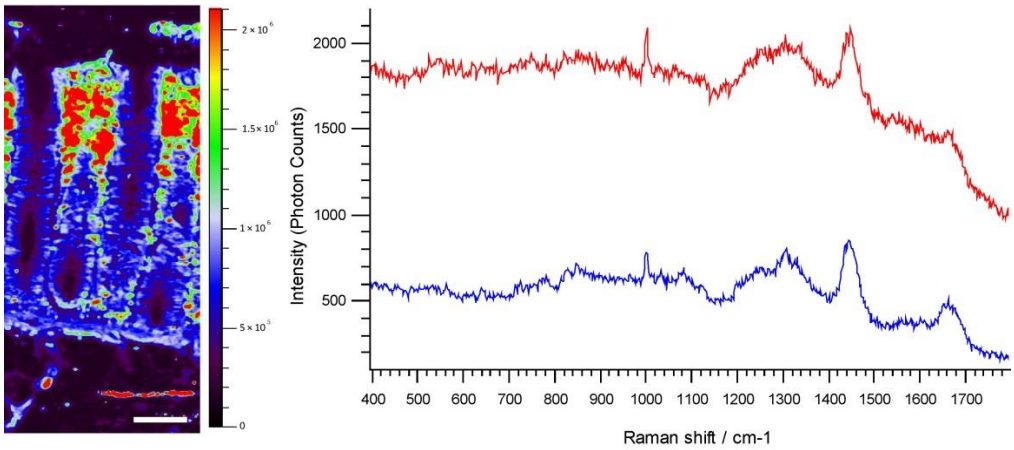

Figure 3.4: Signal to axis image of the colonic mucosa plotted using WiRE 4 software (400-1800 cm-1 wavenumber range). *Red regions of the image correspond to spectra that exhibit elevated fluorescence. The red spectrum is an example spectrum from a single pixel within the red region. Blue regions correspond to tissue regions with low overall fluorescence, the blue spectrum is an example spectrum taken from a corresponding blue pixel. Image consists of 336,512 spectra taken at t = 15s with 158 mW of power using 785 nm excitation. Scale: 100 µm.*

3.3.1.3 Pathology dependent fluorescence

Variation in the optical properties as a result of pathological onset was investigated by comparing spectra collected from tissue undergoing transitional pathological changes. A total of 10 point spectra were collected encompassing the

crypts and the surrounding lamina propria from normal, adenomas and adenocarcinoma tissue.

Tissue fluorescence proved to be independent of pathology and appeared to vary more with the size of the tissue (*fig.3.5b*). On average S/N ratios increased with pathological onset, with best S/N ratios observed in cancerous tissue (*fig.3.5c*). However, a greater deal of variation was present as indicated by the larger boxes and error bars. Normal tissue exhibited much smaller S/N ratios with the data being slightly skewed towards the higher end of the scale – indicating that a large majority of the spectra exhibit good S/N ratios.

Although some disparity in the optical properties from within abnormal tissue constituents was detected, no radical differences between normal, precancerous and cancerous colonic tissue were obvious. As a result, the application of identical experimental parameters throughout should not impose any major issues.

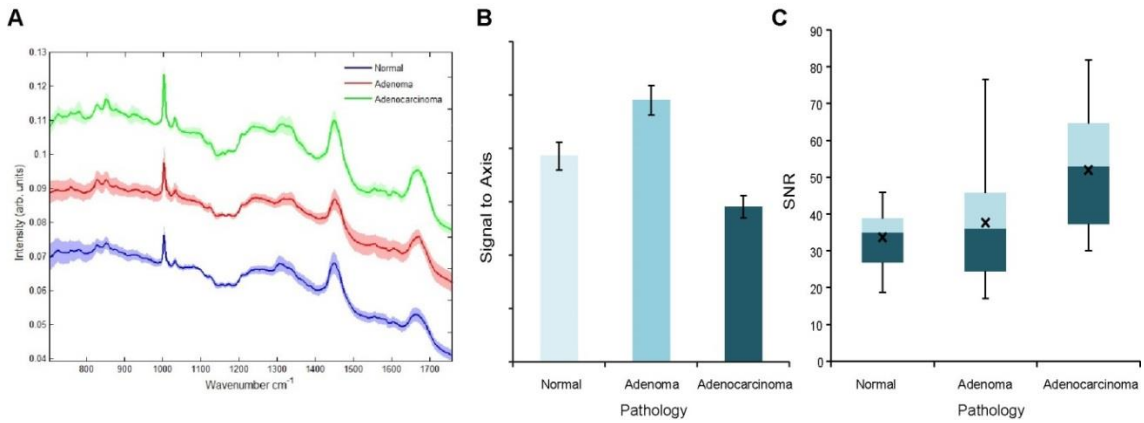

Figure 3.5: Comparison of optical properties from different colonic tissue pathologies. A) *Averaged spectra from each pathological category along with ±1 SD, spectra were offset for visual clarity.* ***B)*** *Bar plot of the AUC averages (encompassing 700-1760 cm^{-1} region) used to quantify the degree of fluorescence exhibited with standard errors of the means. Small adenomas biopsies proved to the most fluorescent in comparison to larger resections.* ***C)*** *Boxplots of S/N ratios. Normal tissue exhibits smaller S/N ratios with less variability, while cancerous and precancerous tissues possess higher S/N ratios with greater variability. S/N ratio averages are marked by the black crosses across the boxplots.*

3.3.2 Other experimental parameters

The next steps to further increase the Raman scattering signal is to raise the power density of the excitation beam. Hence, following the minimization of fluorescence via careful wavelength selection, maximizing the collection and detection efficiency

of the scattered photons must be the next priority. Different microscopes objectives, laser geometries and tissue thicknesses are investigated in the following section.

3.3.2.1 Microscope objectives and laser geometry

The numerical aperture (NA) of the objective determines its light collection efficiency and is defined by:

$$NA = \mu \operatorname{Sin} \alpha_{max} \tag{3.1}$$

Where NA is the numerical aperture, α_{max} is the half angle of the maximum acceptance angle of light that can enter the objective and μ is the index of refraction of the immersion medium, which in this case is air ($\mu = 1$). The higher the numerical aperture, the greater the acceptance angle and hence the better the collection efficiency of the objective (*fig.3.6*) (136).

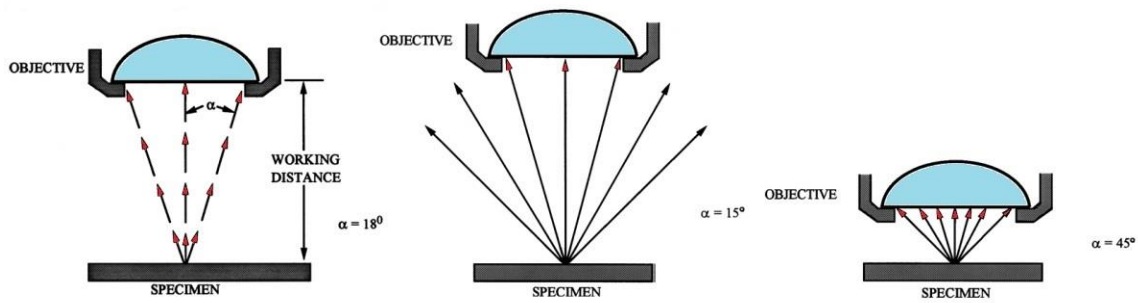

Figure 3.6: Objectives with different acceptance angles and working distances. *Objectives with shorter working distances have larger acceptance angles and therefore better light collection efficiency (136).*

Since it has already been well established that the collection efficiency of an objective increases with the numerical aperture, optimum objective selection was made by evaluating the following parameters:

1) Power density of the laser illumination spot
2) Depth of tissue penetration and hence collection volume
3) Relative glass and fluorescence contribution to the original spectrum

The performance of each objective in analysis of a non-uniform complex biological system such as tissue must also be considered. The objectives tested and their relative specifications are listed in *table 3.2*. All measurements were acquired using 785 nm excitation and super mirror stainless steel substrates. All tissue spectra were collected across the muscle tissue of the colon as this was considered most homogenous containing only one cell type. Given that tissue recovery time is unknown the variable effects of photo-bleaching was avoided through the selection of a new region for each measurement.

1. Power density

Utilizing point illumination with a tightly focused laser source not only generates higher power densities but also enables the production of Raman images with higher spatial resolution. However, this can increase the likelihood of photo-damaging the tissue. In addition a Gaussian beam profile can be reshaped using cylindrical lenses to produce a line illumination. This not only reduces the power density, hence reducing the risk of sample damage, but also reduces the image acquisition time as signals from different regions of the tissue are being generated simultaneously. Beam profiles generated using different objectives and illumination geometries were measured using knife edge measurements.

The beam surface area and laser power density was found to similar for two of the 50× objectives using both point and line illumination. The power density was found to be 1.5 times greater and approximately half the beam area with the 100× objective (*table 3.2*).

Table 3.2: A list of the available Leica microscope objectives and their working specifications. *Laser length and width was calculated using knife edge measurements. Laser surface area was collected for an ellipse using the following equation (Area = πXY, where X and Y are half the major axis of the short and long axis of the laser ellipsoid). Laser power was measured using a handheld Edmund Optics laser power meter.*

Microscope Objective	Fabrication	NA	Laser Geometry	Beam Surface area (μm^2)	Laser Power (mW)	Power Density (W/cm^2)
50× short WD	N PLAN EPI	0.75	SPOT	55.7	113	20.3
			LINE	88.8	108	12.2
50× long WD	N PLAN	0.5	SPOT	52.4	97	18.5
			LINE	74.1	96	13.0
100× short WD	N PLAN EPI	0.85	SPOT	20.3	59	29.1
			LINE	28.8	57	19.8

2. Sampling volume

The sampling volume of each objective was calculated from depth profile measurements of an 8 μm polytetrafluoroethylene sheet (PTFE) and 8 μm colonic tissue section. PTFE of known thickness was hypothesized to be perfectly uniform in comparison to tissue and was used as a control. Each objective was scanned through a depth of ±70 μm at 0.2 μm increments i.e. the objective was used to scan the focus through a distance 70 μm above and below the tissue sample with zero μm being the focal point in the tissue. A height of 70 μm above the sample was selected as this was the height at which there was no detectable Raman scatter from the tissue or PTFE surface. This produced an intensity profile with the maximum intensity corresponding to the focal point of the objective at the tissue/PTFE surface. The intensity profile for the phenylalanine peak at 1002 cm^{-1} in tissue and 1380 cm^{-1} peak in PTFE were then fitted to a Gaussian distribution. The full width half maximum (FWHM) of the depth profile peaks correspond to the axial resolution and hence the depth of penetration and sampling volume of each objective.

Generally poorer results were obtained from PTFE as depicted by the broader peaks and visible left sided protrusions from the depth profiles (*fig.3.7*). This was thought to be due to the deformation of the plastic sheet with the laser heat. As a result PTFE is assumed to not be completely flat during the depth profile measurements. Nonetheless, comparable results were obtained from both of the

50× objectives with an expected smaller sampling volume with the 100× objective. An increase in the sampling volume is observed with the linear laser geometry, this was not the case for the highest NA objective (*table 3.3*).

Better quality results were obtained from tissue sections as the depth profiles were tighter and more uniform in shape. This is likely to be due to the tissue remaining flat and attached to the slide surface during measurement. As observed with PTFE superior axial resolution was achieved with the 100× objective, with negligible effects from changing the laser geometry (*fig.3.7* and *table 3.3*). The short WD 50× objective exhibited a 2.5 times greater sampling depth in the spot geometry, and 3 times greater volume in line geometry in comparison to the 100× objective. The long WD 50× objective exhibited the largest sampling volume in spot geometry with an unusual decrease in the sampling volume following the use of a laser line. This anomaly is likely to be induced by the variable optical properties of the tissue.

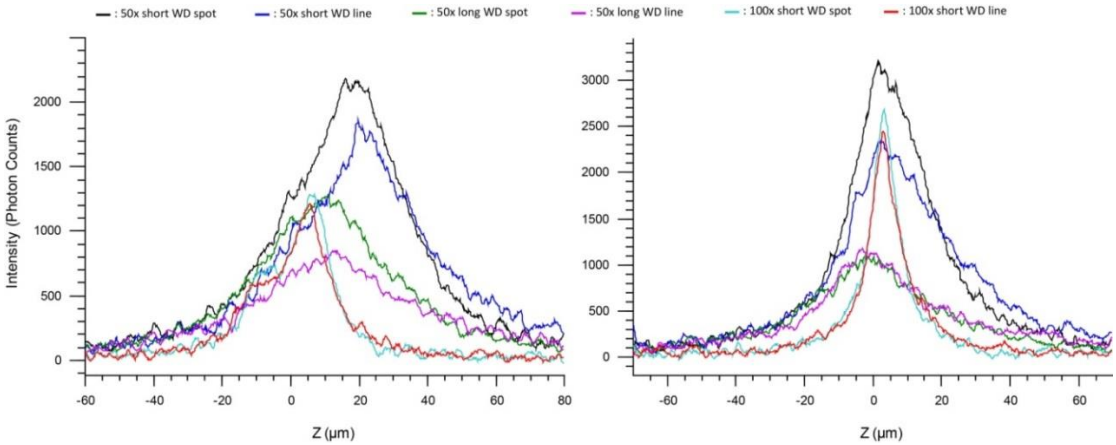

Figure 3.7: The 785 nm laser light distribution along the depth of the PTFE (left) and tissue (right) using different microscope objectives. *Shorter PTFE and tissue penetration was observed from the 100× objective with similar penetration observed from both the 50× objectives. The light collection efficiency is also shown to be the worst with the 50× long working distance objective with the lowest NA of 0.5.*

Table 3.3: Full width half maximums calculated for each objective per laser geometry for 8 µm PTFE and 8 µm colonic tissue sections.

Microscope Objective	NA	Laser Geometry	PTFE FWHM (µm)	Tissue FWHM (µm)
50× short WD	0.75	SPOT	39.5	25.9
		LINE	43.0	33.7
50× long WD	0.5	SPOT	43.7	38.6
		LINE	47.9	31.0
100× short WD	0.85	SPOT	16.5	9.7
		LINE	16.1	10.7

3. Objective contribution and fluorescence

The original spectra in figure 3.8a highlight the 50× short WD objective as the greatest contributor of glass signal to the original Raman spectra. The lowest objective contribution was observed from the 50× long WD objective with moderate contribution from the 100× short WD objective. Average tissue spectra shown in figure 3.8b display the same trend. There was no detectable difference in the glass contribution with changes in laser geometry.

In addition to the elevated objective contribution, the 50× short WD objective also had the highest overall baseline, conversely the highest S/N ratios were also observed with this objective (*fig.3.8c-d*). On average the 50× long WD objective had the lowest overall baseline and second best S/N ratios. In both cases the S/N ratios were higher for laser spot geometries due to the increased power densities. Somewhat unexpected results were observed from the 100× objective where the S/N ratios were similar to that of the 50× long WD objective. The reduced performance of the higher NA objective is likely to be offset by the variable optical properties of tissue material.

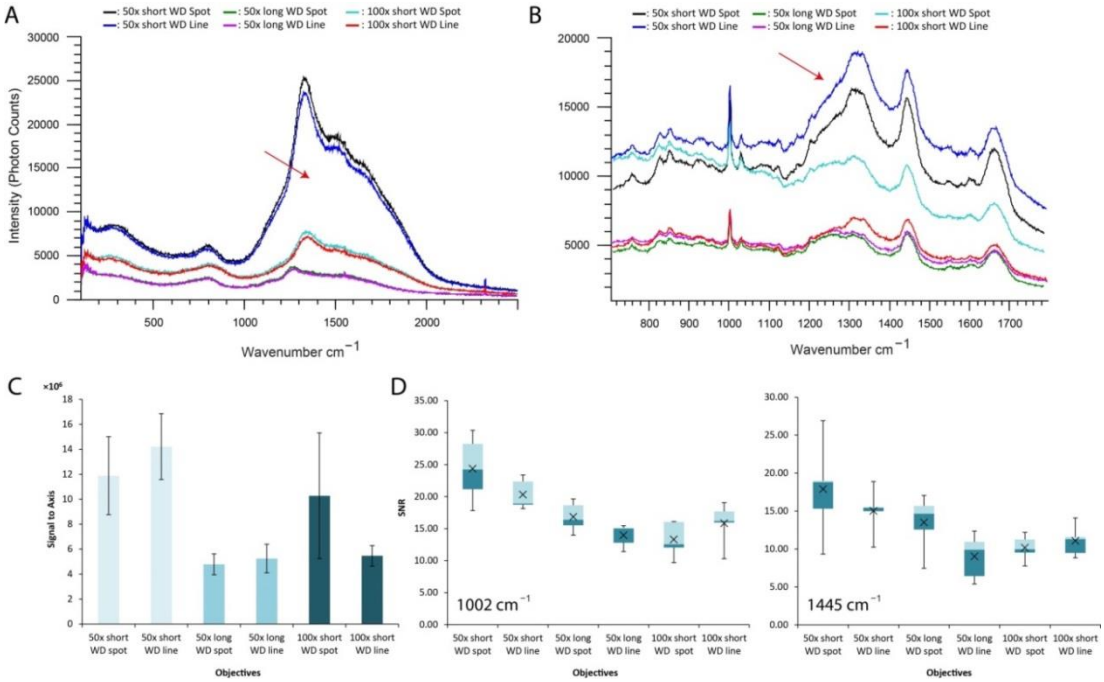

Figure 3.8: Comparison of objective contributions to the original Raman spectra. Red arrows highlight the glass signals contributed by the objective. A) *Extended scans taken using different objectives across super mirror steel covering an extended wavenumber range (t=10s, P=110 mW). B) Average tissue spectra taken using different objectives (t=5s, P=110mW).* ***C)*** *Bar plot of the signal to axis averages used to quantify the degree of fluorescence observed from each microscope objective with ±1 standard deviation from the mean.* ***D)*** *Box and whisker plots of S/N ratios obtained for the 1002 cm-1 (phe) peak and the 1450 cm-1 (CH deform) peak for each objective. S/N ratio averages are marked by the black crosses across the boxplots.*

In summary, the 100× objective exhibited the highest power density and smallest collection volume in both PTFE and tissue, making it appear to be a superior objective over the others. However, when applied to a complex biological system covering variable lateral positions, this superiority did not hold up and lower S/N ratios were obtained, this was observed for two peak positions (1002 and 1445 cm^{-1}). This suggests that even the best performing objectives can produce poor quality spectra if the tissue sample is suboptimal or incompatible. Given that the power density and collection volume did not radically differ from the 50× short WD objective, an objective that provides the best S/N ratios is ideal and will be used for the remaining studies.

3.3.2.2 Tissue thickness

The effect of tissue thickness was investigated using the wavelength previously found to be optimal i.e. 785 nm. Liver tissue mounted onto CaF_2 backing substrate

was used for an investigation to optimize this new parameter. Liver tissue was selected due to its near homogenous nature (around 70% of the tissue is hepatocytes). It was therefore hypothesized that upon cutting little variation in tissue thickness is to be observed as a result of tissue inhomogeneity and regional differences in rigidity or elastic deformation during the passage of the blade. The S/N ratios as well as the AUC was calculated for 10 raw spectra obtained from tissue cut at different thicknesses: 3, 5, 6, 7, 8 and 9 µm.

A gradual proportional elevation in the background intensity is observed as the tissue thickness is increased (*fig.3.9*). An overall consistent size of the box plots indicates similar optical properties of the tissue across different regions; this however did not apply to the 6 µm section. The overall level of tissue fluorescence was therefore found to increase with tissue thickness. As a result increasing the thickness of FFPE sections will increase the likelihood of saturating the CCD.

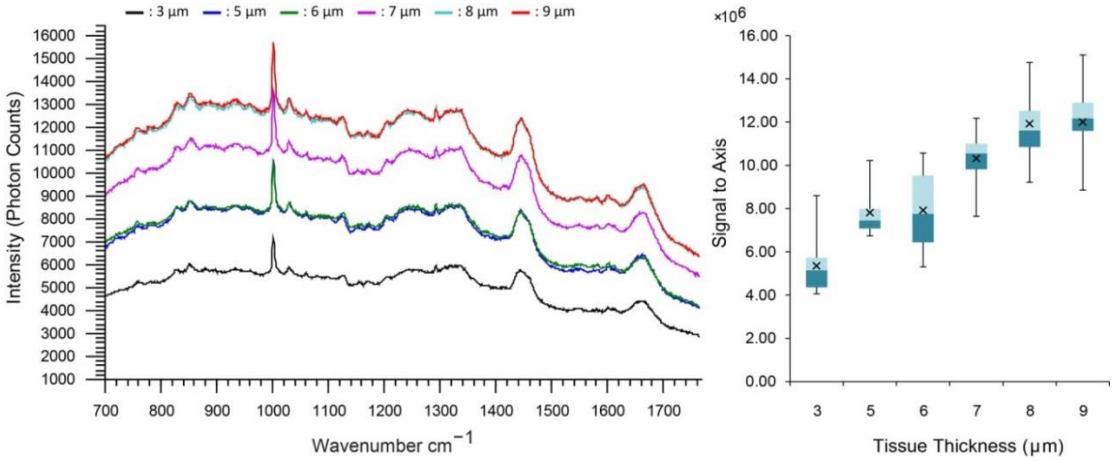

Figure 3.9: Effects of tissue section thickness on fluorescence. (Left) *Average of 10 spectra acquired at different tissue thicknesses (3, 5, 6, 7, 8 and 9 µm) using 2 seconds acquisition time and 110 mW of power.* ***(Right)*** *Box plots of the signal to axis measurements used to approximate the total level of tissue fluorescence. Scatter plot depicts the average SNR. Both show an increase in the level of fluorescence with increasing tissue thickness.*

S/N ratios calculated for the phenylalanine peak at 1002 cm^{-1} reveals a very subtle increase with tissue thickness (*fig.3.10*). The most commonly used H&E staining thickness of 3 µm exhibited the lowest S/N ratio, while the thickest sections of 8 and 9 µm had the highest S/N ratios. A large range of S/N ratios was detected for all thicknesses except the 7 µm section were a greater level of consistency was observed.

This is a likely result of collecting some spectra from Raman 'hotspots' were the S/N will undoubtedly be higher.

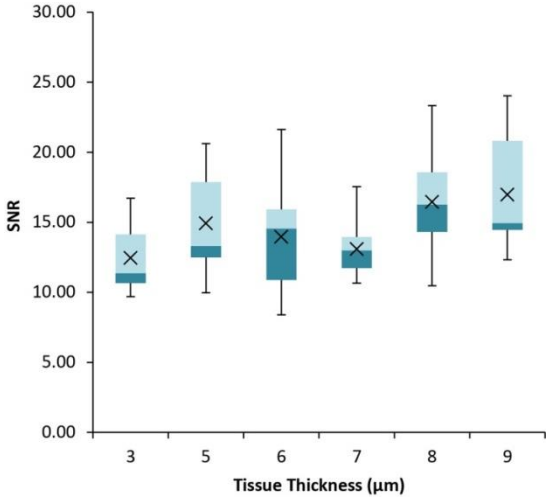

Figure 3.10: Box and whisker plots of S/N ratios observed for all tissue thicknesses. *A subtle but obvious increase in the S/N ratios was observed with increasing tissue thickness. Average S/N ratios are depicted by black crosses and are in agreement with the increasing trend.*

In summary, selecting a thicker tissue section in an attempt to increase the S/N ratios may not be beneficial as this is immediately accompanied by an increase in tissue fluorescence. With a greater majority of S/N ratios being in the lower range for 9 µm sections and only a marginal increase in the SNR from 8 µm, 8 µm was therefore elected as the optimal thickness to proceed with for the remainder of the study.

3.3.3 Backing substrates

At present calcium fluoride (CaF_2) continues to be the unbeatable, widely used substrate of choice for many laboratories employing Raman spectroscopy. However, it is not without its shortcomings as UV-grade CaF_2 is extremely costly, especially when made into standard slide dimensions. CaF_2 has also been shown to be extremely fragile and brittle and is unlikely to withstand the rigorous handling involved during standard pathological practice.

The overall aim here is to provide an overview of the behaviour of a small subset of alternative backing substrates at 785 nm. A cost break down of the trialled backing substrates can be found in *Appendix 3*.

3.3.3.1 Substrate wavelength compatibility

A number of different candidate replacements for UV grade CaF_2 (Crystran UK), were proposed – borosilicate glass, synthetic fused silica ex photomask and aluminium coated glass mirrors (300 nm thickness) all obtained from LG Optical (LG Optical ltd, UK). These were also compared against the conventional microscopy slides made of extra white soda lime glass (Thermo scientific UK). All spectra were collected using the extended scan feature allowing the entire wavenumber range to be viewed with ease. However, some substrate spectra saturated in this mode and were therefore collected using point spectra with either a shorter acquisition time or reduced laser power. To compensate for this discrepancy all spectra were normalized to reduce the impact of variations within the acquisition parameters.

Aside from synthetic fused silica all candidate backing substrates demonstrated poor performance at each wavelength when directly compared against CaF_2. Furthermore, the performance of these substrates was shown to be extremely variable when exposed to different excitation wavelengths (*fig.3.11*). Synthetic fused silica retained a consistent spectral profile at all the excitations and only exhibited an intense broad features below 600 cm^{-1}, which would constrain the analytically useful fingerprint region to 600-1800 cm^{-1}. Aluminium coated glass has previously been shown to be a superior substrate that not only provided similar results to UV-grade CaF_2, but also provided a substantial signal enhancement by a factor of 4 (109,111). Results here however show that the overall background intensity obtained at each wavelength was significantly higher than that of CaF_2.

Other optical glass types measured included N-FK51A (Schott), S-FPL53 (Ohara) and MirrIR slides (Kevley Technologies, USA); all were shown to be unsuitable replacements for CaF_2 at 785 nm (*spectra not shown*).

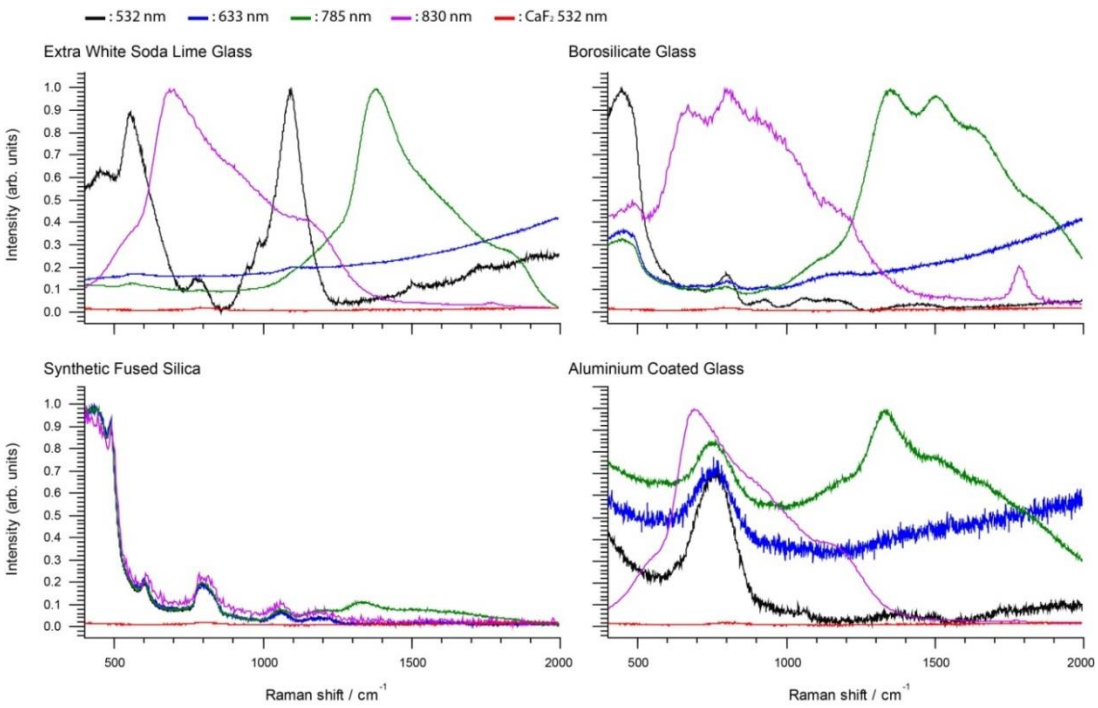

Figure 3.11: Normalized Raman spectra obtained from different backing substrates at different excitation wavelengths. *The behaviour of a single substrate type at different wavelengths is shown; spectra were normalized to facilitate comparison. CaF2 reference (red) measured only at 532 nm was displayed alongside each panel; measurements at other wavelengths were not plotted as there was no delectable spectral difference. A consistent spectral profile at all wavelengths was only observed from synthetic fused silica.*

3.3.3.2 Tissue thickness effects on fused silica spectral features

One of the main concerns with opting for synthetic fused silica as a potential replacement for CaF_2 is the broad feature present at 750 - 850 cm^{-1}, which would inevitably mask a vital nucleic acid vibration at 780 cm^{-1}. The appearance of fused silica spectral features with increasing tissue thickness was therefore tested – 10, 12 and 16 µm sections were trialled. According to the biomedical technicians 16 µm is about the thickest section that can be obtained from FFPE blocks with relative ease.

White light imaging of thick unstained colonic tissue sections reveals a clearly visible thickness variation across the surface (*fig.3.12*). Such variability demonstrates the inability of conventional laboratory microtomes to create a uniform thickness across the whole section; this particularly applies to thicker sections. Point spectra were obtained from regions assigned to thick and thin areas.

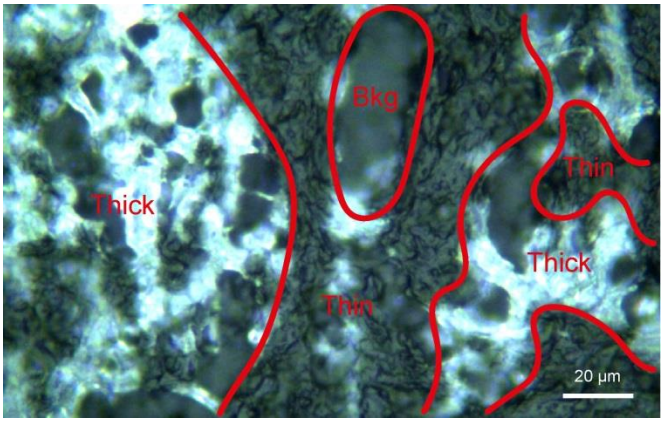

Figure 3.12: White light image of thick and thin regions observed across a colonic tissue cut to 16 µm. *Spectra assigned to thick regions were taken across all white like regions, while spectra assigned to thin regions were taken across the darker more transparent like regions of the tissue. The background is marked by bkg.*

A total of ten point spectra were collected using 785 nm from all tissue thickness and from both the visibly different thick and thin regions. Spectral interference at 750 - 850 cm^{-1} was observed for all the thin regions across all the tissue thicknesses tested, this was not the case for measurements obtained from thick regions (*fig.3.13*). Furthermore, the illumination geometry was not found to influence the collection of backing substrate peaks. These results indicate that if fused silica was to be used for measurements at 785 nm then variable substrate contributions would be widespread across the tissue.

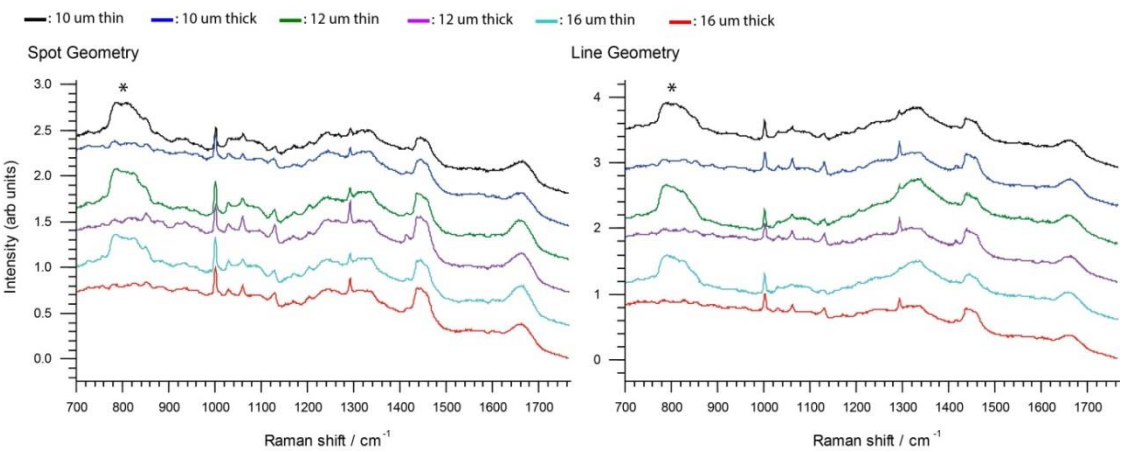

Figure 3.13: Normalized and averaged tissue spectra collected using both spot and line illumination geometry (785 nm) from 10, 12 and 16 µm thick and thin colonic tissue regions. *Substrate peaks are only seen from thin regions from all the tissue thicknesses tested. Asterisks indicate fused silica substrate peaks.*

3.3.3.3 Metallic backing substrates

Comparison of original spectra obtained from CaF_2 and mirrored steel using the same measurement parameters shows that steel exhibits an even lower baseline than CaF_2 (*fig.3.14a*). Five spectra acquired across different locations (each corner of a rectangle and the central region) from each of the backing substrate revealed that the highest background originated from aluminium coated glass (maximum ~40,000 counts) with an intense broad feature around 750 cm^{-1} – attributed to the stretching vibration of the AlO_3 coating (*fig.3.14b*) (137). Furthermore, baseline drift was predominantly observed from CaF_2 indicating that spectra acquired from mirror steel shows no spectral variability.

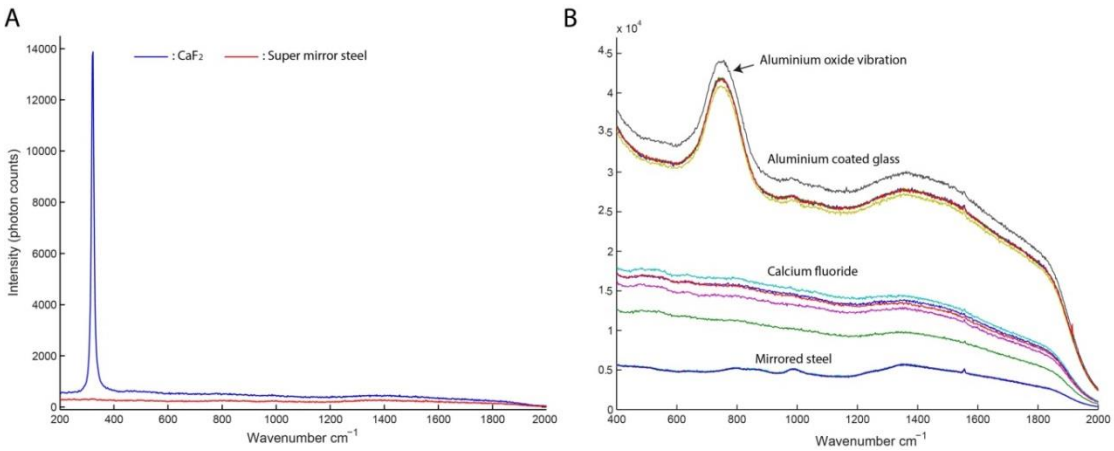

Figure 3.14: Comparison of spectral profiles from reflective backing substrates. A) *Spectral contributions obtained from CaF2 vs super mirror steel using 1 second acquisition and 158 mW of power at 785 nm. Mirror steel exhibited a much lower baseline in comparison to CaF2.* ***B)*** *Comparison of five original spectra acquired from the surface of mirrored steel, aluminium coated glass and CaF2. CaF2 exhibited the greatest baseline drift whereas mirrored steel showed no baseline drift.*

The lack of Raman spectral contribution from metal based substrates has been known for quite some time, yet very few studies opt for using metals over CaF_2. Furthermore, some studies have opted out of using steel due to a background that was shown to be higher than that of glass (130). Seeing as the surface finish of the steel slides used by Stone 2001 is unknown, the variability in the Raman background intensity and spectral profiles of different steel surface finishes was compared.

Natural and aqua finish steel both exhibit a variable degree of background intensity (*fig.3.15*). The rougher looking natural finish displays some variable broad peaks between 470 cm^{-1} and 740 cm^{-1}, these are absent from the smoother looking

aqua finish. Microscopic examination of the surface also reveals that roughened surfaces are highly susceptible to rust formation (*not shown*).

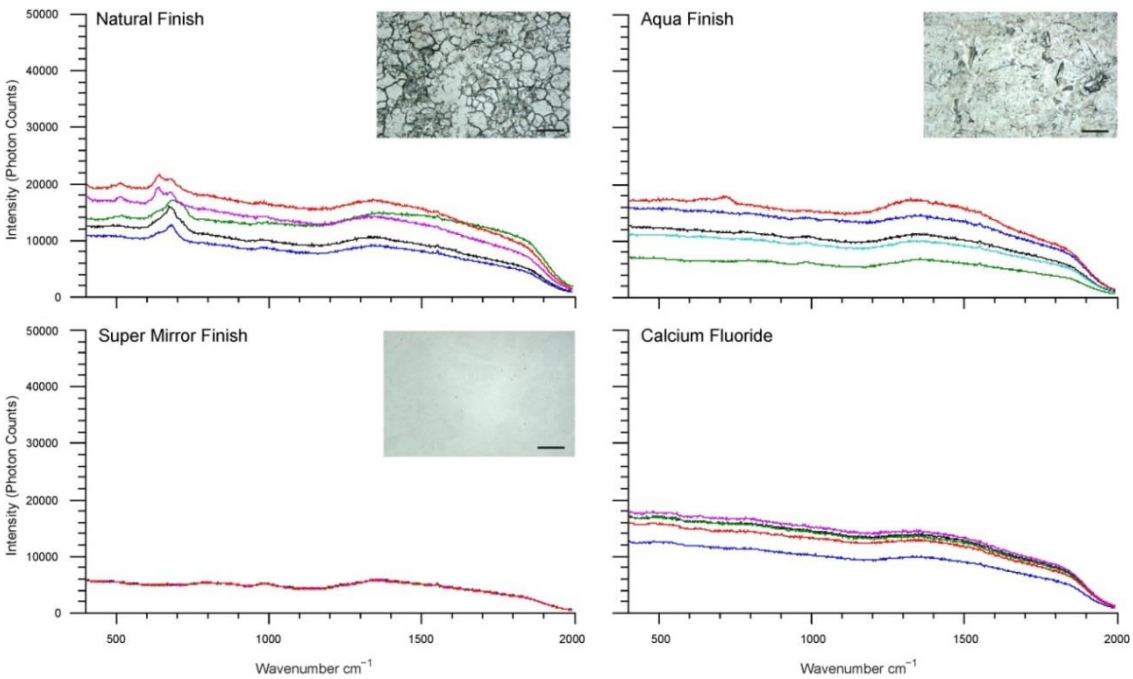

Figure 3.15: Spectral contributions from the surface of different backing substrates, surface finish micrographs are shown to the top right of the spectra (scale: 20 µm). *Elevated baseline drift is observed from rougher finished steel (natural and aqua) with no visible drift from a smooth uniform mirror finish. Baseline drift observed from CaF2 is likely to have been caused by surface scratches inflicted during slide recycling. T = 10 sec, P = 158 mW at 785 nm.*

Given that highly polished super mirror steel is not Raman active and displays no baseline drift then it has significant potential for use as a cheaper alternative to CaF_2. The performance of mirror steel for use with colonic tissue sections will be evaluated in the subsequent sections.

3.3.4 Calcium fluoride vs super mirror stainless steel slides

This section of the thesis aims to provide a direct comparison of the performance of super mirror stainless steel slides against CaF_2 slides. The functionality of each slide will be based on a number of different parameters:

1) Sample visualization from the slide surface.
2) Adhesion of tissue to the slide surface.
3) Quality of the acquired Raman spectra.

4) Paraffin retention properties of FFPE tissues samples mounted on each backing substrate.

3.3.4.1 Sample visualization

Super mirror stainless steel has been shown to be a promising alternative to CaF_2; however sample visualisation cannot be achieved using standard transmission mode microscopy. Here sample visualisation under white light imaging (transmission vs reflective modes) was investigated. Direct comparison of 8 µm unstained colonic tissue sections mounted onto UV grade CaF_2 and mirror steel was made (*fig.3.16*). Although a better image contrast is achieved on CaF_2, lymphocytes within the collagenous network of the lamina propria (*red arrows*) are more easily identified on steel. Furthermore, mucin containing regions within the crypts are more easily differentiated from the backing substrate on steel (*green arrows*).

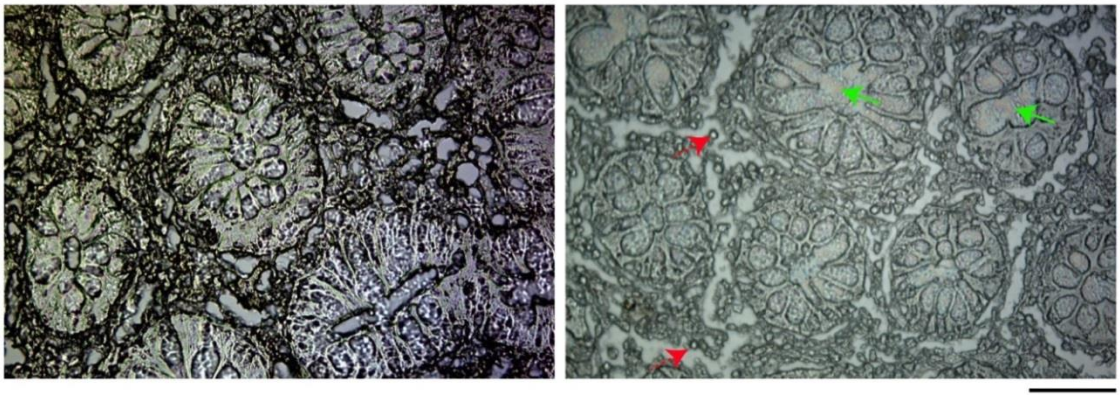

Figure 3.16: White light image of 8 µm unstained human colonic tissue section mounted onto CaF2 (Left) and super mirror stainless steel (Right). *Mirror steel facilitates easier identification of histological features such as lymphocytes (red arrows) and mucin (green arrows). Images were obtained using the Bluefox video camera fitted on the RA802 Renishaw prototype system. Scale: 50 µm.*

H&E staining of 8 µm tissue sections revealed good image quality obtained from both glass and super mirror steel (*fig.3.17a-b*). Sample visualization was confirmed to be of exceptional quality by a resident consultant pathologist Dr Rodriguez-Justo. Roughening the steel surface produces the worst image quality with an almost dirty sample appearance (*fig.3.17c*). These observations confirm that super mirror stainless steel is suitable for both unstained Raman imaging as well as post measurement H&E staining.

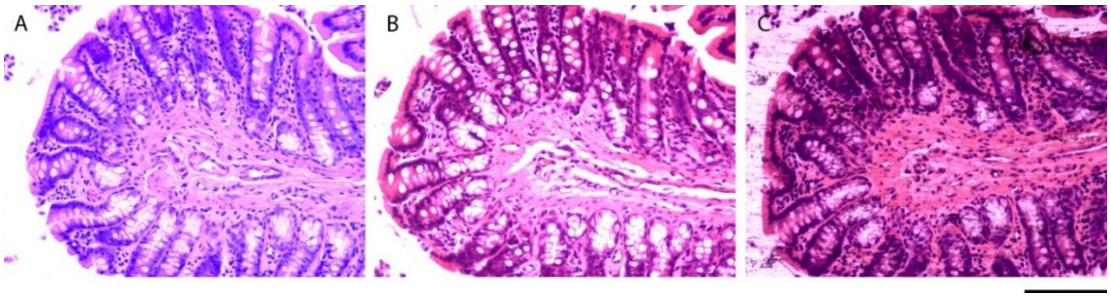

Figure 3.17: White light visualisation of H&E stained 8 µm rat colonic tissue section mounted onto glass (A), super mirror steel (B) and roughened stainless steel (C). *Good sample visualisation was achieved on glass and super mirror steel. Images were obtained using a Nikon microscope equipped with both transmission and reflection modes. Scale: 100 µm.*

3.3.4.2 Tissue section adhesion

The overall tissue adhesion to the super mirror steel surface was found to be extremely poor for some of the tissue pathologies. From the small panel of tissues tested colonic adenocarcinomas appeared to be the most susceptible to loss during the deparaffinization procedure. This has previously been observed in an independent study utilising stainless steel of unknown surface finish as a backing substrate (138). Normal, adenomas as well as hyperplastic polyps were found to be less affected, however only 2-3 samples of each colonic pathology was tested due to the precious nature of the human biobank samples. This suggests that the adhesive properties of the tissue may be altered upon pathological transformation.

There are several well established strategies that have been successfully used in histology to prevent tissue loss during harsh chemical treatments, albeit standard microscopy slides are employed. It is therefore important to first understand the surface structure and general behaviour of super mirror steel slides, only then can the most suitable adhesion technique be selected.

3.3.4.2.1 Stainless steel surface structure:

Stainless steel is composed of three distinct layers: the outer passive layer, the middle transitional zone and the deep alloy bulk zone (*fig.3.18*). The passive layer is around 3-5 nm thick and forms in an oxidizing environment, it is this layer that gives the steel its corrosion resistant properties. The outer layer of the film is hydrated and is composed of a hydroxide film while the inner layer that is closest

to the film/metal interface is an oxide layer. The film however is not static in nature but undergoes constant modification in both thickness and composition depending on the environment. Some of the factors that affect the passive layer include the application of a potential, exposure to anions such as chlorides or sulphates, changes in pH and lastly temperature (139).

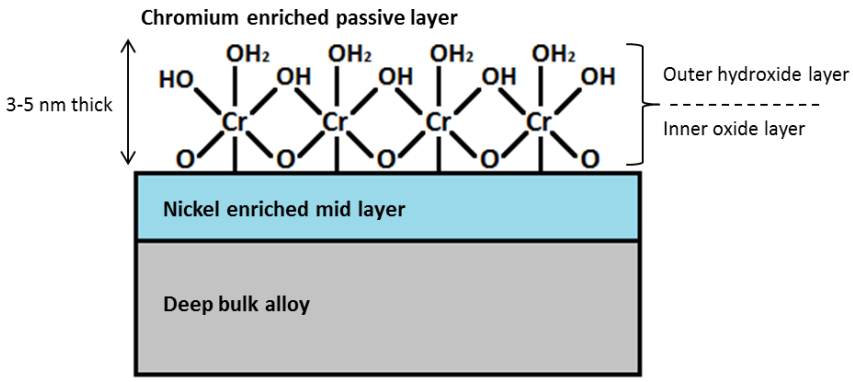

Figure 3.18: Visual representation of the surface structure of stainless steel (139).

The surface charge of stainless steel is also an important parameter to consider for the absorption and adhesion of proteins. Metal oxides are amphoteric in nature because of the ionizing ability of the hydroxyl groups on the surface. The zeta potential of stainless steel is reported to be negative at neutral and alkaline pH and positive at acidic pH. The zero point of charge where the net surface charge diminishes is at a weakly acidic pH (140,141). It is therefore important to consider the pH of the coating environment to predict the behaviour of the surface of steel.

3.3.4.2.2 Slide surface coating techniques

Taking into consideration the structure of stainless steel the following techniques were selected to be tested for compatibility with super mirror steel slides:

1) Poly-L-lysine coating
2) Coating with 3-aminopropyltriethoxysilane (APES) (Silanization)
3) Adaptation of the chrome gelatin technique

The mechanisms underlying each of the coating techniques can be found in table 3.4. It is also important to bear in mind that the thickness of the tissue sections used has also been found to influence the strength of the adherence to the coated slides, 5 µm sections have been found to adhere optimally (142).

Two adenocarcinoma sections were mounted per treated slide to investigate which slide pre-treatment resulted in the loss of sections during the rigorous deparaffinization procedure. The coating protocols are outlined in *Appendix 4*. Remarkably all sections remained attached indicating that all slide pre-treatment techniques were effective. To investigate whether any of the adhesion procedures contribute Raman peaks, five spectra were taken from the four corners and centre of each coated/treated slide surface. Reference spectra were taken from both poly-L-lysine and APES to enable easy detection of any contributing coating peaks. Spectra acquired from the pre-treated steel surface alone as well as with mounted tissue sections were found to contain no contributions from either poly-L-lysine or APES (*data not shown*).

Table 3.4: Summary of the different slide coating techniques and their underlying mechanisms.

Coating Technique	Interaction/Mechanism		References
	Standard Glass	**Super Mirror Stainless Steel**	
Poly-L-lysine coating	The net negative charge of a clean glass surface enables sufficient absorption of the cationic poly-L-lysine polymer onto the surface. The cationic surface left behind by the amine group of poly-L-lysine allows the anionic sites of cells and tissues to bind.	The pH of the poly-L-lysine solution used was around 7, this would mean that the net charge on the stainless steel surface would be negative, therefore promoting electrostatic interactions to form between the positively charged poly-L-lysine and the negatively charged steel.	(143)
APES coating (silanization)	Treating the glass surface with a reactive silicon compound can induce chemical changes on the glass promoting an abundant formation of amino groups, which later ionize to produce a positively charged surface. In the presence of water-activated APES, the hydroxyl groups on the surface of glass can hydrolyze to form siloxane linkages (Si-O-Si) (143). This subsequently results in amino groups being covalently bound to the glass surface (*fig.3.19*).	Hydroxyl groups are also known to be present on the surface of stainless steel (*fig.3.18*); these too can potentially undergo a similar reaction with APES.	(143)
Adaptation of the chrome gelatin technique	Coating slides with a dilute aqueous solution of gelatin and chromium potassium sulphate allows the chromium ion to form up to six covalent bonds between the oxygen atoms on both the glass and those from the carboxyl groups in tissue (144). In this case the gelatin is essentially a carrier of the chromium ion.	Stainless steel on the other hand has a passive layer of chromium oxides and hydroxides removing the requirement of gelatin altogether (*fig.3.20*). To promote the reaction of the chromium ions present on the steel surface it is essential to remove the presently bound oxygen. To free the chromium ion for bonding, the slides were to be incubated in 10% solution of sodium chloride salt, this is thought to strip the oxide layer.	(144)

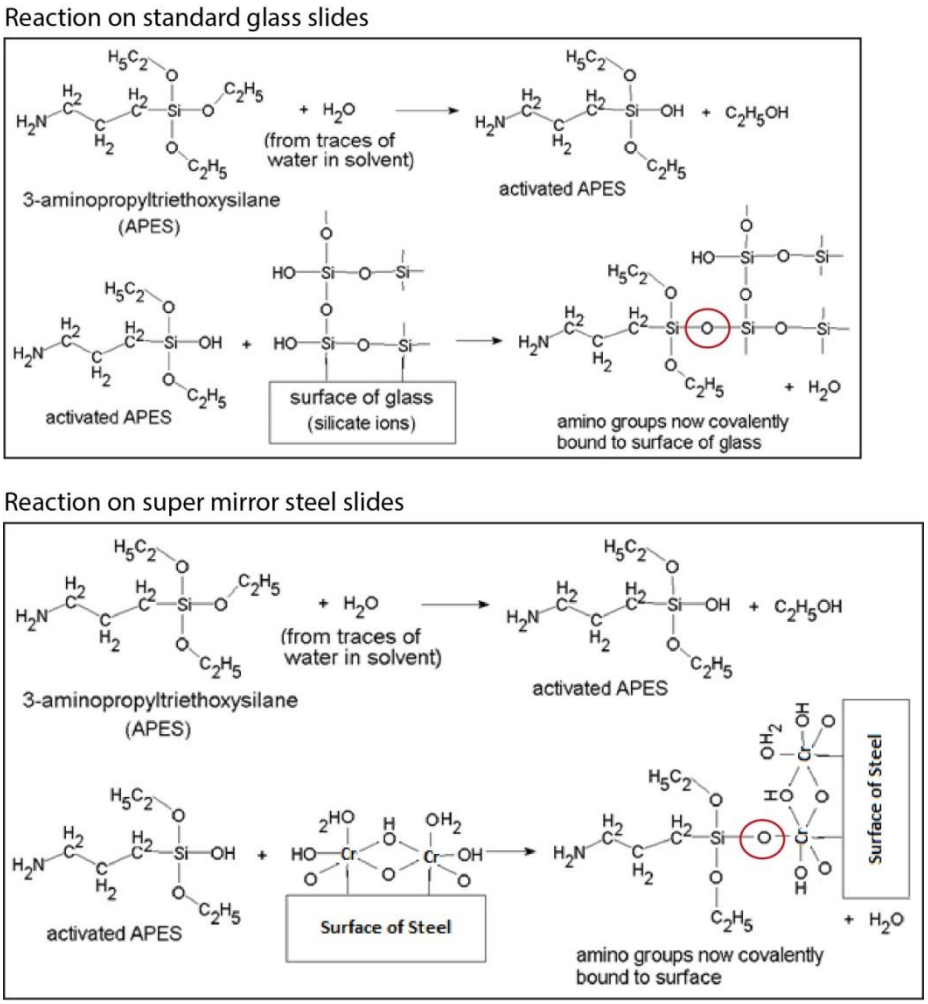

Figure 3.19: Illustration of the chemical reaction occurring during slide surface silanization on standard glass slides (top) and super mirror steel slides (bottom) [adapted from 6].

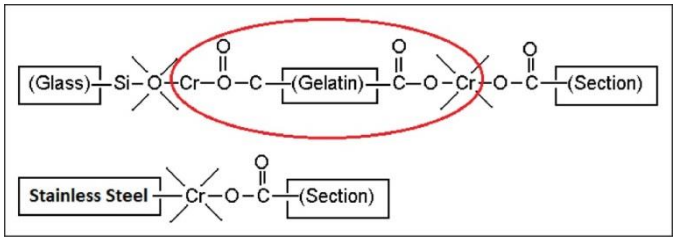

Figure 3.20: Illustration depicting the chemical reaction occurring during the chrome gelatin coating technique. (Top) *Reaction between the silicate ions on glass and the carboxyl groups of tissue with the chrome gelatin conjugate.* ***(Bottom)*** *Expected reaction of the carboxyl groups of tissue with the chromium ions on the surface of stainless steel [adapted from 6].*

Following this preliminary experiment it was later found that research has already been conducted on the silanization of stainless steel, albeit for a different purpose (145). Silanization of stainless steel surfaces has so far been considered difficult due to the limited understanding of the interaction process. Nonetheless, multiple studies have already been conducted that provide a useful foundation for the development of the ideal coating.

To facilitate silanization of the steel surface there must be an adequate concentration of hydroxyl groups present on the steel surface to enable binding of the silane groups. Jussila *et al* reported that different oxidation treatments such as piranha solution as well as different steel polishing mechanisms results in a variable concentration of hydroxyl groups on the steel surface (146). Conversely, Kang *et al* as well as Zammarelli *et al* both used piranha solution to increase the concentration of hydroxyl groups (145,147). This seems to be the most feasible and easy approach to functionalize the stainless steel surface prior to silanization. Electrochemical passivation was also found to increase surface hydroxyl concentration, hence it is important to ensure the steel is fully functionalized prior to silanization (146).

A study by Choveron *et al* found that low silane concentrations ensures that the hydrated APES solution is mainly composed of reactive monomeric silanols that have not aggregated. They found that a concentration of 0.12% v/v silane solution produced the highest bond strength between the silane film and metallic system (148). Jusilla *et al* later confirmed these findings and further went on to show that most of the surface was a uniform 1.3 nm thick film (82% uniform surface coverage) with minimal thick cluster formation (18% coverage of >20 nm clusters). Furthermore, they established that the initial absorption of silanol groups (SiOH) to the steel surface takes place via hydrogen bonding while covalent oxane bonds form during the curing process where two separate condensation reactions occur (146):

1) Condensation at the silane metal interface forming Si-O-M covalent bonds
2) Condensation at the interface between adjacent silanol groups resulting in siloxane network structures Si-O-Si.

Silanization has therefore been shown to produce strong covalent bonds not only between the steel surface and the coating film, but also between the coating and tissue interface. As a result silanization was selected as the optimal coating technique. The finalised silanization protocol that will be used for all the slides in the remainder of this study is outlined in *Appendix 5*.

3.3.4.3 Raman signal enhancement

When an incident laser source interacts with tissue several processes occur, one of which is transmission of the laser light directly through the sample via the transparent backing substrate. Transmission through either glass or CaF_2 facilitates the loss of laser light through the tissue and slide, the same occurs for front scattered Raman that is not collected by the optics. A highly reflective surface on the other hand is likely to induce a 'double pass' effect whereby the laser effectively passes through the tissue twice as it is reflected from the slide surface. This would also enable the collection of front scattered Raman that is often lost through the transparent substrate. This mechanism should in theory enhance the Raman signal by a factor of four, whereby front and backscattered Raman from the incident laser excitation is combined with the front and backscattered Raman originating from the reflected laser excitation (*fig.3.21*). This observation has previously been reported by Kamemoto *et al* using front coated aluminium mirrors using 785 nm excitation (109).

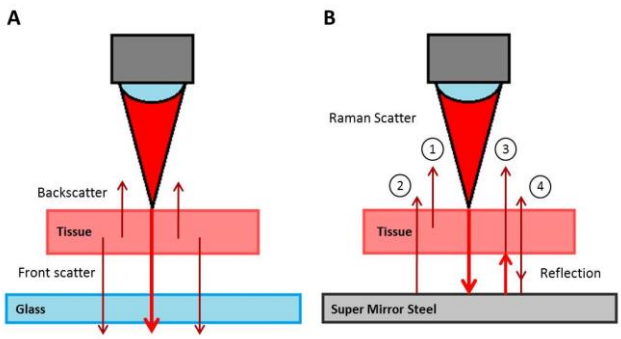

Figure 3.21: Diagrammatic representation of the Raman enhancement from tissue mounted onto super mirror steel slides compared to a transparent backing substrate. A) *Only backscattered Raman is collected, front scattered Raman and the remaining laser power is lost through the transparent substrate.* ***B)*** *1: Backscattered Raman from incident laser excitation, 2: Front scattered Raman that is normally lost is reflected back into the collected optics 3: Front scattered Raman from reflected laser excitation, 4: Backscattered Raman from reflected laser excitation is reflected back into the collection optics.*

To investigate the effects of the enhancement across different tissue compositions two different anatomical regions of the colon were selected: the mucosa representative of dense heterogeneous tissue and the muscularis propria representative of homogenous non-dense regions. Single spectra and maps were obtained from each region at comparable integration times. The relative degree of enhancement was calculated using S/N ratios of the 1002 cm^{-1} phenylalanine ring breathing mode. This peak was selected over the usual 1450 cm^{-1} CH deformation peak as this was contaminated within all CaF_2 data by the paraffin peak 1439 cm^{-1}. Such contamination results in an offset within the automated curve fitting function in WiRE 4.0.

Single spectra obtained at increasing integration times reveal a substantial enhancement of the Raman peak intensity and S/N ratios from both histological regions, but more so from muscle tissue (*fig.3.22-23*). Moreover, the magnitude of the enhancement is further increased with the acquisition time, with a maximum enhancement of 3.6 times achieved with the longest acquisition time on muscle.

To verify the results obtained from the single spectral data, small maps consisting of 336 spectra were taken across the mucosa and muscle regions. The S/N ratios were found to be approximately 1.5 times greater within the mucosa and 1.7 times greater within the muscle when compared to CaF_2 (*fig.3.23b*). A greater spread of the data was also observed across the mucosa validating the variable optical behaviour of heterogeneous tissue regions. The previously observed enhancement of up to a factor of four was not observed in the map data. This is likely to be caused by the reduced dwell time per pixel, which is often found to be in the microsecond range.

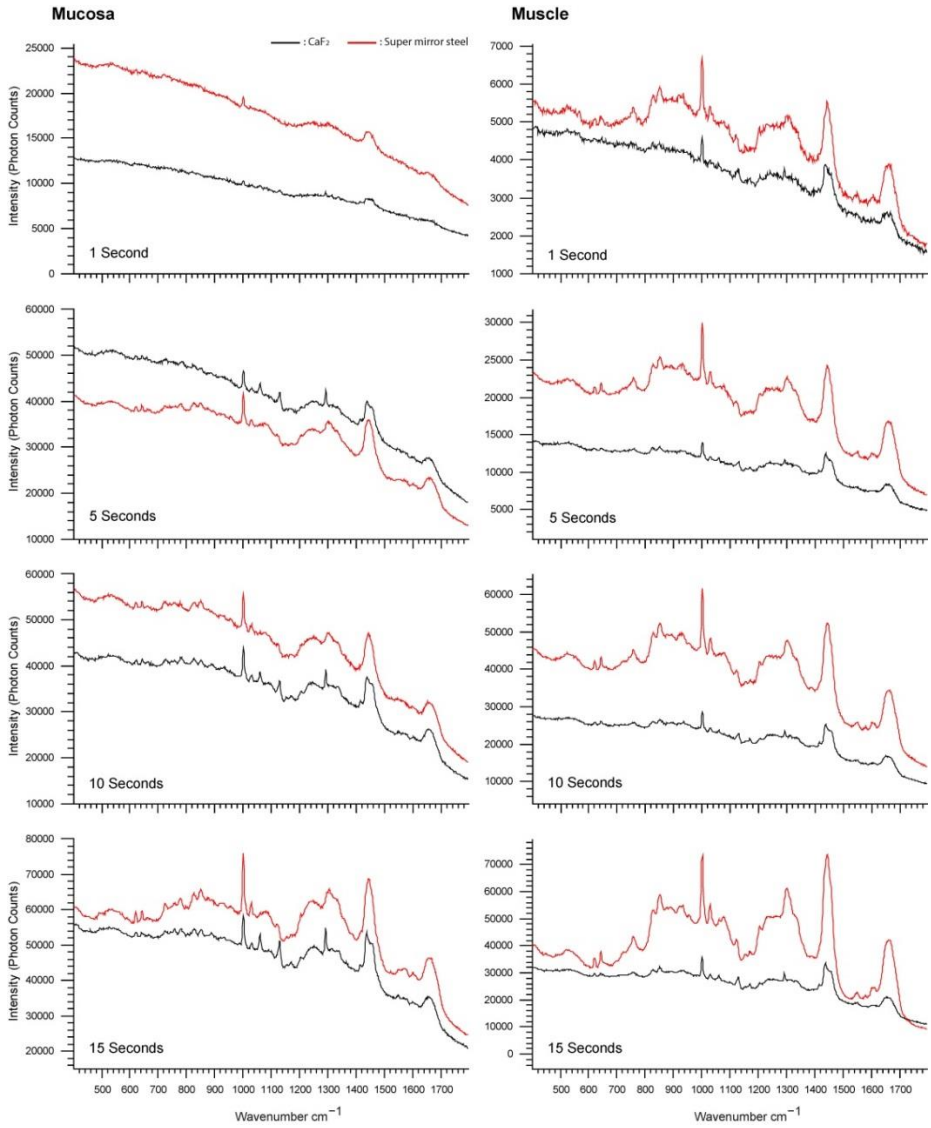

Figure 3.22: Original single spectra acquired using different integration times (1, 5, 10, 15 sec) from mucosal and muscular colonic tissue regions mounted onto calcium fluoride (black) and super mirror stainless steel (red).

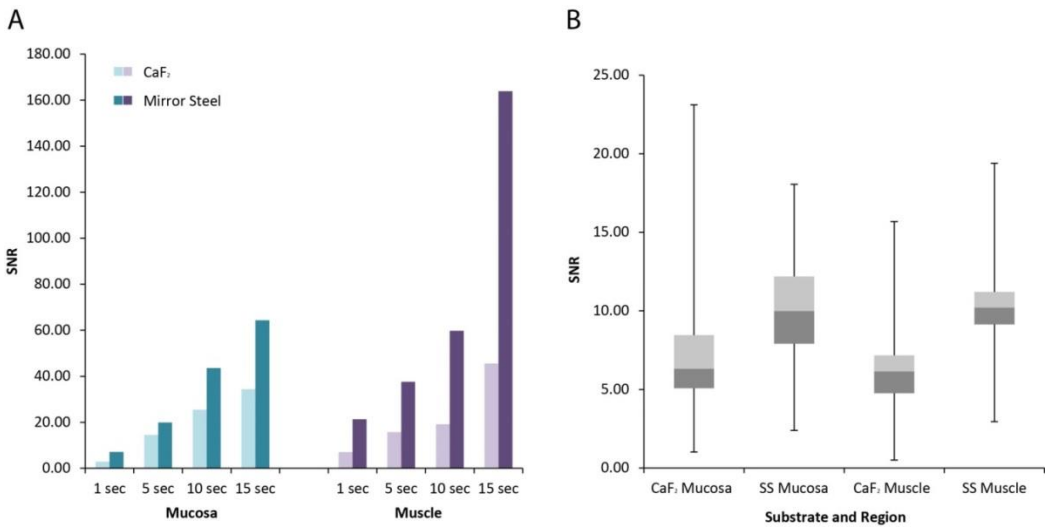

Figure 3.23: Comparison of S/N ratios obtained from CaF2 and mirror steel. A) *Barplots of S/N ratios obtained for the 1003 cm-1 phenylalanine peak from mucosa and muscle regions mounted onto CaF2 and super mirror stainless steel slides. Single spectra were acquired at 1, 5, 10 and 15 seconds using 158 mW of power. Superior results were consistently obtained from muscle tissue mounted onto mirror steel. The noise region used for the SNR calculation was acquired from between 950-990 cm-1.* ***B)*** *Boxplots of SNR values obtained from corresponding map data (t = 15 sec, P = 158 mW, step size = 16 µm).*

3.3.4.4 Comparison of tissue section thickness

Previously, superior S/N ratios were found for thicker tissue sections mounted onto CaF_2. Here, the S/N ratios of 3 µm and 8 µm colonic tissue sections mounted on mirror steel was compared against 8 µm sections mounted on CaF_2.

Thick sections on CaF_2 were found to have the weakest S/N ratios, while sections of equivalent thickness on mirror steel produced almost double the SNR (*fig.3.24*). By reducing the tissue thickness to what is currently accepted in standard practice and mounting onto mirror steel produces S/N ratios that are higher than that achieved from 8 µm thick sections on CaF_2. This indicates that by opting for highly polished mirror steel slides we can incorporate Raman into the work flow of the standard anatomical pathology laboratory with few modifications.

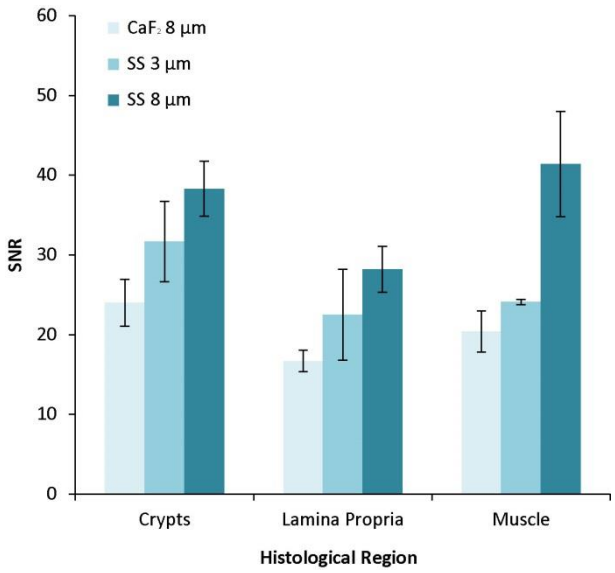

Figure 3.24: S/N ratios estimated for different histological regions across different tissue thicknesses (3 µm and 8 µm) mounted onto CaF_2 and mirror steel. *S/N ratios were found to be almost doubled from comparable tissue thicknesses mounted onto mirror steel. Error bars were calculated from the standard error of the means.*

3.3.4.5 Evaluating paraffin retention properties

Raman spectroscopy enables easy detection of residual paraffin wax via the presence of sharp intense peaks analogous to cosmic ray spikes but distributed across the Raman spectrum in a very characteristic pattern (*fig.3.25a*). A previous study by Faoláin *et al.* extensively evaluated different deparaffinization agents to remove paraffin wax from cervical tissue sections mounted on glass slides (149). After 18 hours of pre-treatment with either xylene or Histoclear it proved impossible completely remove the paraffin from the tissue sample. Hexane on the other hand was found to be superior, removing almost all the paraffin after 18 hours of exposure. These findings were shown to have a significant impact on immunohistochemical staining as deparaffinization in hexane was found to increase positive staining by approximately 28% in comparison to identical pre-treatment with xylene. It is however not feasible to undertake 18 hour deparaffinization steps as it would significantly impede the turnaround times of tissues processed in pathology, and it would also offset the protein to lipid content via lipid leaching and modify the fundamental biochemistry of the sample. A more recent unpublished study by the same group showed that hexane was superior to xylene, histolene, cyclohexane and

diethylether, and resulted in improved immunohistochemical staining in rat oesophagus, skin, kidney and liver tissue (150). Despite this evidence Nallala *et al.* found that xylene was superior to hexane, and that neither solvent was capable of fully removing paraffin after 24 hours. Furthermore, the efficacy of paraffin oil was found to be inferior to the currently used solvents (151). In the light of all these studies it is evident that complete paraffin removal is unlikely in a rapid turnaround clinical environment.

A less rigorous deparaffinization protocol was used here involving four separate 10 minutes washes at room temperature with continuous agitation. The same protocol was also undertaken at 70ºC xylene immersion with little to no effects on the paraffin retention properties (*data not shown*).

3.3.4.5.1 Paraffin contamination of tissues sections

Paraffin was effortlessly detected from colonic sections mounted onto standard microscopy slides, synthetic fused silica and CaF_2 slides that have undergone manual deparaffinization in xylene. Complete paraffin removal was however achieved on super mirror stainless steel slides (*fig.3.25b*). This finding is consistent with complete paraffin removal previously observed from sections mounted on metallic coated low-e MirrIR slides (110).

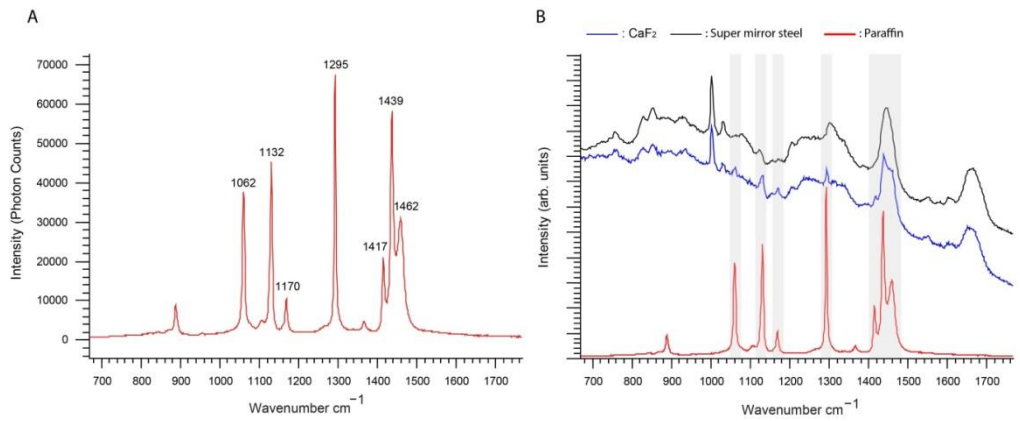

Figure 3.25: Paraffin wax detection in colonic tissue sections. A) *Paraffin reference spectrum with tentative peak assignments.* ***B)*** *Average tissue spectrum acquired from CaF_2 (blue) and mirror steel (black) substrates compared against a paraffin wax reference (red). Complete paraffin removal was achieved on mirror steel. Spectra were offset for visual clarity.*

3.3.4.5.2 Assessment of automated immunostainer performance

To field test the super mirror stainless steel slides in an authentic pathology laboratory setting they were tested in part of a standard laboratory work flow. The deparaffinization programme used by all immunohistochemical (IHC) stainers within the UCLH Advanced Diagnostics unit involves a total of three washes in commercial Bond Dewax solution at 72 ºC, with the first wash lasting for the duration of 30 seconds. The exact chemical composition of the Bond Dewax Solution is however unknown. It is therefore anticipated that complete paraffin removal is very unlikely as deparaffinization has previously been carried for a total of 40 minutes in xylene.

The efficacy of the automated deparaffinization protocol outlined in *Appendix 6* was tested. Synthetic fused silica was selected over standard glass due to the presence of a single broad intense feature (1100-1800 cm^{-1}) that almost covers the entirety of the fingerprint region and hence obscures the large majority of paraffin peaks. CaF_2 was avoided in this case due to the risk of shattering the slide during high temperature exposure.

Two different thicknesses of hyperplastic colonic polyps (3 µm and 8 µm) were mounted onto fused silica and compared against the same tissues mounted onto mirror steel. Prior to deparaffinization the slides were kept on a 70ºC hot plate for 60 minutes before being transferred into an oven for 40 minutes; the oven temperature fluctuates between 57-67 ºC depending on the frequency of door openings. This is the standard procedure for all slides destined for IHC analysis. The slides were then transferred to a Leica Bond III fully automated IHC stainer, which was used to test the efficacy of paraffin removal. The automated stainer was permitted to reach step 9 (Bond wash rinse) of the staining program before manually removing the slides from the tray.

A total of four maps were collected consisting of 1200 spectra from both tissue thicknesses. Paraffin contamination was only found in synthetic fused silica. Comparison of paraffin peak intensities at 1295 cm^{-1} along with 1132 cm^{-1} showed that more paraffin was retained within thicker tissue thicknesses (*fig.3.26*). This is a likely result of a greater number of porous cavities being present with increasing tissue volume. A peak intensity map across the tissue

also shows that majority of all the paraffin signal appears to accumulate at the interface between the crypts and the substrate (*fig.3.27*).

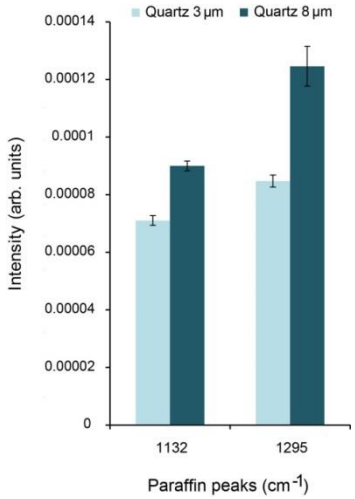

Figure 3.26: Bar plot comparing paraffin retention properties from tissues of different thicknesses mounted into synthetic fused silica. *Paraffin peak intensities at 1132 cm-1 and 1295 cm-1 were plotted against the varying tissue thickness. Spectra were normalized prior to applying the curve fitting feature in WiRE 4 to calculate the peak intensities. More paraffin was found to be retained in thicker tissue sections in comparison to their thinner counterparts.*

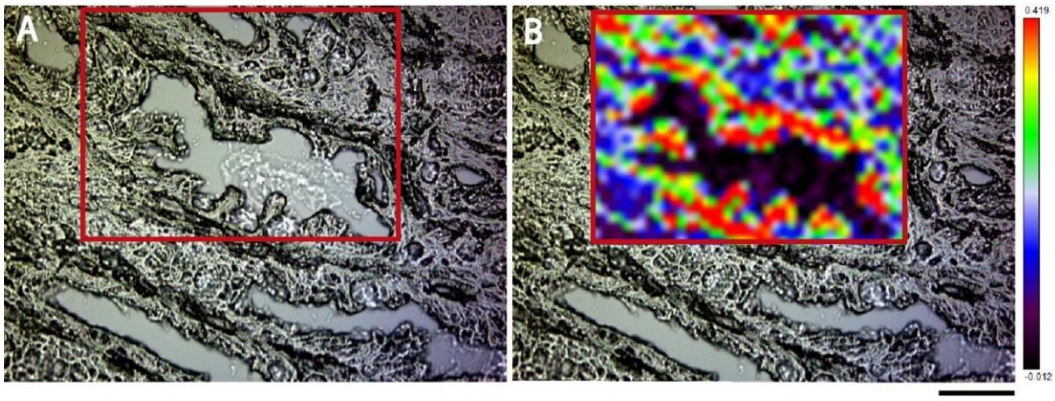

Figure 3.27: Localization of paraffin contamination. A) *White light image of the mapped region of the 8 µm hyperplastic polyp section.* ***B)*** *1295 cm^{-1} paraffin peak intensity map. Red regions highlight regions of high paraffin content. Red box indicates mapped region. Scale: 50 µm.*

In light of these findings the protocol was later modified to reduce the xylene immersion time and frequency to one ten minute wash with agitation. The efficacy of paraffin removal on mirror steel was found to not be affected.

3.3.4.6 Scanning electron microscopy

It was initially postulated that the surface profile of each slide substrate may be dictate the completeness of paraffin removal. The surface profile was investigated using scanning electron microscopy (SEM). Prior to SEM all slides underwent cleaning using a standard degreasing agent trichloroethylene; the full protocol is outlined in *Appendix 7*.

Standard microscopy slides as well as fused silica were found to be completely smooth with no surface features at both high and low magnifications (*fig.3.28a-d*). High magnification images of CaF_2 revealed a rough surface with visible surface scratches, likely to have been induced by means of slide recycling (*fig.3.28f*). A low magnification view of unused mirror stainless steel reveals a relatively large scratch demonstrating the relative ease of surface damage through minor slide handling but thus region is entirely surrounded by a very smooth uniformly featureless surface (*fig.3.28g*). At higher magnification consistent scores were observed on the surface (*fig.3.28h*), this may be a result of the surface polishing technique used to produce the mirror finish. This confirms that mirror steel has a unique surface morphology that is not seen on the other sample backing substrates.

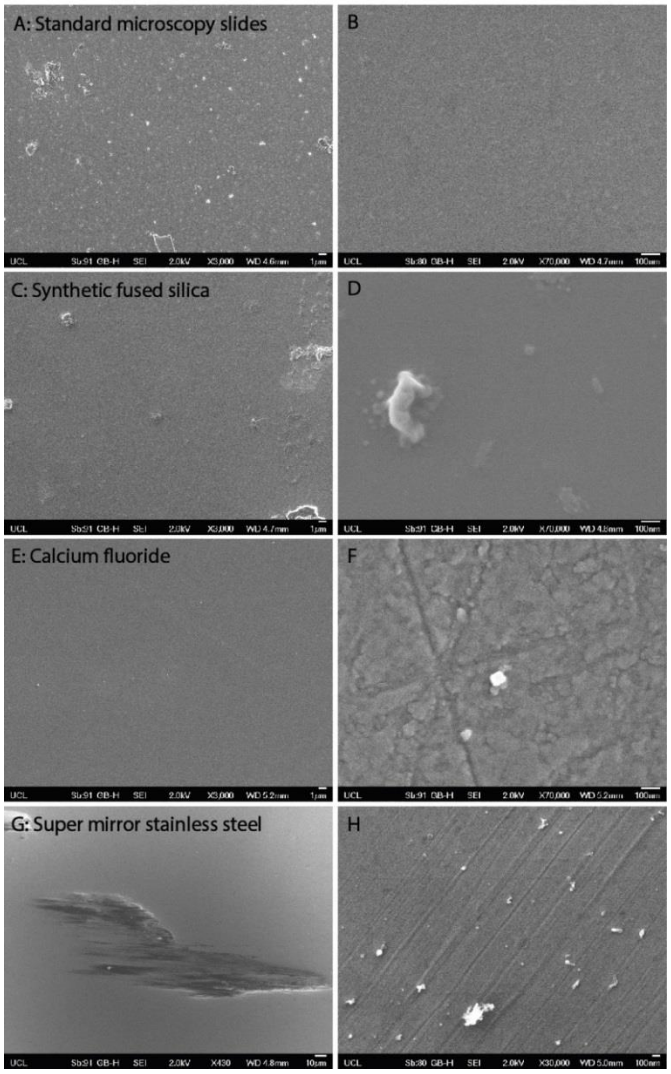

Figure 3.28: SEM images at low (×3,000) and high (×70,000) magnification of the surface features of each slide material. *A: low magnification standard microscopy slides, B: high magnification standard microscopy slides, C: low magnification synthetic fused silica (not previously used), D: high magnification synthetic fused silica, E: low magnification CaF_2, F: high manificationg CaF_2, G: low magnification mirror steel, H: high magnification mirror steel.*

3.3.4.7 Atomic Force microscopy

The overall roughness of the surface profile from each backing substrate was measured using atomic force microscopy (AFM). Measurements were collected from a 5 μm^2 area as well as a small 1 μm^2 area. Initial measurements were collected from slides cleaned using a milder trichloroethylene based protocol, however a more rigorous piranha solution based protocol was later applied because heavy debris contamination was observed during initial measurements. Nonetheless, some debris particles (large bright spots) were still detected on the

surface, as a result average surface roughness (R_a) was calculated from selected debris free regions (*outlined by dashed boxes*).

CaF_2 was shown to have a generally rough surface with an average R_a of approximately 3.7 nm along with visible surface scratches – these results are consistent with previous reports by Fullwood *et al* (110) (*fig.3.29*). Following piranha solution exposure CaF_2 developed a cloudy appearance. AFM revealed that the surface has undergone etching as seen by the granular surface profile with a significant decrease of the R_a to somewhere between 0.3 - 0.5 nm (*fig.3.30*). Synthetic fused silica was found to be unaffected by either of the cleaning protocols and despite the visible surface scratches maintained one of the smoothest surfaces of around 0.3 - 0.5 nm.

Average surface roughness of glass was largely unaffected by piranha solution and was found to be between 0.9 - 1.4 nm, mapping a smaller area revealed a somewhat porous surface. Mirror steel was found to be the roughest surface with an R_a between 1.6 - 1.8 nm. As noted during SEM analysis mirror steel possessed the most distinct profile with a combination of large surface scores and irregular granularity (*fig.3.30*). A summary of all R_a values for each backing substrate can be found in *table 3.5*.

In spite of the surface scratches silica was among the smoothest of all substrates with the least depth variation of around 1 nm across a 1 μm path (*fig.3.31*). Following etching of CaF_2 the depth variation was found to be similar to that of glass and was around 3 nm. Mirror steel on the other hand was found to have the greatest depth variation, with 8 nm across the granular region and a surface score depth of around 4 nm with an average 200 nm width (*fig.3.32*).

Tip artefacts were observed via repeating features across the 5 μm × 5 μm surface of glass, silica and CaF_2. This is likely to have been caused by tip contamination rather than deformation as these features were not observed across all the scans and were of variable shapes. Some external vibration artefacts in the form of oscillations were also present on the 5 μm × 5 μm surface of mirror steel (*fig.3.30: bottom right*).

These findings suggest that the efficacy of paraffin removal is not dependent upon the slide surface roughness, as CaF_2 was almost three times the roughness of silica and glass and approximately twice the roughness of steel prior to

etching in piranha. Albeit steel was the second roughest material it had a distinct surface morphology that was absent from the other surface profiles. Scores detected across the steel surface might conceivably facilitate the flow of xylene between the tissue/slide interfaces. The molecular size of xylene isomers is known to range between 0.56 – 0.68 nm (152), this suggests that the volume of xylene molecules is sufficiently small to flow through the 4 nm crevices present within the scores. Later SEM analysis of the MirrIR slides however showed a lack of such surface features directly contradicting the hypothesis that the surface scores are responsible for the efficiency of paraffin removal.

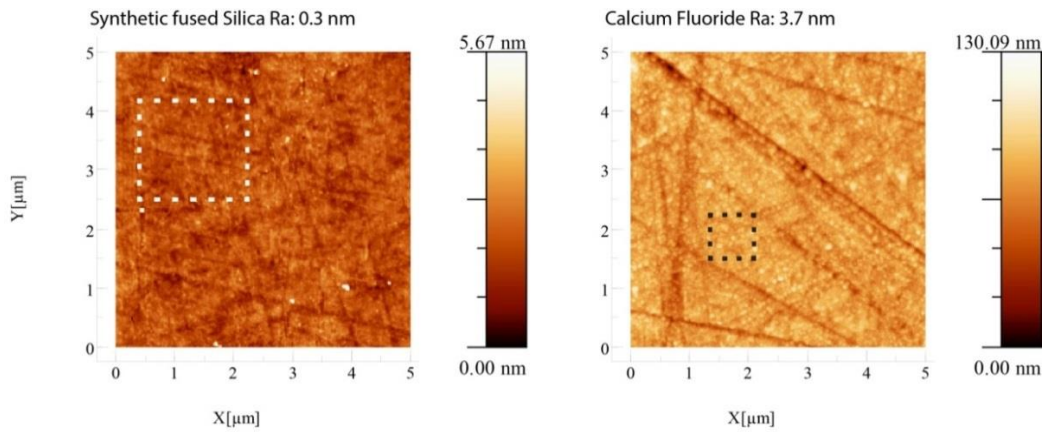

Figure 3.29: AFM images of a 5 µm × 5 µm area on synthetic fused silica and calcium fluoride prior to piranha solution exposure. *Average roughness (Ra) values were obtained from the dashed box regions.CaF2 was found to be significantly rougher than fused silica.*

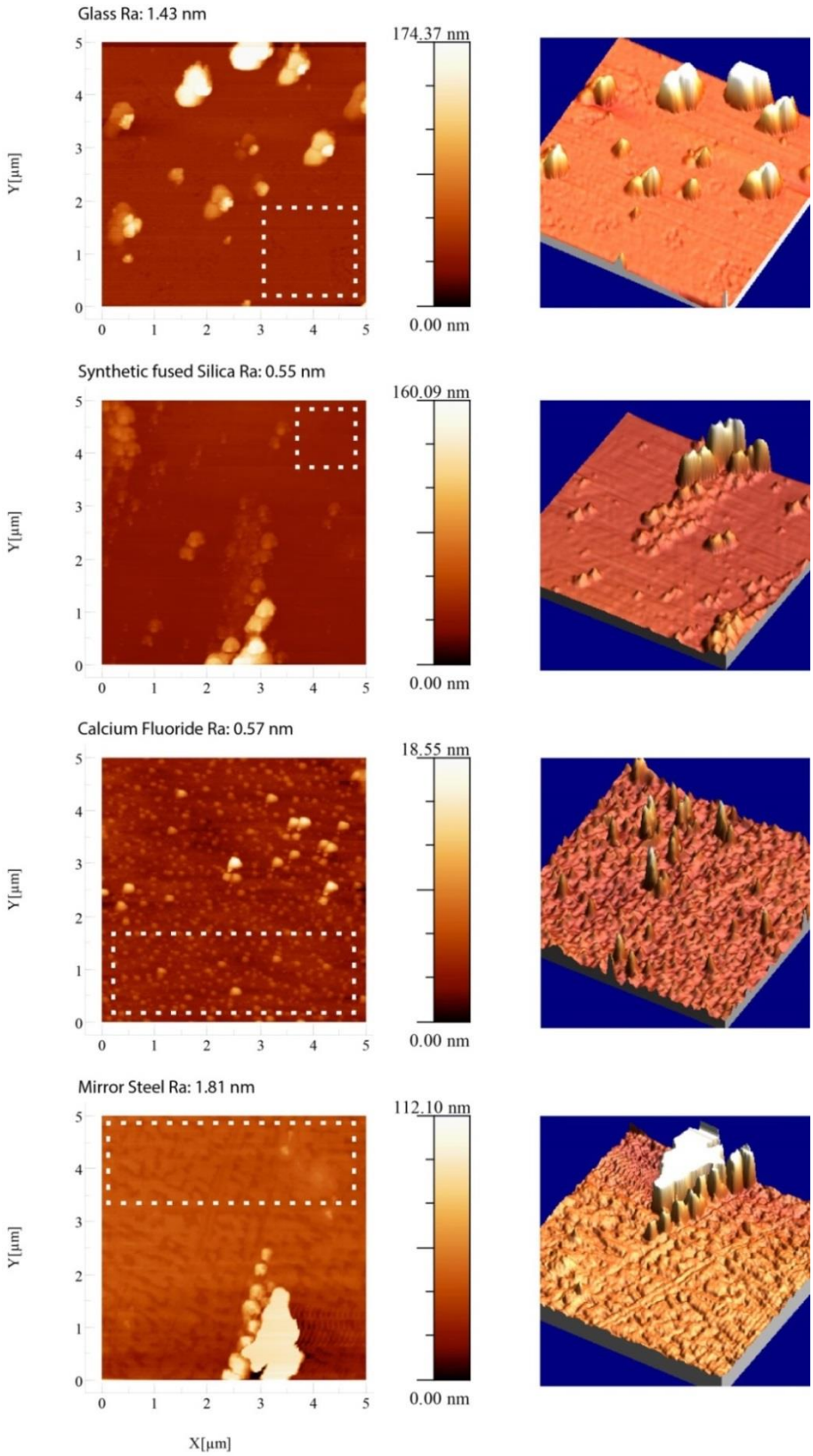

Figure 3.30: AFM images of a 5 µm × 5 µm area on glass, synthetic fused silica, calcium fluoride and mirror steel following cleaning in piranha solution. *Average roughness (Ra) values were obtained from the black dashed box regions on the 2D surface representations. Synthetic fused silica and CaF_2 possessed the smoothest surface profiles (0.55 and 0.57 nm) while mirror steel was found to be the roughest (1.81 nm).*

Table 3.5: Summary of the average surface roughness Ra values of all backing substrates.

Cleaning Method	Substrate Average Surface Roughness Ra (nm)			
	Glass	Synthetic fused silica	Calcium Fluoride	Mirror Steel
Trichloroethylene	0.18 – 0.48	0.25 – 0.36	3.69 – 3.71	1.6 – 2.06
Piranha	0.9 - 1.43	0.33 - 0.55	0.30 - 0.57	1.65 - 1.81

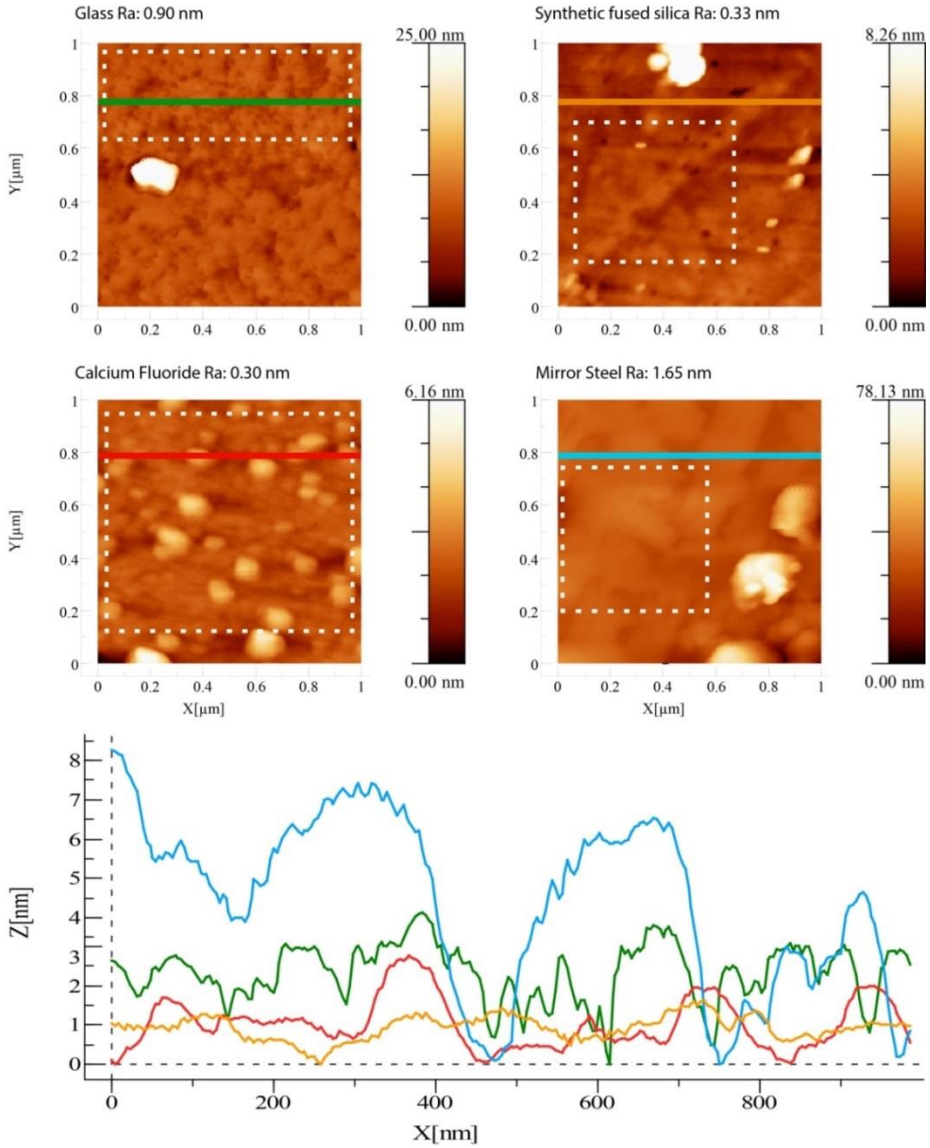

Figure 3.31: AFM images of a 1 µm × 1 µm area on glass, synthetic fused silica, calcium fluoride and mirror steel following a piranha clean. *Average roughness (Ra) values were obtained from the white dashed box regions on the 2D surface representations. Synthetic fused silica and CaF_2 possessed the smoothest surface profiles (0.33 and 0.30 nm) while mirror steel was found to be the roughest (1.65 nm). The surface profile plot displays the average depth variation across 9 nm plotted on the y-axis against a 1 µm line distance across the substrate surface. The peaks and troughs correspond to surface depth changes. Green: glass, orange: synthetic fused silica, red: CaF_2 and blue: super mirror stainless steel.*

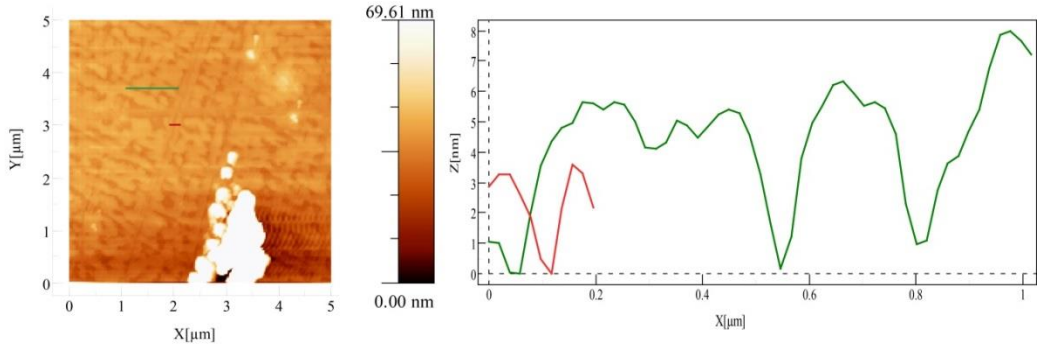

Figure 3.32: (Left Panel) AFM images of a 5 µm × 5 µm area on mirror steel following piranha solution exposure. The red and green lines depict the regions where the depth changes were calculated from. (Right panel) The depth z (y-axis) across the surface was obtained from the red (score) and green (granularity) peaks and troughs that correspond to depth changes across a 1 µm distance. *A score of approximately 200 nm in width possessed a depth of around 4 nm (red line).*

3.3.4.8 Contact angle measurements

Contact angle (CA) measurements were undertaken to determine the wettability of each slide substrate using xylene. This might provide some insight into the variability in the deparaffinization achieved across the different backing substrates.

The surface of the micropipette was found to be extremely lipophilic - as the xylene drop was travelling up towards the needle prior to release of the drop. To compensate for this effect the rate of the drop release had to be increased to 50 µl/min. As a result it was not possible to confirm the true volume of each drop.

The CA measurements for all substrates were found to be extremely low. It is known that accurate CA measurement becomes more complex for wetting systems with CAs below 20°. The intrinsic failure of drop shape analysis lies in the decreasing contrast between the drop, sample surface and background with decreasing CA (153). It was therefore not possible to obtain static CA measurements due to the extremely low CA in this case. Instead the CA behaviour was observed during a time course measurement – at the first point of contact between the drop and solid surface as well as the point where the drop reaches an equilibrium state.

The wetting was found to be extremely rapid and hence measurements were taken across 5 seconds. The CA for all substrates was estimated to be around 10° at first contact and less than 5° following equilibration. There was no obvious

difference between the measured contact angles for xylene on each tissue mounting substrate. Complete wettability is defined by CA values below 5° (153), this suggests that all substrates achieve near complete wettability with xylene. The wettability of each substrate is therefore not likely to be the cause of the variable deparaffinization.

3.3.4.9 Implications of electrochemical effects

Thus far the surface topology, roughness and wettability of the different slides substrates has not revealed a possible mechanism for complete paraffin removal observed on mirror steel; and which would be very desirable in the routine use of Raman microspectroscopy in the analysis of tissues prepared by conventional FFPE techniques. The possibility of electrochemical interactions playing a role within the system became apparent during section mounting on the various slide substrates after ribbons of tissue were cut from the paraffin blocks. An observation was made that the paraffin ribbon was visibly repelled from the stainless steel slide during the mounting step. Parreira and Schulman have previously reported that paraffin wax has a net negative charge above pH5 (154), subsequent pH measurements of xylene indicates a neutral environment (pH7). We can therefore hypothesise that during the xylene deparaffinization procedure the paraffin wax carries a negative charge. In the previous section we have reported that the surface of stainless steel is negative in neutral and alkaline pH environments. One can therefore hypothesize that the negative charge carried by the stainless steel surface and paraffin wax in an insulating xylene environment facilitates repulsion from each surface

Previous work has shown that the work function property of metals is directly correlated to the surface charge. It is defined by the energy required to move an electron from the highest occupied energy level in the metal (Fermi level) to the vacuum level immediately outside the solid surface. A low metal work function correlates to a negative surface charge, whereas a high work function results in a positive surface charge on the dielectric after contact (155).

To test whether metals with different work functions have an impact on paraffin removal, a range of different metals were mounted with 8 μm tissue sections and deparaffinised as before. *Table 3.6* illustrates the paraffin retention properties from metal surfaces with variable work functions. It is apparent that there appears to be a

threshold work function from which complete paraffin removal is possible, whereby a work function above this threshold value facilitates paraffin retention.

Table 3.6: Summary of paraffin retention on metal surfaces with variable work function values (eV).

Metal	Work function (eV)	Paraffin detected (Y/N)
Aluminium coated glass	4.06 – 4.26	No
Titanium	4.33	No
Stainless Steel	4.40	No
Iron	4.67 – 4.81	No
Platinum	5.12 – 5.93	Yes
Gold	5.1 – 5.47	Yes

3.4 Conclusion

In this section the primary aim was to determine the most suitable experimental parameters that will enable rapid acquisition of spectral data with good S/N ratios. Having compared a number of different instrumental and tissue based parameters we are confident that we have found a combination that is suitable for the use of FFPE colonic tissue sections mounted onto a supporting, slide-like backing substrate that is relatively inexpensive and considerably more robust than the CaF_2 substrate widely used in Raman studies.

In summary, best instrumental performance was achieved using 785 nm laser excitation in conjunction with a 50×/0.75 short WD objective and a laser line illumination. Super mirror stainless steel slides coated with APES provided reliable section adhesion, superior deparaffinization along with superior Raman performance over UV grade CaF_2 slides.

Chapter Four

Preliminary Raman imaging of formalin-fixed paraffin embedded rat colonic tissue

4.1 Introduction and Aims[1]

There already exists a large body of work describing the application of Raman spectroscopy in the study of colorectal tissue, however most of this work has focused on discrimination of tissues of colorectal cancer (CRC) and inflammatory bowel disease (IBD) (57–59,63,156). Furthermore, the bulk of these studies are carried out on fresh/frozen tissues because these methods minimise sample handling, are thought to preserve the largest amount of biochemical information and to diminish chemical contamination. Given the low sensitivity of earlier Raman instruments this was thought to be essential because tissue processing procedures used routinely in histopathology reduce Raman signal strengths (157). Nevertheless, it is important to bear in mind that the bulk of all tissues routinely obtained for analysis in clinical investigation undergo fixation and subsequent paraffin embedding (FFPE). These procedures minimise post-mortem changes in tissue morphology and ensure that adequate sample shelf life is maintained over a prolonged storage period. It is unreasonable to expect such routine pathology practice will undergo any significant changes in the coming years.

This preliminary study was carried out to investigate whether sufficiently adequate biochemical information can be extracted from FFPE colonic tissues. The primary aim was to identify and correlate the spectral features from different anatomical layers with the current body of knowledge on the biochemical composition of these regions. Lastly, an attempt was made to ascertain whether any contaminating chemical entities can be identified which may compromise tissue analysis.

In summary, this chapter aims to:

- Identify the spectral features unique to each anatomical layer within the colon.
- Correlate the spectral features to the known biochemical composition of these regions through the use of biomolecular references.

[1] The body of this chapter has been published in the International Journal of Experimental Pathology. *Label-free Raman spectroscopic imaging to extract morphological and chemical information from a formalin-fixed, paraffin embedded rat colon tissue section*. R. Gaifulina *et al*. Int J Exp Pathol. Sep.2016

- Ascertain the presence of any contaminating spectral signatures that may compromise tissue analysis.

4.2 Materials and Methods

4.2.1 Tissue acquisition and preparation

Colonic samples were acquired from a single male Wistar rat obtained from the UCL Biological Services. Euthanasia was conducted using a CO_2 flow chamber. Complete euthanasia was verified using the blink reflex, the colon was then immediately removed and irrigated with ice cold phosphate buffered saline. Multiple colonic resections approximately 5 mm in length were excised and fixed in standard 10% neutral buffered formalin for 24 hours at room temperature. Tissues were then further processed in a Leica automated tissue processor (TP1050) and embedded in standard laboratory histological paraffin wax. Sections were cut at 8 μm thickness and mounted onto CaF_2 slides (Crystran, UK) for Raman measurement. Additional contiguous sections were cut at 3 μm, mounted onto a standard microscope slide and H&E stained for direct comparison. Raman designated slides were subsequently deparaffinized in xylene, rehydrated in alcohol and distilled water and incubated at 37ºC overnight prior to Raman imaging.

4.2.2 Reference biomaterials

Subsets of reference biomolecules were selected and their distribution within the tissue investigated. The most striking feature of the colon is the thick outer layer muscle and inner mucosa containing multiple densely packed cell types. To aid the identification of these components, reference spectra from muscle acetone powder and purified DNA were obtained. The submucosa, known to largely comprise of connective tissue, was referenced by authentic samples of collagen as well as hydroxyproline. Similarly mucin contained within goblet cells was referenced by whole mucin, as well as the two most abundant sugars – *N*-acetyl-galactosamine, *N*-acetyl-glucosamine. Reference spectra were also obtained from a number of lipids, namely phosphatidylcholine, phosphatidylserine, phosphatidylethanolamine, phosphatidic acid, cholesterol, oleic acid, palmitic acid as well as glycerol. Two other carbohydrate molecules glucose and fucose were also used as sugar based references. Specific reference information can be found in *Appendix 8.*

4.2.3 Raman micro-spectroscopic imaging

StreamLine™ Raman imaging was performed using the inVia Raman system (Renishaw plc, Wotton-under-edge, UK) coupled to a 785 nm laser excitation source and a Leica DM2500 microscope. A thermoelectrically cooled charge coupled device (CCD) camera was used for signal detection. StreamLine™ imaging uses cylindrical lenses to reshape the laser illumination to a line geometry, which distributes the laser power along the length of a line rather than a single intense spot. A total laser intensity of approximately 50 mW was focused onto the sample through a 50×/NA 0.75 objective. A 1200 l/mm grating was used to disperse the light providing a spectral range of 400 to 1800 cm^{-1}. A 2.8 μm step size was used with an integration time of 20 seconds producing a Raman map of the sample consisting of 81,405 unique spectra.

Several system checks were conducted before any data collection to ensure that the laser power, alignment and laser line illumination concentricity was optimal. The system was then calibrated using a piece of silicon to the well-characterised reference peak at 520.5 cm^{-1}.

Biomolecular reference spectra were acquired on a Renishaw RA802 Raman prototype micro-spectrometer, equipped with a 785 nm laser source emitting ~150 mW. This system was fitted with a 50×/NA 0.8 objective and provided a spectral resolution of ~2.6 cm^{-1} based on the full width of peaks in the silicon spectrum. Single point measurements were used with integration times ranging between 0.8-10 seconds.

4.2.4 Spectral pre-processing

The Raman map was pre-processed to reduce spectral variances originating from non-chemical effects. This ensures that any instrumental artefacts are removed and the chemical information within the spectra is enhanced. Cosmic ray removal was conducted using the width of feature and nearest neighbour methods in WiRE 4 software (Renishaw plc, Wotton-under-Edge, UK).

The baseline was corrected using third order polynomial and normalisation (i.e., scaling so that each spectrum had a mean intensity of zero and standard deviation equal to one) was carried out using Matlab R2015b (MathWorks, Natick, MA, USA). This ensures that each spectrum had a comparable influence

on all the subsequent statistical analysis. Pre-processed spectra were then analysed in Matlab as well as being reimported into WiRE 4 for a parallel analysis.

4.2.5 Spectral analysis

4.2.5.1 Principal Component Analysis

PCA was carried out using both WiRE 4 and Matlab R2015b. Matlab facilitates the implementation of linear regression analysis following PCA as well as directly matching the spectral similarity of reference biomolecules. WiRE on the other hand allows the generation of superior composite score images that can be compared to H&E stained tissue sections with relative ease. By using both platforms it was possible to provide a good all-round analysis of the image data. Prior to the analysis using either platform the spectra were mean centred and spectrum centred within the specified software.

A linear combination of reference spectra was then fitted to each principal component in an attempt to identify the molecular origin of the difference underpinning the PCA. In this work, in-depth analysis was carried out on four PCs as these were considered to be the most histologically significant. These four PCs and a further six (the first ten PCs) account for 82% of the total biochemical variance present in our data and can be found in *Appendix 9*. PC1 and PC2 were excluded from the analysis, as PC1 captured the difference between the substrate and biological material, whereas PC2 captured the difference between tissue signals with the combined objective signal from the backing substrate. Increasing the number of principal components up to 15 during analysis did not result in the identification of any additional histological features (*data not shown*). The numbers of peaks used for correlation to the different histological regions from the loadings were selected based on their magnitude and tentative assignment in literature.

4.2.5.2 Spectral similarity

The spectral similarity between a reference and each tissue pixel was quantified using cosine similarity. Cosine similarity generates a metric that shows how related the two pixels are by looking at the angle instead of the magnitude. In this case the angles have been constrained such that $-1 \leq \theta \leq 1$, where by $\theta = 1$ indicates the two spectra are identical, $\theta = 0$ indicates the two spectra are not a match and $\theta = -1$

suggests that the two spectra are opposite of each other. Further details on cosine similarity can be found in section 2.6.3 of chapter two.

4.3 Results and Discussion

4.3.1 Overview of H&E stained rat colon

All the main layers of the colon are clearly defined with the thickest regions composed of the mucosa and muscularis propria. The outermost muscularis propria exhibits two distinctly orientated muscular layers: 1) inner circular muscle and 2) outer longitudinal muscle (*fig.4.1a*). The submucosa exhibits a very sparse distribution of connective tissue fibres with embedded lymphocytes and blood vessels. The cells of the mucosa are very densely packed with very little visible lamina propria. The epithelial cells that line the crypts of Lieberkühn are best resolved at the luminal edge of the mucosa, whereas the larger goblet cells are the most easily identified feature (*fig.4.1b*). It is evident that the overall small size of the rat colon makes it almost impossible to identify all the microstructures that constitute the colonic crypts.

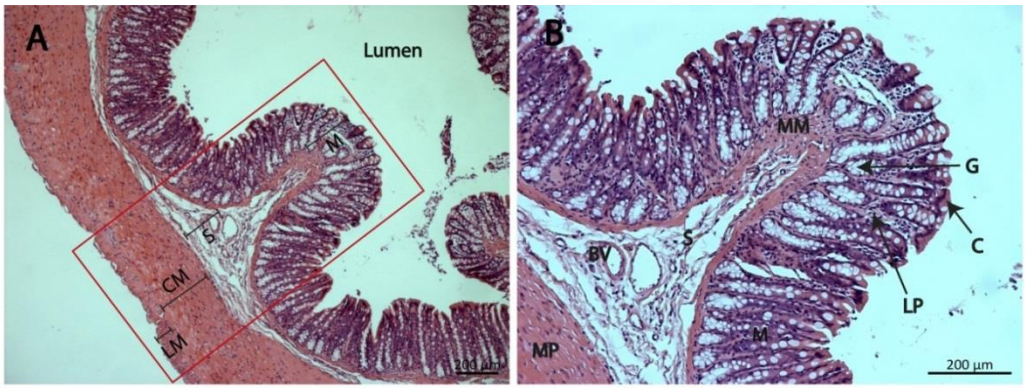

Figure 4.1.1: H&E stained rat colonic sections. A) *Full thickness view of a transversely cut colon section: LM: outer longitudinal muscle, CM: inner circular muscle, S: submucosa, M: mucosa. The red box indicates the area that underwent Raman imaging and subsequent analysis.* ***B)*** *Close up of a mucosal fold with the associated submucosa: M: mucosa, MM: muscularis mucosa, S: submucosa, BV: blood vessel, MP: muscularis propria, LP: lamina propria with visible embedded lymphocytes, G: goblet cells, C: colonocytes.*

4.3.2 Principal component analysis

PCA is an unsupervised multivariate analysis technique that allows an effective reduction of a large and complex spectral dataset to a few most meaningful components. These components capture most of the variability within the dataset and they can then be tentatively assigned to a specific biological component present in abundance within a given anatomical region. This technique provides an overview of which regions might be identified with relative ease by reducing the subjectivity and speculation inherent in any process of manually selecting from amongst the reference spectra. Up to ten components were hypothesized to contain the most relevant biochemical information relating to the biochemical variance of the layers within the sample. However, only the four components considered to be the most histologically relevant will be shown graphically and analysed in detail in this chapter. Details of all ten PC loadings can be found in *Appendix 9*.

H&E stained sections were used as guides to assist in the interpretation of the different component loadings by correlating their relative positions within the Raman map. A linear combination of preselected reference biomolecules was fitted against each PC to identify the biomolecules that contribute most to the loading.

4.3.2.1 Identification of chemical contaminants

The most striking of all PCs was PC4 - characterised by a multitude of intense sharp peaks found in the negative region of the loading and assigned a yellow pixel colour. These features are akin to the unique features of paraffin wax used to embed the tissue. This demonstrates that despite attempts at rigorous paraffin removal in xylene (40 minutes total exposure with agitation) paraffin was well retained within the tissue. Paraffin was sparsely present across the whole tissue section but very strongly retained in the outermost mucosal edge (*fig.4.2a*). Raman imaging facilitates easy identification of paraffin contamination via sharp intense paraffin peaks at 1062, 1132, 1294 and 1439 cm^{-1} in PC4 (*fig.4.2b*). The linear reference fit indicates that PC4 is primarily composed of paraffin, but also exhibits presence of some of the major phospholipids and some nucleic acids (*fig.4.2c*). No other chemical contaminants were detected.

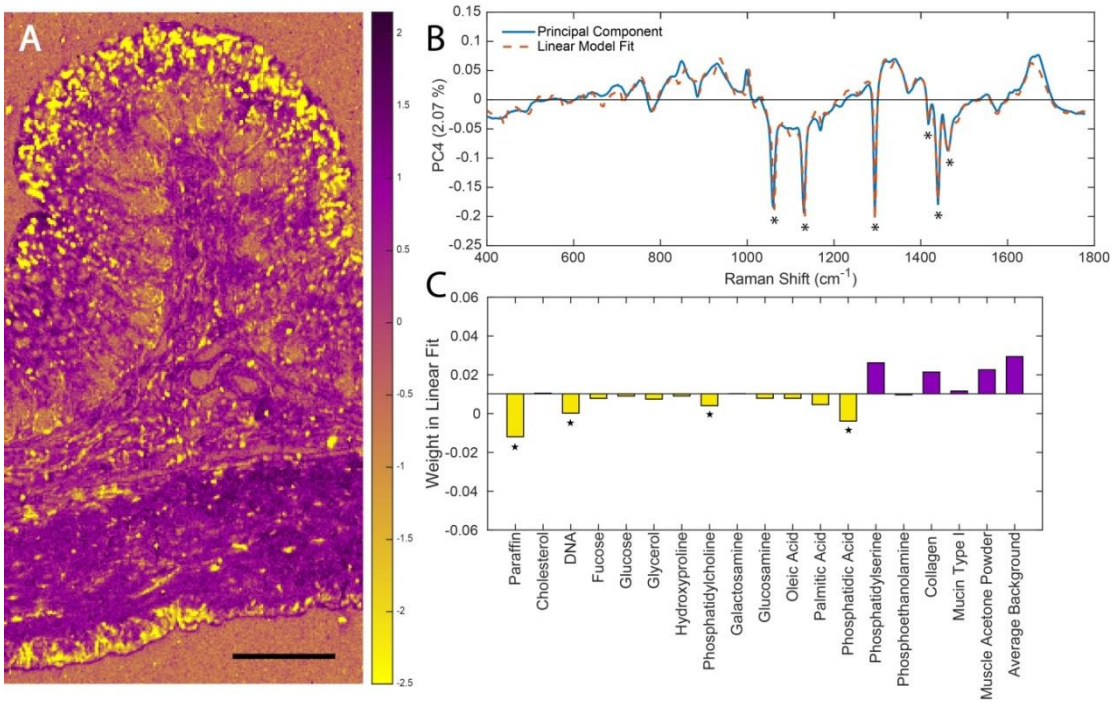

Figure 4.1.2: Detection of paraffin contamination from an 81,405 hyperspectral image. A) *False coloured Raman map depicting the localization of paraffin contamination produced by assigning a user defined colour for the pixels corresponding to PC4, in this case intense yellow pixels correspond to the negative region of the loading and strong paraffin signals (scale bar: 200 µm).* ***B)*** *PC4 loading negatively characterized by paraffin peaks (asterisks) which are shown alongside a linear fit of a combination of reference spectra.* ***C)*** *The weight of each chemical reference spectra used to create the linear fit of PC4.*

4.3.2.2 Identification of tissue related signals

Connective Tissue

Localization of PC3 coincides well with the lamina propria, submucosa and the serosa (*fig.4.3a*). PC3 describes 3.51 % of the total variance and portrays the main difference between collagen components (negative) and combined muscle/mucin/paraffin (positive) signals; this is described in the linear reference combination (*fig.4.4a*). Intense peaks corresponding to proline and hydroxyproline were identified at 852, 916 and 933 cm^{-1}. The positions of the amide bands are critical to determining the secondary structure of the proteins. The intense amide III peaks at 1242 cm^{-1} and 1268 cm^{-1} correspond to the triple helical structure of collagen (158,159). The linear fit coincides well with the first two hydroxyproline peaks.

Muscle Tissue

PC5 accounts for 1.19% of the total variance and depicts the main difference between muscle (negative) and combined paraffin/DNA/collagen/mucin (positive) signals (*fig.4.3b*). The distribution of the loading covers the muscularis propria, muscularis mucosa as well as blood vessels in the submucosa. The most intense peak at 1002 cm^{-1} is attributed to the ring breathing mode of phenylalanine and is a ubiquitous proteinaceous constituent of biological tissue. Peaks at 638 and 1614 cm^{-1} (tyrosine), 1208 and 1550 cm^{-1} (phenylalanine, tryptophan) are all assigned to aromatic amino acids. Other protein-associated peaks include 1121 and 1154 cm^{-1} (C-C, C-N stretch of proteins) and 1652 cm^{-1} (amide I). Some carbohydrate and lipid signals were also detected at 900 cm^{-1} and 955 cm^{-1}, respectively (*fig.4.4b*). Some of these peaks have previously been associated with actin and myosin components of muscle tissue (160–162). The linear reference molecule fit was best described by muscle acetone powder which fits well with the spatial localization of the loading within the map.

Mucin Signals

The localization of PC6 is in good agreement with goblet cell distribution within the H&E stained section (*fig.4.3c*). PC6 is attributed to 0.92% of the total variance and depicts the difference between mucin (negative) signals and combined DNA/muscle (positive) signals (*fig.4.4c).* The most intense peak at 1390 cm^{-1} has been tentatively assigned to *N*-acetyl-galactosamine and *N*-acetyl-glucosamine as these are the most abundant sugar groups within mucins (163). Other associated peaks were at 1426 cm^{-1} (deoxyribose), 1532 cm^{-1} (C=O) and 1635 cm^{-1} (amide I). Lipid peaks were detected at 435 and 1730 cm^{-1}. The linear reference fit indicates that PC6 is abundant in mucins and lipids however the overall fit to the loading could be improved.

Nucleic Acid Signals

PC8 describes 0.43 % of the total variation in the data, and appears to capture the nucleic acid signals (*fig.4.3d*). Nucleic acid signals are most abundant within the mucosa due to the presence of a very dense cell population in comparison to other layers of the colon (*fig.4.1b*). One of the most characteristic peaks in this loading is at 778 cm^{-1}, corresponding to uracil, thymine and cytosine. The

remaining peaks all correspond to either DNA or RNA: 721 cm^{-1} (ring breathing modes of DNA), 1091 cm^{-1} (phosphodeoxy groups of nucleic acid backbone), 1246 cm^{-1} (asymmetric phosphate stretching modes from phosphodiester groups), 1484 cm^{-1} (nucleotide acid purine bases), 1577 cm^{-1} (guanine, adenine) and 1691 cm^{-1} (C=O group of bases). The linear reference fit indicates the loading is primarily composed of nucleic acids, which is in good agreement with the peak assignments and localization of the loading (*fig.4.4d).*

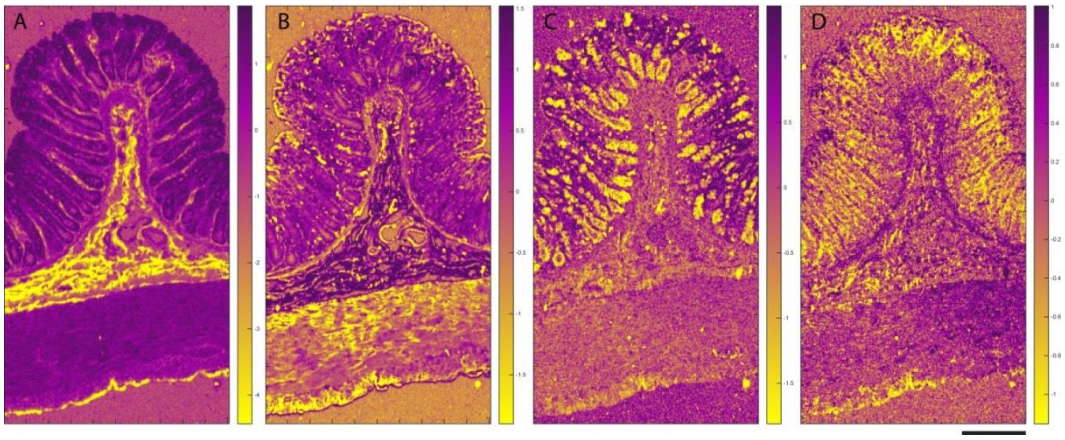

Figure 4.1.3: False-coloured PCA score images colour coded by the associated PC loadings and tentatively assigned to specific histological regions within the colon: A) *PC3: submucosa, lamina propria and serosa,* ***B) PC5: muscle, C)*** *PC6: mucin in goblet cells and* ***D)*** *PC8: nuclei (scale: 200 µm). Note that the images are not heat maps and that the intensity of the purple or the yellow colours indicates the intensity of the component signals either positive or negative. These images were generated using Matlab R2015b.*

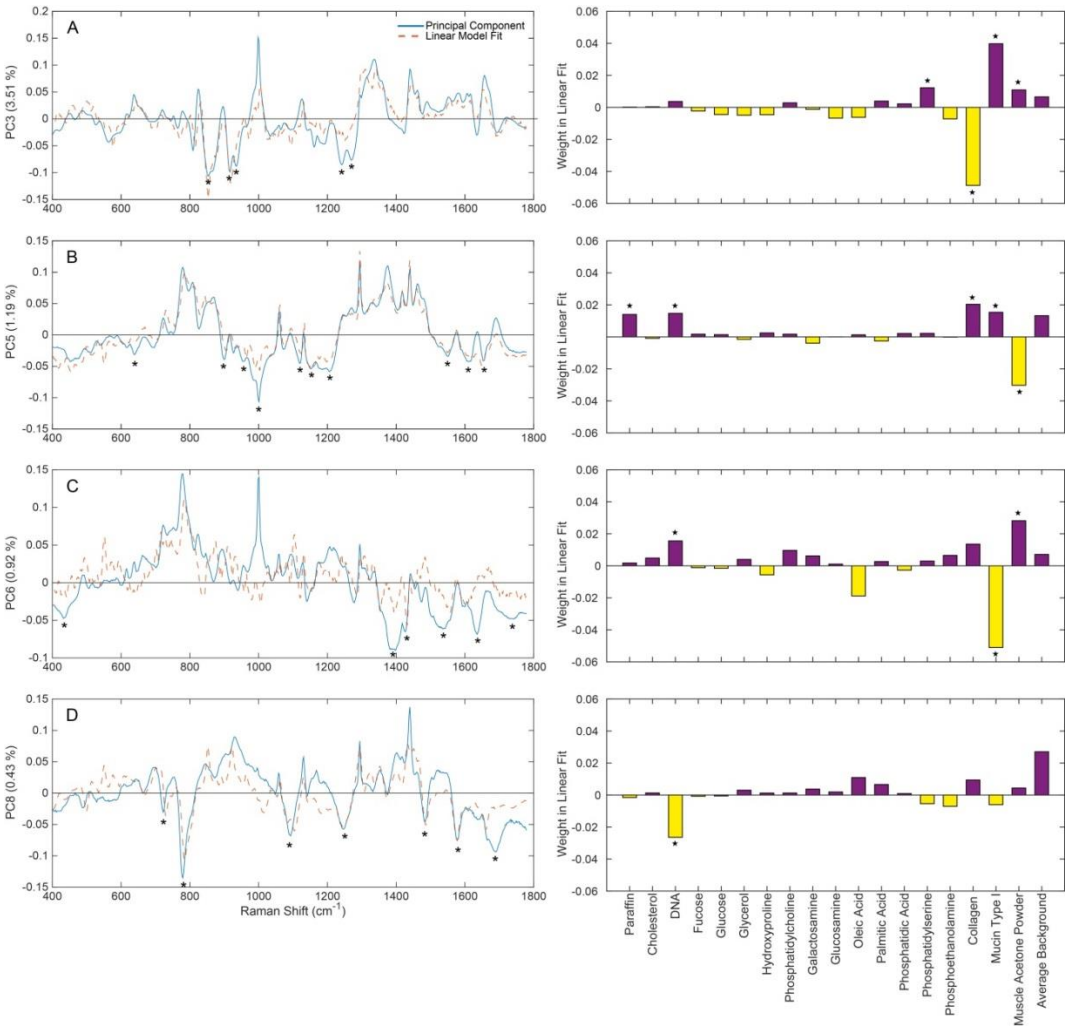

Figure 4.1.4: Loadings of principal components A) three, B) five, C) six and D) eight, each superimposed with a linear fit of the best matching molecular reference. *Note in the right hand panels that the purple and yellow colour coding of the positive or negative contribution of each reference species to the linear fit to the principle component has been preserved and is in accord with Figure 4.3.*

The characteristic loadings can be combined to produce a false coloured composite score image that results in superior contrast to the traditionally used H&E staining techniques (*fig.4.5*).

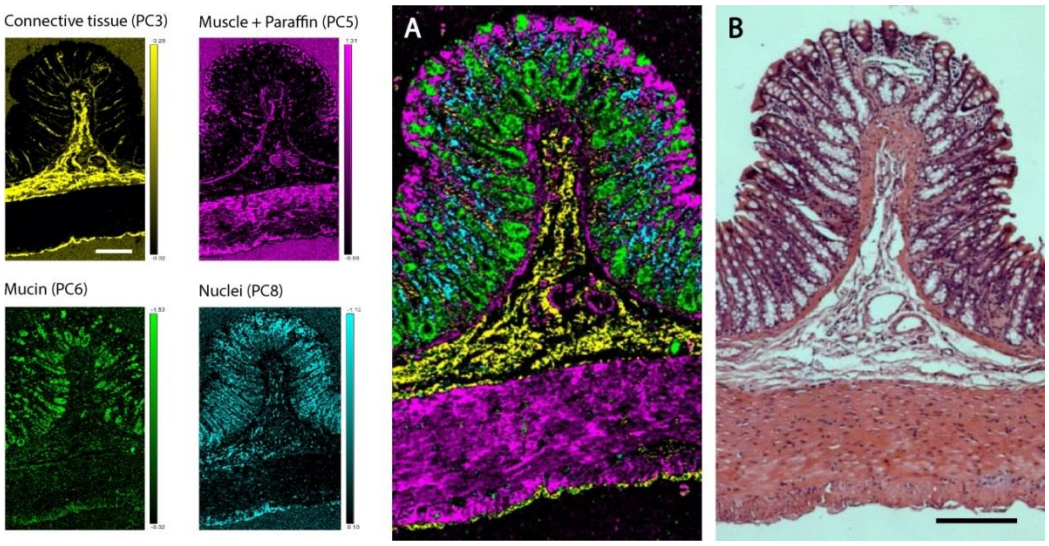

Figure 4.1.5: False coloured PCA composite score maps A) *PCA composite score maps were generated using WiRE 4 software and encompass the individual PC scores characteristic of the unique spectral signatures of the different anatomical layers of the colon (scale: 200 µm). With this method the dominating spectral and chemical properties of each individual pixel in the tissue map are united in a high definition pseudo-stained image.* ***B)*** *Full thickness H&E stained rat colon section (adjacent to the Raman imaged unstained section).*

4.3.3 Spectral similarity maps

Having established the main anatomical regions that can be resolved using unsupervised PCA an attempt was made to match some of the reference biomolecules expected to be abundant within these regions.

Large areas of the Raman map do not contain biological tissue—most prominently the main lumen of the gastrointestinal tract. These areas still produce Raman signal, and can be spuriously labelled as being similar to reference spectra. As such, it is vital to determine and then discard those pixels that do not contain tissue before analysing the spectral similarity maps. This has been achieved by applying a background mask (*fig.4.6a*).

Matching the similarity of a molecular reference to each pixel within the tissue map allows a direct visualisation of the distribution and abundance based on pixel intensity. Use of similarity maps removes the need to tentatively assign peaks from Raman spectral databases. Computing the average of the best matching 100 tissue spectra can be used to reconstruct a best match spectrum. This enables easy identification of the most characteristic features associated with the biomolecular reference.

DNA produced an accurate distribution across the tissue and was localized within the mucosa where the nuclear density is greatest. Similarity was also found across the submucosa where sparse lymphocytes are present as well as the nuclei of muscle cells within the muscularis propria (*fig.4.6b*). The most characteristic peaks that best match the DNA reference spectrum are at 782, 1100, 1335, 1573 and 1662 cm^{-1} (*fig.4.7*).

As expected strong collagen signals were found to be abundant within the lamina propria and the submucosa. Of all the references, the collagen spectrum most closely matched tissue-derived spectra with very high similarity between the reference and the average spectrum of the 100 best matching tissue spectra (θ = 0.92). Collagen associated spectra were also detected within the serosa and across the muscular regions – in particular at the interface between the circular muscle and the submucosa (*fig.4.6c*). Proline and hydroxyproline amino acids unique to collagen were detected at 815, 854, 872, 920 and 935 cm^{-1} in the best matching tissue spectra. Other protein related peaks were detected at 533 and 561 cm^{-1}, along with the amide III band at 1244 cm^{-1}, CH deformation at 1450 cm^{-1} and 1674 cm^{-1} characteristic of amide I (*fig.4.7*).

The muscle reference was found to localize within all muscular regions, but was also found within the submucosa and outermost luminal edge of the mucosa (*fig.4.6d*). Characteristic peaks that were present within the average tissue spectrum and reference were particularly assigned to aromatic amino acids phenylalanine (620, 1002, 1030 cm^{-1}), tyrosine (642, 828, 852 cm^{-1}) and tryptophan (757, 1551 cm^{-1}). Other protein related bands were at 935 cm^{-1} (proline, valine, collagen), 1124 cm^{-1} (C-N protein vibration), 1315 cm^{-1} (CH_3CH_2 twisting mode) and 1447 cm^{-1} (CH_2 bending mode of proteins) (*fig.4.7*). A spectral similarity of θ = 0.81 was achieved.

The most abundant tissue phospholipid – phosphatidylcholine – co-localized with pixel regions that were heavily contaminated with paraffin wax (*fig.4.6e-f*). This is further corroborated by matching the reference spectrum with the average of the hundred most similar tissue spectra. Overlapping peaks were found at 1062, 1132, 1294, 1439 and 1460 cm^{-1} (*fig.4.7)*. The remaining references failed to match – this was detected by poor co-localization within the map and/or an average tissue spectrum corresponding to the background.

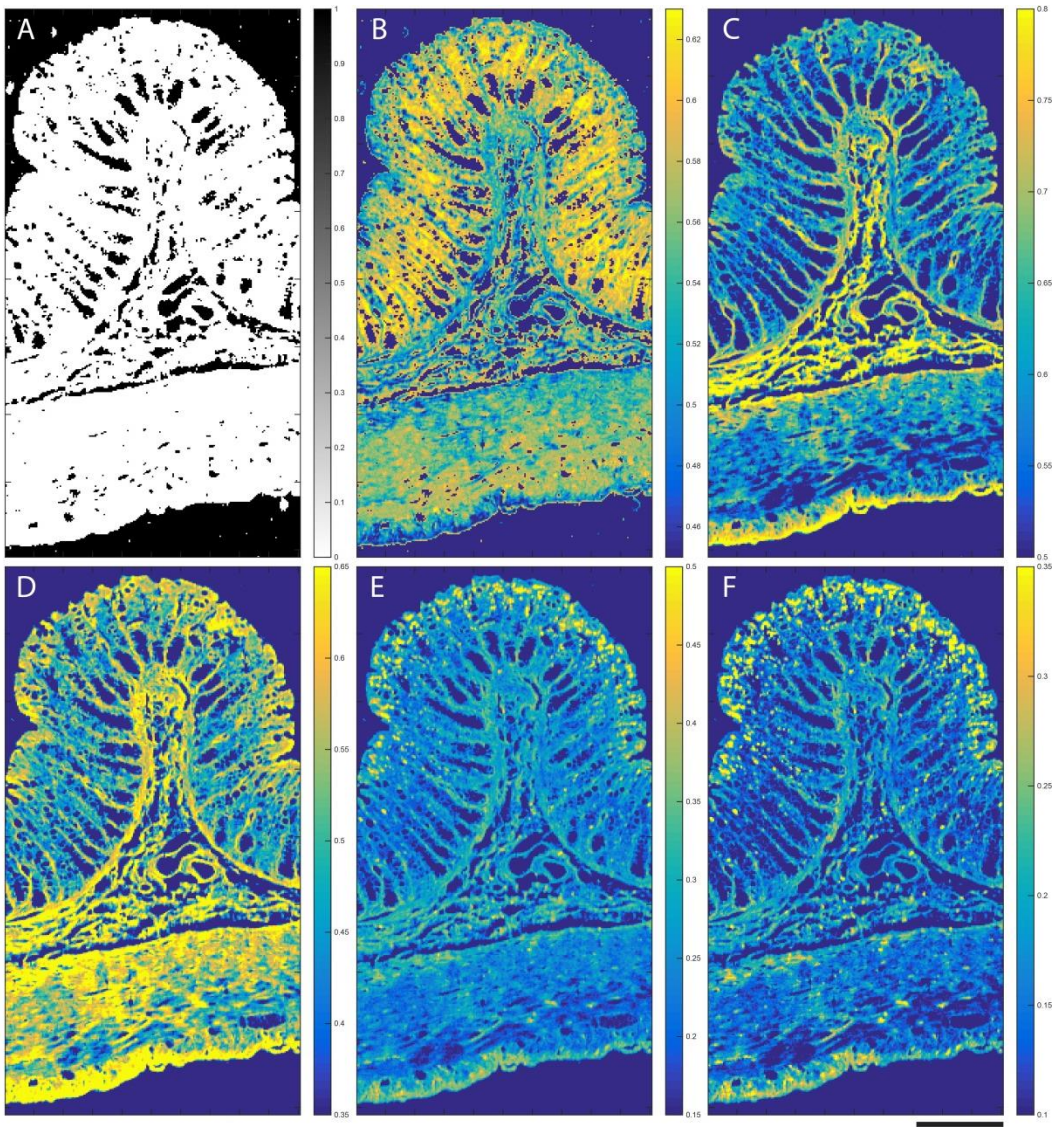

Figure 4.1.6: Spectral similarity maps of molecular references expected to be present within colon tissue. A) *Background mask,* ***B)*** *DNA,* ***C)*** *Collagen,* ***D)*** *Muscle acetone powder,* ***E)*** *Phosphatidylcholine,* ***F)*** *Paraffin wax (scale: 200 µm). Phosphatidylcholine and paraffin signals were found to co-localize suggesting that paraffin contamination hinders lipid identification. Note that in these images the intensity corresponds only to positive scores (within the range 0 to 1) with the brighter yellow colour indicating greater abundance and better spectral similarity to the reference sample.*

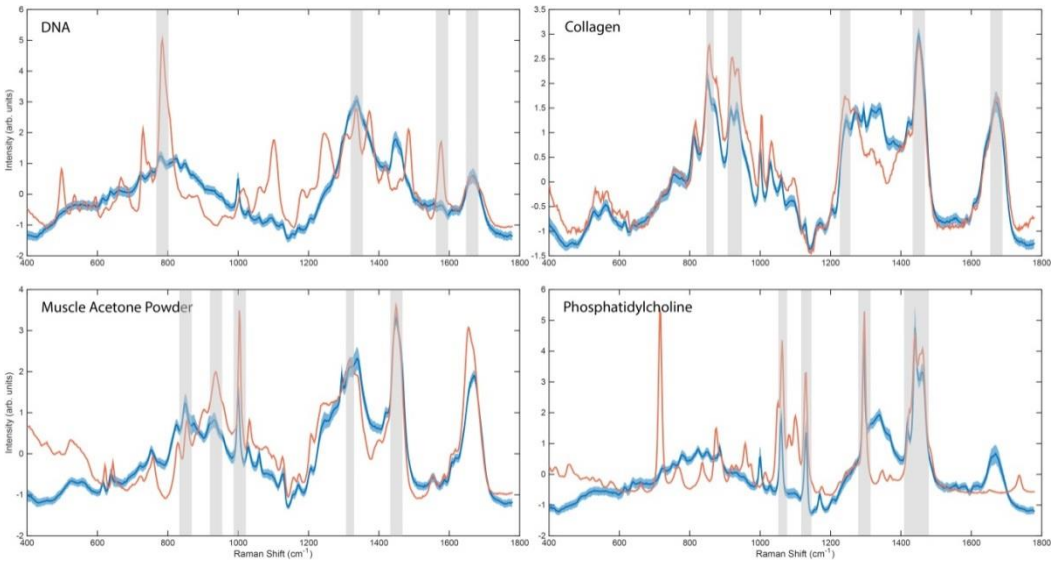

Figure 4.1.7: Reference spectra (orange) displayed alongside the average spectrum (blue) of the 100 best matching tissue map spectra along with their ±1 SD. *Similarity scores of DNA $\theta = 0.65$, collagen $\theta = 0.92$, muscle acetone powder $\theta = 0.81$ and phosphatidylcholine $\theta = 0.60$ were achieved.*

4.4 Discussion

Up until now there have been no previous attempts to provide a detailed biochemical characterisation of the layers of healthy colonic tissue following FFPE treatment. Only one other study has thus far been conducted on frozen human colon that was passively dried prior to Raman analysis. However, the selected spatial resolution was significantly lower than our study at a step size of 10 µm at the mucosal surface, compared to our step size of 2.8 µm (69). Our results clearly indicate that Raman microspectroscopy can discern the biochemical difference from within each layer following extensive chemical processing – resulting in superior contrast to the currently universally used H&E stain (*fig.4.5*).

Before conducting any further biological analysis an effort was made to first identify any chemical contaminants which may interfere with the analysis. PCA revealed widespread paraffin contamination with a good linear fit to a paraffin reference. The distinct difference between true biological material and the added organic paraffin enabled easy identification of such contamination. The incompleteness of paraffin removal has been reported previously in several other studies (151,164) and thus far no mechanism for the complete removal of paraffin with any known deparaffinising agent has been discovered. Discovery of a method

for the complete removal of paraffin with the maintenance of biochemical signals and tissue morphology could have significant benefits in clinical diagnosis or in research. For example prolonged incubation of tissue sections (~18 hrs) in hexane results in near complete removal of paraffin and contributes to a 30% increase in IHC staining (164). Significant wax retention is expected to compromise IHC results by blocking the presentation of antigens to antibodies. This work contributes further to the current body of evidence that Raman analysis can provide the means to assess paraffin retention, which can potentially be used as measures for wax removal efficacy and provide a means of quality control for optimised IHC staining.

Furthermore, clear identification of phospholipid components (such as phosphatidylcholine in this study) is hindered by paraffin retention – in the presence of paraffin the signals from phospholipids cannot be unambiguously monitored. The obvious reason why the majority of all the lipid references tested were found to overlap with pixels containing paraffin is because of the overall structural similarity of fatty acyl groups and paraffins. In order to retrieve biochemical information on tissue phospholipid status it will be essential to ensure close to complete paraffin removal from tissue sections prior to Raman mapping and reference matching. Given the strong diagnostic correlation between aberrant phospholipid metabolism and disease and the prospects for therapy (e.g. cancer) (165) the value of Raman in monitoring and validating complete paraffin removal and recovering data on the remaining tissue phospholipids is self-evident.

Collagen signals were easily identified using both unsupervised PCA as well as spectral similarity maps with the highest similarity score of $\theta=0.92$. Of the biologically relevant PCs the loading associated with collagen accounted for the higher proportion of the variance within the dataset (3.51 %) compared to other components. All collagens consist of a set of three polypeptide chains held together in a helical conformation via hydrogen bonding. Each polypeptide chain is characterized by a repeating Gly-X-Y sequence where X corresponds frequently to proline and Y to hydroxyproline (159,166). The presence of hydroxyproline (rare in most other proteins) therefore makes collagen quite a unique molecular entity that is easily recognized. This might prove to be useful in the detection of collagen elevation associated with fibrostenotic IBD for

example. Using PCA we were able to confine the collagen signals to the submucosa and serosa where connective tissue binds mesothelial cells to the outer longitudinal muscle. On the other hand, similarity maps exhibited some collagen-like signals at the interface between the submucosa and the muscularis propria as well as the outermost edge of the longitudinal muscle. This is likely caused by the overlap of certain vibrational signals that are also present in muscle tissue. More importantly the frequency shifts observed in the amide III bands are in agreement with shifts observed in unfixed/frozen tissue (69), this suggests that formalin fixation did not impose any detrimental effects on the collagen components on this occasion.

Along with collagen, nucleic acid signals were also one of the easiest molecular entities to identify using both similarity maps and PCA. This demonstrates that nucleic acid signals can potentially be quantified with relative ease, facilitating studies in cellular differentiation and carcinogenesis. In this particular case 24 hour formalin fixation and extensive downstream processing along with attempts at rigorous deparaffinization of a small 5 mm by 5 mm rat colon resection had no adverse effects on the detection of nucleic acid signals.

Muscular regions were associated with abundant protein signals, in particular from the aromatic amino acids phenylalanine, tryptophan and tyrosine. This has previously been observed from frozen then passively dried colonic tissue sections (69). PCA shows that some muscle-like signals were also present across the luminal edge of the mucosa (*fig.4.4b*); however the reference linear fit suggests that these signals are of lipid origin and are likely detected from the cytoplasmic components of the luminal epithelial cells (*fig.4.5b*). This is further corroborated by the H&E stained image as the luminal epithelial cells have a clearly visible cytoplasmic component (*fig.4.1b*).

The identification of mucin in FFPE tissue suggests that mucin was not completely removed during chemical processing. However, its retention within goblet cells is also likely to be affected by the extent of rough handling and overall disturbance of the mucosa. Intestinal mucins are composed of approximately 80% carbohydrate side chains bound to a protein core. Five different carbohydrate moieties: N-acetyl-galactosamine, N-acetyl-glucosamine, fucose, galactose and sialic acid are arranged in side chains and trace amounts of mannose and sulfates have also been found (167,168). Using PCA we were able to identify the large carbohydrate content of mucins and therefore isolate the goblet cells (*fig.4.5c*).

Previous Raman studies of mucin molecules have revealed intense signals originating primarily from the carbohydrate moieties and not so much from the proteins (163). The lipid signals detected are a likely result of the presence of polar/neutral lipids and glycolipids that confer surface hydrophobicity, as well as viscous and lubricant properties to mucus (169). Detection of mucins during Raman analysis therefore provides an additional scope for assessing tissue homeostasis and early metastatic potential (170–172).

Conversely some of the tissue components were not easily distinguished such as the epithelial cells lining the inner crypts and the lymphocytes within the lamina propria. The predominant signals from both of these cell types were of nuclear origin as the extremely compact nature of the rat mucosa leaves very little visible cell cytoplasm (*fig.4.1b*). By opting for a near infrared 785 nm wavelength and line illumination geometry I was able to not only reduce the overall tissue auto-fluorescence but also reduce the likelihood of photo-thermally degrading the sample by dispersing the laser density across a line. The spatial resolution of a Raman image is dependent on a number of different parameters: 1) objective NA, 2) laser wavelength, 3) laser geometry and 4) step size used to acquire the image (173). Using a 785 nm laser line for mapping at a 2.8 µm step size would enable features larger than 2.8 µm to be resolved; features below this such as the compact cytoplasm will need to be resolved by sampling at a smaller step size. To distinguish the different cell types we would need to capture the protein expression profiles of each cell and hence the cytoplasm would be a crucial feature. It is likely that the combined signal from both the nucleus and cytoplasm may be crucial for the discrimination of different cell types. It was therefore not possible to distinguish the finer features of the colon such as the stem cells at the base of the crypts. Raman imaging using higher spatial resolution may be required to reveal such fine anatomical structures. This may be realised by employing an objective with a higher NA, shorter laser wavelength e.g. 532 nm, laser spot configuration and a smaller step size.

The ability to successfully detect specific biomolecular references strongly depends on the abundance of the chosen reference. It is important to note that a single band does not correspond to a single chemical entity but instead to the vibrational state of a given chemical bond, which may be shared across several

different molecules. We observed superior performance of more complex reference molecules such as collagen, mucin and muscle over singular molecules such as amino acids and sugars. This was observed on numerous occasions where collagen outperformed hydroxyproline (*fig.4.4a*) and mucin outperformed the most abundant mucin sugars glucosamine and galactosamine (*fig.4.4c*). Furthermore, applying unsupervised PCA led to superior results over similarity maps without the need for selecting biomolecular references.

During the initial map data acquisition, biomolecular reference matching was not anticipated, as only unsupervised analysis was planned. Nevertheless, matching a subset of references acquired on a different bench top Raman system produced good results without any correction for instrumental differences. Correction was not attempted as the map data was acquired on a demonstrator instrument at the Renishaw site, this system undergoes frequent modification and hence it would be very unlikely to obtain identical measurement parameters for the instrument response correction.

This study demonstrates that Raman microspectroscopy can be successfully used to discern all the major anatomical layers of colonic tissue processed with conventional FFPE techniques. Raman is therefore a suitable technique for tissues that have undergone processing using the standard pathological workflow. There is an overall good agreement in the Raman spectral assignments of FFPE colonic tissue layers and chemically untreated biomolecular references. This confirms that chemical processing does not lead to an unacceptable distortion in the spectral profiles of tissues. Additionally, mucin signals were shown to be well retained following extensive chemical processing emphasizing the desirability of gentler handling of the fresh tissue specimens in order to prevent mucin leakage and preserve any signals that may be of diagnostic use. Furthermore, it has also been shown that the detection of specific biomolecular references within the tissue requires careful selection of the reference panel.

4.5 Conclusions

This preliminary study confirms that a good Raman signal and spatial resolution can be achieved from FFPE colonic tissue sections. This in turn facilitates easy identification of all major layers of the colon along with a complete characterisation of the associated spectral signatures. Through the use of PCA, composite score

images provided a superior contrast to the conventional H&E stained sections. The anatomical layer identification was confirmed by similarity maps correlating to the abundance of known chemical components of each layer. Furthermore, extensive chemical pre-processing in formalin, alcohol and xylene did not impede the quality of the spectral signatures in our study, however paraffin contamination was detected.

Chapter Five

Raman imaging of formalin-fixed paraffin-embedded normal human colonic tissue

5.1 Introduction and Aims

I have established in the previous chapter that the major anatomical regions can be identified from FFPE treated rat colonic tissue mounted on CaF_2. This chapter explores whether similar high quality results can be obtained from human colorectal tissue mounted onto silanized super mirror steel slides (prepared using the protocol outlined in Chapter Three). Therefore this exploratory study aims to simultaneously investigate the suitability of super mirror silanized stainless steel slides as a substrate for Raman based tissue analysis and extended methods developed in rat tissue to the human equivalent.

In this chapter I will:

1. Analyse FFPE healthy human colonic tissue that has been mounted onto salinized super mirror steel slides.
2. Identify the biochemical composition of each anatomical layer of the colon using unsupervised multivariate analysis.
3. Correlate the composition of each anatomical layer to known biochemical references.
4. Compare and contrast the visualisation of label-free Raman imaging to contiguous IHC stained sections.

5.2 Materials and Methods

5.2.1 Tissue acquisition and preparation

FFPE human colon samples were obtained from the UCL/UCLH Biobank for Studying Health and Disease (REC 15/YH/0311). A normal resection was selected with no polyps or identifiable cancer within the immediate vicinity of the analysed tissue. One section was cut at 8 μm and mounted onto silanized super mirror stainless steel slides for Raman analysis, while the remaining sections were cut at 3 μm and mounted onto Superfrost™ plus charged slides for immunohistochemical (IHC) staining. Slides destined for Raman analysis were incubated overnight at 37°C and deparaffinized using the manual deparaffinization protocol outlined in chapter three. IHC destined slides were subjected to automated staining described in the following section.

5.2.2 Immunohistochemical staining

Immunostaining of paraffin sections was carried out using a Leica Bond III automated immunostaining platform with a Bond™ Polymer Refine DAB detection system (Leica Microsystems, Nussloch, Germany). All sections were deparaffinized, subjected to epitope retrieval and immunostaining within a single platform. The 15.8.8 protocol for Leica Bond III IHC staining was followed, this has been outlined in *Appendix 10*.

For muscle specific staining three antibodies were selected: desmin for muscle, collagen III for connective tissue and CD117 for the interstitial cells of Cajal. For mucosa specific staining three additional antibodies were used: CK20 for differentiated epithelial cells, Muc-2 for goblet cells and MIB-1 for transit amplifying cells.

Slides were first air-dried on a 70ºC hotplate for one hour before being transferred to an oven to be baked at 60ºC for an additional hour. Sections were then deparaffinized using bond dewax solution for 30 seconds followed by three subsequent washes at 72ºC. The exact steps of the deparaffinization protocol can be found in *Appendix 7* of Chapter Three. The slides were then pre-treated with a heat-induced epitope retrieval step. Leica Bond ER1 (citrate based pH 6.0 epitope retrieval solution) was used for sections destined for staining with CD117, CK20 and col III. Leica Bond ER2 (EDTA based pH 9.0 epitope retrieval solution) was applied to sections destined for muc-2, mib-1 and desmin staining. Separate tissue sections were used as positive controls for each antibody.

Following the washing steps, endogenous peroxidase blocking was carried out using the Bond™ Polymer Refine Detection Kit (Leica, Catalog No: DS9800). Tissues were then washed again with a Leica wash buffer and incubated with the following primary antibodies:

Desmin

Mouse anti-human desmin monoclonal antibody (clone DE-R-11, Leica, cat. No. PA0032) was used without dilution. Appendix tissue was used as a positive control.

Collagen III

Mouse anti-collagen III (clone FH-7A, GeneTex, cat. no. GTX26310, stock concentration: raw ascites) monoclonal antibodies were applied for 15 minutes at a 1:500 dilution. Normal human colon was used as positive controls.

CD117

Rabbit anti-human polyclonal antibody (Dako, cat. no. A4502) against the transmembrane tyrosine kinase receptor CD117/c-kit was applied for 15 minutes at a 1:50 dilution. Gastrointestinal stromal tumours (GIST) and mast cells were used as positive controls.

CK20

Mouse anti-human (clone KS20.8, Leica, cat. no. NCL-L-CK20) monoclonal antibody was applied for 15 minutes at a 1:50 dilution. Normal colonic epithelium was used as a control.

Muc-2

Mouse anti-human MUC-2 (clone Ccp58, Leica, cat. no. NCL-MUC-2) was applied for 15 minutes at a dilution of 1:200. Normal colon and stomach mucosa were used as control tissues.

Subsequently tissues were incubated with a post primary rabbit anti-mouse IgG linker reagent to localise mouse antibodies, and finally with an anti-rabbit poly-horseradish peroxidase IgG reagent (HRP-conjugated secondary antibody) to localise rabbit antibodies as well as detecting the post primary antibody. The complex was then visualised via a brown precipitate generated through incubation with a 3,3'-diaminobenzidine tetrahydrochloride hydrate (DAB) chromogen. Hematoxylin (blue) counterstaining was then used to visualize the cell nuclei.

5.2.3 Reference biomaterials

Two separate groups of bio-reference materials were selected for the muscle only map and mucosal map. For the muscle map the following reference materials were selected: muscle acetone powder, authentic collagen, glutamate, aspartate, hydroxyproline, DNA, phosphatidylcholine, phosphatidylserine, myelin basic protein and paraffin wax. Based on the performance of the references in the muscle only analysis, the reference subset for mucosal analysis was further refined and included: muscle acetone powder, authentic collagen,

mucin type I, glucosamine, galactosamine, phosphatidylserine, FFPE lymphocyte average spectrum, DNA, RNA, paraffin wax and background. All laboratory acquired references were used as solid samples, neat (if in solution), with any volatile solvents evaporated and without any further pre-treatment or dilutions. Specific reference information can be found in *Appendix 8* of Chapter Four, additional references not covered in Chapter Four can be found in *Appendix 11*.

5.2.4 Raman spectroscopic imaging

StreamLine™ Raman imaging was performed using the Renishaw RA802 bench top prototype system (Renishaw plc, Wotton-under-edge, UK) coupled to a 785 nm laser excitation source. A total laser intensity of approximately 158 mW was focused onto the sample through a 50×/NA 0.8 objective. A 1500 l/mm grating was used to disperse the light providing a spectral range of 0 to 2100 cm^{-1} in the low wavenumber range. A 1.0 µm step size was used for all maps with a variable integration time. An integration time of 40 seconds was used for the muscle only region and 60 seconds for the lower mucosal region. All systems checks conducted prior to analysis have already been detailed in section 2.4.2.2 of Chapter Two.

5.2.5 Spectral pre-processing

Cosmic ray removal was conducted using the width of feature and nearest neighbour methods in WiRE 4 software. Baseline correction to a third order polynomial and normalisation was conducted in MATLAB R2013b (MathWorks, Natick, MA, USA). Pre-processed spectra were then analysed in both MATLAB R2013b and WiRE 4.

5.2.6 Statistical analysis

5.2.6.1 Principal Component Analysis

PCA along with linear fits were carried out using MATLAB R2013b. As previously conducted in Chapter Four a linear combination of molecular reference spectra were used to identify the molecular origin of the PCAs. A detailed description of the techniques used can be found in section 2.6.4 of Chapter Two.

An in depth analysis was carried out on four out of ten PCs accounting for 35.7% of the total variance from the muscle religion. Four out of a possible ten PCs

were also analysed from the mucosal crypt region accounting for 59.5% of the total biochemical variance.

5.2.6.2 Multivariate curve resolution-alternating least squares

MCR-ALS analysis was used to ascertain a more realistic pure spectral profile from each histological region of the Raman maps. This is achieved through a linear combination of pure spectra from each pixel weighted according to their abundance within the pixel. The final 'pure component' spectra can allow very significant improvement in the interpretation of the results as described in Chapter Two.

MCR-ALS was conducted using WiRE 4 software using a user defined number of components as the termination method. A detailed description of this technique can be found in the methods and instrumentation chapter, section 2.6.5.

5.3 Results

5.3.1 Comparison of spectral profiles from different anatomical regions

5.3.1.1 Supporting tissues

Supporting tissue constituents included the muscle (muscularis propria and muscularis mucosa), the lamina propria and submucosa (primarily collagen network) as well as the lymphoglandular complexes (lymphocyte clusters). Easy identification of these anatomical regions facilitated a straightforward comparison of their spectral profiles following FFPE treatment (*fig.5.1a*). Ten spectra were acquired from each location and averaged (*fig.5.1b*).

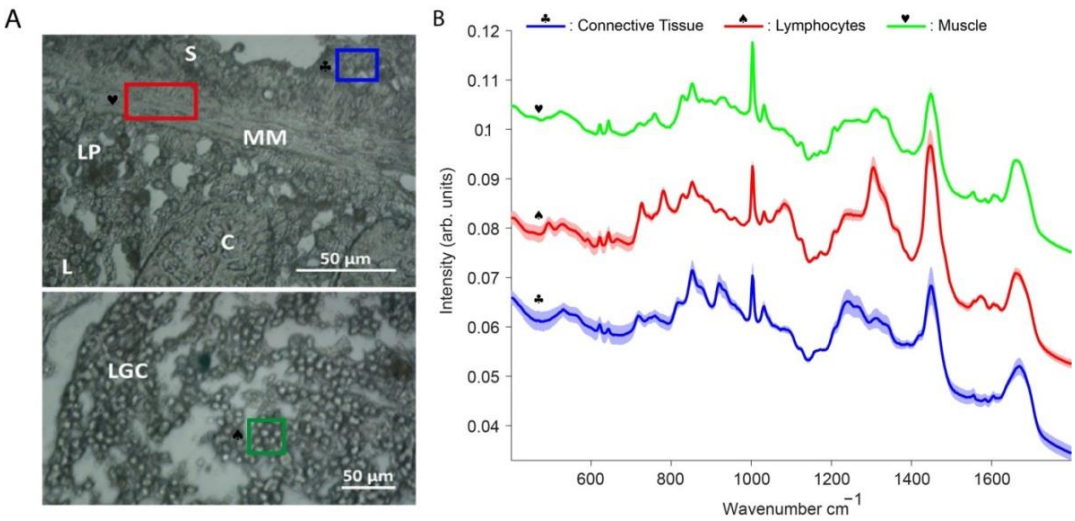

Figure 5.1.1: Acquisition of FFPE tissue based reference spectra obtained from distinct anatomical regions of known origin. A) *White light images of the distinct colonic anatomical regions (S: submucosa, MM: muscularis mucosa, LP: lamina propria, C: crypts, L: lymphocytes, LGC: lymphoglandular complex).* ***B)*** *Averaged spectra per tissue location with ±1 standard deviation (red: muscle, green: lymphocytes, blue: connective tissue). Offset for visual clarity.*

Subtraction of the collagen spectrum from lymphocytes reveals that the lymphocytes spectrum is abundant in glycogen (493 cm^{-1}), nucleic acids (726, 780, 1364, 1485 cm^{-1}) and lipid (1085, 1303, 1440 cm^{-1}) signals (*fig.5.2a*). A strong lipid content of lymphocytes from FFPE colonic tissue has previously been reported by Mavarani *et al* (68). Collagen on the other hand appears to be strongly characterized by peaks at proline, hydroxyproline, tyrosine (814, 855, 870, 919, 933 cm^{-1}), phenylalanine of collagen (1028 cm^{-1}), amide III (1241 and 1265 cm^{-1}) as well as a bending mode of methyl groups often associated with collagen (1405 cm^{-1}).

The difference between collagen and muscle is more subtle in comparison to that of lymphocytes. Muscle appears to exhibit more intense protein peaks at 1003 and 1656 cm^{-1} and lipid peaks at 1311 and 1332 cm^{-1} (*fig.5.2b*). Whilst collagen is strongly characterised by proline, hydroxyproline and tyrosine associated peaks at 812, 870, 919, 1241 cm^{-1} as well as amide III peaks at 1241 and 1265 cm^{-1}.

Subtraction of the average lymphocyte reference from muscle showed that muscle tissue was abundant in protein related peaks at 1003, 1032 and 1667 cm^{-1} (*fig.5.2c*). There was also a substantial peak at 934 cm^{-1}, previously assigned to collagen. Lymphocytes on the other hand had dominating peaks associated with

nucleic acid signals at 726, 780, 1091, 1483 cm^{-1}, as well as lipid peaks at 1303 and 1440 cm^{-1}.

The different supporting tissue networks can therefore be easily distinguished from one another using their variable spectral profiles.

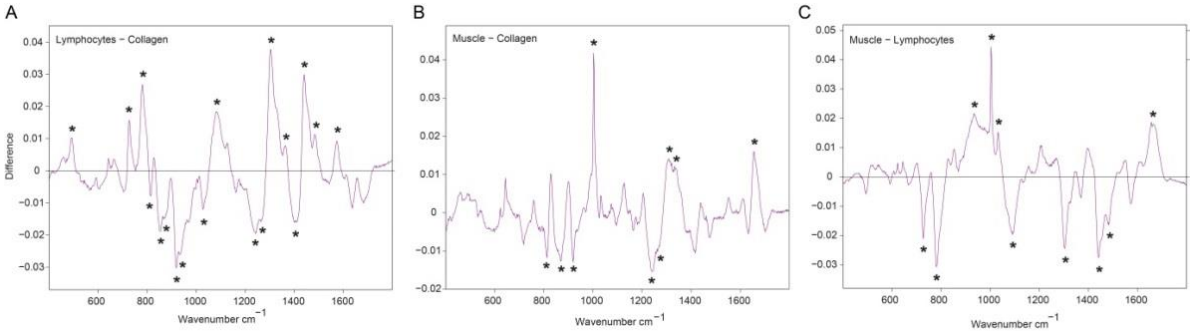

Figure 5.1.2: Difference spectra from supporting tissues. A) *Difference between lymphocytes and collagen average spectra.* ***B)*** *Difference between muscle and collagen average spectra. C) Difference between muscle and lymphocyte average spectra. Asterisks signify the most significant bands.*

5.3.1.2 Functional tissues

Functional tissues of the colon were considered solely as the crypt structures. Small maps were acquired from different locations along the length of the crypt (*fig.5.3*). Averaged maps along with their ±1 standard deviations were plotted in figure 5.4a. Difference spectra were used to isolate some of the obvious spectral differences between the epithelial cells that reside at different locations along the length of the crypt.

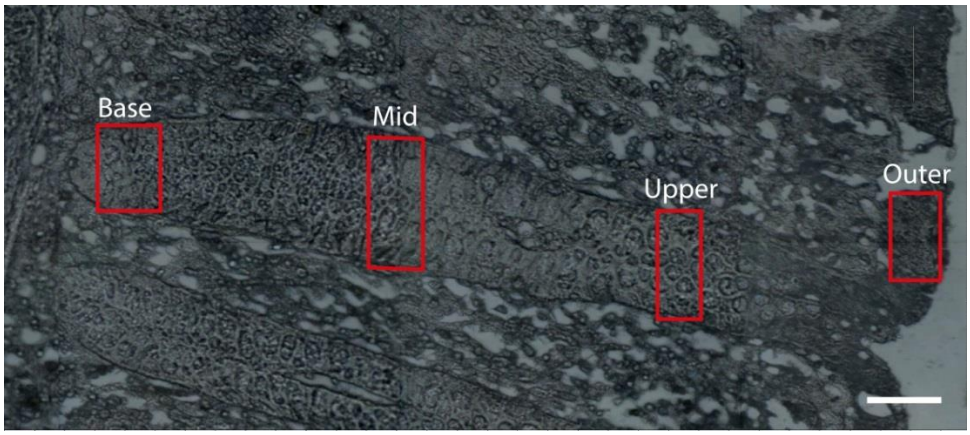

Figure 5.1.3: White light image of the whole length of a normal human colonic crypt (scale: 50 µm). *Small Raman maps were collected at different locations along the length of the crypt in an attempt to capture the variable spectral features of the residing cells: crypt base: 3220 spectra, mid crypt: 4040 spectra, upper crypt: 2465 spectra and outer crypt: 2170 spectra (Time: 15 sec, Power: 158 mW).*

Mid crypt – Crypt base comparison

Subtraction of the average crypt base spectrum from the mid crypt average shows that the mid crypt region possesses dominant protein (1677 cm^{-1}) and lipid (1083, 1304 cm^{-1}) based signals (*fig.5.4b*). The band at 1443 cm^{-1} suggests that the mid crypt region displays a generally higher biomaterial content as this is tentatively assigned to CH deformations. There is a slight reduction in the nucleic acid content in the mid crypt (729 and 784 cm^{-1}) probably indicating that the cells at the base of the crypt are slightly more proliferative.

Upper crypt – Crypt base comparison

Some of the most significant differences in the biochemical profile of cells at the base of the crypt in comparison to the upper crypt lie within the nucleic acid content. Cells at the base have a much richer nuclear content as exhibited by peaks at 727, 782, 1089, 1372 , 1570 and 1698 (C=O) cm^{-1} (*fig.5.4c*) compared to those in the upper crypt. The upper crypt on the other hand has relatively stronger protein related signals 1002 (phenylalanine), 1275 (amide III) and 1604 cm^{-1} (phenylalanine, tyrosine).

Outer crypt – Crypt base comparison

As before the crypt base was more abundant in nucleic acid signals exhibited by negative peaks at 782, 1374 and 1695 cm^{-1} (*fig.5.4d*). Lipid signals at 873 and 1080

cm^{-1} were also found to be slightly higher in crypt base cells. The outer crypt however is characterised by stronger protein peaks at 1171 (phenylalanine, tyrosine), 1269 (amide III), 1472 (C=N) and 1604 (phenylalanine, tyrosine) cm^{-1}.

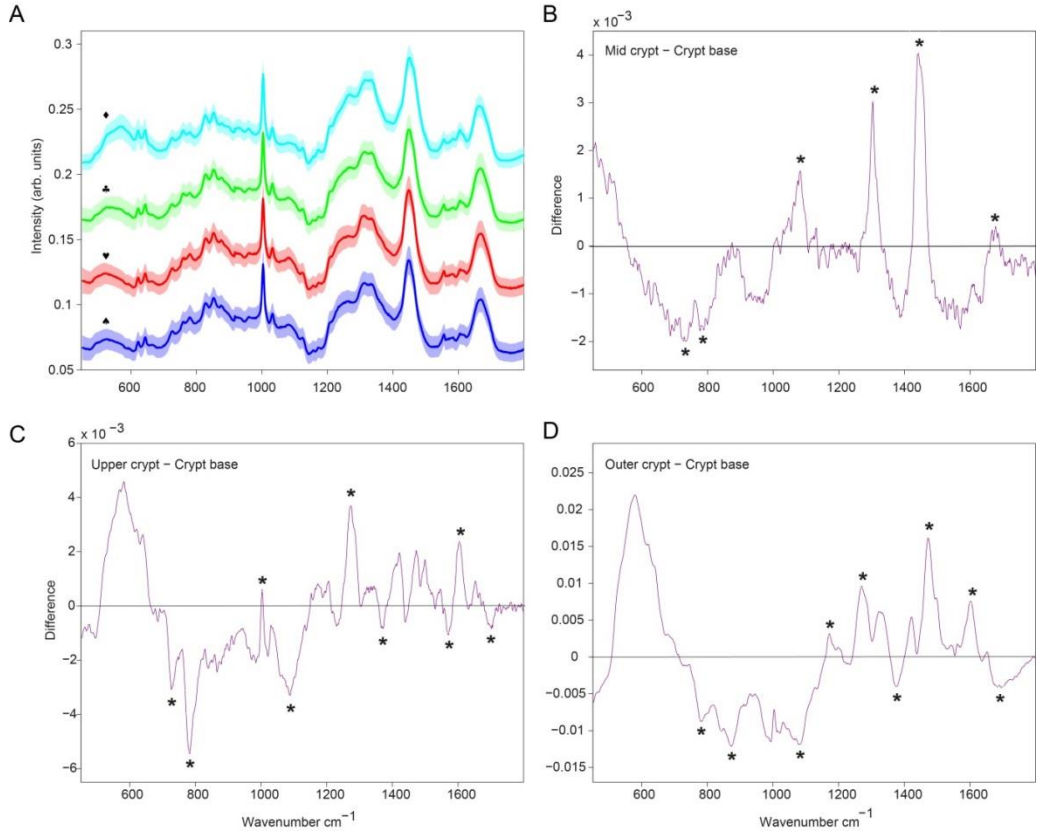

Figure 5.1.4: Comparison of spectral profiles of cells in different positions along the full length of a normal colonic crypt. A) *Averaged normalised spectra with ±1 standard deviation from all four maps (blue (spades): crypt base, red (hearts): mid crypt, green (clubs): upper crypt, cyan (diamonds): outer crypt), offset for visual clarity.* ***B-D)*** *Difference spectra of a crypt base map subtracted from maps from all other crypt locations. Asterisks signify the most significant peaks.*

5.3.2 Comparison of lab based bio-references against tissue acquired references

To identify some of the biochemical differences between laboratory manufactured/purified authentic molecular references and FFPE tissue components, a comparison was made between muscle and collagen. Muscle tissue and collagen networks were selected as they were easily identified in white light images of unstained tissue sections. Muscle acetone powder (rabbit dehydrated muscle) was acquired from Sigma Aldrich and was measured without any additional pre-treatment. Two distinct spectral profiles were

identified from muscle acetone powder; one was assigned to collagen based on the spectral features (852, 1240, 1265 cm^{-1}) previously observed by Krafft *et al* and the other to muscle only (69).

Muscle

On average all the peak intensities were found to be greater in muscle acetone powder. Few minor differences were detected in muscle powder with peaks at 902, 935 and 957 cm^{-1}, which were absent from FFPE muscle (*fig.5.5a*). There was also a noticeable shift in the amide I peak which was around 1654 cm^{-1} in muscle powder and 1661 cm^{-1} in FFPE muscle. These differences may be accounted to the variable FFPE tissue processing and muscle purification steps undertaken commercially. A preparation protocol was requested for comparison from Sigma Aldrich without success.

Collagen (connective tissue)

The overall peak intensities were found to also be more intense for the collagen component within the muscle acetone powder (*fig.5.5b*). The spectral profiles and peak positions however from both the FFPE collagen and collagen from muscle acetone powder were found to be identical. This may indicate that collagen is less susceptible to spectral perturbations from different preparation protocols.

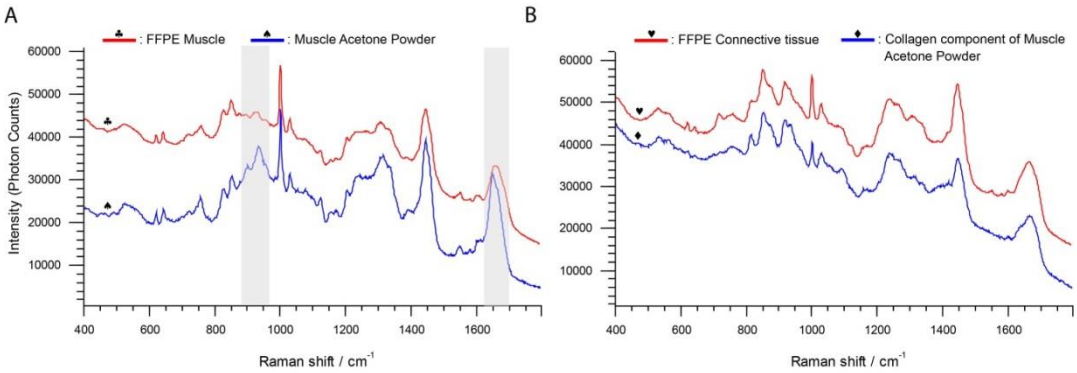

Figure 5.1.5: Comparison of spectral profiles from FFPE treated tissue components and those obtained/purified from a laboratory. A) *Muscle comparison, grey regions indicate areas of spectral difference.* ***B)*** *Collagen from connective tissue comparison.*

5.3.3 Analysis of the outer muscularis propria

5.3.3.1 Immunohistochemical evaluation

Adjacent sections were cut to facilitate immunohistochemical staining to identify specific anatomical regions of the muscle. Three different antibodies were used – desmin for muscle, collagen III for connective tissue and CD117 for the interstitial cells of Cajal.

The desmin stained muscle shows a clear orientation difference in the two layers of the muscularis propria (*fig.5.6*). The inner circular muscle cells are sectioned longitudinally revealing an elongated muscle cell profile, while the outer longitudinal muscle is sectioned transversely. Connective tissue stained by col III appears to be present both at the interface of the two muscle layers as well as between the muscle cells. CD117 staining is most sparse with most intense staining found within the close vicinity of the myenteric plexus.

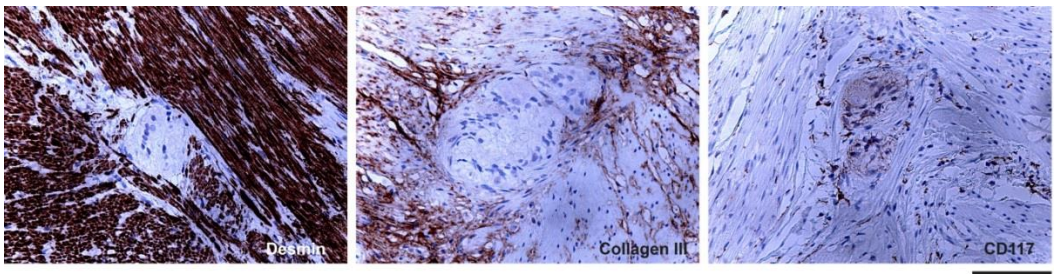

Figure 5.1.6: Immunohistochemical staining of the outer muscular propria transition encompassing the myenteric plexus. *Left panel: desmin stain for muscle tissue. Central panel: collagen III stain for connective tissue. Right panel: CD117 stain for pacemaker interstitial cells of Cajal. Scale: 100 µm.*

5.3.3.2 Principal Component Analysis

A small map approximately 351 µm by 528 µm (351 by 528 pixels) was taken across a muscle transition encompassing the myenteric plexus. The map consisted of 185,328 individual spectra acquired at a 1 µm step size.

PC1

PC1 depicts the difference between the myenteric plexus (negative) and the surrounding tissues (positive) (*fig.5.7a*). The surrounding tissues are

predominantly characterised by peaks at 1447 and 1664 cm^{-1}. This suggests that on average the surrounding tissue is more abundant in biomaterial and in particular proteins. The myenteric plexus is predominantly characterised by nucleic acids (727, 781 cm^{-1}), lipids (1367 cm^{-1}) and some protein signals (1555 cm^{-1}). The reference linear fit correctly identified both the myenteric plexus and the surrounding tissues which are assigned to collagen and muscle (*fig.5.8a*).

PC4

Visual examination of the PC4 score map appears to show the difference between a combination of connective tissue and nuclei (negative) from the remaining surrounding tissue (positive) (*fig.5.7b*). The surrounding tissue identified in yellow is primarily characterised by aromatic amino acids (620, 641, 1002, 1204, 1339, 1553 cm^{-1}) and amide I at 1655 cm^{-1}. Here the protein rich component of both the muscle and myenteric plexus is identified, however the linear fit only identified the muscle tissue (*fig.5.8b*). The variability in the loading intensity (brighter in longitudinal muscle) appears to suggest that the outer longitudinal muscle has a greater protein contribution.

The nuclei are identified through a number of DNA associated peaks at 727, 781,810, 1089 cm^{-1}, while the connective tissue components are characterised by peaks at 846, 869, 917 cm^{-1}(*fig.5.8b*). The linear fit correctly identified the collagen component of connective tissue but failed to identify the nuclear contribution. Some of the cytoplasmic component of muscle as well as nerve cell bodies in the myenteric plexus is also recognised through a number of lipid associated peaks at 1064, 1301, 1440, 1451 cm^{-1}. This is also identified through the linear fit but more so for phosphatidylserine than the more abundant lipid phosphatidylcholine. This might indicate that phosphatidylcholine may be more sensitive to lipid leaching through the previous xylene deparaffinization step.

PC5

Comparison of the PC4 and PC5 score maps (*fig.5.7b-c*) reveals some similarity, with both maps highlighting regions of connective tissue (purple). PC5 however has a more substantial lipid contribution evident through more intense lipid peaks at 1302 and 1440 cm^{-1}. This however was not captured as well by the linear fit as the lipid associated bars were smaller in comparison (*fig.5.8c*). The presence of

elevated lipid content in the inner circular muscle may be a result of longitudinal sectioning, which facilitates the visualization of the larger cytoplasmic component of muscle cells. Presence of nucleic acids (724, 779, 897 cm^{-1}) as well as some protein related peaks (1002 and 1654 cm^{-1}) was also detected. The reference linear fit performed sub-optimally as the muscle reference appeared to be the greatest contributor to this loading, with poor identification of lipids and nucleic acids. It is therefore apparent that these individual components have been grouped and encompass a single reference component - muscle.

As with PC4 the negative region of the PC5 loading appeared to have characterised the connective tissue region, with numerous collagen peaks present at 814, 856, 917, 1243, 1263 cm^{-1}. However, other protein related peaks were also detected at 1026, 1410, 1630, 1695 cm^{-1}. The reference linear fit was in agreement with this observation.

PC6

The difference between nuclei (positive) and the remaining tissue (negative) is captured within PC6 (*fig.5.7d*). The variable orientation of the nuclei in the muscle is clearly evident – cigar shaped in inner circular muscle and circular in outer longitudinal muscle. Nucleic acid associated peaks were detected at 495, 725, 778, 1098, 1330, 1367 cm^{-1}. Some marginal collagen contribution was also evident via the score image and is emphasized by protein peaks at 1237 and 1687 cm^{-1}. The reference linear fit correctly identifies nuclei and collagen, but wrongly identifies the muscle contribution. It has also wrongly assigned the surrounding tissue to myelin basic protein alone (a standard taken to be representative of non-muscle non-collagen protein) (*fig.5.8d*).

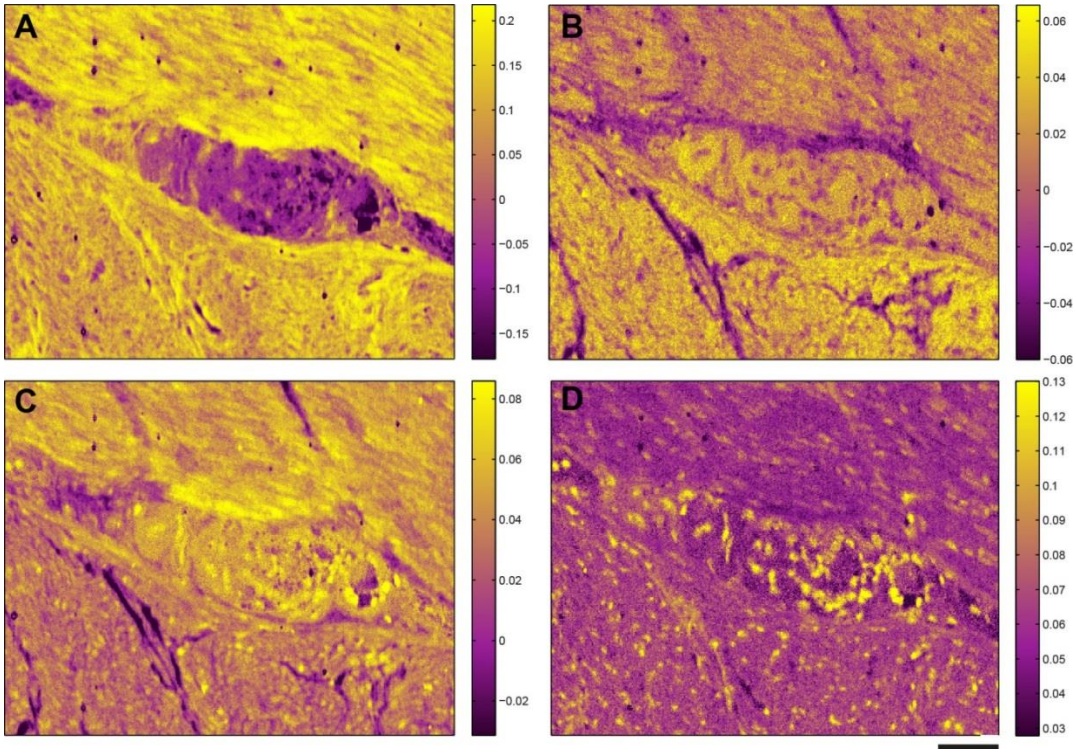

Figure 5.1.7: False-coloured PCA score images colour coded by the associated PC loadings and tentatively assigned to specific histological regions within the muscularis propria of the human colon: A) *PC1: difference between myenteric plexus and remaining tissue,* ***B)*** *PC4: difference between a combination of collagen and nuclei from the remaining tissue,* ***C)*** *PC5: difference between the lipid and collagen component and* ***D)*** *PC6: nuclei (scale: 100 µm). Note that the images are not heat maps and that the intensity of the purple or the yellow colours indicates the intensity of the component signals either positive or negative. These images were generated using Matlab R2013b.*

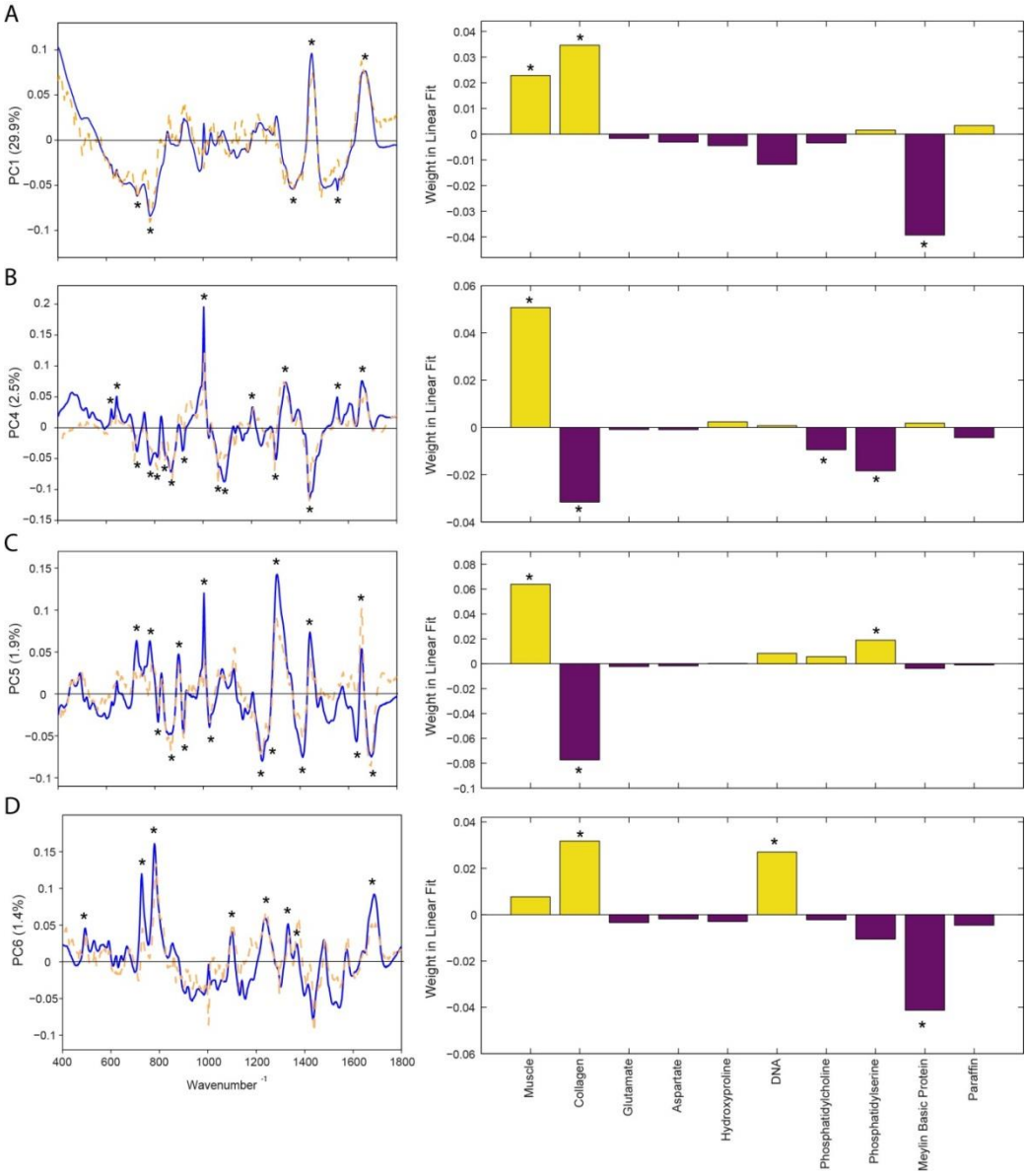

Figure 5.1.8: Loadings of principal components A) one, B) four, C) five and D) six, each superimposed with a linear fit of the best matching molecular reference. *Note in the right hand panels that the purple and yellow colour coding of the positive or negative contribution of each reference species to the linear fit to the principle component has been preserved and is in accord with Figure 7.*

The overall performance of PCA and linear fitting was not as good as was previously observed in the analysis of the full thickness rat tissue. The results shown here indicate that the histological features are further broken down into their subcomponents consisting of proteins, lipids and nucleic acids. It was therefore not possible to use PCA for the unsupervised identification of different histological features within muscle tissue.

5.3.3.3 Multivariate curve resolution-alternating least square analysis

Due to the poor performance of PCA a different unsupervised multivariate data analysis technique was applied. Multivariate curve resolution-alternating least square analysis (MCR-ALS) is an alternative technique that allows the decomposition of the hyperspectral dataset into a number of pure constituent spectral signatures estimated at a pixel level within the image. Figure 5.9 shows the resolved MCR-ALS empty modelled images (components 1-3, 6 and 8) alongside the corresponding spectral profiles for each estimated pure component.

The first and second component of MCR-ALS is clearly able to discriminate distinct zones of muscle tissue from the myenteric plexus. The resolved component curves for each of these zones represents a consistent spectral signature whereby there is a homogenous mixture of pure components. The spectral profile of the muscle associated component one (red spectral profile) was overlaid with a muscle spectral reference (black spectrum) acquired from FFPE human muscle tissue. Both the MCR-ALS resolved curve and the average muscle reference spectrum exhibit a high degree of similarity (*fig.5.9a*). The myenteric plexus resolved by component two shows a homogenous mixture of pure components similar to that of the muscle spectral profile with additional nucleic acid (724, 778, 894, 1574 cm^{-1}) and lipid (1078 and 1305 cm^{-1}) contributions (*fig.5.9b*). There is also an additional peak at 492 cm^{-1} attributed to glycogen as well as a shift in the amide I peak to 1656 cm^{-1}, which is likely to be attributed to lipids instead of proteins.

Lipid features of the muscle tissue were resolved by component three (*fig.5.9c*). Like PCA there appears to be an elevated lipid contribution within the inner circular muscle. The lipid associated peaks were present at 717 cm^{-1} (membrane phospholipids), 860 cm^{-1} (phosphatidic acid), 892 and 924 cm^{-1}(C-C skeletal), 1078 cm^{-1} (phospholipids), 1301 cm^{-1} (lipids), 1441 cm^{-1} (CH deformation) and 1652 cm^{-1} (lipid C=C stretch).

Connective tissue constituents were easily resolved by component six (*fig. 5.9d*). Multiple collagen associated peaks were identified at 812 cm^{-1}(C-C stretching), 855 cm^{-1} (proline, hydroxyproline), 916 cm^{-1} (proline, hydroxyproline), 1241 cm^{-1} (amide III of collagen), 1264 cm^{-1} (amide III of collagen), 1634 cm^{-1} (amide I) and 1687 cm^{-1} (amide I). Other non-collagen specific peaks were present at 1026, 1062, 1090, 1414 and 1449 cm^{-1}.

The nuclei of all cells were identified in component eight (*fig. 5.9e*). As with PCA the orientation difference of nuclei within the different muscle layers is evident. DNA associated peaks were detected at 726 cm^{-1} (ring breathing mode of bases), 780 cm^{-1} (ring breathing mode of bases), 1099 cm^{-1} (phosphodioxy groups PO_2^-), 1236 cm^{-1} (asymmetric phosphate stretching mode), 1331 cm^{-1} (nucleic acids), 1365 cm^{-1} (guanine), 1480 cm^{-1} (G and A ring breathing modes), 1572 cm^{-1} (G and A) and 1685 cm^{-1} (C=O).

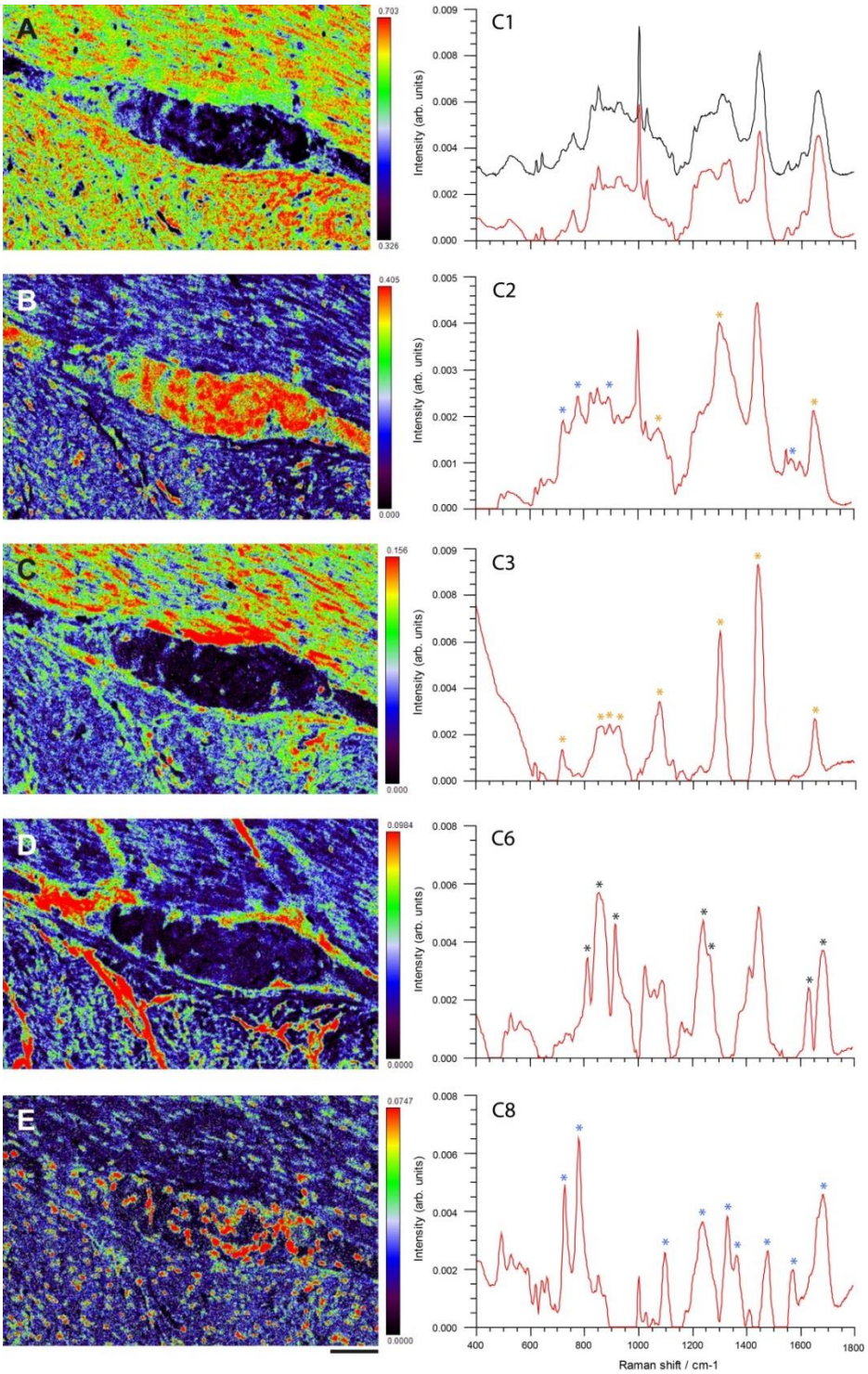

Figure 5.1.9: MCR-ALS reconstruction of Raman imaged muscularis propria transition. *A 351 by 528 pixels Raman map was acquired at a 1 µm step size. On the left are MCR-ALS empty modelled images (scale: 50 µm) and on the right are the resolved curves.* ***A)*** *Component 1 resolves the muscle tissue which is shown to be almost identical to a muscle reference spectrum shown in black.* ***B)*** *Component 2 corresponds to the myenteric plexus; nucleic acid associated peaks are marked with blue asterisks while lipid features are marked with orange asterisks.* ***C)*** *Component 3 resolves the lipid constituents of muscle tissue (lipid associated peaks marked with orange asterisk.* ***D)*** *Component 6 resolves connective tissue constituents (collagen associated peaks are marked with black asterisks).****E)*** *Component 8 resolves the nuclei of all cells (nucleic acid peaks marked with blue asterisks).*

Using the individually resolved MCR-ALS 'pure component' images a single composite image can be generated in WiRE showing biochemically dissimilar histological regions (*fig.5.10*). For visual clarity the lipid component of muscle tissue was omitted from the image. This form of Raman based digital staining is shown to produce a label-free image that contains significantly more spatial information than the conventional H&E stain. By gathering the essential biochemical information from the tissue we are able to produce images highlighting multiple histological sites that are not limited by the same challenges as those currently imposed on IHC.

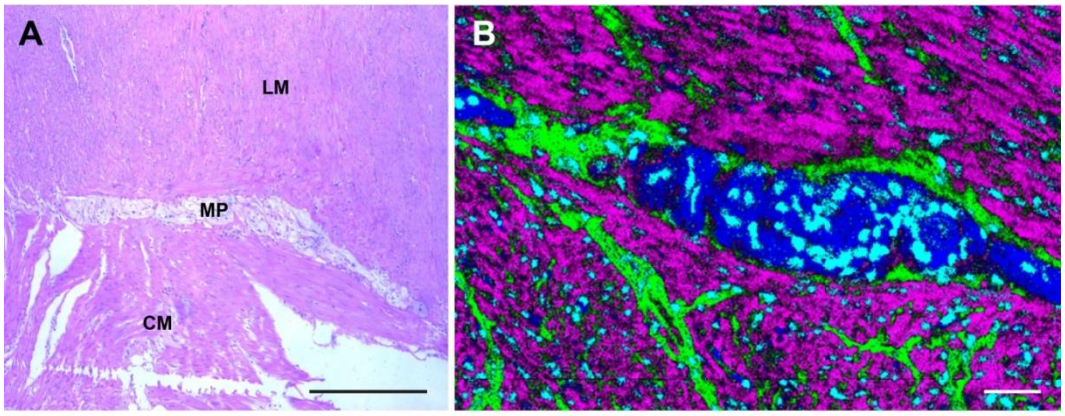

Figure 5.1.10: Demonstration of the use of Raman microspectroscopic imaging to produce label-free human colon tissue staining. A) *H&E stain of a small region of the muscularis propria with the myenteric plexus, MP: myenteric plexus, CM, circular muscle, LM: longitudinal muscle. Scale: 500 µm.* ***B)*** *MCR-ALS generated composite image produced using Renishaw's WiRE 4.2 software to highlight the different histological regions. Scale: 50 µm.*

5.3.4 Analysis of the lower mucosal region

5.3.4.1 Immunohistochemical evaluation

To identify the different histological regions of the mucosa, immunohistochemical staining was undertaken using an additional panel of antibodies. Desmin staining clearly shows the muscularis mucosa as well as the numerous blood vessels within the submucosa (*fig.5.11a*). As expected collagen III staining was evident across the lamina propria as well as the submucosa, however some staining was also present across the luminal epithelial cells with intense staining across some of the lymphocytes (*fig.5.11b*). Goblet cells were labelled with muc2 antibodies and were shown to be present across the full length of the crypt (*fig.5.11c*). Given that this is a protein marker, the mucin

itself was not stained. Differentiated epithelial cells labelled with CK20 antibodies were present across the upper third region of the crypts (*fig.5.11d*).

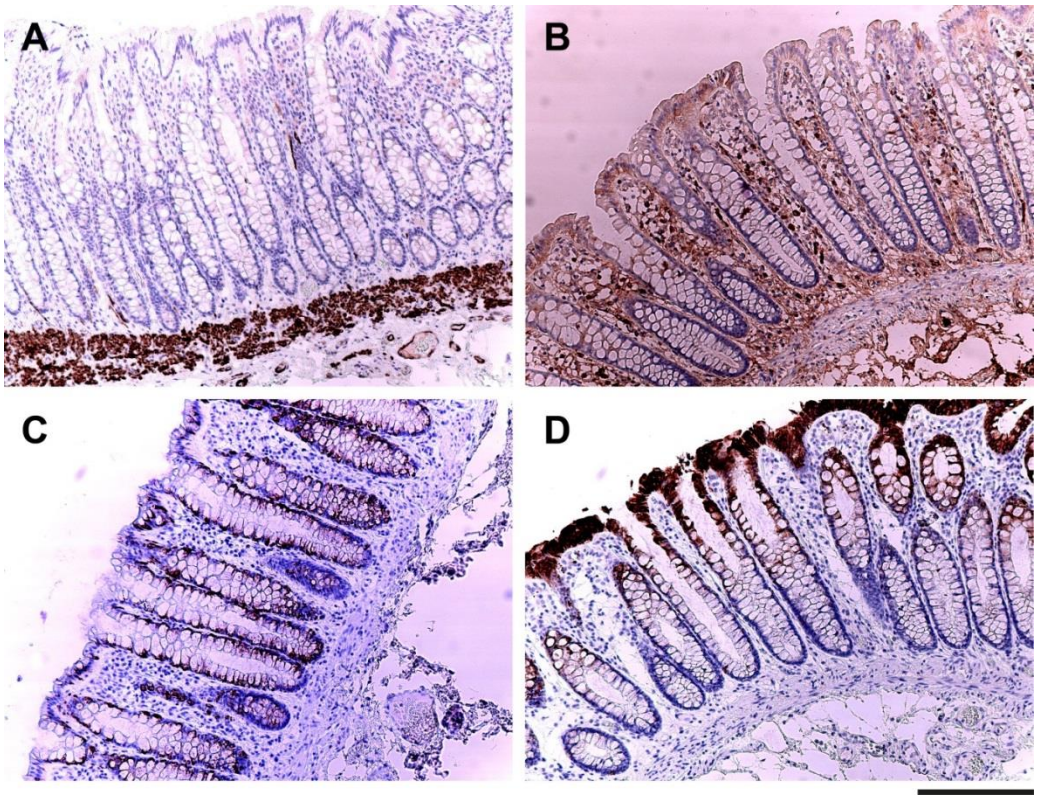

Figure 5.1.11: Immunohistochemical staining of the mucosa using a panel of different antibodies. A) *Desmin staining of the muscularis mucosa and blood vessels.* ***B)*** *Collagen III staining of the lamina propria and submucosa.* ***C)*** *Muc2 staining of goblet cells.* ***D)*** *CK20 staining of differentiated epithelial cells. (Scale: 200 µm).*

5.3.4.2 Principal Component Analysis

A map of approximately 304 by 226 µm (304 by 226 pixels) was taken across the bottom crypt region of the mucosa. The map consists of 68,704 individual spectra acquired at a 1 µm step size.

PC1

The first component corresponds to the difference between the mucinous regions (negative) and the muscularis mucosa (positive) (*fig.5.12a*). The main mucin peaks were found at 800 (ring breathing mode), 834 (mucin), 870 (mucin), 980 (glucosamine), 1140, 1377 (glucosamine and galactosamine) and 1512 (C=C) cm^{-1}. The bands associated with the muscle tissue were predominantly of protein origin

and were found at 1002, 1204, 1228, 1302, 1447 and 1667 cm^{-1} (*fig.5.13a*). The reference linear fit correctly identified the mucin component but wrongly assigned the muscularis mucosa to an average spectrum obtained from FFPE lymphocytes.

PC2

The second component appears to show the difference between a combination of the lamina propria and nuclei (negative) from the cytoplasmic component of epithelial cell and muscle cells (positive) (*fig.5.12b*). The nucleic acid components were identified through the bands at 731 (adenine), 744 (ring breathing mode of bases), 778 (ring breathing mode of bases) and 1685 (C=O) cm^{-1}. While the collagen associated bands were found at 853, 918, 1204, 1236, 1640 and 1686 cm^{-1} (*fig.5.13b*). The reference linear fit has correctly identified both the collagen and nucleic acid component, but wrongly assigns an additional mucin component.

The lipid region of the cytoplasmic component is captured by lipid peaks at 1079, 1129, 1302, 1377, 1437, 1736 cm^{-1}. The remaining peaks at 438, 639 and 833 cm^{-1} are protein associated (*fig.5.13b*). The reference linear fit correctly assigns this region to phosphatidylserine and muscle, but wrongly assigns it to the FFPE lymphocyte reference. This might be a direct result of the remaining protein associated peaks.

PC3

The difference between the nuclei of all cells and the remaining tissue are differentiated by PC3 (*fig.5.12c*). Nucleic acid associated peaks were found at 726, 778, 1327, 1361, 1484 and 1572 cm^{-1} (*fig.5.13c*). The two remaining bands at 1304 and 1440 cm^{-1} are assigned to non-specific CH vibrations. In this case the reference linear fit was incapable of identifying the correct DNA reference but instead assigned this region of the loading to lymphocytes. This is likely to be due to the presence of bands at 1304 and 1440 cm^{-1}, which were very prominent in the lymphocyte average reference (*fig.5.1b*). Spectral features of the remaining tissue components were mostly assigned to collagen at 852, 870, 918, 933, 970 and 1026 cm^{-1}. The collagen reference was correctly assigned via the linear fit.

PC7

The remaining principal component shows the difference between features only present within the lamina propria (positive) from the remaining surrounding tissue (negative) (*fig.5.12d*). The loading characterises these features as being dominated by phenylalanine or other molecules with abundant ring breathing modes (*fig.5.13d*). Although it is not possible to be absolutely sure about what these features are one can speculate that they are related to the immunological cells present in abundance within the lamina propria. The reference linear fit has assigned this unusual feature to muscle and lymphocytes, however this is likely due to the presence of the ubiquitous phenylalanine peak in all homogenous mixtures of tissue spectra.

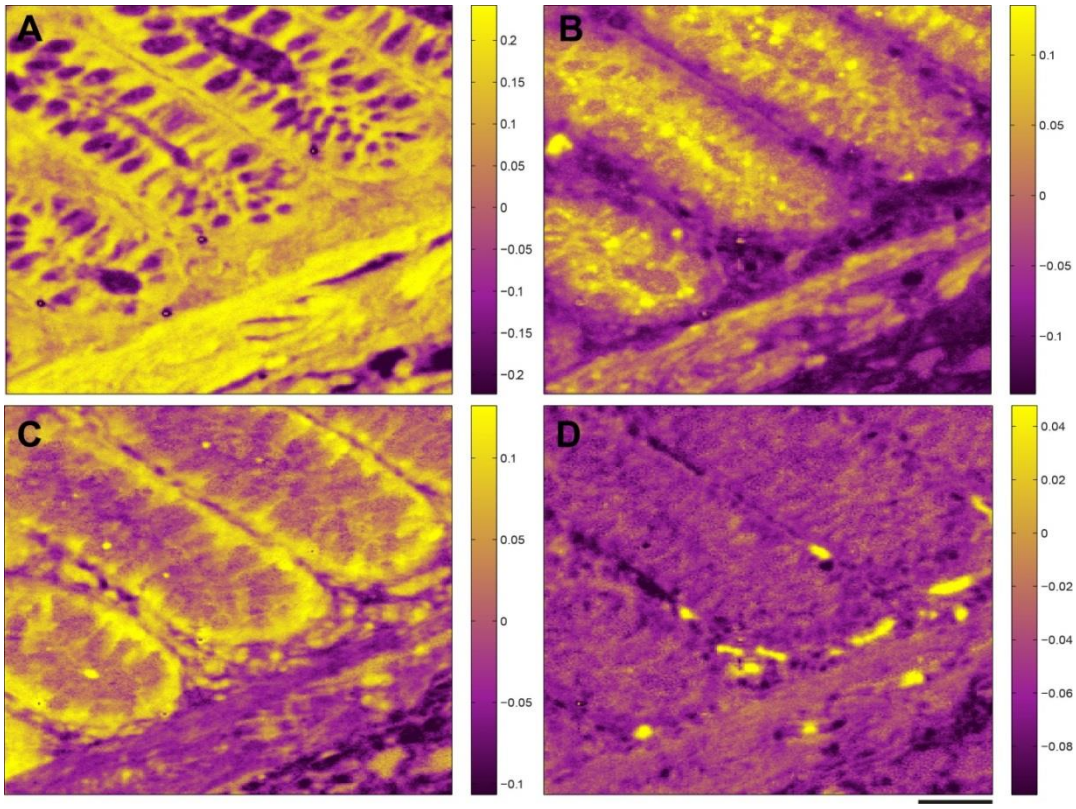

Figure 5.1.12: False-coloured PCA score images colour coded by the associated PC loadings and tentatively assigned to specific histological regions within the mucosa: A) *PC1: difference between mucinous regions of goblet cells and muscularis mucosa,* ***B)*** *PC2: difference between a combination of the lamina propria and nuclei from the cytoplasmic component of epithelial cell and muscle cells,* ***C)*** *PC3: difference between the nuclei of all cells and the remaining tissue* ***D)*** *PC7: difference between features only present within the lamina propria and the remaining tissue (scale: 50 µm). Note that the images are not heat maps and that the intensity of the purple or the yellow colours indicates the intensity of the component signals either positive or negative. These images were generated using Matlab R2013b.*

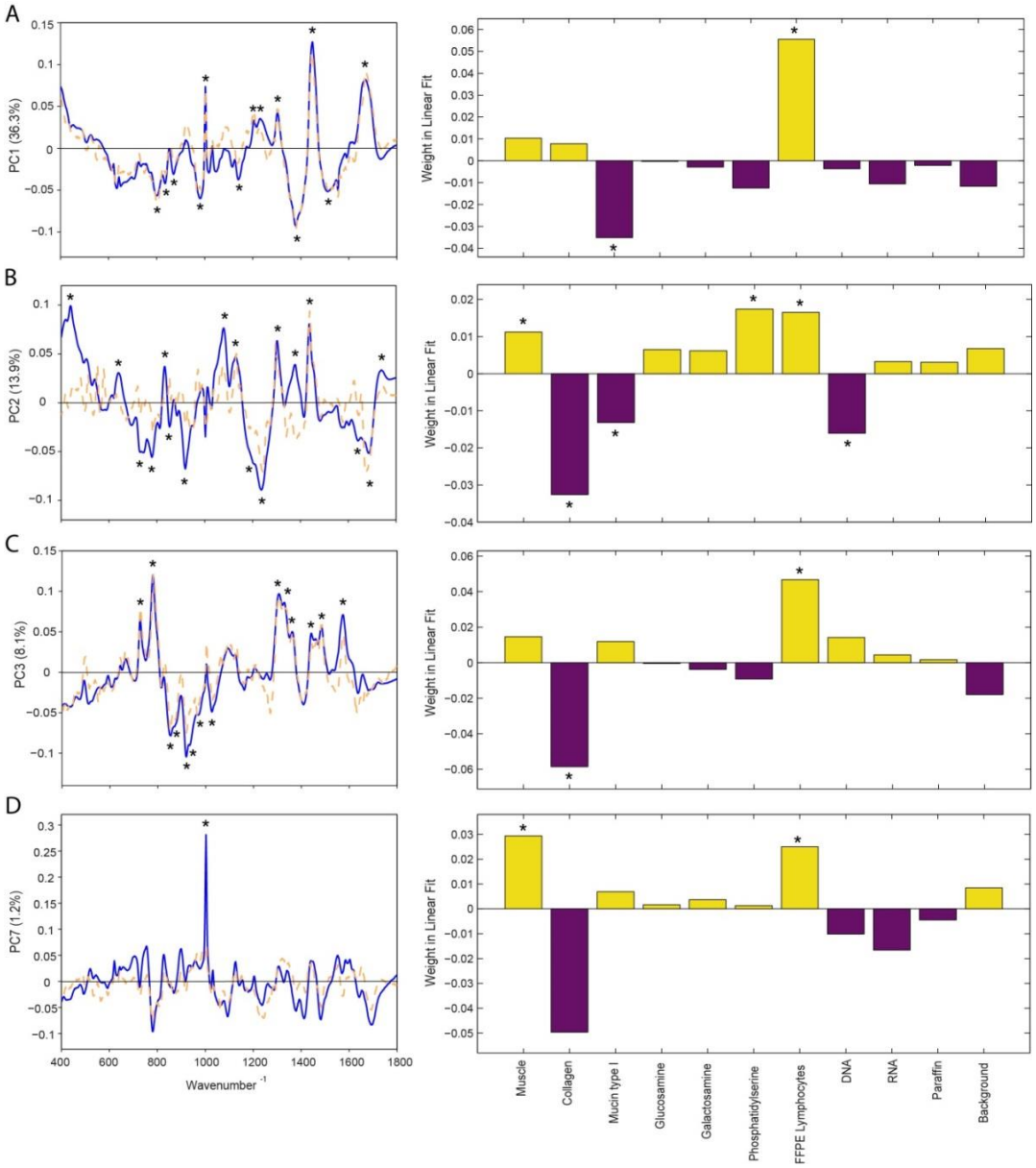

Figure 5.1.13: Loadings of principal components A) one, B) two, C) three and D) seven, each superimposed with a linear fit of the best matching molecular reference. *Note in the right hand panels that the purple and yellow colour coding of the positive or negative contribution of each reference species to the linear fit to the principle component has been preserved and is in accord with Figure 5.12.*

Once again the performance of PCA and linear fitting was similar to that of the previous muscle map and was not comparable to the histological features identified through IHC. It was further noted that the FFPE lymphocyte reference obtained directly from the tissue had a negative impact on the linear reference fitting, whereby FFPE lymphocytes were consistently matched across all the PC loadings.

5.3.4.3 Multivariate curve resolution-alternating least square analysis

The first MCR-ALS component resolved several prominent specks within the lamina propria as well as some features lining the colonic crypts. Similar lamina propria confined features were also resolved via PCA (*fig.5.12d*) and were identified as having dominating ring breathing modes likely to be assigned to proteins. The MCR-ALS resolved spectral profile is consistent with a homogenous mixture of pure components with prominent protein features at 1002, 1313, 1335 and 1663 cm^{-1} (*fig.5.14a*). Although the exact histological feature cannot be confidently assigned, it is speculated to originate from mucosal leukocytes.

The mucinous regions of goblet cells were resolved by component two (*fig.5.14b*). Four of the most intense mucin associated bands within the resolved curve were located at 832 (mucin), 978 (glucosamine), 1357 (unassigned) and 1378 (glucosamine and galactosamine) cm^{-1}. The remaining bands were found at 640 (mucin), 871 (mucin), 1010 (polysaccharides), 1042 (carbohydrates), 1116 (glucose) and 1272 (galactosamine) cm^{-1}.

The lipid and protein component of both the epithelial and muscle cells in the muscularis propria was captured by component three (*fig.5.14c*). The main lipid bands were found at 1079 (phospholipids), 1302 (phospholipids), 1444 (CH deformation) and 1667cm^{-1} (C=C). The remaining bands were that of collagen at 831, 850 and 872 cm^{-1}, as well as phenylalanine at 1002 cm^{-1}.

Component four resolved the connective tissue constituents across the submucosa, but also to some extent across the lamina propria and the muscularis propria (*fig.5.14d*). Collagen associated peaks were found at 814, 852, 877, 919, 1239 and 1262 cm^{-1}. Bands at 1415 and 1450 cm^{-1} have previously been associated with collagen regions in the previous muscle analysis. Protein bands associated with phenylalanine at 1002, 1028 as well as an amide I peak at 1675 cm^{-1} were also detected. Identical collagen related peaks were previously identified in the rat tissue analysis using PCA and cosine similarity.

The nuclei of crypt cells and some of the lymphocytes within the lamina propria were resolved by component eight (*fig.5.14e*). DNA associated bands were at 726, 780, 1095, 1235, 1329, 1369, 1481, 1572 and 1684 cm^{-1}. These bands were found to be identical to those identified in the nuclei of the muscle transition map.

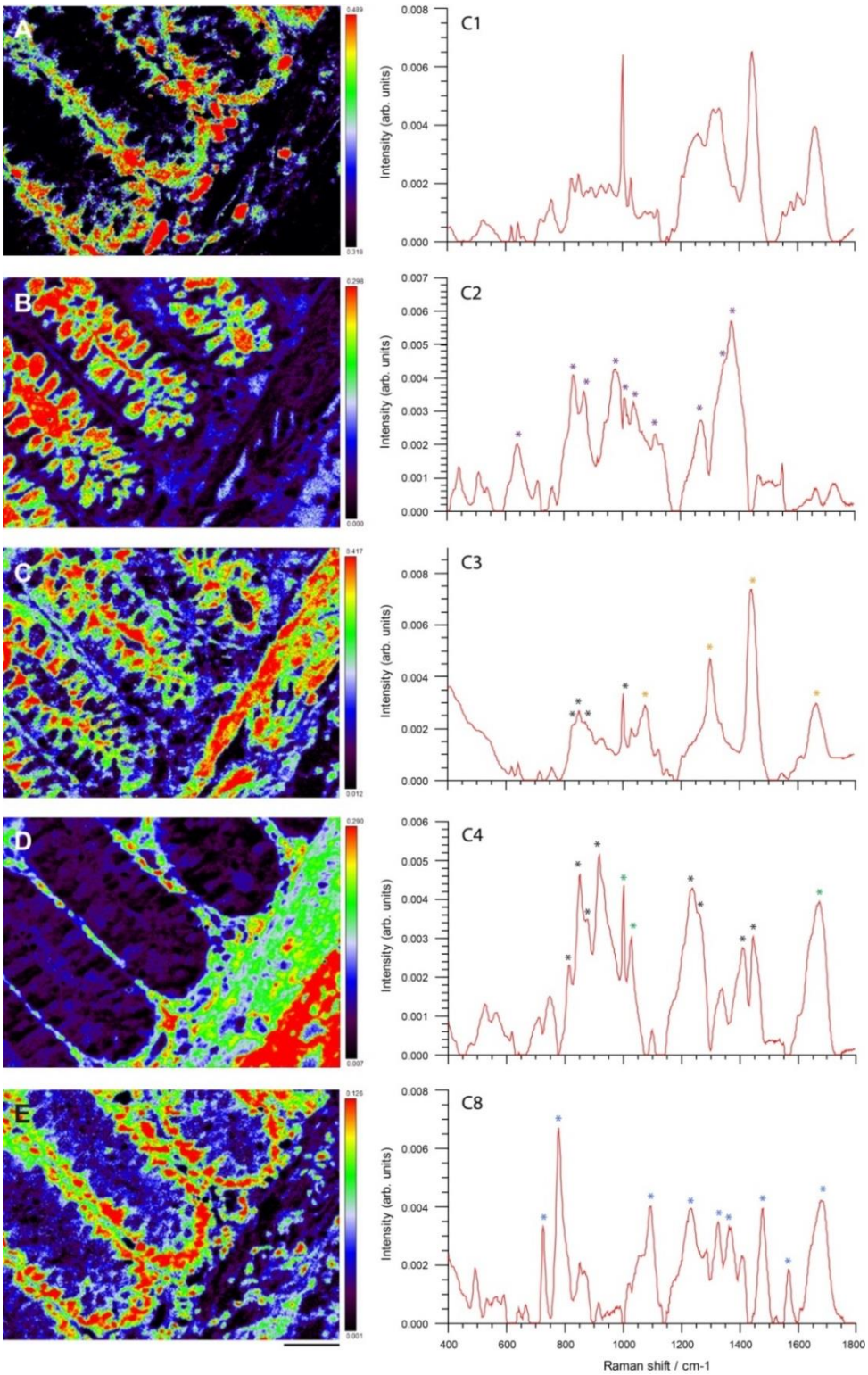

Figure 5.1.14: MCR-ALS reconstruction of Raman imaged mucosa. *A 304 by 226 pixels Raman map was acquired at a 1 µm step size. On the left are MCR-ALS empty modelled images (scale: 50 µm) and on the right are the resolved curves.* ***A)*** *Component 1 resolves a feature that has been tentatively assigned to mucosal leukocytes,* ***B)*** *Component 2 corresponds to the mucinous regions of goblet cells,* ***C)*** *Component 3 resolves the lipid and protein component of both the epithelial and muscle cells in the muscularis propria,* ***D)*** *Component 4 resolves connective tissue constituents across the submucosa, but also to some extent across the lamina propria and the muscularis propria (collagen associated peaks are marked with black asterisks).****E)*** *Component 8 resolves the nuclei of all cells (nucleic acid peaks marked with blue asterisks).*

Using the individually resolved MCR-ALS 'pure component' images a single composite image can be generated showing all the identified histological regions with superior contrast to that of H&E staining (*fig.5.15*). Unlike IHC staining multiple features can be captured within a single image.

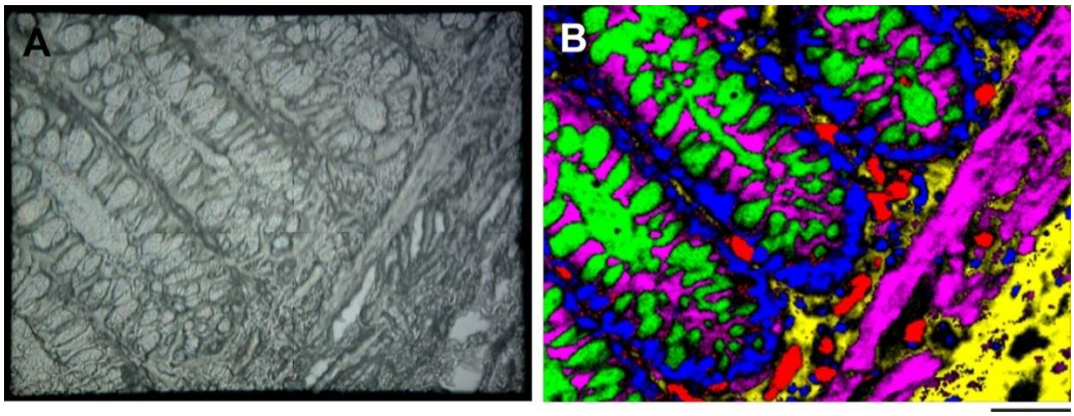

Figure 5.1.15: Demonstration of the use of Raman microspectroscopic imaging to produce label-free human colon tissue staining. A) *White light image of the base of the mucosa.* ***B)*** *MCR-ALS generated composite image produced using Renishaw's WiRE 4.2 software to highlight the different histological regions. Scale: 50 µm.*

5.4 Discussion and Conclusions

Silanized mirror steel slides have never before been used for Raman investigations on FFPE colonic tissue. In the past multiple studies that have attempted to use stainless steel slides for tissue based Raman analysis have reported tissue adhesion issues (138) as well as a high Raman background (130). This has been rectified here by opting for a silane coating to ensure adhesion as well as a super mirror finish to guarantee a Raman background that has proven to be lower than that of CaF_2 (174).

Extensive investigation of the silanized steel surface has previously demonstrated that tissues that have undergone xylene deparaffinization from a silanized surface do not retain paraffin wax. This observation has been further confirmed here via Raman maps taken from tissues at a much higher spatial resolution. This is an extremely beneficial discovery in two ways. Firstly, IHC staining is known to be hindered by incomplete paraffin removal resulting in fainter staining (164). Therefore by incorporating such cost effective silanized steel slides investigators and clinicians can ensure complete paraffin removal eliminating the

possibility of false positive or negative results. By omitting the contaminating paraffin signals it was also possible to identify with Raman the remaining lipid features within the tissue. Changes in lipid turnover are known to be crucial in cancer-associated metabolic reprogramming (175).

Raman imaging of FFPE colon tissue mounted onto silanized steel slides has shown superior contrast to that of H&E stained sections and the potential of displaying multiple histological features within a single image. There is therefore no need to cut multiple contiguous sections for histochemical staining, which may result in the presence of different features as the depth of the tissue changes with every cut. However, this has only been achieved using MCR-ALS analysis in this instance as the overall performance of PCA and linear fitting was inferior to the previously analysed rat colon tissue outlined in Chapter Four. This demonstrates the hazards surrounding reproducibility using PCA as an unsupervised multivariate data analysis technique. Using MCR-ALS it was possible to identify all the main mucosal features, however it was not possible to discriminate the crypt base stem cells, enteroendocrine cells or the leukocytes within the lamina propria. It is hypothesized that these features may be revealed by opting for confocal Raman imaging where it is possible to focus on very tightly defined sample areas resulting in spatial resolutions in the order of 0.5-1.0 μm.

As well as being able to clearly differentiate single spectra acquired from muscle, submucosa and lymphocytes, it was also possible to discriminate spectra acquired at different locations along the full length of the colonic crypt. Single spectra collected from four different locations along the length of the crypt has revealed that the crypt base possesses the strongest nucleic acid signals suggesting that this region is the most proliferative. The higher biomaterial content of mid crypt cells may indicate that the cells are rapidly manufacturing proteins and lipids as they begin to differentiate into their specialised cell forms. This is corroborated by the CK20 differentiated epithelial cell stain showing that differentiated cells begin to form from the mid crypt region (*fig.5.11d*). This is also evident from the mucosal Raman map whereby the nuclei signals appear to be most evident at the base of the crypt and begin to diminish further up the crypt (*fig.5.14e*). Seeing as the proliferative zone is known to expand in patients at high risk of developing CRCs or those with previous CRCs it would be very

beneficial to be able to track this expansion without the use of antibodies prior to H&E staining (29,176). Such label-free imaging would allow clinicians to identify and hence closely monitor high risk patients.

It is common practice within vibrational spectroscopy to acquire biological reference spectra that can later be matched to spectra found within mapped tissue components of a similar composition. This in turn can assist in the generation of the false-coloured images, where each colour can then be assigned to a specific biological component based on reference matching. These reference materials are often laboratory grade purified components, however it is uncertain how relevant these references are to tissues that are both chemically processed (FFPE then dewaxed) and not purified.

A comparison of FFPE muscle and FFPE collagen tissue was made to laboratory grade collagen and muscle acetone powder. These components were specifically selected due to their ease of identification in the white light image of the unstained tissue section for tissue reference acquisition. Tissue collagen and laboratory grade collagen were found to have an almost identical spectral profile, whereas muscle exhibited some minor difference. Furthermore, muscle acetone powder was found to contain two distinct spectral features: one attributed to muscle and one to collagen. This indicates that the stromal components of muscle tissue were not separated. These findings suggest that caution should be exercised when using laboratory grade biological references when trying to identify the different spectral signatures within tissues. The minor spectral difference detected in muscle may be attributed to the difference in muscle preparation/purification (proprietary information) or the type of muscle used e.g. smooth vs skeletal.

As with the previously analysed rat tissue, mucin was also easily detected and unlike the muc2 antibody stain that only marks the goblet cells the biochemical signals portraying the characteristic composition of mucin itself were discerned. This is of clinical interest as the terminal sugar sequence of mucin has been known to be altered in colorectal cancer. Most cancers have also been shown to express up-regulated MUC1 glycoproteins carrying ‘cancer-associated’ carbohydrate structures such as Lewis^{y} and Lewis^{x} antigens (12). Identification of the type of mucin secreted by the cancer may assist in the classification of the cancer type and hence selection of the best possible treatment.

In summary, this exploratory study has demonstrated the superiority of silanized super mirror steel slides over CaF_2 and its suitability for Raman based studies undertaken on FFPE tissue sections. It has also been confirmed that these Raman images are free from paraffin contamination facilitating the identification of the remaining lipid components. Additionally it was possible to demonstrate the capability of Raman in identifying nucleic acid signals that can be used to track the expansion of the proliferative zone within crypts that has been postulated to be a predictive factor in the risk of developing CRC.

Chapter Six

A preliminary study in the diagnostic potential of Raman spectroscopy for Lynch Syndrome

6.1 Introduction and Aims

The use of Raman spectroscopy for discrimination of the different initiation pathways in colorectal cancer has never before been attempted. To assess whether Raman spectroscopy can potentially be used to discriminate chromosomal instability in sporadic tumours that are MSI-L from microsatellite unstable or MSI-H tumours, a first of its kind proof-of-principle study was conducted.

Tumours that arise as a result of microsatellite instability such as those in LS, are a direct result of a defective DNA mismatch repair pathway, responsible for housekeeping process that maintain chromosomal stability by correcting environmental or replication driven mutations. These tumours arise from mutations in MMR proteins and are hence well characterised. Unlike MSI-H tumours, CIN tumours are not as well defined and may arise from mutations in over 100 candidate genes. One of the distinguishing features of CIN tumours is numeric aberrations in chromosomes, referred to as aneuploidy. MSI-H tumours on the other hand are chromosomally stable with a near-diploid DNA content. In the previous chapters, Raman's exceptional ability in identifying cell nuclear content has been demonstrated. It is therefore anticipated that Raman microspectroscopy may potentially be able to distinguish CIN from MSI tumours based on the DNA ploidy level.

Aside from a lack of chromosomal aberration, MSI-H tumours are also known to have very distinct clinicopathological features that vary from tumours arising from chromosomal instability that are MSI-L. MSI-H tumours exhibit a high lymphocytes infiltrate, large mucinous pools and are often poorly differentiated. Although they progress through the adenoma to carcinoma sequence much faster, patients with MSI-H tumours have a much better prognosis compared to CIN type tumours that take 8-10 years to develop. The metabolic changes that drive the different pathological features that arise as a result of the two CRC pathways may therefore be potentially discerned through Raman spectroscopy.

Due to the very rare nature of Lynch Syndrome (3% of all CRCs) and the concurrent commencement of a large scale LS clinical trial, it was not possible to acquire a large enough sample size from biobank archives; consequently only

ten samples of each pathology class including 10 normal samples were used in this study. It was therefore not possible to conduct this study on cases of the same tumour stage; however MSI and CIN cases were matched by tumour stage (ranging from T2 to T4). As a result, the main purpose of this preliminary study was to try and identify the gross metabolic differences between the two tumour pathways irrespective of the tumour stage, specific MMR mutation or MSI resulting from promoter hypermethylation. The aim was then to try and build a classification model for the discrimination of MSI-H tumours from CIN tumours, and make an overall judgement on the feasibility of using Raman-based classification in the diagnosis of at least one very difficult test case.

To summarise, this chapter aims to:

1. Identify some of the potential spectral features that facilitate discrimination of CIN sporadic adenocarcinoma from LS MSI-H adenocarcinomas.
2. Build a linear discriminant analysis (LDA) classification model for the discrimination of LS MSI-H and test its performance using a leave-one-map-out cross-validation (LOMO) procedure.

6.2 Materials and Methods

6.2.1 Tissue acquisition and preparation

FFPE human colon samples were obtained from the UCL/UCLH Biobank for Studying Health and Disease (REC 15/YH/0311). A total of 10 normal formalin fixed paraffin embedded (FFPE) resection blocks were obtained along with matching adenocarcinoma samples from the same patients. The 10 archival LS blocks were matched to the sporadic adenocarcinoma samples by cancer stage (T stage). The histopathology of all samples was confirmed by a resident consultant pathologist Dr Manuel Rodriguez-Justo. Staging was conducted using the TNM system. A full breakdown of the patient samples and cancer stages can be found in *Appendix 12*.

One section was cut at 8 μm thickness and mounted onto silanized super mirror stainless steel slides for Raman analysis and one 3 μm section was cut and mounted

onto standard glass slides for H&E staining. Slides destined for Raman analysis were incubated overnight at 37°C and deparaffinized using the manual deparaffinization protocol outlined in Chapter Three. Tissues were then analysed without further pre-treatment and kept refrigerated in between measurements. H&E destined slides were subjected to automated staining and coverslipping.

6.2.2 Raman spectroscopic measurements

Point spectra were acquired using the Renishaw RA802 bench top prototype system (Renishaw plc, Wotton-under-edge, UK) coupled to a 785 nm laser excitation source. A total laser intensity of approximately 158 mW was focused onto the sample through a 50×/NA 0.8 objective. A 1500 l/mm grating was used to disperse the light providing a spectral range of 0 to 2100 cm^{-1} in the low wavenumber range. An integration time of 20 seconds was used for all measurements resulting in S/N ratios between 50 and 100. A total of 50 individual spectra were collected from each tissue sample, these were then collated into a map per tissue using the Renishaw Create Map from Singles tool. All spectra were acquired from the glandular mucosal region only in normal samples and from confirmed cancerous regions in all cancer samples; these were located by the resident pathologist prior to Raman measurement.

All systems checks conducted prior to measurement have already been detailed in section 2.4.2.2 of Chapter Two.

6.2.3 Spectral pre-processing

Cosmic ray removal was conducted using the width of feature and nearest neighbour methods in WiRE 4 software. All spectra used for the calculation of the average spectra, difference spectra and initial PCA analysis underwent baseline correction to a third order polynomial and vector normalisation in MATLAB R2013b (MathWorks, Natick, MA, USA). All spectra destined for PCA analysis were further mean centred to ensure that the PCs form an orthogonal basis.

Conversely all spectra used within the initial optimization steps of the LDA classification model underwent Extended Multiplicative Scatter Correction (EMSC). Objective subtraction was also used as part of the optimization step during the initial LDA model phase. This ensures that the broad objective glass

features contributing to each spectrum are removed. Spectra input into the LDA underwent further truncation to 460 – 1740 cm^{-1} to remove the edge effects of pre-processing.

6.2.4 Statistical analysis

The difference spectrum was computed by subtracting a mean spectrum of the whole adenocarcinoma dataset from the mean spectrum of the whole LS dataset. Peak comparisons were then made.

LDA was conducted by first performing PCA to reduce the dimensionality of the dataset while retaining the most diagnostically significant information for the classification. The resultant PC scores comprise a reduced number of orthogonal variables that account for most of the variance in the original spectra. ANOVA was then used to determine the most diagnostically significant PCs, which were then used to perform LDA. All PCs with an F-value below the critical F-statistic were excluded as inputs for the classifier. LDA was used to determine the discriminant function that maximises the variance between the pathological groups while minimising the variance between members of the same group.

The performance of the diagnostic algorithm was estimated using the leave-one-map-out cross-validation (LOMO) method whereby a whole sample map was withheld from the dataset. This allowed the remaining spectra to be used to train the classifier while the withheld map was used for classification. This was repeated until all the withheld spectra were classified.

To compare the performance of tissue classification using the Raman datasets, receiver operator characteristic (ROC) curves were generated using the Renishaw Data Classification Tool. These curves are generated by successively changing the thresholds to determine the correct and incorrect classification for all tissue samples.

The whole LDA procedure was conducted using the novel Renishaw Data Classification Tool version 2.10.

6.3 Results

6.3.1 Average and difference spectra

Spectra acquired from samples belonging to each pathological group were collated together and an average spectrum calculated. The baseline corrected and vector normalised average spectra from each group is shown in figure 6.1a. From this plot it is clear that the spectral difference between normal and cancerous are the most obvious, while the difference observed between CIN tumours and MSI Lynch tumours are very subtle. Closer inspection of the spectra reveals miniscule differences between the two pathologies and this is further enhanced by calculating the difference spectrum of the two pathologies. Figure 6.1b shows the resulting difference spectrum obtained when subtracting the mean normalised CIN tumour spectrum from the mean normalised MSI LS spectrum. The peaks in the difference plot greater than zero correspond to tissue constituents in excess in that pathology group, whereas those with a negative relative intensity correspond to a lower concentration of that constituent relative to that found in the spectrum of the subtracted pathology.

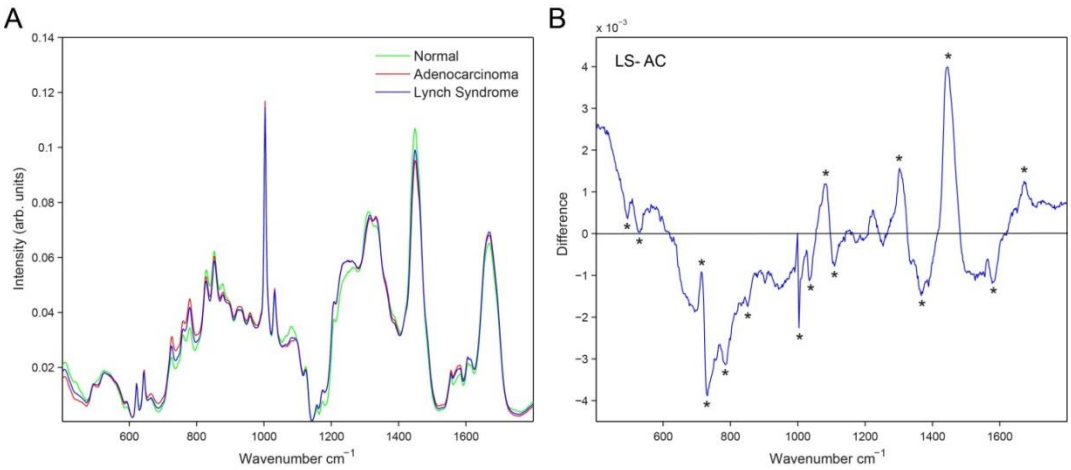

Figure 6.1.1: Spectral comparison of normal, CIN tumours and Lynch Syndrome MSI tumours. ***A)*** *Mean vector normalised and baseline corrected Raman spectra from each pathological group.* ***B)*** *Difference spectrum of mean normalised and baseline corrected Raman spectrum of CIN adenocarcinoma subtracted from the mean normalised and baseline corrected LS MSI spectrum. Spectral features that were distinct from each pathology group are marked by asterisks.*

The difference spectrum indicates that spectra collected from an LS MSI-H pathology display elevated intensities of peaks at 714, 1081, 1302, 1445 and 1672 cm^{-1} (*fig.6.1b*). The former four peaks have been tentatively assigned to

lipids while the later peak at 1672 cm^{-1} has been tentatively assigned to cholesterol. The average LS MSI-H spectrum was also shown to have reduced levels of constituents present at 494 cm^{-1} (glycogen, nucleic acids), 529 cm^{-1} (amino acids), 732 (phosphatidylserine, adenine) and 787cm^{-1} (nucleic acids), 852 cm^{-1} (ring-breathing mode of proline, hydroxyproline, tyrosine), 1003 and 1034 cm^{-1} (phenylalanine, polysaccharides), 1110 cm^{-1} (lipids, proteins), 1366 cm^{-1} (tryptophan, lipids, guanine) and 1583 cm^{-1} (C=C bending mode of phenylalanine). Overall, there seems to be a reduction in the levels of nucleic acids and amino acids.

6.3.2 Principal Component Analysis

Unsupervised principal component analysis was used in an attempt to group the two pathological classes and normal mucosa based on their spectral variation (normal vs LS MSI-H tumours vs CIN tumours). The weights of the first five principal components plotted against the first component is shown in figure 6.2. From this it can be seen that without any manipulation normal tissue can be easily discriminated from cancer as a whole regardless of its initiation pathway (*fig.6.2*).

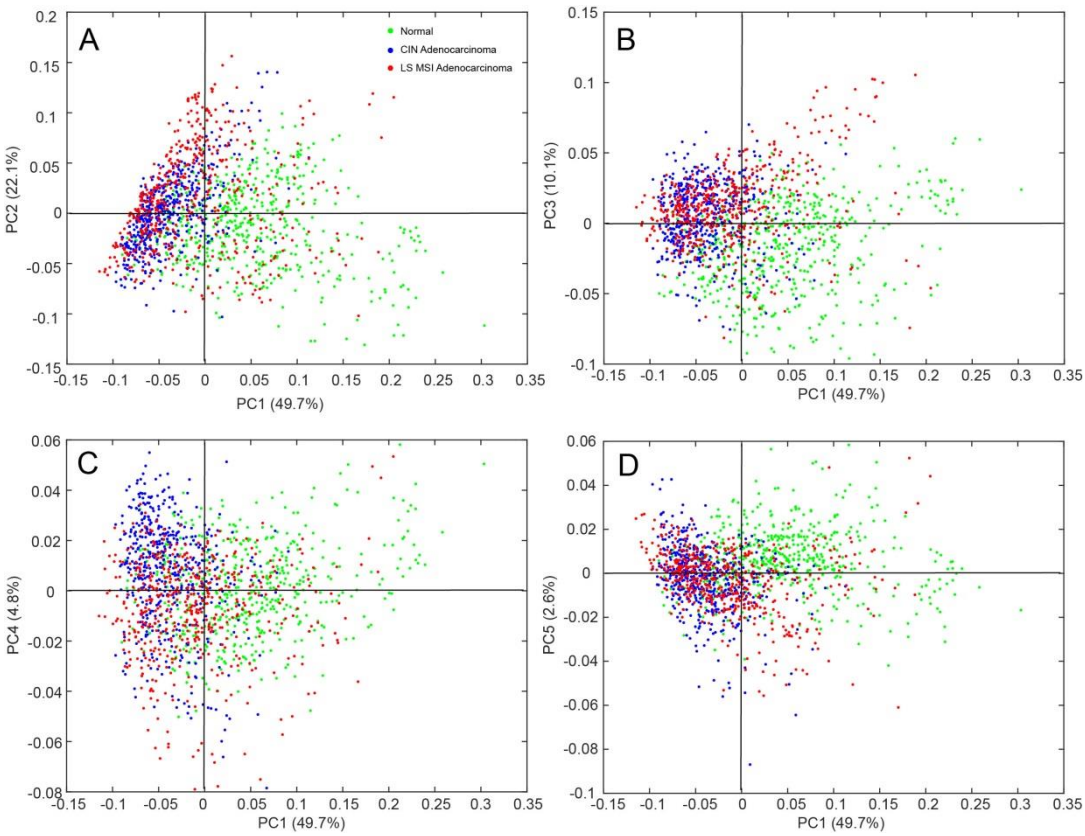

Figure 6.1.2: 2D scatter plot of principal component weights from PC1 vs PC2-5. *The scatter plot demonstrates that normal tissue can be easily discriminated from cancer as a whole (combination of LS and sporadic CRC); however LS cannot be distinguished from sporadic adenocarcinoma due to cluster overlap. The percentage variance explained by each PC is shown in brackets.*

Seeing as the CIN tumour data points cannot be clearly seen to cluster separately from LS MSI-H data points, 1D PCA scatter plots were plotted in figure 6.3, this facilitates a clearer visualisation of cluster separation across each PC. Both tumour types are seen to be negatively characterised by PC1, while normal mucosa is positively characterised (*fig.6.3a*). Some separation of CIN MSI-L tumours and LS MSI-H tumours can be seen across the 1D PC4 plot, albeit not very clearly (*fig.6.3d*). The remaining PCs do not yield a subspace where the three groups separate well (*fig.6.3b-c*).

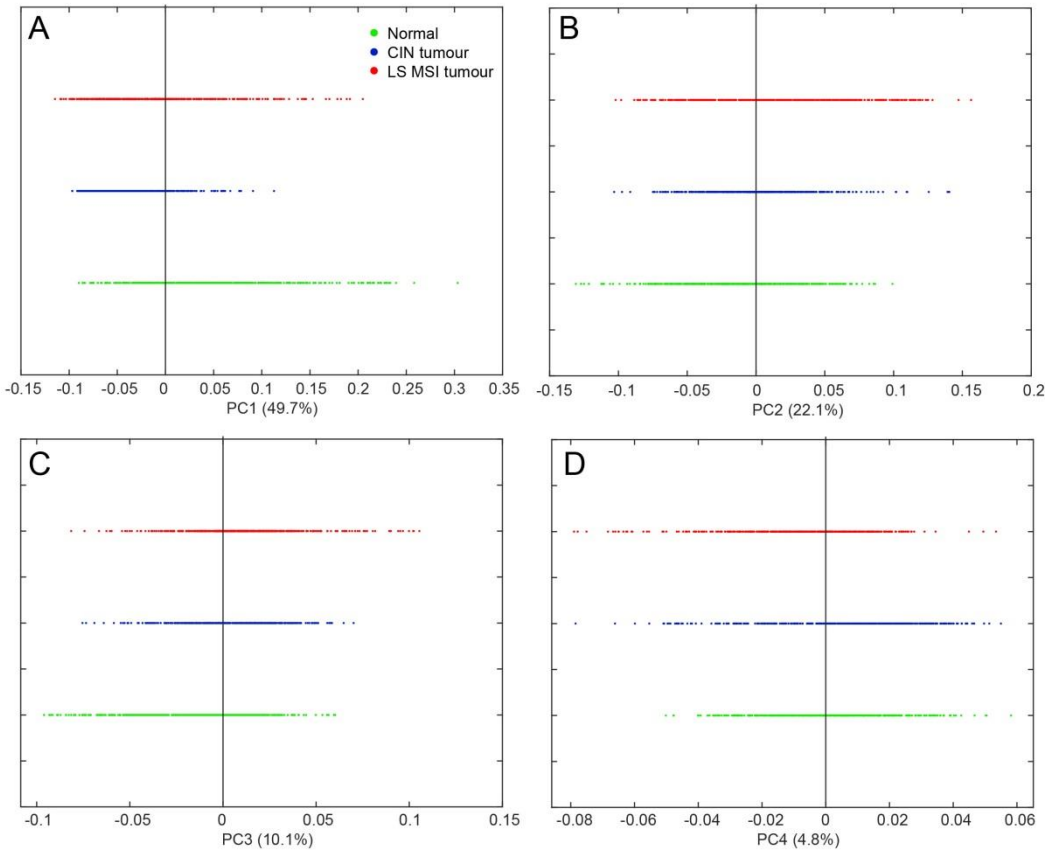

Figure 6.1.3: 1D linear scatter plots of principal component weights from PC1 through to PC4. *Clear separation across normal and both tumour types can be seen across PC1, no separation is observed across the remaining PCs. CIN tumours are not seen to be discriminated from LS MSI tumours. The percentage variance explained by each PC is shown in brackets.*

An attempt was made to try and improve the cluster separation of each tumour group by excluding the normal mucosa group from PCA analysis. Two dimensional scatter plots of the first component plotted against the first five components is displayed in figure 6.4, as well as their subsequent one dimensional plots in figure 6.5. As observed previously with three groups, PCA analysis does not yield a subspace where the two tumour subtypes separate any better (*fig.6.4-5*).

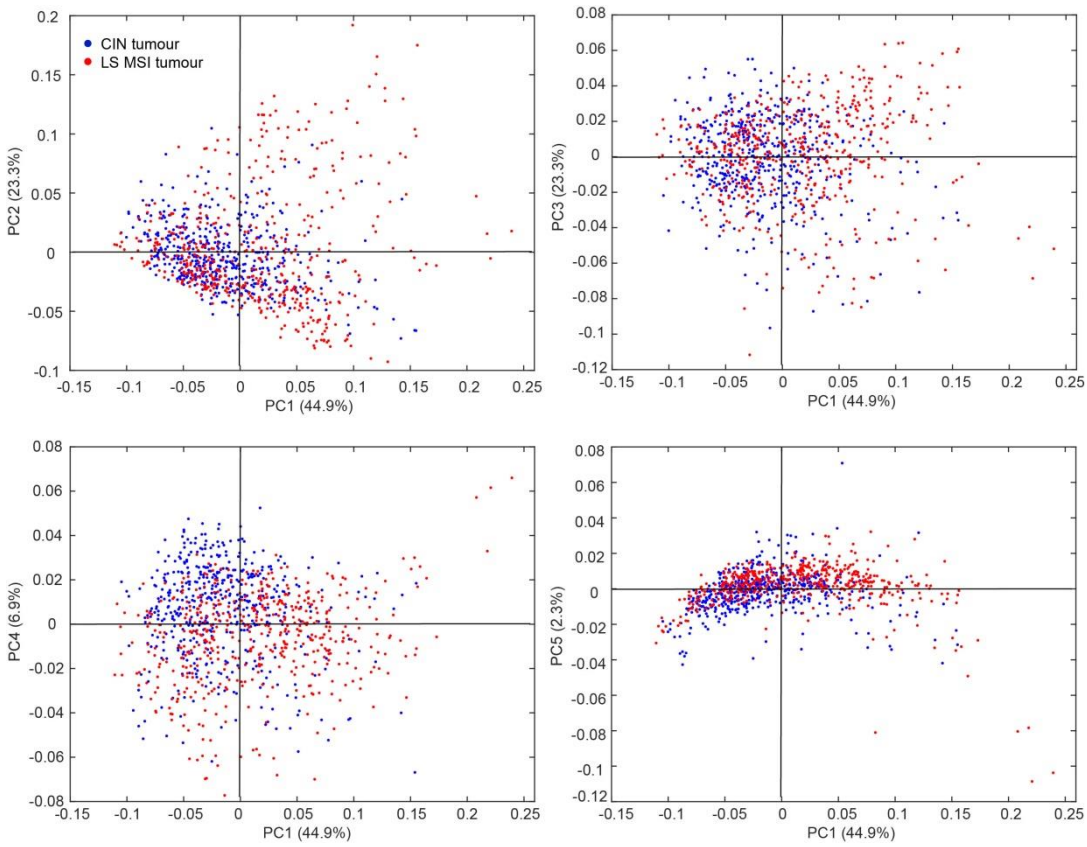

Figure 6.1.4: 2D scatter plot of principal component weights of PC1 vs PC2-5 for two tumour groups. *The scatter plots demonstrate that by excluding the normal group from PCA analysis segregation of CIN tumours from LS MSI tumours is not improved. The percentage variance explained by each PC is shown in brackets.*

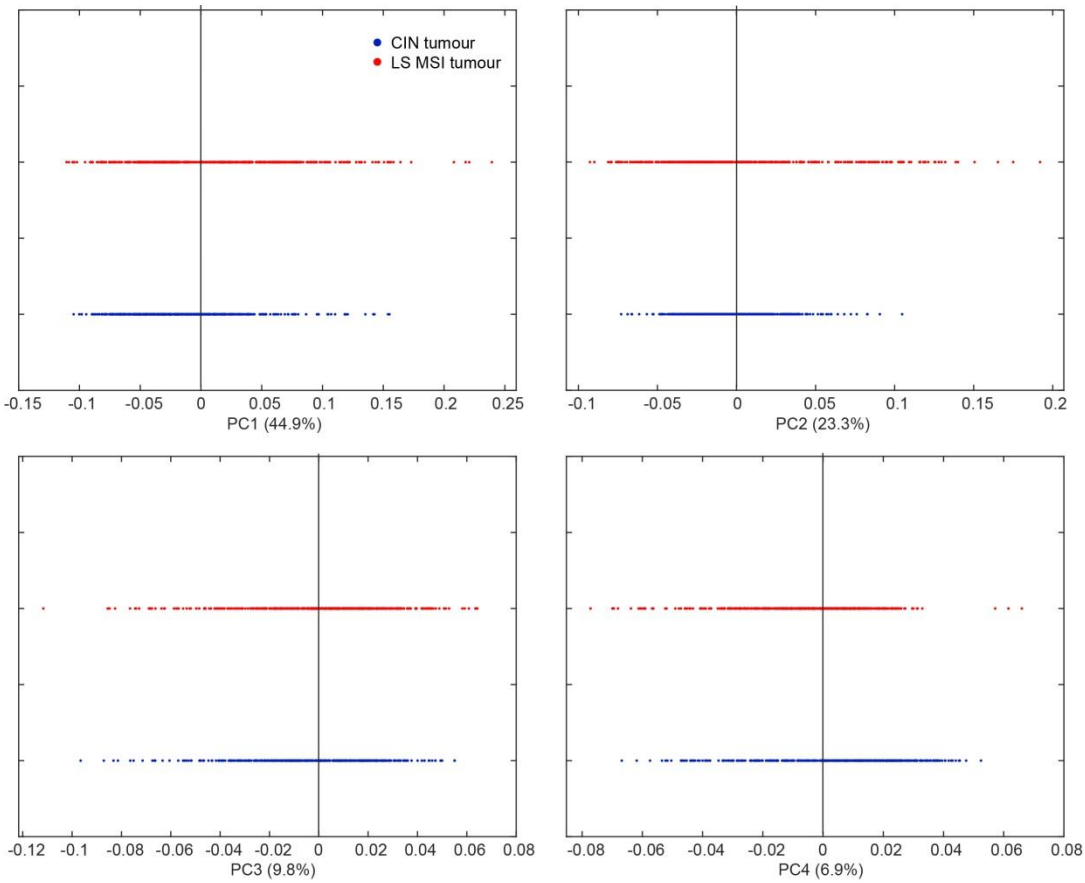

Figure 6.1.5: 1D linear scatter plots of principal component weights from PC1 through to PC4 of two tumour subtypes. *Removal of the normal group does not yield an improvement in the separation of the two tumour subtypes. The percentage variance explained by each PC is shown in brackets.*

The associated PC loadings facilitate a qualitative biochemical analysis of the features that are responsible for the group discrimination. In PC1 normal tissue is predominantly characterised by peaks at 840 (glucose-saccharide), 873 (polysaccharides), 1081 (lipids/carbohydrates), 1301 (lipids) and 1441 (CH deformation) cm^{-1}. Cancerous tissue is characterised by peaks at 727 (nucleic acids), 780 (nucleic acids), 1003 (ring breathing mode) and 1570 (G/A) cm^{-1} (*fig.6.3a*). This means that one of the principal differences between normal tissue and cancer lies in the elevated lipid and carbohydrate content of normal tissue and increased nucleic acid content of cancer tissue.

There was some marginal separation observed between CIN tumours and LS MSI-H tumours across PC4 during all group PCA analysis. Sporadic CIN tumours were positively characterised by PC4, whilst LS MSI-H tumours were negatively characterised by PC4.

LS MSI-H tumours are negatively characterised by PC4 and are dominated by peaks at 1003 (C-C aromatic ring stretching in proteins), 1259 (amide III, adenine, cytosine, lipids), 1343 (CH deformation of proteins and lipids), 1450 (CH deformation), 1605 (phenylalanine, tyrosine) and 1672 cm-1(amide I, ceramide, cholesterol).

CIN tumours are positively characterised by PC4 and are dominated by peaks at 442 (N-C-S stretch), 491 (nucleic acids, glycogen), 727 (nucleic acids), 780 (nucleic acids), 870 (hydroxyproline, tryptophan, polysaccharides), 990 (unknown) and 1097 cm^{-1} (PO_2^- in nucleic acids) (*fig.6.6b*).

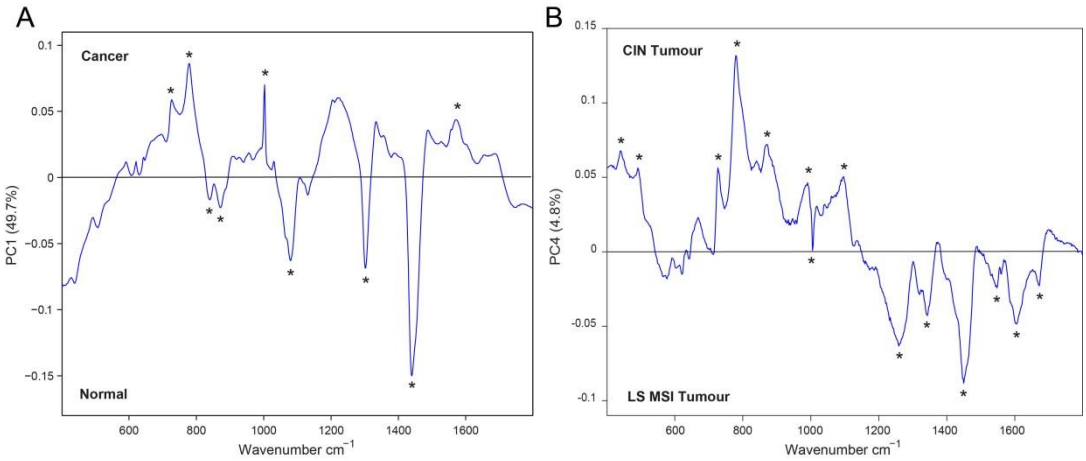

Figure 6.1.6: Principal component loadings of PC1 and PC4 used to pinpoint the biochemical variance that allows cluster separation. A) *PC1 is positively characterised by cancer tissue and negatively characterised by normal tissue.* ***B)*** *PC4 is positively characterised by CIN tumours and negatively characterised by LS MSI tumours.*

6.3.3 Linear Discriminant Model

Principal component analysis was initially performed to reduce the dimensionality of the data into a specified number of orthogonal variables. A significance threshold of 95% was selected given the small sample size. ANOVA was then used to ascertain the most diagnostically significant PCs to be used as inputs into the LDA. Prior to performing the LDA analysis some optimization was first carried out. The performance of the LDA was evaluated by comparison of the sensitivity and specificity values obtained for LS MSI-H classification only.

The effect of spectral pre-processing on the performance of the classifier was investigated. An initial run of the classifier involved normalisation using EMSC, baseline correction using a third order polynomial and subtraction of the objective lens. Without the subtraction of the objective lens there was a negligible difference to the performance. The effect of the polynomial order used in the baseline correction is shown in figure 6.7. Exclusion of baseline correction alone and in combination with objective subtraction resulted in the best specificities of 89.5%. However, baseline correction to a first and second order polynomial produced slightly higher sensitivities of 66.6%, this was only 3.6% higher compared to no baseline correction or objective subtraction. It is therefore likely that the baseline correction procedure results in some sort of spectral distortion that is affecting the classifier performance (126).

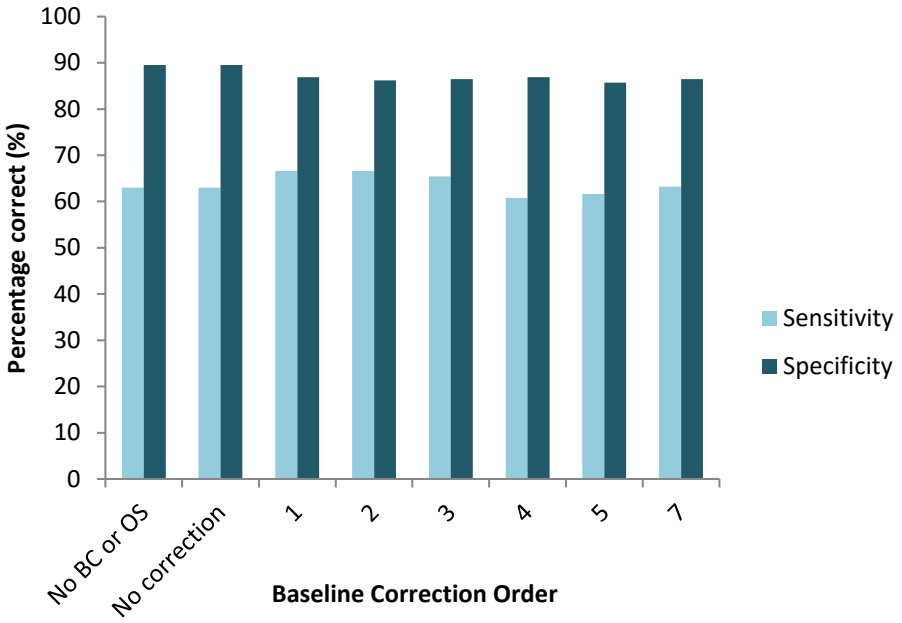

Figure 6.1.7: Bar plot illustrating the impact of baseline correction polynomial order and objective subtraction on the performance of the classifier for the identification of Lynch Syndrome. *No baseline correction alone and in combination with the exclusion of objective subtraction results in the highest achievable specificities of 89.5%, while baseline correction to a first and second order polynomial produces the highest sensitivities of 66.6%. Baseline correction (BC), Objective Subtraction OS. The classification of Lynch Syndrome consisting of 500 spectra from 10 resections only was evaluated.*

The effect of varying the number of PCs input into the model was assessed based on the changes in the sensitivity and specificity values (*fig.6.8*). Introducing fewer PCs into the LDA was shown to reduce the prediction achieved. An input of only 10 PCs destroys the performance of the classifier, resulting in a substantial drop in LS MSI-H detection sensitivity to 43%. Increasing the number of input PCs to 15 all the way through to 30 increases the sensitivity from 63% to 64%. This suggests that the performance of the classifier remains fairly constant at around 25 input PCs. The number of input PCs also had an effect on the specificity, which fell from 89% with 30 PCs to 82% with 10 PCs. This implies that the excluded PCs are vital in the separation of the pathology groups.

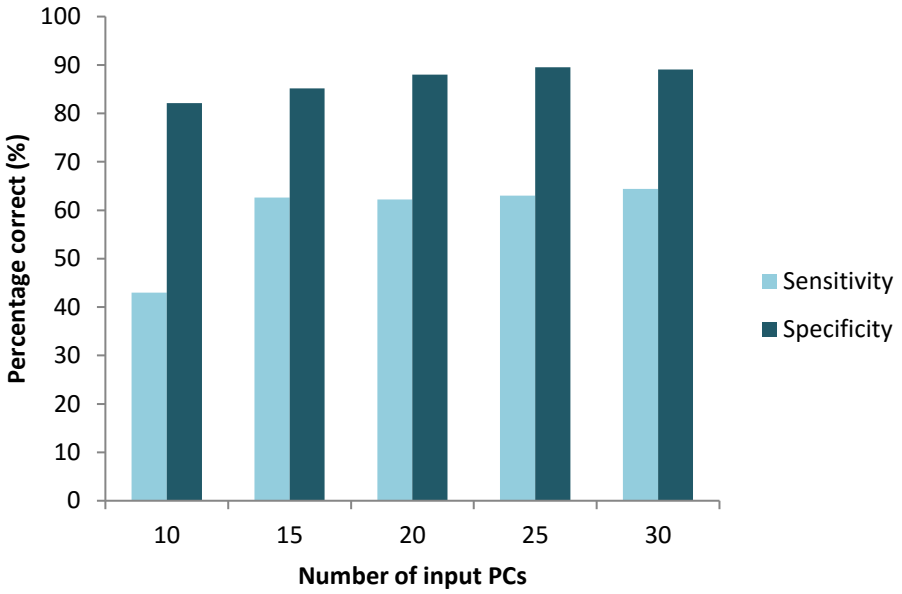

Figure 6.1.8: Spectral prediction achieved by the PCA-LDA model developed with variable numbers of input PCs. *The classification of Lynch Syndrome consisting of 500 spectra from 10 resections only was evaluated. There was no further improvement in the performance of the classifier after 25 PCs.*

For the final classification, EMSC was used for normalisation with no baseline correction or objective subtraction. The spectra were further truncated to remove the edge effects of spectral pre-processing; as a result the total wavenumber range used was 460 – 1740 cm^{-1}. The first 25 PCs (describing

approximately 99.1% of the total variance) were selected to build the LDA classifier at a 95% significance level. ANOVA was used to identify the most diagnostically significant PCs. The critical F-statistic was calculated and found to be 3.0018, PCs with F-values above 3.0018 (PCs 1-23 with the exclusion of PC 22) were used to perform LDA. PC22 was excluded as the F-value was below 3.0018 suggesting that this component is not diagnostically useful. Table 6.1 lists each PC with the corresponding cumulative percentage variance described, as well as the calculated F-statistic. The PC loadings of the first 20 plots can be found in figure 6.9, along with major peak assignments; these components describe over 99.1% of the total variance in the dataset. PC loadings 1 through to 10 appear to show the greatest spectral variation with multiple biological peaks characteristic of nucleic acids (727, 780, 1097, 1573 cm^{-1}), lipids (1079, 1301, 1330 cm^{-1}) and proteins (1002, 1030, 1236, 1668 cm^{-1}). PC loadings 11 through to 20, albeit much noisier still exhibit a substantial amount of spectral information which are likely to be the contributors towards the improvement in the classifier performance observed in figure 6.8.

Table 6.1.1: Results of ANOVA testing of the first 25 PCs used to identify the most diagnostically significant PCs. *The critical F-statistic was found to be 3.0018, hence all PCs with an F-value above 3.0018 were used for the LDA.*

Principal Component	Cumulative % Variance	Value of F-statistic
1	72.75	**52.6162**
2	84.33	**99.0323**
3	92.55	**198.9863**
4	95.65	**94.7241**
5	96.57	**25.2255**
6	97.26	**98.5544**
7	97.74	**30.3629**
8	98.07	**33.0229**
9	98.31	**6.6954**
10	98.49	**11.4737**
11	98.61	**70.5215**
12	98.72	**40.1042**
13	98.81	**91.3909**
14	98.87	**8.5172**
15	98.92	**109.0102**
16	98.97	**24.7369**
17	99.00	**16.8095**
18	99.03	**5.0549**
19	99.05	**6.5763**
20	99.07	**19.5471**
21	99.09	**4.8648**
22	99.11	2.4407
23	99.12	**7.4502**
24	99.13	1.0867
25	99.14	0.6459

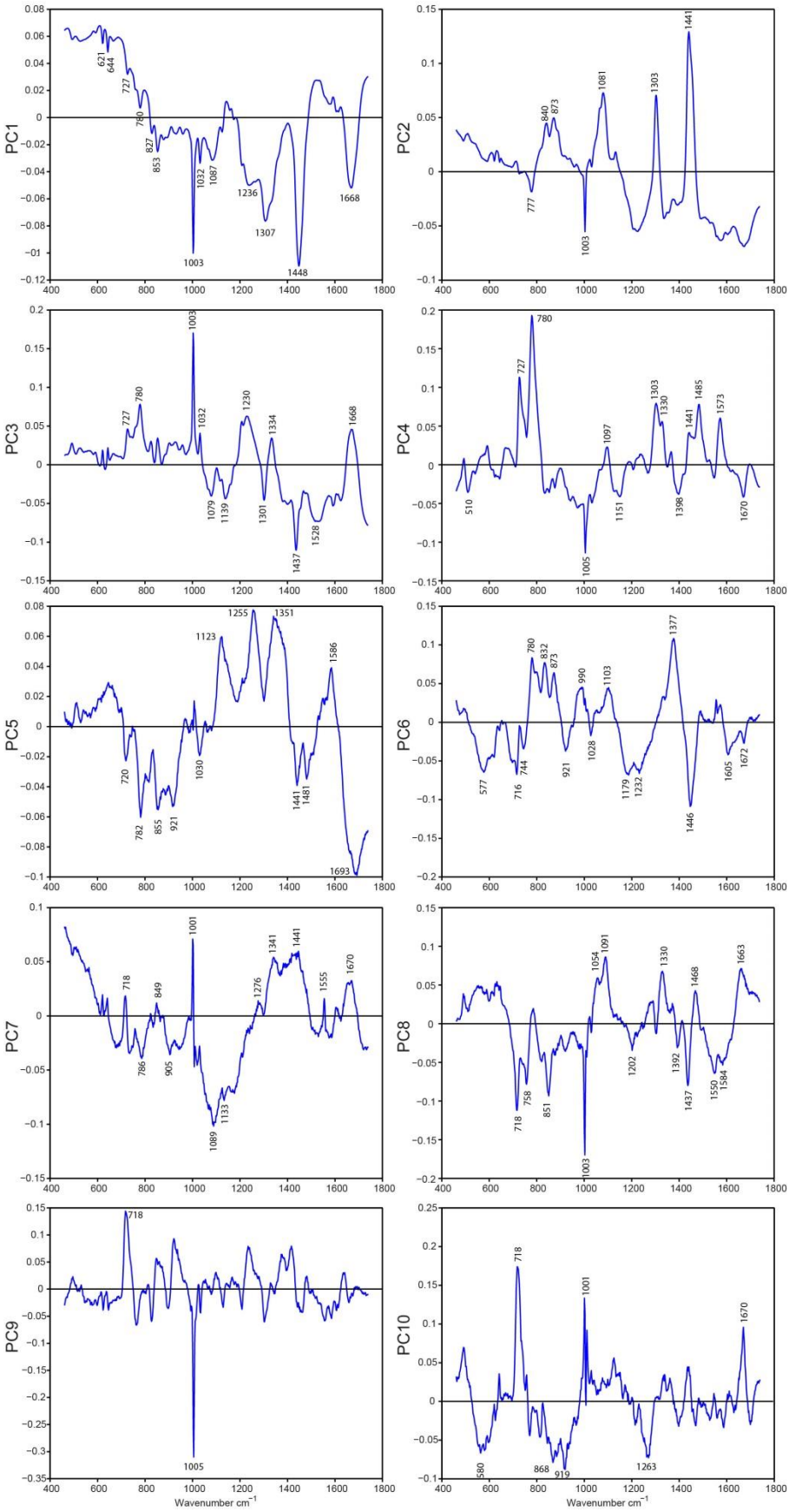

Figure 6.1.9(a): Principal component loadings of the first 10 components plotted against the wavenumber shift.

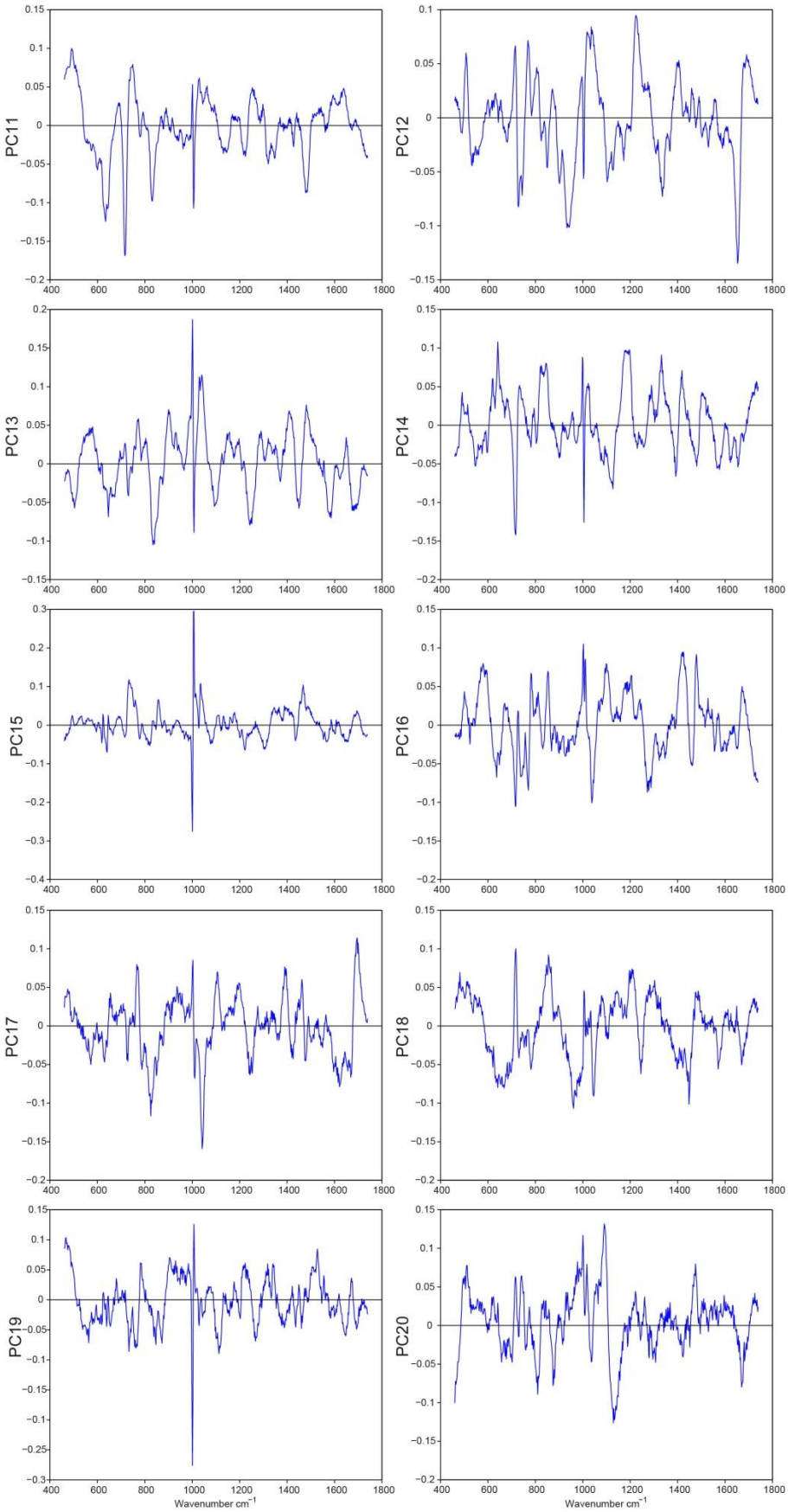

Figure 6.1.9(b): Principal component loadings of components 11 through to 20 plotted against the wavenumber shift.

6.3.3.1 Prediction of Lynch Syndrome

The prediction accuracy of the model was tested using a LOMO cross-validation procedure. Such validation involves each dataset to be held back in turn whilst the remaining datasets were used to calculate the discriminant functions. The measurement that was held back was then classified by the model. This procedure was then iterated until all the tissue samples had undergone prediction by the model. Table 6.2 displays the confusion matrix resulting from the predictions against the true pathologies, while table 6.3 shows the calculated sensitivities and specificities, as well as the areas under the receiver operating characteristic (ROC) curves.

To test the diagnostic model performance for the classification of normal colon, 50 point spectra were collected per resection from a total of 10 patients. Point spectra were collected from the mucosal region only resulting in a total of 500 normal spectra. The sensitivity was found to be 85%, while the specificity was around 95%. CIN tumours were matched to each of the normal resections; again 50 spectra were collected per resection with the exception of one sample consisting of 40 spectra. CIN tumours had the second highest sensitivity of 79% but the lowest specificity of 80%. LS MSI-H tumours were matched to the CIN tumour samples by the tumour stage (T: size and spread into nearby tissue). LS MSI-H had the lowest sensitivity of 63%, which means that approximately a third of the patients will be misclassified as having CIN sporadic adenocarcinoma. However, a reasonably high specificity of 89% suggests that the current training dataset facilitates better recognition of patients without LS MSI-H resulting in fewer patients being flagged as false positives.

Table 6.1.2: Confusion matrix of the prediction of Lynch Syndrome MSI-H versus CIN sporadic adenocarcinoma and normal healthy colon. *LDA utilising LOMO cross-validation was used to generate the matrix.*

	Classification	**Raman Predicted Class**		
		Normal	**CIN**	**LS MSI-H**
Actual Class	**Normal**	426	27	36
	CIN	44	389	149
	LS MSI-H	30	74	315
	Total	500	490	500

Table 6.1.3: Sensitivity and specificity measures of Raman spectroscopy as a diagnostic classifier of Lynch Syndrome MSI-H in CRC. *Sensitivity, specificity and areas under the curve (AUC) were calculated from the linear discriminant model performed using the Renishaw Classification Tool version 2.9.*

Pathology	Sensitivity	Specificity	AUC
Normal	0.8520	0.9363	0.9478
CIN	0.7939	0.8070	0.8582
LS MSI-H	0.6300	0.8949	0.8558

6.3.3.2 Receiver operating characteristic curves

ROC curves were plotted to compare the accuracy of the classification of each pathological group as well as normal mucosa. Here, a plot of the true positive fraction (sensitivity) vs the false positive fraction (1-specificity) is generated and demonstrates a trade-off between sensitivity and specificity. ROC curves with progressively greater discriminant ability are located closer to the upper left hand corner in the 'ROC space'. The area under the ROC curve previously calculated in table 6.3 is an effective combined measure of sensitivity and specificity that defines the ability of the classifier to correctly classify the pathology in question (177). Figure 6.11 shows the three ROC curves for each pathology group.

The ROC curve corresponding to the classification of normal colon has the highest AUC of 0.95 and is located closer to the upper left corner of the plot (*fig.6.11*). This signifies that the classification accuracy is the best for normal tissue. This means that a positive classification is only made with strong evidence hence fewer false positive errors are made. ROC curves corresponding to the classification of sporadic CIN tumours and LS-MSI tumours are almost identical in shape with an AUC of 0.86 for both pathologies. This indicates that the diagnostic performance of the classifier for each of these pathology groups is the same.

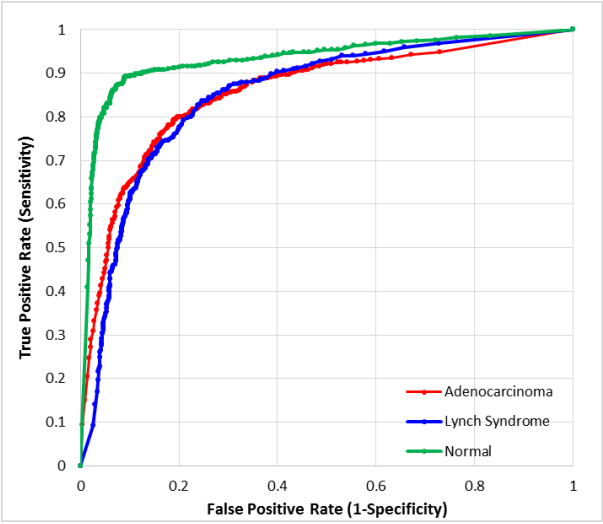

Figure 6.1.10: ROC curve illustrating the ability of Raman spectroscopy to discriminate resections diagnosed as Lynch Syndrome from sporadic adenocarcinoma and normal colonic tissue. *ROC curve for the classification of normal tissue (green) had an AUC of 0.9478. ROC curve for the classification of sporadic adenocarcinoma (red) had an AUC of 0.8582, while LS (blue) had an AUC of 0.8558.*

6.3.3.3 Three-group Linear Discriminant Model

The three-group linear discriminant model was constructed using the 23 PCs to calculate two linear discriminant (LD) functions that maximised the variance between the groups whilst minimising the variance within the groups. The weights of the LD functions for each spectrum were plotted against each other to produce a scatter plot, whereby group separation can be easily visualised. Figure 6.11 shows the scatter plot of the LD weights as well as the two LD functions that facilitate maximal separation of the three groups.

Through supervised training of a linear discriminant model, separation of CIN tumour types from LS MSI-H tumour types can be achieved (*fig.6.11a*). The LD scatter plot shows that the CIN tumours separate from LS MSI-H tumours across LD1. The majority of the difference between CIN tumours and LS MSI-H tumours were attributed to peaks at 731 cm^{-1} (adenine, phosphotidylserine), 1007 cm^{-1}(carotenoids, polysaccharides, phenylalanine), 1040 cm^{-1} (carbohydrates, collagen) characteristic of CIN tumours and 716 cm^{-1} (adenine, phospholipids), 1001 cm^{-1} (C-C aromatic ring stretching, phenylalanine), 1091 cm^{-1} (phosphate stretching vibrations) and 1222 cm^{-1} (amide III, nucleic acids) attributed to LS MSI-H tumours (*fig.6.11b*).

Normal tissue separated from both tumour types across LD2. Normal tissue was characterised by peaks at 840 cm^{-1} (polysaccharides), 966 cm^{-1} (lipids, triple helix vibration), 1005 cm^{-1} (proteins, phenylalanine), 1103 cm^{-1} (phenylalanine, carbohydrates), 1251 cm^{-1} (amide III), 1453 cm^{-1} (CH vibrations, proteins associated with elastin, collagen and phospholipids), and 1586 cm^{-1} (protein band, phenylalanine). Whereas, both tumour types collectively were characterised by peaks at 682 cm^{-1} (guanine), 715 cm^{-1} (adenine, phospholipids), 748 cm^{-1} (nucleic acids, tryptophan), 900 cm^{-1} (deoxyribose, saccharides), 1026 cm^{-1} (carbohydrates, glycogen), 1218 cm^{-1} (C-N, amide III), 1296 cm^{-1} (CH deformation, lipids), 1528 cm^{-1} (carotenoids (absent in normal tissue)) and 1672 cm^{-1} (amide I, cholesterol) (*fig.6.11c*).

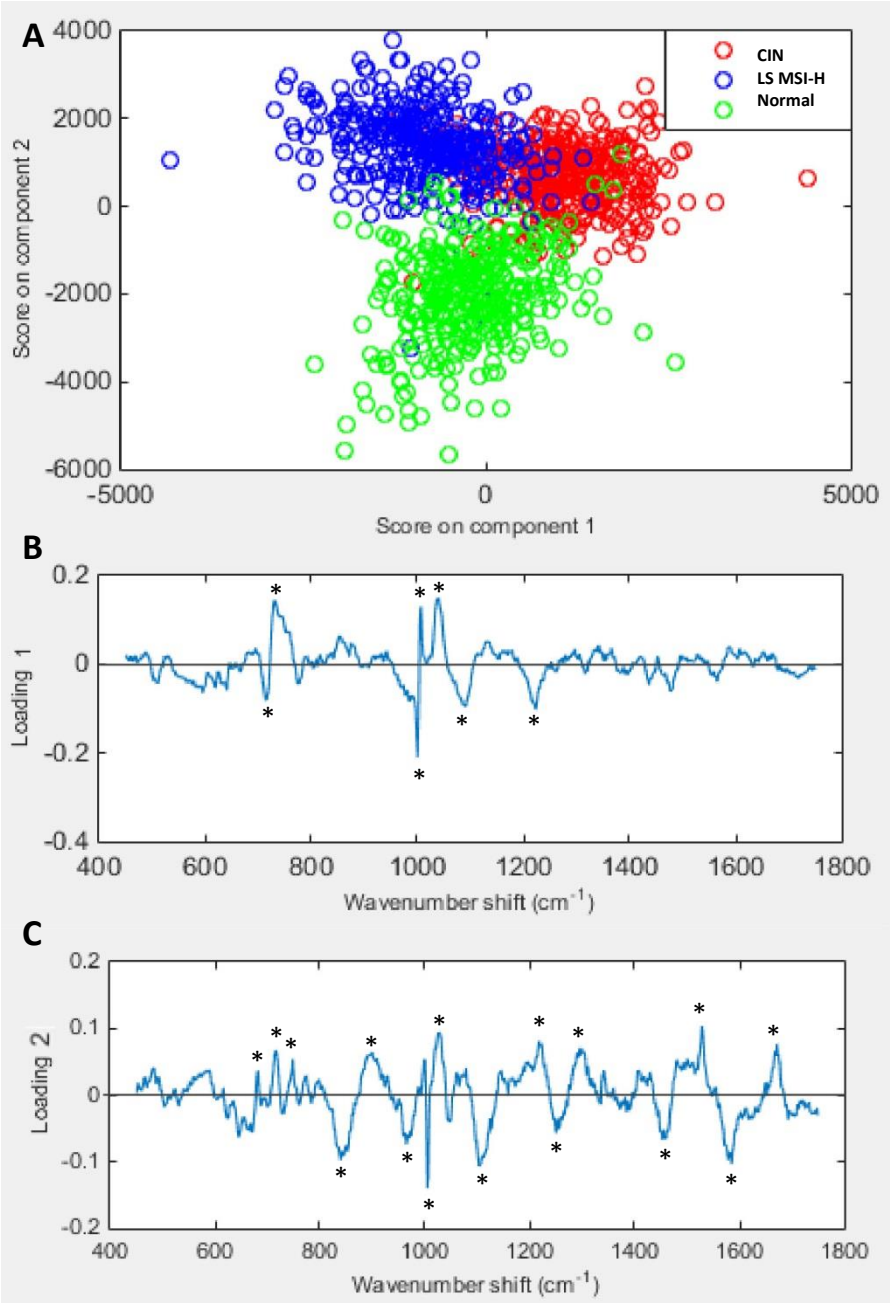

Figure 6.1.11:Three-group linear discriminant model generated using the Renishaw Data Classification Tool. A) *Plot of linear discriminant function scores for each spectrum. Separation of all three groups was achieved.* ***B-C)*** *Linear discriminant functions calculated for optimal separation of the three groups.*

6.4 Discussion and Conclusions

This study is the first of its kind to carry out a preliminary investigation into the use of Raman spectroscopy as a clinical diagnostic tool in discriminating chromosomal instability from microsatellite instability in FFPE colonic tissues. From a very small sample size (10 samples per group) promising results have been

achieved with the use of multivariate linear discriminant models, which go on to show a reasonable degree of discrimination is possible from samples that appear to be spectrally very similar. This is the first of its kind proof-of-principle study that is both label-free and has a rapid sample turnaround time.

The mean spectra obtained from CIN sporadic tumours and LS MSI-H tumours were shown to be spectrally very similar. To tease out the subtle differences between the two pathological groups required the use of complex chemometric techniques. Empirical peak analysis was carried out first in the form of difference spectra, whereby the mean normalised spectrum of CIN adenocarcinoma was subtracted from the mean normalised LS MSI-H spectrum. This enabled the most obvious spectral variations to be compared via the magnitude of the peaks and troughs in the difference spectrum. Through tentative peak assignments it was possible to make some inference about the biochemical differences that exist between CIN sporadic adenocarcinoma and LS MSI-H adenocarcinomas. LS MSI-H was dominantly characterised by peaks at 714, 1081, 1302 and 1445 cm^{-1} which are tentatively assigned to lipids, along with a peak at 1672 cm^{-1} assigned to cholesterol. Elevated lipid and cholesterol levels have already been reported in highly proliferative cancer cells and are now considered hallmarks of cancer aggressiveness (178,179). The adenoma-carcinoma progression rate is already known to be increased in LS and this might be an indication of this observation (180). LS also exhibited reduced levels of nucleic acids identified through tentatively assigned peaks at 494, 732 and 787 cm^{-1}. MSI-H type tumours are known to be chromosomally stable and possess a near-diploid DNA content compared to CIN MSI-S tumours that possess an imbalance in the number of chromosomes per cell or aneuploidy (181).

Unsupervised multivariate analysis, specifically PCA, was then used to see whether pathological grouping can be achieved based purely on spectral variance. With each component, describing the ever decreasing levels of variance between the groups, it was possible to identify the most significant biochemical variance by analysing the peaks and troughs of the loadings. Normal mucosa was found to separate well from both the tumour subtypes across PC1 (*fig.6.6a*), while the CIN MSI-S tumours were found to marginally separate from LS MSI-H tumours across PC4, this is more evident from the 1D

score plots (*fig.6.6b*). This suggests that the biochemical difference between these two cancer subtypes is very subtle, in comparison to the more obvious differences from normal mucosa.

Normal tissue was found to be positively characterised by carbohydrate peaks at 840 (glucose, polysaccharides) and 873 (polysaccharides), as well as lipid peaks at 1081, 1301 and 1441 cm^{-1}. Metabolic profiling of normal colorectal mucosa by Chun *et al* using High-Resolution Magic Angle Spinning Nuclear Magnetic Resonance and Gas Chromatography Mass Spectrometry have demonstrated higher levels of both saturated and unsaturated lipids and/or fatty acids as well as glucose in normal mucosa compared to CRCs (182). Reduced levels of glucose in CRCs is consistent with the "Warburg effect", whereby cancer cells rely on aerobic glycolysis to generate energy instead of mitochondrial oxidative phosphorylation (183,185,186,188). The reduced lipid signals in CRCs may be associated with a higher metabolic turnover and demand in membrane biosynthesis for cell proliferation leading to a higher rate of lipid utilization, this particularly applies to polyunsaturated fatty acids (182,184).

Conversely spectra originating from cancerous tissues were dominated by nucleic acid signals tentatively assigned to peaks at 491, 727, 780, 1095, 1187, 1228, 1483 and 1570 cm^{-1}. This is indicative of a higher rate of nucleic acid synthesis characteristic of highly proliferative malignant tissue as well as a gradual increase in the mean nuclear area and the nuclei to cytoplasm ratios in colonic adenocarcinomas (185–187). Raman based detection of elevated nuclear content in colorectal cancer and dominating lipid and carbohydrate signals in normal tissues has previously been reported (50,54,60,63,78,188).

Marginal separation of LS MSI-H tumours from CIN MSI-L tumours was observed across PC4. Tumours originating via the chromosomal instability pathway that are microsatellite stable/low were mainly dominated by peaks originating from nucleic acids (491, 727, 780 and 1097 cm^{-1}). This may be indicative of the common product of CIN tumours: aneuploidy. Aneuploidy is associated with the gain or loss of small segments of chromosomes or the whole chromosome altogether resulting in genomic imbalances. A recent study by Staarmann *et al* found considerable variation in DNA ploidy through the transition of the adenoma to carcinoma sequence. Adenomas were associated with hypodiploidy and hence chromosomal loss. Stage I carcinomas were mostly found to be hyperdiploid, whereas stage II

and higher exhibited near tetraploid DNA content. Carcinomas with lymph node metastases showed a near triploid DNA content (189). They concluded that the initial chromosomal loss seen in adenomas may potentially be associated with inactivation of tumour suppressor genes (190) and near-triploidy may be associated with a more aggressive course of the disease (189).

Tumours with high microsatellite instability such as in LS were found to be negatively characterised by PC4, with dominating protein peaks. Given that MSI-H tumours are near diploid and chromosomally stable, there was no detectable increase in nucleic acid content, as was seen in CIN tumours. The presence of multiple aromatic amino acid associated peaks may be indicative of the immunological response commonly seen in LS tumours via the elevated lymphocyte infiltrate. Amino-acid sensing and degradation pathways have been known to influence immunologic responses to antigenic cues through the production of amino acid catabolites with immune modulatory properties (191,192). Glutamine usage has been found to be significantly increased upon both T cell and B cell activation, and both require glutamine to respond to antigen receptor stimulation (193,194). Arginine has been found to regulate the expression of specific components of the T cell receptor as well as promote T cell proliferation (195). Whereas tryptophan has been shown to be necessary for T cell proliferation *in vitro* (196). Hence, the observed changes in amino acid content may be consistent with the elevated immunological response seen in MSI-H tumours. A similar trend was observed from the linear discriminant function plots, whereby LS MSI-H tumours were negatively characterised nucleic acid and amino acid signals (*fig.6.11b*).

Application of linear discriminant analysis via the Renishaw Data Classification Tool has enabled group separation by maximising the variance between the groups and minimizing the variance within the groups (*fig.6.11*). Considering the low sample numbers used within this study the classifier performance was reasonable. When tested with the LOMO cross-validation procedure the sensitivity and specificity for the detection of LS MSI-H was 63% and 89%, respectively, on a per spectrum basis. The classification of CIN sporadic adenocarcinoma performed slightly better with a sensitivity of 79% and specificity of 81%. Best performance was achieved from normal tissue with a sensitivity of 85% and specificity of 94%, on a per spectrum basis; this was

further confirmed by the ROC curves. The current sensitivities obtain for LS MSI-H are comparable to the Amsterdam I criteria, while the specificity was slightly better than that of Amsterdam II criteria. It was also superior to the 25% specificity obtained from the best performing revised Bethesda guidelines (43). These results are therefore very promising as a reasonably high specificity in the detection of LS means that there will be fewer false positive results and hence more patients that do not have the disease will be correctly identified. This is potentially clinically important as it saves the patient from unnecessary worry and costly further investigations.

The performance of the classifier was also not far off from the estimated sensitivities and specificities of the molecular IHC and MSI testing. A systematic review of 9 published studies conducted by Snowill *et al* found that the sensitivity of IHC and MSI ranged between 73.3 % to 100.0% and 88% to 100%, respectively (45). The performance of the classification model produced here was found to be on the lower end of the scale; however this is not unexpected due to the extremely small sample size. This is anticipated to improve with larger cohorts. The specificities of IHC and MSI ranged between 12.5% to 100% and 68% to 84%, respectively. The specificity of the classifier was found to be 89% which is comparable to the molecular tests. It is therefore clear that with such a small sample size Raman spectroscopy stands as a strong competitor to the currently recognized tests used to identify true LS individuals.

There are however a number of limitations to this study, with the main shortcoming being that of the small sample size. Due to the rarity of the condition in question it was not possible to acquire a large enough sample size within the lifetime of this project. To build a truly robust classification model a large sample size representative of the population is required. A sample size calculation would therefore need to be performed to ensure adequate patient numbers are recruited. To obtain an accurate representation of the true performance of the current classification model, the model should also be tested using a new unseen dataset. This was not possible in this scenario as the number of input datasets was already small and would compromise the model further. Instead the model was tested using a LOMO cross-validation procedure, were a single dataset was held back during model training and was classified upon the completion of training. This was then iterated until all the datasets were predicted. A further improvement can potentially

be made by using small segments of the wavenumber region with known spectral differences. Throwing out diagnostically insignificant regions should result in an improvement in the prediction capacity of the model.

This study was conducted using a purpose built Renishaw RA802 bench top prototype system designed for the sole purpose of being used in a clinical setting. The tissue sections used within the study were also mounted onto a novel Raman substrate that has proven to not only be a fraction of the cost of CaF_2 but provides a superior background and signal enhancement. Furthermore, the LDA model built for LS discrimination was carried out using a specially designed Renishaw Data Classification Tool that is foreseen to be integrated into the Raman prototype system for complete diagnostic automation. Although not quite ready for integration into the clinic, this project demonstrates that a full diagnostic package with affordable slides is close to being commercialised.

In conclusion, this preliminary work shows that Raman spectroscopy can potentially be used as a clinical tool to discriminate the presence of hereditary MSI-H colorectal cancer from the more common CIN sporadic form. Although a much larger study would need to be conducted to prove this further, nevertheless this study opens the scope for using Raman spectroscopy in the diagnosis of other hereditary cancers and colon pathologies.

Chapter Seven

Overall conclusions and future work

7.1 Contribution to Knowledge

The primary aim of this study was not only to test whether Raman can be used as a diagnostic platform for subtle hereditary variants of CRC, but also to test the suitability of the novel purpose-built prototype Raman benchtop spectrometer with its associated Data Classification Tool.

This study was:

- The first to demonstrate a lower Raman background of super mirror stainless steel slides when directly compared to UV grade CaF_2 the standard substrate in the field
- The first to use silane coatings on steel for the sole purpose of tissue adhesion for Raman studies.
- The first to demonstrate complete paraffin removal from FFPE tissue sections mounted onto silanized steel slides and propose an explanation for this very desirable effect.
- The first to analyse large high resolution tissue maps of normal colon mounted onto silanized steel slides that are free-from paraffin contamination.
- The first to demonstrate the feasibility of using Raman spectroscopy as a clinical diagnostic tool for the discrimination of hereditary CRC variant known as Lynch Syndrome.

One of the key successes of this study I believe lies in the discovery of a cheaper alternative backing substrates to CaF_2. This single step brings the possibility of translating Raman spectroscopy into a clinical setting that much closer to reality. Previous studies that have attempted to use steel reported high backgrounds and poor tissue adhesion (130,138), this has been overcome with a mirror finish and steel specific silane coating for adhesion. In addition to that the proposed alternative substrate was unexpectedly found to facilitate complete paraffin removal from FFPE sections. Not only has paraffin retention previously been shown to be an issue in Raman based tissue imaging (197) but it is also known to affect staining intensity in IHC (164). Although these metal substrates were only used once for the duration of this study, it may be possible to reuse

them by cleaning the tissue off without damaging the mirror surface. It is anticipated that sonication in soapy warm water may prove effective, but this requires further investigation.

One of the main limitations of these novel substrates lies in the surface preparation and coating steps to ensure tissue adhesion. Producing adequate hydroxyl groups on the metal surface requires washing the slides using piranha solution, this is not only highly corrosive and but also explosive. Furthermore, producing a streak-free silane coating demands that the slides are coated in small batches as the surface is dried under a single nitrogen stream before oven curing. Although this is laborious and time consuming, the results achieved are comparable if not better than those achieved on CaF_2. The production of these coated slides may potentially be commercialised on a larger scale facilitating implementation into the clinic.

High resolution false-coloured Raman maps consisting of hundredths of thousands of spectra from normal colonic tissue is to date some of the largest maps acquired from the colon. These maps not only provide a superior contrast to the standard H&E stained sections, but also ensures that multiple contiguous sections do not need to be obtained for molecular staining techniques such as IHC since numerous histological features can be identified within a single image. This essentially delivers the multiplexing goal sought in many immunohistochemical diagnostic discovery programmes. By making a very useful and serendipitous observation that paraffin was not retained within these sections means that lipids that have not been leached out during deparaffinization can be visualised. Identification of the spectral features unique to each histological site also means that a classifier can potentially be trained to identify the normal regions within the chaos that is adenocarcinoma (68).

This study has successfully demonstrated the potential of using Raman spectroscopy to distinguish the very subtle biochemical difference between sporadic CRC and hereditary LS. Using the LOMO cross-validation procedure a sensitivity of 63% and a specificity of 89% was achieved. This is on par with the estimated sensitivity of the initial Amsterdam criteria while the specificity was higher than that achieved on the best performing Bethesda criteria (43). Given that the sample size consisted of only ten samples per pathology and 500 point spectra per sample the performance of the classification model was reasonably good and

competitive with current standards in the field, although further validation on a larger sample size is required.

7.2 Recommendations for future work

Here, only a brief analysis of the biochemical basis of the spectral changes between sporadic CIN adenocarcinoma and LS MSI-H was undertaken. To accurately analyse the full repertoire of changes that occur between LS MSI-H and sporadic CIN cancer pathways a comparison needs to be made between a large cohort matched by cancer TNM stage. In the present study cancer stages T2 through to T4 were collated together due to the extremely small sample size available. However, by removing the variability of cancer stage within the dataset it should be possible to gain a more accurate representation of the metabolic changes associated with each pathological group. Large multicentre studies such as that of Isabelle *et al* would also need to be implemented (198). Such larger studies would also allow the identification and elimination of confounding factors such as age, gender and smoking status that may potentially invalidate the results.

To further analyse the tissue changes Raman analysis would need to be carried out in parallel with histochemical analysis performed on the same sections after Raman measurements had been taken. This would ensure that a direct, one-to-one histological comparison could be made. This is quite often not possible with adjacently cut sections as the histology is likely to change with increased depth of penetration into the tissue block.

To further corroborate the metabolic changes observed through Raman spectroscopy, such as those observed in lipids and amino acids, it may be very beneficial to couple Raman spectroscopy with other sophisticated metabolic profiling techniques such as high-resolution magic angle spinning nuclear magnetic resonance and gas chromatography mass spectrometry (199), whereby the individual metabolites can be analysed in greater detail.

Around 10-15% of all MSI-H tumours are of sporadic CIN origin; this poses an inherent problem with the identification of true Lynch Syndrome cases. These sporadic cancers share similar clinic-pathological features but are primarily caused by somatically acquired hypermethylation of both alleles of the MLH1 promoter, resulting in the loss of MLH1 protein expression. An extension of this

study could be carried out by testing whether Raman can be used to distinguish genuine MLH1 mutations from MLH1 silencing through promoter hypermethylation. At present the only means of distinguishing these two pathologies is through testing for the oncogenic BRAF-V600E mutation (an activating mutation in the B-Raf kinase), that has been shown to be a predictive marker capable of successfully distinguishing true LS from CIN sporadic MSI-H-associated disease (200). It would also be of great benefit to compare the metabolic changes arising from mutations in different MMR proteins, as these are known to have a variable predisposition to developing cancer.

Aside from relying purely on the spectral features produced through Raman spectroscopy it may also be usefully to compare the overall level of fluorescence from each pathological group and normal tissue as this has previously been shown to be diagnostically useful (201). In addition to that, other sophisticated Raman techniques such as Surface-Enhanced or Tip-Enhanced Raman Spectroscopy can be used to selectively enhance the Raman signal and potentially improve the diagnostic capability of this technology.

Further work is required on the different spectral pre-processing methodologies employed in the field, and in this study, and how they affect the performance of the classifier. Improvements on the spectral analysis techniques are also required. Selection of only a subset of the most significant spectral regions may enhance the overall sensitivity and specificity of the classifier by removing diagnostically irrelevant data. The LOMO cross-validation procedure presented here was used as an indicator of the performance of the classification model in a clinical setting. However, for a more accurate evaluation of the performance a previously unseen sample must be used. In addition to that it would be useful to compare and contrast the performance of different machine learning algorithms such as SVM and ANN in the identification of LS.

This proof of concept study has successfully demonstrated the use of Raman spectroscopy as a clinical diagnostic tool for the identification of a hereditary variant of CRC known as Lynch Syndrome originating from the MSI pathway. Rapid and cost effective identification of MSI originating tumours via Raman can selectively identify the small percentage of patients that would benefit from further downstream testing for Lynch Syndrome as well as the section of more effective drug treatments. This is a truly exciting prospect as it circumvents the need of a

multitude of costly and laborious molecular tests and clinical guidelines that have been shown to be very stringent in their performance.

Appendix

Appendix 1: ***Automated tissue processor Leica TP1050 workflow***

Reagent	Time	Temp (ºC)
10% Formal Saline	30 mins	50
Alcohol 70%	1 hour	40
Alcohol 90%		
Ind. Meth. Spirit		
Ind. Meth. Spirit	45 mins	
Ind. Meth. Spirit		
Ind. Meth. Spirit		
Xylene	1 hour	
Xylene	45 mins	
Xylene		
Tissue Tek II Wax	1.5 hours	62
Tissue Tek II Wax	2 hours	
Tissue Tek II Wax		

Appendix 2: ***Laser power measurements.***

Measured with and without the 50×/0.75 short WD objective using a handheld laser power meter (Edmund Scientific ltd).

Wavelength	100 % Laser power (mW) without objective	100 % Laser power (mW) with 50x short WD objective
532 nm	110	70
633 nm	7.5	6
785 nm	215	110
830 nm	145	22

Appendix 3: *Cost breakdown per backing substrate*

Material	Approximate cost (£)	Supplier
Calcium fluoride	~ £100	Crystran UK
Synthetic fused silica (quartz)	~ £30	LG Optical UK
Aluminium coated glass	~ £15	
Borosilicate glass	~ £7	
Extra white soda lime glass	~ £0.01	Thermo scientific UK
Super mirror steel	~ £0.05	Renishaw UK

Appendix 4: *Slide Coating Protocols*

Poly-L-Lysine Coating

1. Prepare a 0.1% (w/v) poly-L-lysine hydrochloride solution using distilled water in a glass slide staining dish.
2. Incubate slide in solution for five minutes.
3. Drain slides and dry at room temperature overnight or in an oven (~60 °C) for ~1 hour.

Adaptation of the chrome gelatin technique

1. Clean slides using trichloroethylene solution.
2. Strip the oxide coating from the stainless steel by incubating in 10% sodium chloride solution (in distilled water).
3. Mount the tissue immediately following removal from NaCl solution.

Coating with 3-aminopropyltriethoxysilane (APES) (Silanization)

Slides should be "soaked" in methanol or acetone for about two minutes, then air-dried. This assures that the slides are free of any trace of oil or water. Alternatively use the degreasing protocol (trichloroethylene solution).

1. Mix 10 mL of the silane (Sigma-Aldrich, UK) with 500 mL acetone. (This makes a 2% solution, which is stable for 8 hours, after which the colour will change.)
2. Dip clean dry slides in silane solution for 2 minutes.
3. Wash the slides in 2 changes of distilled water.
4. Dry completely in oven and cool. Autoclaving, if desired, will not harm the coating.
5. Store treated slides in boxes at room temperature.

Appendix 5: *Finalised Silanization Slide Protocols*

Due to the time limitations of this study the silanization protocol will be optimized based on the currently known knowledge. The protocol is based on the studies carried out by Kang et al, Zammarelli et al and Jussila et al (145–148).

1. **Piranha Treatment:**
   - Immerse slides in 4:1 piranha solution for 1 hour.
   - Clean slides by ultrasonication for 10 minutes in deionized water, then ethanol and finally acetone (total time: 30 minutes).
   - Dry by nitrogen blowing.

Piranha solution: make a 4:1 mixture of sulphuric acid (H_2SO_4) and 30% hydrogen peroxide (H_2O_2).
Purpose: Removes surface contaminants and exposes the reactive hydroxyl groups on the steel surface to prep for silanization.

2. **Silanization with 3-Aminopropyltriethoxysilane (APES):**
   - Prep 0.12% v/v of APTES in a mixture of ethanol and deionized water and use at natural pH.
   - Age solution for 1 minute prior to use, this allows for hydrolyzation of the alkoxy group without any significant oligomer formation.
   - Immerse slides in solution for 1 minute at 300K (27 ºC).
   - Remove slides and blow dry in nitrogen.
   - Cure in oven at 373K (100 ºC) for 15 minutes.

APES solution: 0.12% v/v silane: 0.6 ml APES solution to 500 ml mix of 25/75 ration ethanol and deionized water.
25/75 mix of ethanol/water ratio: 125 ml ethanol and 375 ml deionized water.
Purpose: Ensures tissue sections remain adhered to the stainless steel slide during processing. 0.12% v/v silane ensures a 1.3 nm thick coating with approximately 82% of the surface achieving a uniform coating and only 18% cluster formation (146).
Low concentrations of APES are mainly composed of reactive monomeric silanols that have not undergone polymerization. The role of ethanol is to delay the formation of large and highly-oligopolymerized aggregates (148).

Appendix 6

Summary table depicting the first 9 steps followed by all the automated IHC stainers in UCLH advanced diagnostics.

Step	Reagent	Time	Temperature (ºC)
1	Bond dewax solution	0.30	72
2	Bond dewax solution	0.00	72
3	Bond dewax solution	0.00	0
4	Alcohol	0.00	0
5	Alcohol	0.00	0
6	Alcohol	0.00	0
7	Bond wash solution	0.00	0
8	Bond wash solution	0.00	0
9	Bond wash solution	0.00	0

Appendix 7: *Slide Cleaning Protocol (Industry Grade)*

Apply this protocol to all super mirror 304 stainless slides as a **noticeable sticky film** appears to be left on the surface following the removal of the protective plastic film.

SAFETY: Perform in fume hood, do not inhale trichloroethylene (Sigma-Aldrich, UK).

Ultrasonic cleaning with the following sequential baths:

1. Trichloroethylene (degreasing agent)
2. Acetone (removes trichloroethylene)
3. Isopropanol (removes acetone and leaves no residue)

Allow to air dry.

Appendix 8

Summary of all the reference biomolecules used within this study as well as their origins.

Reference Compound	Supplier	Country
Paraffin wax (Tissue-Tek®II)	Sakura	UK
DNA (*herring testes*)	Sigma Aldrich	
Cholesterol		
Mucin type I (*bovine submaxillary glands*)		
Muscle acetone powder (*rabbit*)		
Glycerol		
Hydroxyproline		
Phosphatidylcholine		
Galactosamine		
Glucosamine		
Oleic acid		
Palmitic acid		
Phosphatidic acid		
Phosphatidylserine (*bovine brain*)		
Phosphoethanolamine (*egg yolks*)		
Collagen		
Fucose	Alfa Aesar	
Glucose	BDH Laboratory Supplies	

Appendix 9

PC loadings 1-10 (blue) with a superimposed linear fit of the best matching molecular reference (orange). The first 10 loadings explain 82 % of the total variance in the dataset.

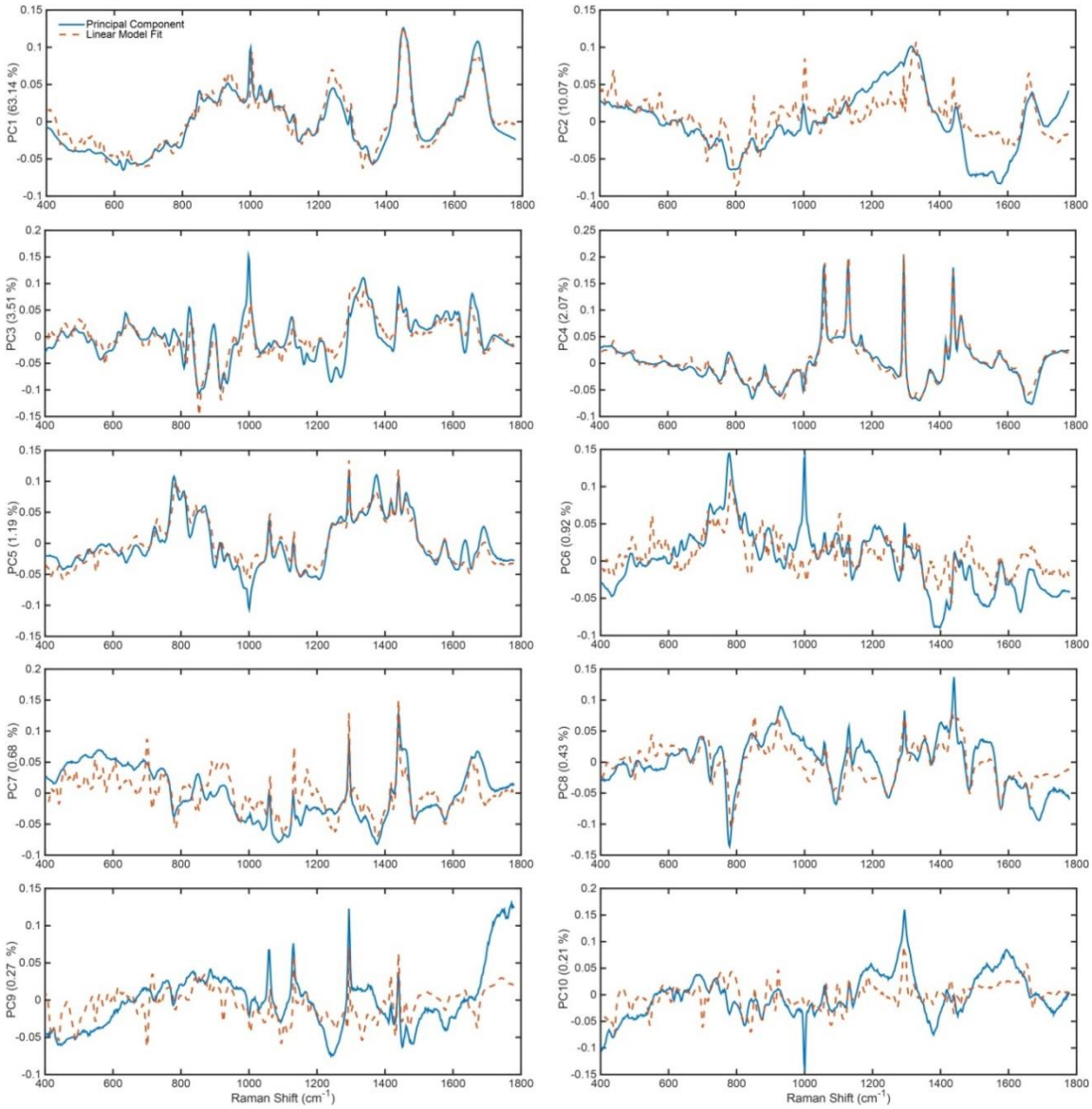

Appendix 10

Protocol 15.8.8 used for Leica Bond III IHC staining

Step	Reagent used	Step Type	Temperature	Time (min)
1	Peroxide Block	Reagent	Ambient	5.00
2	Bond Wash Solution	Wash		0.00
3	Bond Wash Solution	Wash		0.00
4	Bond Wash Solution	Wash		0.00
5	Primary	Reagent		15.00
6	Bond Wash Solution	Wash		2.00
7	Bond Wash Solution	Wash		2.00
8	Bond Wash Solution	Wash		2.00
9	Post Primary	Reagent		8.00
10	Bond Wash Solution	Wash		2.00
11	Bond Wash Solution	Wash		2.00
12	Bond Wash Solution	Wash		2.00
13	Polymer	Reagent		8.00
14	Bond Wash Solution	Wash		2.00
15	Bond Wash Solution	Wash		2.00
16	Deionized water	Wash		0.00
17	Mixed DAB Refine	Reagent		0.00
18	Mixed DAB Refine	Reagent		10.00
19	Deionized water	Wash		1.00
20	Deionized water	Wash		1.00
21	Deionized water	Wash		0.00
22	DAB Enhancer	Reagent		10.00
23	Bond Wash Solution	Wash		1.00
24	Bond Wash Solution	Wash		1.00
25	Bond Wash Solution	Wash		0.00
26	Hematoxylin	Reagent		0.45
27	Deionized Water	Wash		1.00
28	Bond Wash Solution	Wash		1.00
29	Deionized Water	Wash		0.00

Appendix 11

Summary of additional reference biomolecules used within this study as well as their origins.

Reference Compound	Supplier	Country
Glutamate	Sigma Aldrich	UK
Aspartate		
RNA		
Myelin Basic Protein		

Appendix 12

Breakdown of patient samples used to build the LDA model for the classification of normal, sporadic adenocarcinoma and LS patients. Lynch Syndrome (LS), Adenocarcinoma (AC), Normal (N).

Patient ID	Sample Type	TNM Stage	Tumour Grade
LS1-UH15	Resection cancer	T2 N0 M0	Mod. Diff.
LS2-UH15	Resection cancer	T2 N0 M0	Mod. Diff.
LS3-UH12	Resection cancer	T2 N0 M0	Mod. Diff.
LS4-UH13	Resection cancer	T3 N0 M0	Poor diff.
LS5-UH13	Resection cancer	T3 N0 M0	Mod. Diff
LS6-UH14	Resection cancer	T3 N0 M0	Mod. Diff.
LS7-UH06	Resection cancer	T3.N1.Mx	Poor. diff
LS8-UH15	Resection cancer	T3 N1 M0	Poor diff.
LS9-UH13	Resection cancer	T4 N0 M0	Mod. Diff.
LS10-UH13	Resection cancer	T4 N1 M0	Mod. Diff.

Patient ID	Sample Type	TNM Stage	Tumour Grade
AC1-UH13	Resection cancer	T2 N2 M0	Mod. Diff.
N1-UH13	Normal	-	-
AC2-UH15	Resection cancer	T2 N0 M0	Mod. Dif.
N2-UH15	Normal	-	-
AC3-UH15	Resection cancer	T2 N0 M0	Mod. Dif.
N3-UH15	Normal	-	-
AC4-UH14	Resection cancer	T3 N1 M0	Mod. Diff.
N4-UH14	Normal	-	-
AC5-UH14	Resection Cancer	T3 N3 M0	Mod. Dif.
N5-UH14	Normal	-	-
AC6-UH15	Resection Cancer	T3 N0 M0	Mod. Dif.
N6-UH15	Normal	-	-
AC7-UH15	Resection cancer	T3 N0 M0	Mod. Diff.
N7-UH15	Normal	-	-
AC8-UH15	Resection cancer	T3 N0 M0	Mod. Diff.
N8-UH15	Normal	-	-
AC9-UH15	Resection cancer	T4 N2 M0	Mod. Diff.
N9-UH15	Normal	-	-
AC10-UH15	Resection cancer	T4 N0 M1	Poor diff.
N10-UH15	Normal	-	-

Bibliography

1. Bowel cancer statistics | Cancer Research UK [Internet]. Cancer Research UK; [cited 2013 Jun 7]. Available from: http://www.cancerresearchuk.org/cancer-info/cancerstats/types/bowel/

2. Ahmed S, Eng C. Colorectal Cancer. In: Jankowski J, Hawk E, editors. Handbook of Gastrointestinal Cancer. 1st ed. Hoboken, NJ, USA: John Wiley & Sons, Inc.; 2012. p. 86–136.

3. Sabine T. Familial Cancer Management. In: Cassidy J, Johnston P, Van Cutsem E, editors. Colorectal Cancer. New York: CRC Press; 2007. p. 125–39.

4. Fleshman J, Wolff B, editors. The Ascrs Textbook of Colon And Rectal Surgery. 2nd ed. New York: Springer; 2007. 810 p.

5. Lawrence P, Bell R, Dayton M, editors. Essentials of General Surgery. 4th ed. Lippincott Williams & Wilkins; 2006. 308-321 p.

6. 10 Reasons To Feel Great Again! | Colon Cleanse and Colon Hydrotherapy | Oasis Colonics Portland [Internet]. [cited 2015 Jun 17]. Available from: http://www.oasiscolonics.com/2012/06/10-reasons-to-get-colonics.html

7. Taylor I, Garcia-Aguilar J, Robyn W. Fast Facts: Colorectal Cancer. 3rd ed. Health Press Limited; 2010. 7-88 p.

8. Tortora G, Derrickson B. Essentials of Anatomy and Physiology. 8th ed. Wiley; 2010. 624 p.

9. Levine DS, Haggitt RC. Normal histology of the colon. Am J Surg Pathol. 1989;13(11):966–84.

10. Greaves P. Histopathology of Preclinical Toxicity Studies: Interpretation and Relevance in Drug Safety Evaluation. 4th ed. Academic Press; 2012. 892 p.

11. Brunner T. Living on the edge : immune cells and immunopathology in the intestinal mucosa. 2009;31:143–4.

12. Williams G, Sloan J, Talbot I. Epithelial tumours of the large intestine. In: Morson and Dawson's Gastrointestinal Pathology. 4th ed. John Wiley & Sons; 2008. p. 582–3.

13. Irving T, Julio G-A, Robyn W. Fast Facts: Colorectal Cancer. 3rd ed. Health Press Limited; 2010. 7-88 p.

14. Potten CS, Kellett M, Roberts SA, Rew DA, Wilson GD. Measurement of in vivo proliferation in human colorectal mucosa using bromodeoxyuridine. Gut. 1992;33(1):71–8.

15. Grondin M V, Chang WW, Gaskins RD. Crypt alterations and collagen deposition in hyperplastic polyps of colorectum. Dig Dis Sci. 1990;35(1):12–9.

16. Humphries A, Wright N a. Colonic crypt organization and tumorigenesis. Nat Rev Cancer. 2008;8(6):415–24.

17. Rothenberg ME, Nusse Y, Kalisky T, Lee JJ, Dalerba P, Scheeren F, et al. Identification of a cKit(+) colonic crypt base secretory cell that supports Lgr5(+) stem cells in mice. Gastroenterology. 2012;142(5):1195–205.

18. Abdul Khalek FJ, Gallicano GI, Mishra L. Colon cancer stem cells. Gastrointest Cancer Res. 2010;(Suppl 1):S16-23.

19. Barker N. Adult intestinal stem cells: critical drivers of epithelial homeostasis and regeneration. Nat Rev Mol Cell Biol. 2014;15(1):19–33.

20. Barker N, van de Wetering M, Clevers H. The intestinal stem cell. Genes Dev. 2008;22(14):1856–64.

21. Mills SE, editor. Histology for Pathologists. 4th ed. Lippincott Williams & Wilkins; 2012. 1328 p.

22. Stanley JR, Woodley DT, Katz SI, Martin GR. Structure and function of basement membrane. J Invest Dermatol. 1982;79 Suppl 1:S69-72.

23. LeBleu VS, Macdonald B, Kalluri R. Structure and function of basement membranes. Exp Biol Med. 2007;232(9):1121–9.

24. Graham MF. Pathogenesis of intestinal strictures in Crohn's disease—an update. Inflamm Bowel Dis. 1995;1(3):220–7.

25. Lee E, Schiller LR, Fordtran JS. Quantification of colonic lamina propria cells by means of a morphometric point-counting method. Gastroenterology. 1988;94(2):409–18.

26. Sellers RS, Morton D. The colon: from banal to brilliant. Toxicol Pathol. 2014;42(1):67–81.

27. Potten CS, Kellett M, Rew D a, Roberts S a. Proliferation in human gastrointestinal epithelium using bromodeoxyuridine in vivo: data for different sites, proximity to a tumour, and polyposis coli. Gut. 1992;33(4):524–9.

28. Moyer M, Poste G, editors. Colon Cancer Cells. Academic Press; 2012. 255 p.

29. Gerdes H, Gillin JS, Zimbalist E, Urmacher C, Lipkin M, Winawer SJ. Expansion of the epithelial cell proliferative compartment and frequency of adenomatous polyps in the colon correlate with the strength of family history of colorectal cancer. Cancer Res. 1993;53(2):279–82.

30. Mills SJ, Shepherd NA, Hall PA, Hastings A, Mathers JC, Gunn A. Proliferative compartment deregulation in the non-neoplastic colonic epithelium of familial adenomatous polyposis. Gut. 1995;36(3):391–4.

31. Lane DP, Benchimol S. p53: oncogene or anti-oncogene? Genes Dev. 1990;4(1):1–8.

32. Armaghany T, Wilson JD, Chu Q, Mills G. Genetic alterations in colorectal cancer. Gastrointest Cancer Res. 2012;5(1):19–27.

33. Mundade R, Imperiale TF, Prabhu L, Loehrer PJ, Lu T. Genetic pathways, prevention, and treatment of sporadic colorectal cancer. Oncoscience. 2014;1(6):400–6.

34. Grady WM. Genomic instability and colon cancer. Cancer Metastasis Rev. 2004;23(1–2):11–27.

35. Weisenberger DJ, Siegmund KD, Campan M, Young J, Long TI, Faasse MA, et al. CpG island methylator phenotype underlies sporadic microsatellite instability and is tightly associated with BRAF mutation in colorectal cancer. Nat Genet. 2006;38(7):787–93.

36. de la Chapelle A. The incidence of Lynch syndrome. Fam Cancer. 2005;4(3):233–7.

37. Møller P, Seppälä T, Bernstein I, Holinski-Feder E, Sala P, Evans DG, et al. Cancer incidence and survival in Lynch syndrome patients receiving colonoscopic and gynaecological surveillance: first report from the prospective Lynch syndrome database. Gut. 2015;0:1–9.

38. Sabine T. Colorectal Cancer. In: Cassidy J, Johnston P, Van Cutsem E, editors. Colorectal Cancer. New York: Informa Healthcare; 2007. p. 131–9.

39. Hamilton SR, Aaltonen LA. Pathology and Genetics of Tumours of the Digestive System. Int Agency Res Cancer. 2006;16(7):8–3.

40. Walsh MD, Buchanan DD, Pearson S-A, Clendenning M, Jenkins MA, Win AK, et al. Immunohistochemical testing of conventional adenomas for loss of expression of mismatch repair proteins in Lynch syndrome mutation carriers: a case series from the Australasian site of the colon cancer family registry. Mod Pathol. 2012;25(5):722–30.

41. Truta B, Chen Y-Y, Blanco AM, Deng G, Conrad PG, Kim YH, et al. Tumor histology helps to identify Lynch syndrome among colorectal cancer patients. Fam Cancer. 2008;7(3):267–74.

42. Bellizzi AM, Frankel WL. Colorectal cancer due to deficiency in DNA mismatch repair function: a review. Adv Anat Pathol. 2009;16(6):405–17.

43. Syngal S, Fox EA, Eng C, Kolodner RD, Garber JE. Sensitivity and specificity of clinical criteria for hereditary non-polyposis colorectal cancer associated mutations in MSH2 and MLH1. J Med Genet. 2000;37(9):641–5.

44. Hampel H, Frankel WL, Martin E, Arnold M, Comeras I, Chapelle A De, et al. Screening for the Lynch Syndrome (Hereditary Nonpolyposis Colorectal Cancer). N Engl J Med. 2005;352(18):1851–60.

45. Snowsill T, Huxley N, Hoyle M, Jones-Hughes T, Coelho H, Cooper C, et al. A systematic review and economic evaluation of diagnostic strategies for Lynch syndrome. Health Technol Assess. 2014;18(58).

46. Thibodeau SN, Bren G, Schaid D. Microsatellite instability in cancer of the proximal colon. Science. 1993;260(5109):816–9.

47. Sinicrope FA, Yang ZJ. Prognostic and predictive impact of DNA mismatch repair in the management of colorectal cancer. Future Oncol. 2011;7(3):467–74.

48. Ribic CM, Sargent DJ, Moore MJ, Thibodeau SN, French AJ, Goldberg RM, et al. Tumor microsatellite-instability status as a predictor of benefit from fluorouracil-based adjuvant chemotherapy for colon cancer. N Engl J Med. 2003;349(3):247–57.

49. Redd DCB, Frank CJ, Feng ZC, Gansler TS, McCreery RL. Raman spectroscopic characterization of human malignant tissues: implications for a percutaneous optical biopsy technique for in-situ tissue diagnosis. In: Cubeddu R, Svanberg S, van den Bergh H, editors. Europto Biomedical Optics ’93. International Society for Optics and Photonics; 1994. p. 185–90.

50. Manoharan R, Wang Y, Boustany N, Brennan JF, Baraga JJ, Dasari RR, et al. Raman spectroscopy for cancer detection : Instrument development and tissue diagnosis. 1994;2328:128–32.

51. Fodor SPA, Copeland RA, Grygon CA, Spiro TG. Deep-ultraviolet Raman excitation profiles and vibronic scattering mechanisms of phenylalanine, tyrosine, and tryptophan. J Am Chem Soc. 1989;111(15):5509–18.

52. Perno JR, Grygon CA, Spiro TG. Ultraviolet Raman excitation profiles for the nucleotides and for the nucleic acid duplexes poly(rA)-poly-(rU) and poly(dG-dC). J Phys Chem. 1989;93(15):5672–8.

53. Manoharan, R. Wang, Y. Dasari, R. R. Singer S. Ultraviolet Resonance Raman Spectroscopy for Detection of Colon Cancer. Lasers Life Sci. 1995;6(4):217–28.

54. Feld MS, Manoharan R, Salenius J, Orensteincarndona J, Römer TJ, Ill JFB, et al. Detection and characterization of human tissue lesions with near-infrared Raman spectroscopy. Proc SPIE. 1995;2388:99–104.

55. Boustany Nada, Manoharan Ramasamy D. Analysis of normal and diseased colon mucosa using ultraviolet resonance Raman spectroscopy. In: Photonics West ’96. 1996. p. 66–70.

56. Boustany NN, Manoharan RY, Dasari RR, Feld MS. Ultraviolet Resonance Raman Spectroscopy of Bulk and Microscopic Human Colon Tissue. Appl Spectrosc. 2000;54(1):1–7.

57. Molckovsky A, Song L-MWK, Shim MG, Marcon NE, Wilson BC. Diagnostic potential of near-infrared Raman spectroscopy in the colon: Differentiating adenomatous from hyperplastic polyps. Gastrointest Endosc. 2003;57(3):396–402.

58. Widjaja E, Zheng W, Huang Z. Classification of colonic tissues using near-infrared Raman spectroscopy and support vector machines. Int J Oncol. 2008;32(3):653–62.

59. Beljebbar A, Bouché O, Diébold MD, Guillou PJ, Palot JP, Eudes D, et al. Identification of Raman spectroscopic markers for the characterization of normal and adenocarcinomatous colonic tissues. Crit Rev Oncol Hematol. 2009;72(3):255–64.

60. Lopes PC, Moreira JA, Almeida A, Esteves A, Gregora I, Ledinsky M, et al. Discriminating adenocarcinoma from normal colonic mucosa through deconvolution of Raman spectra. J Biomed Opt. 2011;16(12):1–12.

61. Wang Z, Zheng W, Lin J, Huang Z. Hyperspectral stimulated Raman scattering and multiphoton imaging for digital pathology of colonic disease. In: SPIE Proceedings. 2016. p. 1–6.

62. Li S, Chen G, Zhang Y, Guo Z, Liu Z, Xu J, et al. Identification and characterization of colorectal cancer using Raman spectroscopy and feature selection techniques. Opt Express. 2014;22(21):25895–908.

63. Chowdary MVP, Kumar KK, Thakur K, Anand A, Kurien J, Krishna CM, et al. Discrimination of normal and malignant mucosal tissues of the colon by Raman spectroscopy. Photomed Laser Surg. 2007;25(4):269–74.

64. Ghanate a D, Kothiwale S, Singh SP, Bertrand D, Krishna CM. Comparative evaluation of spectroscopic models using different multivariate statistical tools in a multicancer scenario. J Biomed Opt. 2011;16(2):1–9.

65. Bi X, Walsh A, Mahadevan-Jansen A, Herline A. Development of spectral markers for the discrimination of ulcerative colitis and Crohn's disease using Raman spectroscopy. Dis Colon Rectum. 2011;54(1):48–53.

66. Bielecki C, Bocklitz TW, Schmitt M, Krafft C, Marquardt C, Gharbi A, et al. Classification of inflammatory bowel diseases by means of Raman spectroscopic imaging of epithelium cells. J Biomed Opt. 2012;17(7):1–8.

67. Ding H, Cao M, DuPont AW, Scott LD, Guha S, Singhal S, et al. Discrimination of inflammatory bowel disease using Raman spectroscopy and linear discriminant analysis methods. In: SPIE Proceedings 9704. 2016. p. 97040W.

68. Mavarani L, Petersen D, El-Mashtoly SF, Mosig A, Tannapfel A, Kötting C, et al. Spectral histopathology of colon cancer tissue sections by Raman imaging with 532 nm excitation provides label free annotation of lymphocytes, erythrocytes and proliferating nuclei of cancer cells. Analyst. 2013;138(14):4035–9.

69. Krafft C, Codrich D, Pelizzo G, Sergo V. Raman and FTIR microscopic imaging of colon tissue: a comparative study. J Biophotonics. 2008;1(2):154–69.

70. Krafft C, Ramoji AA, Bielecki C, Vogler N, Meyer T, Akimov D, et al. A comparative Raman and CARS imaging study of colon tissue. J Biophotonics. 2009;2(5):303–12.

71. Lloyd GR, Wood J, Kendall C, Cook T, Shepherd N, Stone N. Histological imaging of a human colon polyp sample using Raman spectroscopy and self

organising maps. Vib Spectrosc. 2012;60:43–9.

72. Andrade PO, Bitar R a, Yassoyama K, Martinho H, Santo a ME, Bruno PM, et al. Study of normal colorectal tissue by FT-Raman spectroscopy. Anal Bioanal Chem. 2007;387(5):1643–8.

73. Bergholt MS, Zheng W, Lin K, Wang J, Xu H, Ren JL, et al. Characterizing variability of in vivo Raman spectroscopic properties of different anatomical sites of normal colorectal tissue towards cancer diagnosis at colonoscopy. Anal Chem. 2015;87(2):960–6.

74. Cope SE, Freeman TL, Rembacken BJ, Stringer MR, Batchelder DN, Brown SB. Analysis of human colon tissue using Raman spectroscopy. Opt Biopsies Microsc Tech II. 1997;3197:110–4.

75. Boustany NN, Crawford JM, Manoharan R, Dasari RR, Feld MS. Effects of freeze-thaw and photobleaching on the ultraviolet resonance Raman spectra of human colon biopsies. Appl Spectrosc. 2001;55(11):1506–13.

76. Li R, Verreault D, Payne A, Hitchcock CL, Povoski SP, Martin EW, et al. Effects of laser excitation wavelength and optical mode on Raman spectra of human fresh colon, pancreas, and prostate tissues. J Raman Spectrosc. 2014;45(9):773–80.

77. Synytsya A, Judexova M, Hoskovec D, Miskovicova M, Petruzelka L. Raman spectroscopy at different excitation wavelengths (1064, 785 and 532 nm) as a tool for diagnosis of colon cancer. J Raman Spectrosc. 2014;45(10):903–11.

78. Chen K, Qin Y, Zheng F, Sun M, Shi D. Diagnosis of colorectal cancer using Raman spectroscopy of laser-trapped single living epithelial cells. Opt Lett. 2006;31(13):2015–7.

79. Zheng F, Qin Y, Chen K. Sensitivity map of laser tweezers Raman spectroscopy for single-cell analysis of colorectal cancer. J Biomed Opt. 2007;12(3):34002.

80. Scalfi-Happ C, Udart M, Hauser C, Rück A. Investigation of lipid bodies in a colon carcinoma cell line by confocal Raman microscopy. Med Laser Appl. 2011;26(4):152–7.

81. Ranc V, Srovnal J, Kvítek L, Hajduch M. Discrimination of circulating tumor cells of breast cancer and colorectal cancer from normal human mononuclear cells using Raman spectroscopy. Analyst. 2013;138(20):5983–8.

82. Shim MG, Song LWK, Marcon NE, Wilson BC. In vivo Near-infrared Raman Spectroscopy : Demonstration of Feasibility During Clinical Gastrointestinal Endoscopy. Photochem Photobiol. 2000;72(1):146–50.

83. Taketani A, Ishigaki M, Andriana BB, Sato H. Raman endoscopy for real time monitoring of anticancer drug treatment in colorectal tumors of live model mice. In: SPIE BiOS. 2014. p. 1–8.

84. Wood JJ, Kendall C, Hutchings J, Lloyd GR, Stone N, Shepherd N, et al. Evaluation of a confocal Raman probe for pathological diagnosis during colonoscopy. Colorectal Dis. 2014;16(9):732–8.

85. Almond LM, Hutchings J, Lloyd G, Barr H, Shepherd N, Day J, et al. Endoscopic Raman spectroscopy enables objective diagnosis of dysplasia in Barrett's esophagus. Gastrointest Endosc. 2014;79(1):37–45.

86. Li X, Wang Y, Zhang X, Wang D, Lin J. Detection and identification of Colon Cancer and Rectum Cancer Using Fluorescence and Raman Spectrum. Conf Proc IEEE Eng Med Biol Soc. 2005;2:1453–6.

87. Li X, Yang T, Li S, Wang D, Song Y, Zhang S, et al. Raman spectroscopy combined with principal component analysis and k nearest neighbour analysis for non-invasive detection of colon cancer. Laser Phys. 2016;26(3):35702.

88. Jain AK. Data Clustering: 50 Years Beyond K-means. In: Machine Learning and Knowledge Discovery in Databases. Berlin, Heidelberg: Springer Berlin Heidelberg; 2008. p. 698.

89. Almeida JAS, Barbosa LMS, Pais AACC, Formosinho SJ. Improving hierarchical cluster analysis: A new method with outlier detection and automatic clustering. Chemom Intell Lab Syst. 2007;87(2):208–17.

90. Gautam R, Vanga S, Ariese F, Umapathy S. Review of multidimensional data processing approaches for Raman and infrared spectroscopy. EPJ Tech Instrum. 2015;2(1):8.

91. Hutchings J, Kendall C, Shepherd N, Barr H, Stone N. Evaluation of linear discriminant analysis for automated Raman histological mapping of esophageal high-grade dysplasia. J Biomed Opt. 2010;15(6):66015.

92. Li Y, Pan J, Chen G, Li C, Lin S, Shao Y, et al. Micro-Raman spectroscopy study of cancerous and normal nasopharyngeal tissues. J Biomed Opt. 2013;18(2):27003.

93. Hsu C-W, Huang C-C, Sheu J-H, Lin C-W, Lin L-F, Jin J-S, et al. Novel Method for Differentiating Histological Types of Gastric Adenocarcinoma by Using Confocal Raman Microspectroscopy. PLoS One. 2016;11(7):e0159829.

94. Bell J. Support Vector Machines. In: Machine Learning: Hands-On for Developers and Technical Professionals. Indianapolis, IN, USA: John Wiley & Sons, Inc; 2014. p. 139–60.

95. Pyrgiotakis G, Kundakcioglu OE, Finton K, Pardalos PM, Powers K, Moudgil BM. Cell death discrimination with Raman spectroscopy and support vector machines. Ann Biomed Eng. 2009;37(7):1464–73.

96. Sattlecker M, Bessant C, Smith J, Stone N. Investigation of support vector machines and Raman spectroscopy for lymph node diagnostics. Analyst. 2010;135(5):895–901.

97. Khan S, Ullah R, Khan A, Wahab N, Bilal M, Ahmed M. Analysis of dengue infection based on Raman spectroscopy and support vector machine (SVM). Biomed Opt Express. 2016;7(6):2249–56.

98. Agatonovic-Kustrin S, Beresford R. Basic concepts of artificial neural network (ANN) modeling and its application in pharmaceutical research. J Pharm Biomed Anal. 2000;22(5):717–27.

99. Shaver JM. Chemometrics for Raman Spectroscopy. In: Lewis IR, Edwards H, editors. Handbook of Raman spectroscopy from the research laboratory to the process line. CRC Press; 2001. p. 275–306.

100. Gniadecka M, Philipsen PA, Wessel S, Gniadecki R, Wulf HC, Sigurdsson S, et al. Melanoma Diagnosis by Raman Spectroscopy and Neural Networks: Structure Alterations in Proteins and Lipids in Intact Cancer Tissue. J Invest Dermatol. 2004;122(2):443–9.

101. Cover T, Hart P. Nearest neighbor pattern classification. IEEE Trans Inf Theory. 1967;13(1):21–7.

102. Li X, Yang T, Li S, Wang D, Song Y, Zhang S. Raman spectroscopy combined with principal component analysis and k nearest neighbour analysis for non-invasive detection of colon cancer. Laser Phys. 2016;26(3):1–9.

103. Chen Y, Su Y, Ou L, Zou C, Chen Z. Classification of nasopharyngeal cell lines (C666-1, CNE2, NP69) via Raman spectroscopy and decision tree. Vib Spectrosc. 2015;80:24–9.

104. Aitkenhead MJ. A co-evolving decision tree classification method. Expert Syst Appl. 2008;34(1):18–25.

105. Gao Q, Liu Y, Li H, Chen H, Chai Y, Lu F. Comparison of several chemometric methods of libraries and classifiers for the analysis of expired drugs based on Raman spectra. J Pharm Biomed Anal. 2014;94:58–64.

106. Liu W, Sun Z, Chen J, Jing C. Raman Spectroscopy in Colorectal Cancer Diagnostics: Comparison of PCA-LDA and PLS-DA Models. J Spectrosc. 2016;2016:1–6.

107. Dingari NC, Barman I, Saha A, McGee S, Galindo LH, Liu W, et al. Development and comparative assessment of Raman spectroscopic classification algorithms for lesion discrimination in stereotactic breast biopsies with microcalcifications. J Biophotonics. 2013;6(4):371–81.

108. Kemmler M, Denzler J, Rösch P, Popp J. Classification of Microorganisms via Raman Spectroscopy Using Gaussian Processes. In: Goesele M, Roth S, Kuijper A, Schiele B, Schindler K, editors. Pattern Recognition. Springer, Berlin, Heidelberg; 2010. p. 81–90.

109. Kamemoto LE, Misra AK, Sharma SK, Goodman MT, Luk H, Dykes AC, et al. Near-infrared micro-Raman spectroscopy for in vitro detection of cervical cancer. Appl Spectrosc. 2010;64(3):255–61.

110. Fullwood LM, Griffiths D, Ashton K, Dawson T, Lea RW, Davis C, et al. Effect of substrate choice and tissue type on tissue preparation for spectral histopathology by Raman microspectroscopy. Analyst. 2014;139(2):446–54.

111. Kerr LT, Byrne HJ, Hennelly BM. Optimal choice of sample substrate and laser wavelength for Raman spectroscopic analysis of biological specimen. Anal Methods. 2015;7(12):5041–52.

112. Mikoliunaite L, Rodriguez RD, Sheremet E, Kolchuzhin V, Mehner J, Ramanavicius A, et al. The substrate matters in the Raman spectroscopy analysis of cells. Sci Rep. 2015;5:13150.

113. Le Ru E, Etchegoin P. Raman Spectroscopy and related optical techniques. In: Principles of Surface-Enhanced Raman Spectroscopy: and related plasmonic effects. Elsevier; 2008. p. 89–98.

114. Smith, E, Dent G. The Theory of Raman Spectroscopy. In: Modern Raman Spectroscopy: A Practical Approach. Wiley; 2005. p. 71–91.

115. Ferraro J, Nakamoto K, Brown C. Basic Theory. In: Introductory Raman Spectroscopy. 2nd ed. Academic Press; 2003. p. 1–91.

116. B.W Tek “Theory of Raman Scattering” [Internet]. Available from: http://bwtek.com/raman-theory-of-raman-scattering/

117. Nakamoto K. Theory of Normal Vibrations. In: Infrared and Raman Spectra of Inorganic and Coordination Compounds. 6th ed. Wiley; 2009. p. 1–141.

118. Krafft C, Dietzek B, Schmitt M PJ. Raman and coherent anti-Stokes Raman scattering microspectroscopy for biomedical applications. J Biomed Opt. 2012;17(4):1–15.

119. Tsia K. Raman Spectroscopy of Single Cells. In: Understanding Biophotonics: Fundamentals, Advances and Applications. Pan Stanford; 2015. p. 259–300.

120. McCash CNB and EM. Raman Spectroscopy. In: Fundamentals of molecular spectroscopy. 4th ed. McGraw-Hill Publishing Company; 1994. p. 100–24.

121. Stone N. Raman Spectroscopy of biological tissue for application in optical diagnosis of malignancy. Cranfield University; 2001.

122. Krafft C, Popp J. Volume 4: Raman based technologies for biomedical diagnostics. In: Brahme A, editor. Comprehensive Biomedical Physics. Newnes; 2014. p. 189–209.

123. Tu AT. Basic concepts and elementary theory. In: Raman spectroscopy in biology: principles and applications. New York: Wiley-Blackwell; 1982. p. 3–43.

124. Acharya AS, Manning JM. Reaction of glycolaldehyde with proteins: latent crosslinking potential of alpha-hydroxyaldehydes. Proc Natl Acad Sci U S A. 1983;80(12):3590–4.

125. Lieber CA, Mahadevan-Jansen A. Automated Method for Subtraction of Fluorescence from Biological Raman Spectra. Appl Spectrosc. 2003;57(11):1363–7.

126. Ferraro J, Nakamoto K, Brown C. Analytical Chemistry. In: Introductory Raman Spectroscopy. 2nd ed. Academic Press; 2003. p. 267–92.

127. Patel II, Trevisan J, Evans G, Llabjani V, Martin-Hirsch PL, Stringfellow HF, et al. High contrast images of uterine tissue derived using Raman microspectroscopy with the empty modelling approach of multivariate curve resolution-alternating least squares. Analyst. 2011;136(23):4950–9.

128. Azzouz T, Tauler R. Application of multivariate curve resolution alternating least squares (MCR-ALS) to the quantitative analysis of pharmaceutical and agricultural samples. Talanta. 2008;74(5):1201–10.

129. Felten J, Hall H, Jaumot J, Tauler R, de Juan A, Gorzsás A. Vibrational spectroscopic image analysis of biological material using multivariate curve resolution–alternating least squares (MCR-ALS). Nat Protoc. 2015;10(2):217–40.

130. Stone N. Raman Spectroscopy of Biological Tissue for Application in Optical Diagnosis of Malignancy. Cranfield University; 2001.

131. Zhu W, Zeng N, Wang N. Sensitivity , Specificity , Accuracy , Associated Confidence Interval and ROC Analysis with Practical SAS Implementations. NESUG Heal Care Life Sci. 2010;1–9.

132. Mosier-Boss PA, Lieberman SH, Newbery R. Fluorescence Rejection in Raman Spectroscopy by Shifted-Spectra, Edge Detection, and FFT Filtering Techniques. Appl Spectrosc. 1995;49(5):630–8.

133. Ferraro JR, Nakamoto K. Instrumentation and Experimental Techniques. In: Introductory Raman Spectroscopy. 2nd ed. Academic Press; 2003. p. 137.

134. Vlček Jr. A, Farrell IR, Liard DJ, Matousek P, Towrie M, Parker AW, et al. Early photochemical dynamics of organometallic compounds studied by ultrafast time-resolved spectroscopic techniques. J Chem Soc Dalt Trans. 2002;(5):701–12.

135. Gebrekidan MT, Knipfer C, Stelzle F, Popp J, Will S, Braeuer A. A shifted-excitation Raman difference spectroscopy (SERDS) evaluation strategy for the efficient isolation of Raman spectra from extreme fluorescence interference. J Raman Spectrosc. 2016;47:198–209.

136. Bramfitt BL, Benscoter AO. Metallographer's Guide: Practice and Procedures for Irons and Steels. ASM International; 2001. 354 p.

137. Licheron M, Montouillout V, Millot F, Neuville DR. Raman and 27Al NMR structure investigations of aluminate glasses: (1−x)Al2O3−x MO, with M=Ca, Sr, Ba and 0.5<x<0.75). J Non Cryst Solids. 2011;357(15):2796–801.

138. Dai H. Raman Spectroscopic Studies of Human Tumors. ProQuest Dissertations Publishing; 2008.

139. Olsson C-O., Landolt D. Passive films on stainless steels—chemistry, structure and growth. Electrochim Acta. 2003;48(9):1093–104.

140. Hedberg Y, Karlsson M-E, Blomberg E, Odnevall Wallinder I, Hedberg J. Correlation between surface physicochemical properties and the release of iron from stainless steel AISI 304 in biological media. Colloids Surf B Biointerfaces. 2014;122:216–22.

141. Nakanishi K, Sakiyama T, Imamura K. On the adsorption of proteins on solid surfaces, a common but very complicated phenomenon. J Biosci Bioeng. 2001;91(3):233–44.

142. Huang WM, Gibson SJ, Facer P, Gu J, Polak JM. Improved section adhesion for immunocytochemistry using high molecular weight polymers of l-lysine as a slide coating. Histochemistry. 1983;77(2):275–9.

143. Kiernan J. Histological & Histochemical Methods Theory and Practice. 3rd ed. Histological & Histochemical Methods Theory and Practice. Taylor & Francis Group; 2000. 477 p.

144. Pappas PW. The use of a chrome alum-gelatin (subbing) solution as a general adhesive for paraffin sections. Stain Technol. 1971 May;46(3):121–4.

145. Kang C-K, Lee Y-S. The surface modification of stainless steel and the correlation between the surface properties and protein adsorption. J Mater Sci Mater Med. 2007;18(7):1389–98.

146. Jussila P, Ali-Löytty H, Lahtonen K, Hirsimäki M, Valden M. Effect of surface hydroxyl concentration on the bonding and morphology of aminopropylsilane thin films on austenitic stainless steel. Surf Interface Anal. 2010;42(3):157–64.

147. Zammarelli N, Luksin M, Raschke H, Der RH, Weberskirch R. “ Grafting-from ” Polymerization of PMMA from Stainless Steel Surfaces by a RAFT-Mediated Polymerization Process. Langmuir. 2013;29:12834–12843.

148. Chovelon JM, Aarch LE, Charbonnier M, Romand M. Silanization of Stainless Steel Surfaces: Influence of Application Parameters. J Adhes. 1995;50(1):43–58.

149. Faoláin EO, Hunter MB, Byrne JM, Kelehan P, Lambkin H a, Byrne HJ, et al. Raman spectroscopic evaluation of efficacy of current paraffin wax section dewaxing agents. J Histochem Cytochem. 2005;53(1):121–9.

150. Lyng F, Gazi E, Gardner P. Preparation of Tissues and Cells for Infrared and Raman Spectroscopy and Imaging. Biomed Appl Synchrotron Infrared Microspectrosc. 2011;145–89.

151. Nallala J, Lloyd GR, Stone N. Evaluation of different tissue de-paraffinization procedures for infrared spectral imaging. Analyst. 2015;2369–75.

152. Yuan W, Lin YS, Yang W. Molecular sieving MFI-type zeolite membranes

for pervaporation separation of xylene isomers. J Am Chem Soc. 2004;126(15):4776–7.

153. Mittal KL, editor. Advances in Contact Angle, Wettability and Adhesion, Volume Two. John Wiley & Sons; 2015. 464 p.

154. Botsaris G, Glazman Y. Interfacial Phenomena in Coal Technology. CRC Press; 1988. 301 p.

155. Miller LS, Mullin JB, editors. Electronic Materials: From Silicon to Organics. New York: Springer Science & Business Media; 2012. 542 p.

156. Piva JAAC, Silva JLR, Raniero L, Martin AA, Bohr HG, Jalkanen KJ. Overview of the use of theory to understand infrared and Raman spectra and images of biomolecules: colorectal cancer as an example. Theor Chem Acc. 2011;130(4–6):1261–73.

157. Devpura S, Thakur JS, Poulik JM, Rabah R, Naik VM, Naik R. Raman spectroscopic investigation of frozen and deparaffinized tissue sections of pediatric tumors: neuroblastoma and ganglioneuroma. J Raman Spectrosc. 2013;44(3):370–6.

158. Gąsior-Głogowska M, Komorowska M, Hanuza J, Ptak M, Kobielarz M. Structural alteration of collagen fibres--spectroscopic and mechanical studies. Acta Bioeng Biomech / Wrocław Univ Technol. 2010;12(4):55–62.

159. Nguyen TT, Gobinet C, Feru J, -Pasco SB, Manfait M, Piot O. Characterization of Type I and IV Collagens by Raman Microspectroscopy: Identification of Spectral Markers of the Dermo-Epidermal Junction. Spectrosc An Int J. 2012;27(5):421–7.

160. Barrett TW, Peticolas WL, Robson RM. Laser Raman light-scattering observations of conformational changes in myosin induced by inorganic salts. Biophys J. 1978;23(3):349–58.

161. Carew EB, Stanley HE, Seidel JC, Gergely J. Studies of myosin and its proteolytic fragments by laser Raman spectroscopy. Biophys J. 1983;44(2):219–24.

162. de Jong BWD, Bakker Schut TC, Wolffenbuttel KP, Nijman JM, Kok DJ, Puppels GJ. Identification of bladder wall layers by Raman spectroscopy. J Urol. 2002;168(4 Pt 2):1771–8.

163. Ashton L, Pudney PDA, Blanch EW, Yakubov GE. Understanding glycoprotein behaviours using Raman and Raman optical activity spectroscopies: characterising the entanglement induced conformational changes in oligosaccharide chains of mucin. Adv Colloid Interface Sci. 2013;199–200:66–77.

164. Faoláin EO, Hunter MB, Byrne JM, Kelehan P, Lambkin H a, Byrne HJ, et al. Raman spectroscopic evaluation of efficacy of current paraffin wax section dewaxing agents. J Histochem Cytochem. 2005;53(1):121–9.

165. Ackerstaff E, Glunde K, Bhujwalla ZM. Choline phospholipid metabolism: a

target in cancer cells? J Cell Biochem. 2003;90(3):525–33.

166. Shoulders MD, Raines RT. Collagen structure and stability. Annu Rev Biochem. 2009;78:929–58.

167. Johansson ME V, Ambort D, Pelaseyed T, Schütte A, Gustafsson JK, Ermund A, et al. Composition and functional role of the mucus layers in the intestine. Cell Mol Life Sci. 2011;68(22):3635–41.

168. Fogg FJ, Hutton DA, Jumel K, Pearson JP, Harding SE, Allen A. Characterization of pig colonic mucins. Biochem J. 1996;316:937–42.

169. Lichtenberger LM. The hydrophobic barrier properties of gastrointestinal mucus. Annu Rev Physiol. 1995;57:565–83.

170. Bresalier R, Ho S, Schoeppner H, Kim Y, Sleisenger M, Brodt P, et al. Enhanced sialylation of mucin-associated carbohydrate structures in human colon cancer metastasis. Gastroenterology. 1996;110(5):1354–67.

171. Kufe DW. Mucins in cancer: function, prognosis and therapy. Nat Rev Cancer. 2009;9(12):874–85.

172. Mekenkamp LJM, Heesterbeek KJ, Koopman M, Tol J, Teerenstra S, Venderbosch S, et al. Mucinous adenocarcinomas: poor prognosis in metastatic colorectal cancer. Eur J Cancer. 2012;48(4):501–9.

173. Pascut FC, Goh HT, Welch N, Buttery LD, Denning C, Notingher I. Noninvasive detection and imaging of molecular markers in live cardiomyocytes derived from human embryonic stem cells. Biophys J. 2011;100(1):251–9.

174. Lewis AT, Gaifulina R, Isabelle M, Dorney J, Woods ML, Lloyd GR, et al. Mirrored stainless steel substrate provides improved signal for Raman spectroscopy of tissue and cells. J Raman Spectrosc. 2016;48(1):119–125.

175. Baenke F, Peck B, Miess H, Schulze A. Hooked on fat: the role of lipid synthesis in cancer metabolism and tumour development. Dis Model Mech. 2013;6(6):1353–63.

176. Paspatis GA, Zizi A, Chlouverakis GJ, Giannikaki ES, Vasilakaki T, Elemenoglou I, et al. Proliferative patterns of rectal mucosa as predictors of advanced colonic neoplasms in routinely processed rectal biopsies. Am J Gastroenterol. 1998;93(9):1472–7.

177. Hajian-Tilaki K. Receiver Operating Characteristic (ROC) Curve Analysis for Medical Diagnostic Test Evaluation. Casp J Intern Med. 2013;4(2):627–35.

178. Dessì S, Batetta B, Pulisci D, Spano O, Anchisi C, Tessitore L, et al. Cholesterol content in tumor tissues is inversely associated with high-density lipoprotein cholesterol in serum in patients with gastrointestinal cancer. Cancer. 1994;73(2):253–8.

179. Beloribi-Djefaflia S, Vasseur S, Guillaumond F. Lipid metabolic

reprogramming in cancer cells. Oncogenesis. 2016;5(1):1–10.

180. Hodgson S V., Foulkes WD, Eng C, Maher E. Inherited Cancer Predisposing Syndromes. In: A Practical Guide to Human Cancer Genetics. 4th ed. Springer Science & Business Media; 2013. p. 257–64.

181. Lengauer C, Kinzler KW, Vogelstein B. Genetic instability in colorectal cancers. Nature. 1997;386(6625):623–7.

182. Chan ECY, Koh PK, Mal M, Cheah PY, Eu KW, Backshall A, et al. Metabolic profiling of human colorectal cancer using high-resolution magic angle spinning nuclear magnetic resonance (HR-MAS NMR) spectroscopy and gas chromatography mass spectrometry (GC/MS). J Proteome Res. 2009;8(1):352–61.

183. Vander Heiden MG, Cantley LC, Thompson CB. Understanding the Warburg effect: the metabolic requirements of cell proliferation. Science. 2009;324(5930):1029–33.

184. Yang K, Li H, Dong J, Dong Y, Wang CZ. Expression profile of polyunsaturated fatty acids in colorectal cancer. World J Gastroenterol. 2015;21(8):2405–12.

185. Su Lim C, Sun Kim E, Yeon Kim J, Taek Hong S, Jai Chun H, Eun Kang D, et al. Measurement of the Nucleus Area and Nucleus/Cytoplasm and Mitochondria/Nucleus Ratios in Human Colon Tissues by Dual-Colour Two-Photon Microscopy Imaging. Sci Rep. 2015;5:18521.

186. Mills SJ, Mathers JC, Chapman PD, Burn J, Gunn A. Colonic crypt cell proliferation state assessed by whole crypt microdissection in sporadic neoplasia and familial adenomatous polyposis. Gut. 2001;48(1):41–6.

187. Denkert C, Budczies J, Weichert W, Wohlgemuth G, Scholz M, Kind T, et al. Metabolite profiling of human colon carcinoma--deregulation of TCA cycle and amino acid turnover. Mol Cancer. 2008;7(1):72.

188. Pînzaru SC, Andronie LM, Domsa I, Cozar O, Astilean S. Bridging biomolecules with nanoparticles: surface-enhanced Raman scattering from colon carcinoma and normal tissue. J Raman Spectrosc. 2008;39(3):331–4.

189. Petersen I, Staarmann J, Kotb WFA, Petersen I. DNA ploidy and morphology of colon tumors in the adenoma–carcinoma sequence. Folia Histochem Cytobiol. 2015;53(1):11–8.

190. Habermann JK, Brucker CA, Freitag-Wolf S, Heselmeyer-Haddad K, Krü Ger S, Barenboim L, et al. Genomic instability and oncogene amplifications in colorectal adenomas predict recurrence and synchronous carcinoma. Mod Pathol. 2010;24(4):542–55.

191. Grohmann U, Mondanelli G, Belladonna ML, Orabona C, Pallotta MT, Iacono A, et al. Amino-acid sensing and degrading pathways in immune regulation. Cytokine Growth Factor Rev. 2017;35:37–45.

192. Travers MT, Gow IF, Barber MC, Thomson J, Shennan DB. Indoleamine

2,3-dioxygenase activity and L-tryptophan transport in human breast cancer cells. Biochim Biophys Acta - Biomembr. 2004;1661(1):106–12.

193. Carr EL, Kelman A, Wu GS, Gopaul R, Senkevitch E, Aghvanyan A, et al. Glutamine Uptake and Metabolism Are Coordinately Regulated by ERK/MAPK during T Lymphocyte Activation. J Immunol. 2010;185(2):1037–44.

194. Crawford J, Cohen HJ. The essential role of L-glutamine in lymphocyte differentiation in vitro. J Cell Physiol. 1985;124(2):275–82.

195. Rodriguez PC, Quiceno DG, Ochoa AC. L-arginine availability regulates T-lymphocyte cell-cycle progression. Blood. 2007;109(4):1568–73.

196. Lee GK, Park HJ, Macleod M, Chandler P, Munn DH, Mellor AL. Tryptophan deprivation sensitizes activated T cells to apoptosis prior to cell division. Immunology. 2002;107(4):452–60.

197. Gaifulina R, Maher AT, Kendall C, Nelson J, Rodriguez-Justo M, Lau K, et al. Label-free Raman spectroscopic imaging to extract morphological and chemical information from a formalin-fixed, paraffin-embedded rat colon tissue section. Int J Exp Pathol. 2016;97(4):337–50.

198. Isabelle M, Dorney J, Lewis A, Lloyd GR, Old O, Shepherd N, et al. Multi-centre Raman spectral mapping of oesophageal cancer tissues: a study to assess system transferability. Faraday Discuss. 2016;187:87–103.

199. Chun Yong Chan E, Koon Koh P, Mal M, Yean Cheah P, Weng Eu K, Backshall A, et al. Metabolic Profiling of Human Colorectal Cancer Using High-Resolution Magic Angle Spinning Nuclear Magnetic Resonance (HR-MAS NMR) Spectroscopy and Gas Chromatography Mass Spectrometry (GC/MS). J Proteome Res. 2009;8(1):352–61.

200. Capper D, Voigt A, Bozukova G, Ahadova A, Kickingereder P, von Deimling A, et al. BRAF V600E-specific immunohistochemistry for the exclusion of Lynch syndrome in MSI-H colorectal cancer. Int J cancer. 2013;133(7):1624–30.

201. Bratchenko IA, Artemyev DN, Myakinin OO, Khristoforova YA, Moryatov AA, Kozlov S V., et al. Combined Raman and autofluorescence ex vivo diagnostics of skin cancer in near-infrared and visible regions. J Biomed Opt. 2017;22(2):27005.